Plasmonic resonances of metallic nanoparticles in arrays and in isolation

Submitted by Christopher Burrows

to the University of Exeter
as a thesis for the degree of

Doctor of Philosophy in Physics

October 2010

I certify that all material in this thesis which is not my own work has been identified and that no material has previously been submitted and approved for the award of a degree by this or any other university.

Signature _____

Abstract

Plasmonics is the branch of photonics that is concerned with the interactions which take place between metallic structures and incident electromagnetic radiation. It is a field which has seen a recent resurgence of interest, predominantly due to the emerging fields of metamaterials and sub-wavelength optics. The original work contained within this thesis is concerned with the plasmonic resonances of metallic nanoparticles which can be excited with visible light. These structures have been placed in a variety of configurations, and the optical response of each of these configurations has been probed both experimentally, and with numerical simulations.

The first chapter contains some background and describes some recent advances in the literature, set against the broad background of more general concepts which are important in plasmonics.

The best starting point in describing the response of plasmonic systems is to consider individual metallic particles and this is the subject of the second chapter. Three separate modelling techniques are described and compared, and dark-field spectroscopy is used to produce experimental scattering spectra of single particles which support dipolar and higher order modes. Mie theory is used as a starting point in understanding these modes, and finite element method (FEM) modelling is used to make numerical comparisons with dark-field data.

When two plasmonic particles are placed close to each other, interactions take place between them and their response is modified, sometimes considerably. This effect can be even stronger if particles are placed in large arrays. Interactions between the dipolar modes of gold particles form the basis of the third chapter. The discussion begins with pairs of particles, and the coupled dipole approximation (CDA) is introduced to describe the response. Ordered square arrays are considered and different modelling techniques are compared to experimental data. Also, random arrays have been investigated with a view to inferring the extinction spectrum of a single particle from a carefully chosen array of particles in which the inter-particle interactions are suppressed.

The fourth chapter continues the theme of particles interacting in arrays, but the particles considered support quadrupolar modes (and they are silver instead of gold). The optical response is strongly modified, and an explanation is provided which overturns the accepted explanation.

The final chapter of new results is somewhat different to the others in that a very different structure is considered and different parameters are extracted. Instead of far-field quantities, here, near-fields of composite structures are of interest; they can generate greatly enhanced fields in the vicinity of the structure. These enhanced fields, in turn, enhance the fluorescence and Raman emission of nearby dye molecules. A novel field integration technique is proposed which aims to mimic the experiments which were carried out using fluorescence confocal microscopy.

Acknowledgements

I would like to thank a number of people who have given me help and advice over the past three years. Firstly I would like to thank Bill Barnes, my supervisor whose style of supervision has given support whilst providing me with a degree of autonomy, without which any successes arising from this project would have been dissatisfying in comparison. I would also like to thank Bill for chairing "back to basics" meetings in which my (and others') understanding of basic plasmonics improved significantly. Finally, Bill's talent for scientific writing has been impressive to witness, and I am sure that the lessons I have learnt from him will be useful in the future. I should also like to mention Chris Lawrence, my supervisor at QinetiQ, for his sense of humour during his visits, and for his refreshing ideas for possible applications. Thanks also to Chris, along with GWR for funding this project.

In the Electromagnetic Materials group I have been assisted by a number of people who deserve my gratitude. The time I was sharing an office with George Zoriniants was the most productive and enjoyable period of this project. I learnt something new from him every day and he was always a patient teacher. I hope we are able to keep in touch as we have been since he left for Cardiff. Andy Murray's help with equipment was invaluable, and he even had a go at fixing the SEM several months after his contract finished (!). He always made time to help me early on in the project and I'm grateful for that. Baptiste Auguié also spent a great deal of time with me, and his dedication to understanding difficult concepts was enviable. I'm sure the odd innocent question from me may have spawned a weekend-long literature search, and as a result of that he would always respond with a full and helpful answer. The other plasmonics student who was always on hand to have a useful discussion with was James Parsons. Figuring things out together was enjoyable and satisfying. Since he moved to AMOLF, his absence has been noticeable and I have missed having the opportunity to discuss optical plasmonics with a fellow PhD student.

I have known GP Srivastava for many years and I would like to thank him not only for his support as my mentor but for his assistance throughout my undergraduate days as well.

Someone I never anticipated working with during this project was Sasha Grigorenko, yet the collaboration with him allowed me to extend my area of study beyond what was originally intended. It was fascinating to observe Sasha at work in Manchester, and his dedication to only carrying out truly original research was inspiring.

I have shared offices with several people, all of whom I would like to thank for their support. Particularly I would like to thank Tomek Trzeciak who started at the same time as me and left at the same time to pursue a similar career to me. He was my "Matlab Helpdesk", and taught me some programming tricks which became very useful. I'm looking forward to meeting up with him again soon. Also, more recently, I would like to thank Ciaran Stewart, Bert, James Edmunds and Evgeny Sirotkin for being on hand to keep me calm while I have been writing

up. Also, thanks to the rest of the group for their input during group meetings, and Steve Luke whom I regularly visited to let off steam.

The support staff are often neglected when the focus is on research, but they all play important roles. Of all those who helped me specifically, I would like to thank Chris Forrest for getting me through a hard-disk crash and a laptop failure, and also Dave Anderson for being on hand to sort the EBL system, or contact the engineers on the many recent occasions when it was out of action.

Finally, and most importantly, I would like to thank the people who have supported me behind the scenes. Sharon, Rob King and Judy Mead have been far more important than they realise in getting me to where I am today. Also, everyone in my family has been amazing, past and present. I would, however, like to say a very special thank you to my cousin Paul for his pragmatic advice, grizzly bears and all!

Contents

List of Figures

Chapter 1

The optical response of metallic nanoparticles

1.1 Introduction to particle plasmons

When a metal particle is subject to an external, static, electric field, the conduction electrons are relatively free to move in the opposite direction to the field. As a result, a net negative charge accumulates on one side of the particle, and a net positive charge remains at the other side, hence a dipole is induced. The important consequence of this separation of charge is that the net negative charge on one side is attracted by the net positive charge on the other, and *vice versa*. This is in contrast to an infinite, bulk metal, where no surfaces are present to confine the charges. This attraction acts as a restoring force on the electrons in the particle, hence, from elementary harmonic motion, it is clear that a resonant condition will exist if a time-varying electric field is applied. To begin with, Newton's second law can be written as follows (where $\mathbf{F}$ is the net force, m is the mass of the particle in motion and $\mathbf{r}$ is the particle's position):

$$\mathbf{F} = m\frac{d^2\mathbf{r}}{dt^2} \tag{1.1.1}$$

Initially, the driving force may be neglected and it can be seen that the charges are displaced from equilibrium and are subject solely to the restoring force $\mathbf{F}_r$:

$$m\frac{d^2\mathbf{r}}{dt^2} = \mathbf{F}_r(t) \tag{1.1.2}$$

Assuming a harmonic solution of the form $\mathbf{r} = \mathbf{r}_0 e^{i\omega t}$ and $\mathbf{F}_r = \mathbf{F}_{r,0} e^{i\omega t}$, and if the restoring force is proportional to the displacement (as in Hooke's law), we obtain:

$$-\omega^2 m\mathbf{r} = -k\mathbf{r} \tag{1.1.3}$$

and hence the frequency of oscillation is expressed as

$$\omega = \sqrt{\frac{k}{m}} \tag{1.1.4}$$

This is a highly simplified and general case, but it demonstrates that the existence of a restoring force in a static situation alone is sufficient information to be able to recognise and calculate the natural frequency of oscillation of the system, be it a mass on a spring or an electron in a nanoparticle. The oscillation of electrons in such a nanoparticle is known as a particle plasmon (also called a localised surface plasmon resonance, LSPR). For metallic nanoparticles, these resonances can occur in the visible range, and the nanoparticles scatter light strongly at this wavelength — see figure 1.1.1.

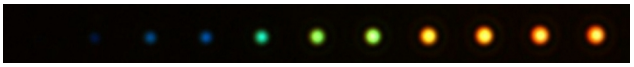

Figure 1.1.1: A dark-field microscope image of 50nm thick silver discs (diameter 50 to 150nm) surrounded by glass. This demonstrates the dependence of the resonance wavelength on the geometry of the particles.

1.2 Material parameters

It is worthwhile, at this stage, to consider the reason that the optical properties of metals allow such a restoring force to be produced. This effect can be described quantitatively in terms of the frequency dependent permittivity (or refractive index — the two are interchangeable for non-magnetic materials). The frequency dependence of these parameters, i.e. the dispersion, is key to many of the optical effects which shall be discussed in this thesis. Dispersion gives rise to atmospheric optical phenomena such as rainbows and glories[1] due to the frequency-dependent refractive index of water across the visible range. Similar effects can be seen with glass prisms which disperse white light over a range of angles. Though these are clear demonstrations of dispersion, the level of variation is very small compared to that exhibited by a metal such as silver over the same frequency range. As my research is concerned with the optical properties of structures made of noble metals, a survey of the optical properties of the bulk materials is a good place to start the discussion.

1.2.1 The Drude-Lorentz model

The frequency response of many materials can be described by the Drude-Lorentz model.[2] This model considers the effect of applying a time-varying electric field on the electrons within

a bulk medium. The analysis begins by calculating the net force on an electron in the material which is bound to its ion core.

$$m\frac{\partial^2 \mathbf{r}}{\partial t^2} = q\mathbf{E} - G\frac{\partial \mathbf{r}}{\partial t} - C\mathbf{r} \tag{1.2.1}$$

Here, m is the mass of an electron, q is the charge on the electron, $\mathbf{r}$ is the electron's displacement from equilibrium, $\mathbf{E}$ is the applied electric field, G is the damping constant and C is the restoring force. Hence, the first term on the right describes the force the electron experiences as a result of the applied field, the second term denotes the force due to damping through electron scattering and the third term is due to the attraction of the electron to the ion core (i.e. the restoring force). If we allow the position of the electron to adopt a harmonic oscillation at the same frequency as the electric field (much like the general case for simple harmonic motion) we can substitute $\mathbf{E} = \mathbf{E}_0 e^{-i\omega t}$ and $\mathbf{r} = \mathbf{r}_0 e^{-i\omega t}$. This produces:

$$-\omega^2 m\mathbf{r} = q\mathbf{E} + i\omega G\mathbf{r} - C\mathbf{r} \tag{1.2.2}$$

This equation of motion becomes clearer if we make the driving term the subject:

$$q\mathbf{E} = -i\omega G\mathbf{r} + C\mathbf{r} - \omega^2 m\mathbf{r} \tag{1.2.3}$$

There are three regimes in this system — low frequency, high frequency and on resonance. At high frequencies the ω^2 term dominates and we are in the regime where the electron is effectively a free particle and there is no force acting to restore it to equilibrium or damp its motion. There is also a π phase difference between the applied field and the motion:

$$q\mathbf{E} = -\omega^2 m\mathbf{r} \tag{1.2.4}$$

At low frequencies, the terms which include ω are negligible, so the force applied by the electric field is supported by the restoring force — this is analogous to Hooke's law and represents the quasi-static limit in which there is no phase difference.

$$q\mathbf{E} = C\mathbf{r} \tag{1.2.5}$$

On resonance, the damping term dominates and acts to constrain the velocity and hence the displacement of the electrons. This equation indicates that the displacement lags the electric field by $\pi/2$:

$$q\mathbf{E} = -i\omega G\mathbf{r} \tag{1.2.6}$$

Equation 1.2.3 can be rewritten in the following form:

$$\mathbf{r} = \frac{q\mathbf{E}}{-i\omega G + C - \omega^2 m} = \frac{q\mathbf{E}/m}{-i\omega\frac{G}{m} + \frac{C}{m} - \omega^2} \tag{1.2.7}$$

This can be tidied up by making these substitutions $\gamma = \frac{G}{m}$ and $\omega_0 = \sqrt{\frac{C}{m}}$, where ω_0 is the resonant frequency:

$$\mathbf{r} = \frac{q\mathbf{E}/m}{-i\omega\gamma + \omega_0^2 - \omega^2} \tag{1.2.8}$$

It can now be seen that on resonance, the position of the electron as a function of time is governed by the damping term in the denominator of equation 1.2.8.

We now have all the tools we need to begin to describe the frequency response of a generic material in the form of a permittivity, ϵ. We begin by expressing the polarisation as a density of individual dipole moments and make a helpful substitution for the electric susceptibility ($\chi = \epsilon - 1$):

$$\mathbf{P} = N\mathbf{p} = Nq\mathbf{r} = \epsilon_0\chi\mathbf{E} = \epsilon_0(\epsilon - 1)\mathbf{E} \tag{1.2.9}$$

where $\mathbf{P}$ is the dipole density and $\mathbf{p}$ is the dipole moment produced by displacing an electron of charge q a distance $\mathbf{r}$ from its equilibrium position. Until this point we have been considering individual dipoles, but now we need to transform 1.2.8 to describe the response of entire materials. Upon substituting equation 1.2.8 into equations 1.2.9 we arrive at the following expression for the relative permittivity of a metal:

$$\epsilon = 1 + \frac{Nq^2/m}{\epsilon_0(-i\omega\gamma + \omega_0^2 - \omega^2)} \tag{1.2.10}$$

This is commonly written slightly differently, and with the the plasma frequency included $\omega_p = \sqrt{\frac{Nq^2}{\epsilon_0 m}}$:

$$\epsilon = 1 - \frac{\omega_p^2}{\omega^2 - \omega_0^2 + i\omega\gamma} \tag{1.2.11}$$

The real and imaginary parts of the Drude-Lorentz permittivity are shown in figure 1.2.1. The imaginary part peaks at ω_0 and at the same point the real part crosses the origin.

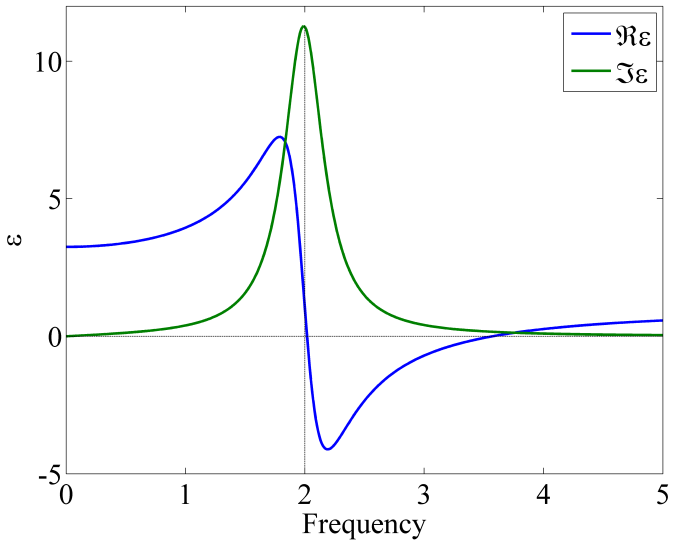

Figure 1.2.1: The Drude-Lorentz permittivity (real and imaginary) for a hypothetical material (in order to illustrate the main features) with $\omega_0 = 2$, $\omega_p = 3$, and $\gamma = 0.4$.

1.2.2 The Drude model

A special case of the Drude-Lorentz model is where there is no restoring force due to the Coulomb interaction between the electrons and the ion cores* (this is equivalent to setting the resonant frequency to be equal to zero). This is simply known as the Drude model and is used to describe only the free electrons — hence it provides a good description for metals. As an applied electric field interacts so strongly with the conduction electrons, it seems sensible to neglect the restoring force, and indeed the full Drude-Lorentz model only needs to be applied to dielectrics where the electrons are tightly bound to the atoms. The Drude response is given below and plotted in figure 1.2.2.

$$\epsilon = 1 - \frac{\omega_p^2}{\omega^2 + i\omega\gamma} \tag{1.2.12}$$

*For greater accuracy, one should take a weighted sum of the contributions from all the electronic states of the atom.

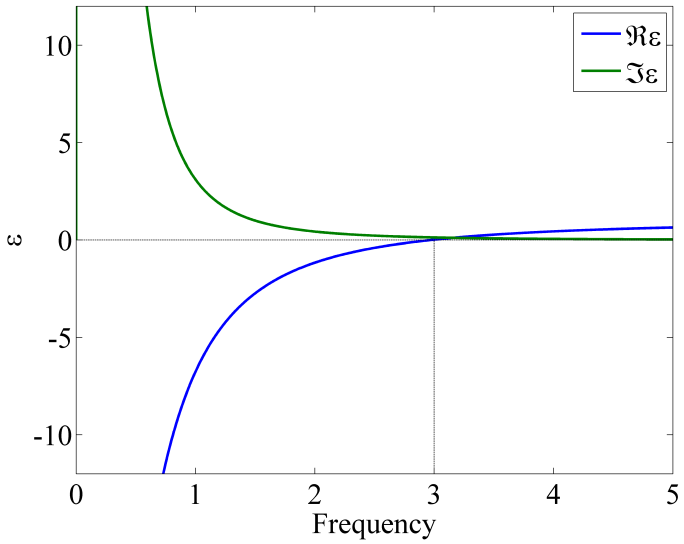

Figure 1.2.2: The Drude model of a hypothetical material shows no resonance compared to the Drude-Lorentz model — the 'spring constant' has been set to zero. The plasma frequency is $\omega_p = 3$ which is the point at which the real part of the permittivity changes from positive to negative.

The most important feature of the Drude-model is that the real part of the permittivity becomes negative below the plasma frequency ω_p. At frequencies lower than ω_p, the material is said to be 'metallic' due to the fact that the electrons in the surface of the material respond to the incident field in antiphase. Hence, their out-of-phase oscillations act to produce a reflected field. A propagating field is given as follows (ignoring time oscillations):

$$E = E_0 e^{ikx} = E_0 e^{ink_0 x} = E_0 e^{i\sqrt{\epsilon}k_0 x} \tag{1.2.13}$$

where n is the refractive index of the material and k_0 is the free-space wave number. If the real part of the permittivity is negative the plane wave can no longer propagate and the wave becomes an exponentially decaying evanescent wave:

$$E = E_0 e^{i\sqrt{\epsilon}k_0 x} = E_0 e^{i\sqrt{-|\epsilon|}k_0 x} = E_0 e^{-\sqrt{|\epsilon|}k_0 x} \tag{1.2.14}$$

For most calculations it is preferable to use permittivity values which have been measured experimentally as the Drude model is a first approximation. It does, however, give excellent physical insight into the behaviour of conduction electrons which have been excited by an incident, time-harmonic field. Two commonly used sources of permittivity values for bulk silver and gold are those of Palik[3] and Johnson & Christy.[4]

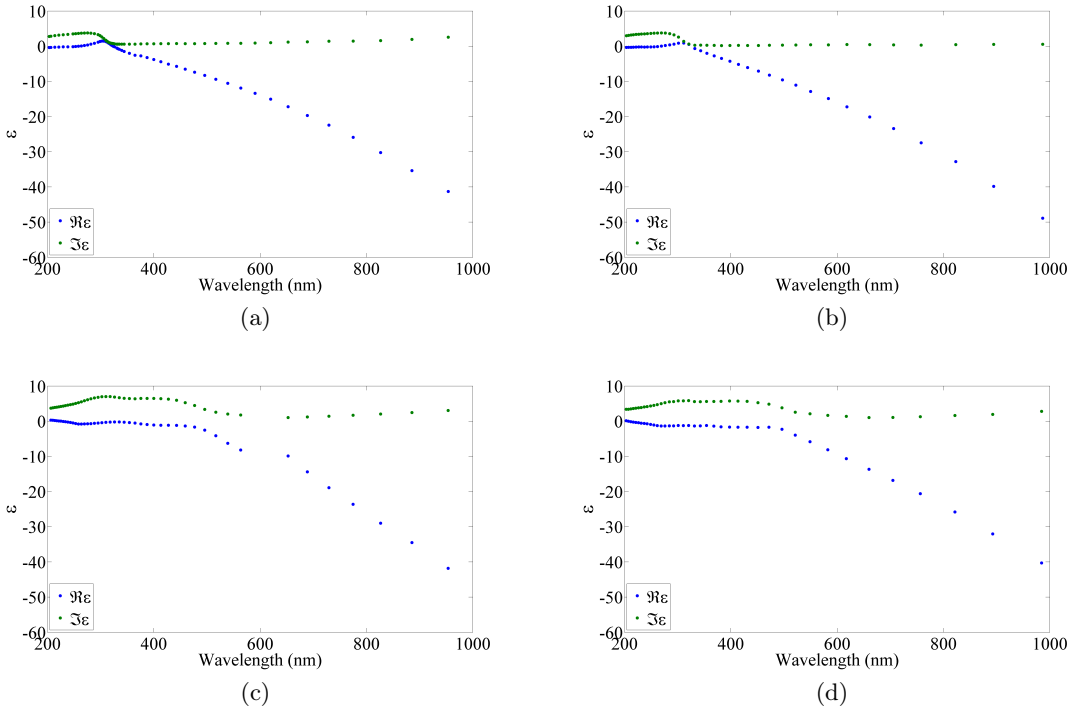

Figure 1.2.3: Real and imaginary permittivity values for (a) Ag from Palik, (b) Ag from Johnson & Christy, (c) Au from Palik and (d) Au from Johnson & Christy. Note that these figures are plotted as functions of wavelength as opposed to frequency (figure 1.2.2).

It can be seen from figure 1.2.3 that for silver, the permittivity values measured by Palik and Johnson & Christy are very similar, though there are more discrepancies between the values for gold from the two sources. The Palik data are sourced from two data-sets, and the cross-over shows a discontinuity at around 600nm which is undesirable. For this reason, I have chosen to use the Johnson & Christy values for gold, and the Palik values for silver (this is consistent with a large proportion of the literature).

For numerical modelling it may be necessary to carry out calculations for frequencies other than the specific values provided here experimentally. In this situation I have used a cubic spline to interpolate the values. An example of such a fit is shown in figure 1.2.4.

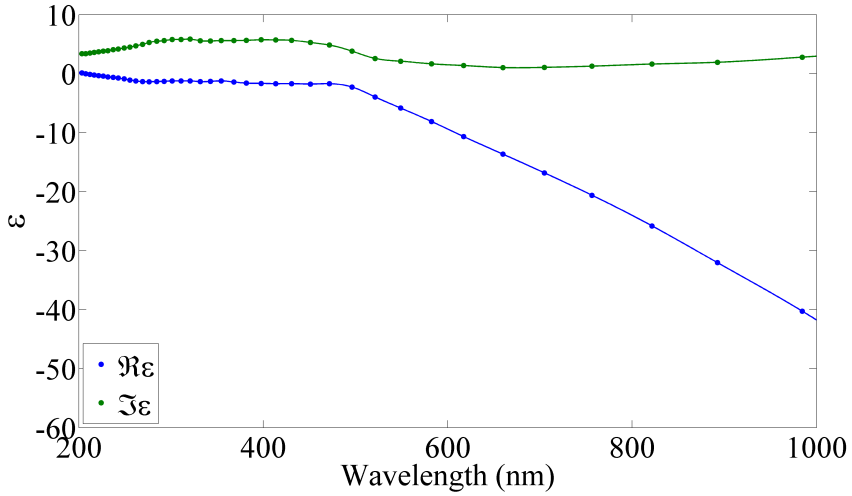

Figure 1.2.4: Permittivity values for Au taken from Johnson & Christy. The lines plotted are interpolated in the form of a cubic spline (one point per nanometre in the range 200-1000nm).

1.3 Plasmonics

1.3.1 Resonances in metallic wires and particles

The fact that metals contain free electrons (and hence have a negative real part of the permittivity) is very important in the field of plasmonics which is concerned with the interaction between light and metallic structures.

Briefly, to provide a feel for the physics involved, let's consider an electric field applied along a metal wire in the electrostatic regime. If the wire is metallic and infinitely long, the applied field will cause a continuous current to flow. If the wire is cut to a finite length, current will flow for a time until a dipole is formed whose restoring force exactly opposes that of the incident field. If the wire was made of a dielectric, no current would flow, and the accumulation of charge at the ends of the wire would be known as *bound* charge. If the field is now set to oscillate in time, the dielectric wire will re-radiate some, but very little light due to a weak dipole moment being induced. The metal wire, on the other hand, will scatter light much more strongly as the induced dipole moment will be a lot stronger. An important feature of this scattering is that it is dependent on the wavelength of light, and the wire will scatter most strongly when the length of the wire is equal to $\lambda/2$ (i.e. radio antennas) because the wire is a perfect metal in this regime. This resonance is an example of a very large-scale particle plasmon and for radio wavelengths the metal can be described as a perfect conductor. At optical frequencies, metals are not perfect conductors, and their dispersions have been shown above. This dispersion allows surface waves to exist on metals at optical frequencies and are known as surface plasmon polaritons (SPPs).[5] These SPPs have very short wavelengths compared to the wavelengths of the light which excite them due to the dispersion relation of SPPs. This is

the key to plasmonics — light can be confined to volumes much smaller than the wavelength of light.[6,7] Experimental work has been carried out on nanowires which demonstrates that at optical wavelengths they can be significantly shorter than their wavelength of resonance.[8]

An extreme case of sub-wavelength particles which exhibit a resonance wavelength much longer than their size are spheres whose polarisability is described by the Clausius-Mossotti equation where ϵ_d is the permittivity of the surrounding dielectric (polarisability will be discussed more fully later in this chapter and in appendix B):

$$\alpha = 4\pi a^3 \frac{\epsilon - \epsilon_d}{\epsilon + 2\epsilon_d} \tag{1.3.1}$$

This relation holds for all spherical particles which are deeply sub-wavelength. The resonance condition is provided by the equality $\epsilon = -2\epsilon_d$ and when $\epsilon_d > 0$, ϵ must be negative in order to establish a resonance. This occurs at a wavelength specific to the material in question and at this wavelength, a particle whose radius is $a = \lambda/1000$ will have the same resonance wavelength as one whose radius is $a = \lambda/100$, in stark contrast to the radio antenna whose resonance is always comparable to the wavelength.

1.3.2 Local field enhancement

Nanoparticles which support particle plasmons are much smaller than the wavelength of light, so when a particle plasmon is excited by light of a relatively long wavelength, the light which is harvested by the optical cross-section (more on this in chapter 5) will be confined to a volume not much larger than the geometrical volume of the nanoparticle.[9] The strength of these local fields can be significantly stronger than the incident field, and this has applications in surface enhanced Raman spectroscopy (SERS) and biosensing.[10–12] For example, field enhancements have been investigated for nanorods[13] and chains of particles, where "squeezing" of the near-fields has been observed experimentally and theoretically.[14,15] In order to probe these near-fields experimentally, often, fluorescent dye molecules are often used,[16,17] and theoretical work has been carried out to investigate the properties of the molecules next to (for example) metallic nanoparticles[18] and tips.[19] The fluorescence enhancement of single particles, though strong, can be very much weaker than composites of several particles. A good example of this is pairs of particles close together which can have high fields in between. This has been investigated for fabricated nanorods[20,21] but currently there seems to be more interest in the enhancement at the centre of bow-tie structures[22,23] as they can be fabricated easily (e.g. using nanosphere lithography) and produce large local field enhancements. Near-field imaging of metallic nanoparticles[24] provides an important comparison for numerical modelling.

Recently some interesting work has been carried out in order to use polarisation anisotropy in the near-field to probe the temperature of metallic nanoparticles coated with fluorescent

dye.[25,26] In chapter 5 we will consider a method of enhancing the field which is similar to a theoretical proposal by Li *et al.*[27] whereby the near-field of a large particle enhances the local field of a smaller particle which in turn enhances the field of a still smaller particle and so on. Although the theoretical proposal utilised the electrostatic approximation and was specific to self-similar structures, the experimental and theoretical results presented in chapter 5 demonstrate that such a cascaded enhancement can be obtained at optical frequencies.

1.3.3 Metamaterials

So far I have only been discussing single particles and isolated nanostructures. The collective electromagnetic response of arrays of particles to incident light can produce highly modified spectral characteristics and carefully designed plasmonic elements can, in arrays with sub-wavelength periodicity, produce effective material responses. Such composites are known as *metamaterials* and they will be described briefly here..

In 1968, Veselago published an important paper[28] which established that (in theory) Maxwell's equations supported the possibility of negative refractive index materials (i.e. when both ϵ and μ are negative). This would mean that in such a material the Poynting vector would be in the opposite direction to the k-vector and hence light passing from a dielectric into such a material at an angle from the normal would be refracted 'backwards'. This theory received very little attention until Pendry theoretically suggested tailoring the properties of materials in the microwave regime.[29] Pendry succeeded in using periodic arrays of wires to create a 'dilute metal' with a lower plasma frequency (thus allowing plasmonics to become a reality at microwave frequencies). By changing the plasma frequency, Pendry was changing the permittivity. The word 'metamaterial' has since been used to describe any material whose properties originate from sub-wavelength structure rather than the properties of the materials which constitute it. This work was followed up by the introduction of structures which have tailored magnetic responses in the form of, for example, split-ring resonators.[30] These resonant elements can support magnetic dipole moments which create a magnetisation which hence modifies the effective permeability of the material in which they are embedded. As well as providing theoretical suggestions as to the possible structures which could be used to create a negative refractive index, Pendry also proposed that a negative index slab could create a 'perfect lens' which restored the evanescent near-field of the object being imaged thereby allowing the usual diffraction limit to be overcome.[31]

Experimentally, Shelby *et al.*[32] created the first negative index material at microwave frequencies using wires and split-ring resonators and these elements continue to be studied.[33] Further structures such as the fishnet[34,35] and cut-wire pairs[36–38] have brought the resonant frequency into the near-infrared. Grigorenko came close to the optical regime with coupled pairs of nanodots which effectively, through displacement currents, operate as a split-ring resonator on its end,[39,40] but recently Xiao *et al.* succeeded in producing a negative-index metamaterial

that operates for yellow light.[41] Although firmly rooted in plasmonics, the field of metamaterials has taken on a life of its own and entire conferences are now devoted solely to tailoring the properties of materials. This thesis is, however, concerned with the physics of plasmonic particles, and not effective material parameters.

1.4 The physics of particle plasmons

Here we will discuss general aspects of plasmonics in the context of the recent literature, to provide background and to set the scene for later chapters which describe new results.

1.4.1 Scattering by particles in the electrostatic regime

A metallic nanoparticle can have an oscillating dipole induced in it by an oscillating external electric field. This oscillating dipole re-radiates light as the electrons are accelerating. *Scattering* by small particles is simply this re-radiation. The frequency of the scattered light is the same as the incident light, and the scattering distribution is well known from the theory of electrodynamics.[42] The key property of a particle which characterises its scattering is its *polarisability*. The polarisability is the degree to which a field of a given strength is able to induce a dipole moment in a particle. A commonly used polarisability for spherical nanoparticles in the electrostatic limit (i.e. $\lambda \gg a$ where a is the particle radius) is equivalent to the Clausius-Mossotti equation (which describes the polarisation of a single molecule within a bulk material). The form of the Clausius Mossotti relation is (repeated from above):

$$\alpha = 4\pi a^3 \frac{\epsilon - \epsilon_d}{\epsilon + 2\epsilon_d} \tag{1.4.1}$$

Interestingly, although this relation was intended to be used to obtain the polarisability of molecules within a bulk medium with an applied electrostatic field, it can give excellent insight into dynamic problems. For example, in the electrostatic regime, the permittivities of the two media are constants, but for electrodynamic situations they are dispersive. This allows us to discover the frequency for which there is a pole in the polarisability and hence the resonant frequency (as stated above this occurs when $\epsilon = -2\epsilon_d$). This is a reliable method and it agrees with rigorous electrodynamic calculations (see chapter 2). As an example, if an electrostatically small particle is embedded in glass ($\epsilon_d = 2.25$), to be on resonance it should have a permittivity of -4.5. This corresponds to a wavelength of approximately 415nm for silver and 530nm for gold using the values from Palik and Johnson & Christy respectively. Note that we have only been using the real part of the permittivity so far in the Clausius-Mossotti formula. For complete accuracy, the full complex value of permittivity should be used (the imaginary part just describes the phase relation between the dipole moment and the incident field — this is

important, as it 'damps' the resonance, though it is not essential for calculating the resonance wavelength).

1.4.2 Cross-sections of particles in the electrostatic regime

Computationally, the polarisability is an important quantity for single particle studies as it can be used to derive measurable quantities, i.e. the scattering, absorption and extinction cross-sections (where the extinction is the sum of scattering and absorption). Interpreting the physical meaning of cross-sections is not straight-forward, so it will be worth discussing some of the details here.

The unit of cross-section is that of area. The cross-sections are distinctly different from the geometrical cross-section of the particle in question and can be much larger than the geometrical cross-section.[43] If a plane wave is incident on a particle, the particle will remove a certain amount of light from the transmitted beam — this is known as the extinction. If the particle was macroscopically large and opaque, the light removed from the beam would effectively be a shadow which is equal in area to the size of the particle. The extinction cross-section is hence the same area as this shadow (in fact, the extinction paradox states that twice as much light is removed due to edge diffraction[44]). For particles very much smaller than the wavelength of light, the ray optics picture no longer holds true. Still, the particle can remove light from the beam, and the extinction cross-section tells us how much light is removed as if the ray optics picture were still applicable. The same is true for the scattering and absorption cross-sections. A sub-wavelength particle has an absorption cross-section which is equal to the geometrical area of the perfect absorber needed to remove the same amount of light from the beam in an equivalent ray-optics picture. For the scattering cross section the same is true but with a perfect scatterer instead of absorber (this includes a perfect mirror for example).

As stated above, the scattering cross-section is not concerned with the direction in which light is scattered — it is simply an integral of the scattered Poynting vector over a sphere which encloses the particle and whose radius is much larger than the radius of the particle. Note that this Poynting vector does not include fields of the incident wave - only those scattered ($\mathbf{S}_{scattered} = \mathbf{S}_{total} - \mathbf{S}_{incident}$). Similarly, the absorption cross-section can be thought of as the integral of the total Poynting vector over the surface of the particle (i.e. the net amount of light which goes into the particle). A more physical insight (which ties in with the discussion of the polarisability) is the situation in which light incident upon a polarisable particle induces an oscillating dipole moment in the particle. This oscillating dipole moment radiates, i.e. scatters, light and so by exciting this dipole moment, not only does scattering exist, but there are also losses as discussed above which lead to absorption. This is due to the damping of the electrons' motion by collisions within the metal. This gives rise to the absorption cross-section.

Mathematically, the cross-sections of a particle with a known polarisability are:

$$\sigma_{ext} = k\Im(\alpha) \tag{1.4.2}$$

$$\sigma_{scatt} = \frac{k^4}{6\pi}\left|\alpha\right|^2 \tag{1.4.3}$$

$$\sigma_{abs} = k\Im(\alpha) - \frac{k^4}{6\pi}\left|\alpha\right|^2 \tag{1.4.4}$$

where σ_{ext}, σ_{scatt} and σ_{abs} are the extinction, scattering and absorption cross-sections respectively, k is the wave number and $\alpha$is the particle's polarisability.Scattering cross-sections are useful quantities, but they can be difficult to measure experimentally (this will be discussed in chapter 3 with some suggestions as to how these issues can be addressed). For most situations, where non-electrostatic particles are concerned, more rigorous analysis is required in order to make comparisons with experimental measurements. For example, Mie theory is a complete analytical description of particles which are spherically symmetrical. This includes the electrostatic regime (where it converges to the Clausius-Mossotti result, equation 1.4.1), up to the limit of geometrical optics where, for example, the optics of water droplets can be accurately described in order to explain atmospheric optical phenomena.[1,44] Mie theory is a useful tool in that it can provide the scattering intensity as a function of angle as well as optical cross-sections. It is also very quick to solve computationally.

1.4.3 Larger particles and other geometries

For larger particles compared to the wavelength, the electrostatic regime no longer holds because, in particular, there is phase retardation across the particles to consider. This becomes significant when the particle is larger than about $\lambda/10$. This phase retardation gives rise to a weakening of the restoring force (dynamic depolarisation) and hence a red shift of the dipolar resonance (an increase in radiative damping also occurs in proportion to the volume of the particle). These effects will be discussed in more detail in chapter 2. Despite this red-shift, the dispersion of the two metals in question dictates that a large gold nanoparticle would have a resonance to the red of the resonance of an otherwise identical silver nanoparticle. To take into account the dynamic depolarisation and radiative damping (and also geometrical variations), an empirical polarisability function may be used as proposed by Kuwata *et al.*[45] This polarisability function applies to ellipsoidal particles which are small compared to the wavelength, Agreement with analytical models is poorer for larger particles. This will be discussed fully in chapter 2.

The electrodynamics of non-spherical objects cannot be solved analytically, so different techniques need to be employed to allow them to be studied theoretically. In this thesis finite element modelling (FEM) is carried out for such problems (Ansoft HFSS versions 11 and 12). This involves using a computer to draw a three-dimensional geometry, specifying material parameters and excitation conditions, and then allowing the software to discretise the geometry

into a large number of elements. At the boundaries between these elements Maxwell's equations are solved and the fields are calculated subject to appropriate boundary conditions. This is an extremely powerful technique with a wealth of possibilities for simulating the response of different particle geometries and arrangements.[46,47] It is, however, very computationally demanding and a model which reproduces the results of Mie theory can take hours to solve (with some assumptions made) in comparison to less than a second for Mie theory itself.

Other techniques include finite-difference time domain (FDTD),[48] the coupled dipole approximation (CDA)[49,50] and the discontinuous Galerkin time domain method (DGTD)[51] all of which are capable of performing similar calculations to FEM with similar levels of accuracy. See reference[52] for details.

Chapter 2

Single particle response

2.1 Introduction

This chapter is concerned with the response of metallic particles in isolation. I begin by describing the methods for performing scattering calculations and for taking experimental data. Following this I discuss results from these techniques regarding the scattering from spheres, notably the angular scattering response of higher-order modes. Also discussed are experimental dark-field scattering spectra of metallic discs which have been compared to modelling. A key paper by Kelly *et al.*[53] contains useful details regarding the modes of plasmonic discs along with their damping mechanisms which have helped in understanding some of the results presented here.

2.2 Modelling techniques

The three main techniques used here to calculate properties of individual metallic nanoparticles are Mie theory,[54] finite-element method (FEM) and the use of the Kuwata polarisability[45] (which is empirical). I will start by discussing the details regarding the use of these techniques and will then provide a quantitative comparison of the three techniques for a range of sphere radii.

2.2.1 Mie theory

Mie theory is an exact analytical description of the electrodynamic response of spherical objects with no assumptions made (other than the truncation point of the series of modes which are supported by the sphere). It is applicable for all size-wavelength ratios and it has been shown to agree well with experiments on metallic nanospheres.[55] In brief, Mie theory is derived by

expressing an incident plane wave in terms of spherical harmonics and calculating the degree to which this field overlaps with the spherical harmonic modes which can be supported by the particle, which are calculated separately. It is a completely rigorous theory and takes into account phase retardation across the particles, something that leads to the prediction of the excitation of higher-order spherical harmonic modes which cannot be calculated if just the dipolar mode of the particle is considered (as is the case when using the Kuwata polarisability). From the exact solution it is possible for the cross-sections and the angular scattering profile to be calculated, as well as any phase information which may be required. All Mie calculations are extremely fast to perform computationally even for a large number of frequencies. A full derivation of Mie theory is provided in appendix D.

The Mie theory codes used here were written by myself but were heavily influenced by the approach of Christian Mätzler.[56] Note that the visualisation of the scattered intensity in three dimensions is original here.

2.2.2 Finite element modelling (FEM)

HFSS is a commercial FEM package developed by Ansoft (results from versions 11 and 12 are presented here). It is very flexible as to the geometries which can be modelled. This technique has been used extensively for work which is included in this thesis. FEM operates by splitting the chosen geometry into a large number of tetrahedral elements. The number of elements and their locations are specified by an internal refinement procedure which adapts the mesh to improve the accuracy of the fields which are represented once the boundary conditions which result from Maxwell's equations are solved at the boundaries between the elements. Once the model is solved, the fields at any point within the model geometry can be accessed — the field at the centre of the tetrahedra are interpolated from the fields at the boundaries. Also, far-field quantities may be inferred by internally performing a near-field to far-field conversion.

There are two main modes for which FEM has been used here — for single particles and for infinite, ordered arrays of particles. For single particles the particle is surrounded by a sphere (1 to 2μm in radius) which consists of the surrounding medium. The fields are calculated at all points within this sphere, and the sphere is set so that no radiation is reflected, i.e. this approximates to a particle embedded in a homogeneous environment whose scattered fields have nothing to interact with which could otherwise produce spurious fields. With this one-particle setup, it is possible to perform a near-field to far-field conversion in order to calculate the scattered power, for example, or angular scattering profiles. Also, near-field quantities can be exported. This is described in detail in chapter 5 along with a much more detailed description of the FEM method in general. Though it cannot be used for analysing the response of large finite ordered or random arrays of particles (the reasons will be explained in detail in subsequent chapters), FEM can be used to analyse infinite periodic arrays of particles. In this case, the particles are not enclosed in a sphere, but in the unit cell of the array. Periodic

boundary conditions are set at the walls of the unit cell to ensure that the fields are the same at opposite sides of the unit cell. Once this model is solved, the transmission can be calculated by either using the S-parameter[57] $S_{2,1}$ or by integrating the normal component of the Poynting vector in the following way (where the incident light is directed from the top to the bottom of the cell with respect to the z-axis, see figure 2.2.1):

$$T = \frac{\int \mathbf{S}_{total} \cdot d\mathbf{A}_{bottom}}{\int \mathbf{S}_{incident} \cdot d\mathbf{A}_{top}} \tag{2.2.1}$$

where $\mathbf{S}$ is the Poynting vector (subscripts indicate whether it is the total Poynting vector or the incident Poynting vector). The integrals are carried out over the top and bottom of the unit cell (as indicated by the subscripts of the area elements). Despite the flexibility and power of FEM, it is time-consuming to calculate the fields even on a reasonably powerful computer. All models presented here were performed on a PC running Windows XP Professional x64 with an Intel Core2-Dual 3.16GHz CPU and 4GB of RAM.

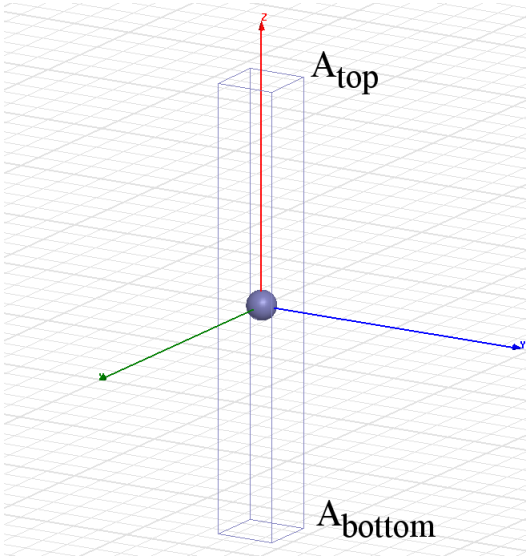

Figure 2.2.1: Image exported from HFSS showing a unit cell containing a sphere. The top and bottom of the unit cell are labelled The incident light here is in the negative z-direction.

2.2.3 Empirical polarisability functions

Although Mie theory provides analytical accuracy and good computational speed, it is only applicable to spheres, and while FEM is powerful and flexible, it is slow. An additional technique is to use an empirical polarisability function which can allow extinction cross-sections to be calculated very quickly. In principle, this is of little use for our purposes in the discussion of single particles as more exact calculations can be performed for known geometries, but its use will become important in chapter 3 when the coupled dipole approximation is introduced properly.

The Kuwata function[45] is a function which describes the degree by which a particle may be polarised (i.e. its polarisability) based on its properties. It is based on the Mie response, but contains empirical constants which allow it to be extended to ellipsoidal particles. The form of the polarisability can be written as follows:

$$\alpha_{kuwata} = \frac{V}{\left(L + \frac{\epsilon_d}{\epsilon - \epsilon_d}\right) + A\epsilon_d x^2 + B\epsilon_d^2 x^4 - i\frac{4\pi^2\epsilon_d^{3/2}}{3}\frac{V}{\lambda_0^3}} \tag{2.2.2}$$

Here, V is the volume of the particle, ϵ is the permittivity of the metal, ϵ_d is the permittivity of the surrounding medium, λ is the wavelength, x is the size parameter ($x = 2\pi a/\lambda$ where a is the size along the direction of incident polarisation) and A and B are the empirical constants:

$$\begin{aligned} A(L) &= -0.4865L - 1.046L^2 + 0.8481L^3 \\ B(L) &= 0.01909L + 0.1999L^2 + 0.6077L^3 \end{aligned} \tag{2.2.3}$$

and where L is defined for prolate spheroids to be:[2]

$$L_{prolate} = \frac{1-e^2}{e^2}\left[-1 + \frac{1}{2e}\ln\left(\frac{1+e}{1-e}\right)\right] \tag{2.2.4}$$

where $e^2 = 1 - b^2/a^2$.

For oblate spheres, L is defined as:

$$L_{oblate} = \frac{g(e)}{2e^2}\left[\frac{\pi}{2} - \tan^{-1} g(e)\right] - \frac{g^2(e)}{2} \tag{2.2.5}$$

where $g(e) = ((1-e^2)/e^2)^{1/2}$ and $e^2 = 1 - c^2/a^2$.

The Kuwata polarisability is useful in that it is able to accurately predict the red-shift due to dynamic depolarisation[58] and the effect of radiative damping[59–62] which the Clausius-Mossotti equation (see appendix B) does not embody. It is particularly useful to use this function when a nanoparticle needs to be represented by a single polarisability function for quick computations. The electrodynamics of more complex geometries can be calculated using numerical techniques such as the finite element method (FEM), and for the case of a spherical particle, Mie theory provides an analytical solution (a comparison of the three techniques is provided in chapter 3 including a discussion of the extent to which the Kuwata polarisability can be used with confidence).

2.3 Particle fabrication

Particles such as discs are fabricated here using electron beam lithography (EBL).[63,64] This technique allows structures to be created with a resolution of approximately 15nm. Initially, a film of poly(methyl methacrylate) (PMMA) is spin-coated* onto a glass substrate to a thickness of approximately 200nm. A thin film of silver or gold is evaporated onto the PMMA to make it conductive (20-25nm thickness is required to exceed the percolation threshold and enable d.c. conductivity). The sample is then placed in an SEM chamber and the 30kV electron beam is scanned across the sample, exposing circles to create discs, rectangles to create cuboids, etc. When the beam strikes the PMMA (it is scattered very little by the metallic layer), it breaks the polymer chains into smaller, more soluble, molecules. The sample is removed from the chamber and is immersed in etchant to remove the metallic over-layer. The exposed resist is dissolved in a 9:1 mixture of isopropyl alcohol and water, leaving holes which are similar to the nominal shapes exposed by the electron beam. Metal is then evaporated onto the sample at normal incidence. This metal should be evaporated to the required thickness of the particles (this should be significantly thinner than the layer of PMMA). The metal will make contact with the glass where it fills the holes, and it will also coat the top surface of the PMMA. Once the evaporation is complete, immersion of the sample in acetone dissolves the PMMA and hence removes the metal film. This is either carried out overnight at room temperature or for approximately one hour with the acetone boiling ($T > 57°\mathrm{C}$). This leaves the nanoparticles on the substrate, and they can then undergo optical characterisation procedures such as dark-field spectroscopy. A more detailed description of EBL is provided in appendix A.

2.4 Dark-field scattering spectroscopy

Dark-field spectroscopy[65–67] (figure 2.4.1) uses a condenser lens to illuminate the particle under observation. This lens has a 'patch stop' which is a black disc that excludes all incident light within a range of angles from the normal. The dark-field condenser has maximum and minimum numerical apertures ($\mathrm{NA} = n \sin\theta$) which convert collimated light into a focused cone which lies within a range of angles set by the particular lens (50-70 degrees in air is a typical range). The light then illuminates the particle, and the scattered light is collected by an objective lens whose NA is smaller than the minimum NA of the condenser lens. This is the key to dark-field spectroscopy as the difference in numerical apertures is such that none of the incident light is collected — only the light scattered from the particle can reach the detector. In order to obtain the spectrum of a single particle, it is necessary to exclude scattered light from particles other than the one in question. To achieve this, a slit is used at the entrance to the spectrometer to spatially filter the focused light in one dimension. This produces an image similar to that shown in figure 1.1.1 This light is then dispersed by a grating and focused on

*Spin-coating is where a solution is placed on a substrate which is rotated at high speed (approx 4000rpm). This produces a uniform thickness of deposited material.

a CCD camera. The camera used here has 256 × 1024 pixels and can have a spectral range of 400-1000nm depending on the pitch of the grating. This spectral image is spread over the longer length of the CCD. The shorter length is simply a translation of a line on the sample which has finite thickness and corresponds to the image focussed on the slit. Thus, selecting the range in the other direction is simply carried out by only considering the rows of pixels which correspond to the particle under investigation. This signal is then normalised by the background, the dark-counts and the spectrum of the illumination source by the following equation,

$$I_{DF} = \frac{I_{signal} - I_{background}}{I_{lamp} - I_{dark\ counts}} \tag{2.4.1}$$

Here, I_{signal} is the measured intensity from the nanoparticle, $I_{background}$ is the intensity measured in the absence of a nanoparticle, I_{lamp} is the intensity of the lamp scattered from a diffuser, and $I_{dark\ counts}$ is the intensity measured by the CCD with no light being collected.

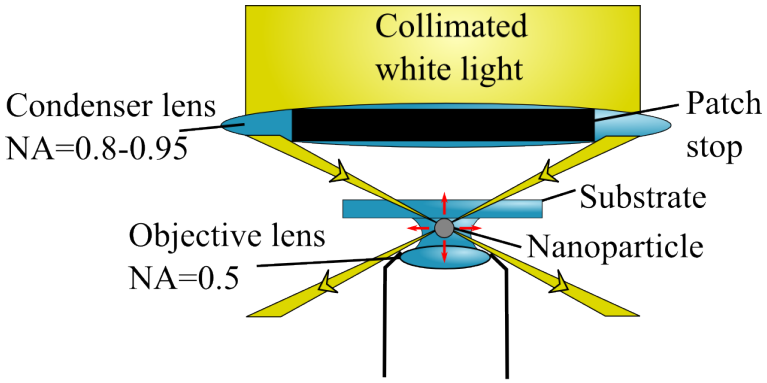

Figure 2.4.1: Schematic of the illumination/collection optics used to obtain dark-field spectra with an oil-immersion lens and an inverted microscope. The numerical aperture of the objective is smaller than that of the condenser, so the incident light is excluded from the measurements. The light scattered by the nanoparticle is indicated in red and the refraction at the surface of the substrate has not been indicated.

Dark-field spectroscopy does allow scattering information to be obtained for single particles, but the information is very specific – the illumination conditions and collection optics cannot readily be changed. As the particles have been fabricated on a glass substrate it is desirable to index-match them to the objective lens. This allows improved optical resolution as well as ensuring that the particle is surrounded by a homogeneous environment. This is particularly important for comparisons with FEM modelling (figure 2.4.2) where an inhomogeneous environment is difficult to model.

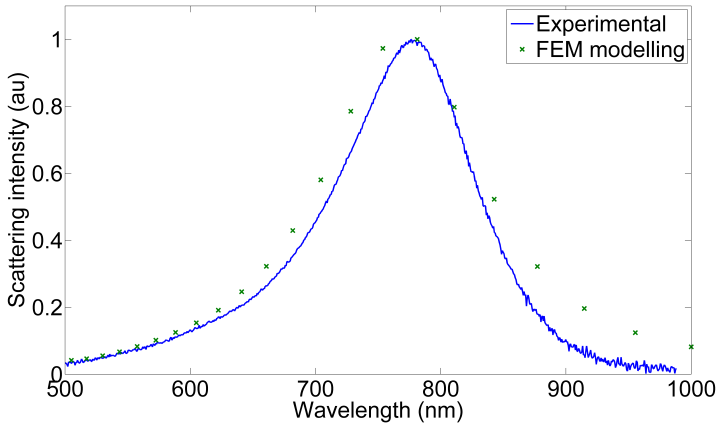

(a)

(b)

Figure 2.4.2: (a) Dark-field spectrum of a gold disc 120nm in diameter and 30nm thick fabricated by EBL (reproduced from Barnes[68] where a detailed discussion of the theory-experiment agreement is provided). The particle was index-matched to a glass objective lens. Also shown is the spectrum as calculated by FEM modelling. The discrepancy at long wavelengths is due to chromatic aberration in the system and some second order diffraction from the spectrometer grating. (b) an SEM image of the particle whose spectrum was measured in (a).

2.4.1 Dark-field procedure

Dark-field microscopy produces images which have a black background and show bright regions where scattering is present. This is seen in figure 2.4.3 which shows the scattering from a number of gold discs of different sizes (there is a 10μm gap between the particles).

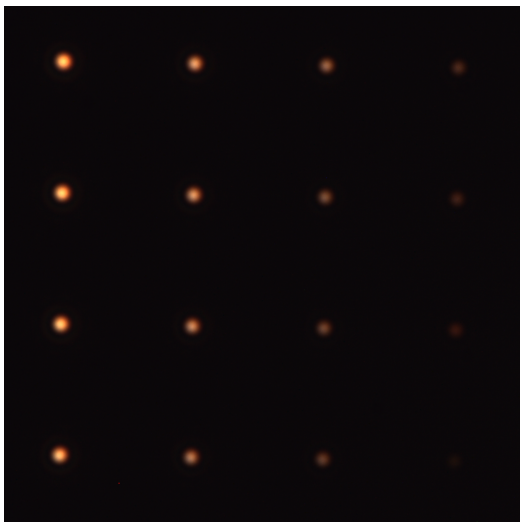

Figure 2.4.3: Colour dark-field image of 16 gold nanoparticles of different sizes in order to illustrate the appearance of nanoparticles under dark-field illumination. The image was taken with a colour camera and the size of the array is 40μm $\times$ 40μm.

When the scattered light is directed onto the spectrometer grating by a mirror (or grating in the zero-order regime), the CCD used for acquiring spectra can obtain an image which is equivalent to that shown in figure 2.4.3. This focussed image is shown in figure 2.4.4.

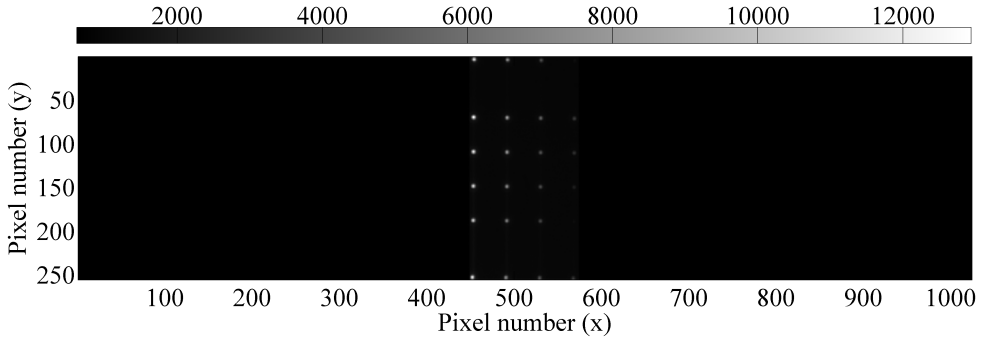

Figure 2.4.4: CCD image of 16 gold nanoparticles of different sizes as collected by the CCD used for acquisition of spectra. The slit is open just enough to collect the light from all the particles in the array. At the top and bottom of the image the edges of neighbouring arrays can be seen.

The microscope stage which supports the sample is moved in the x-direction so that the column of particles of interest appear at the centre of the slit. Then the slit is closed in order to exclude light from all other neighbouring scatterers in the x-direction. These two steps are shown in figure 2.4.5.

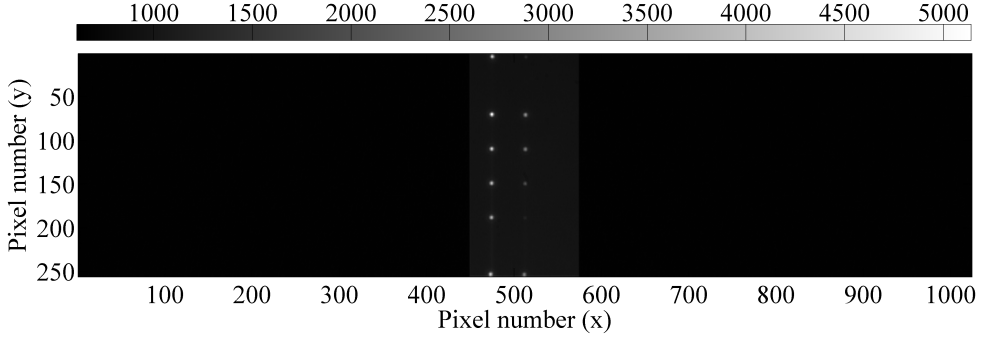

(a)

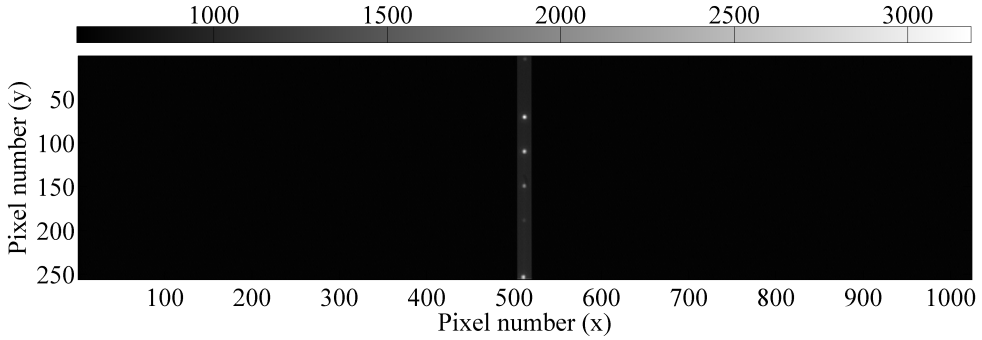

(b)

Figure 2.4.5: CCD images of (a) the particles of interest being aligned with the centre of the slit and (b) the slit being closed as much as possible to exclude other sources of light whilst ensuring that all light from the particles of interest is collected.

Once the sample is spatially filtered in this way, the light can be dispersed over the CCD using a diffraction grating in the first-order regime. An image collected in this manner is shown in figure 2.4.6 (note the calibrated wavelength scale).

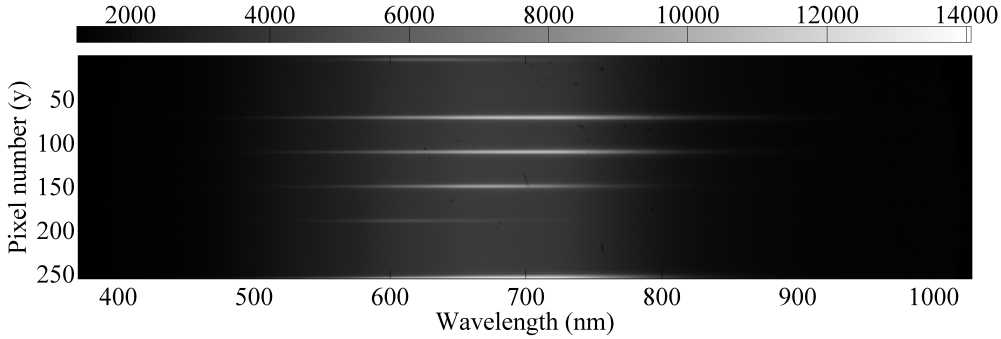

Figure 2.4.6: CCD image of the light scattered from four gold discs when dispersed over a CCD. The image effectively shows a continuous set of spectra from the light which passed through the slit (figure 2.4.5b).

Finally, in order to normalise the spectra, three more images are required — the dark-counts, the background and the lamp spectrum. The dark counts is simply measured by closing the CCD's shutter, the background is taken by moving the slit so that it samples a blank area of the substrate close to the region of interest, and the lamp spectrum is measured by replacing the sample with a white diffuser. These three spectra are shown in figure 2.4.7.

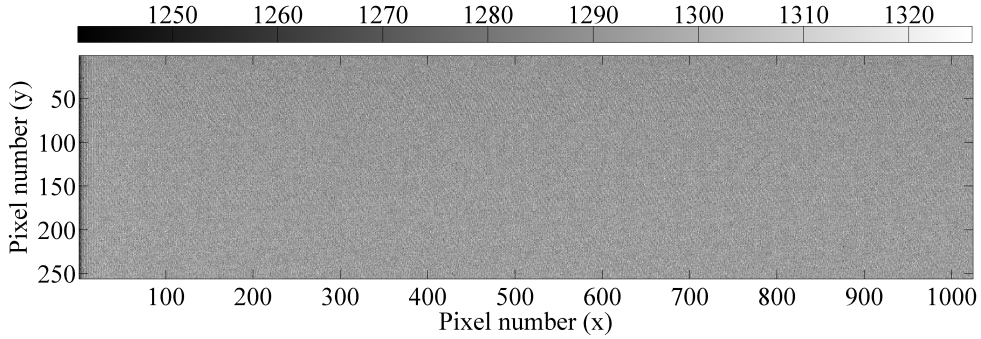

(a)

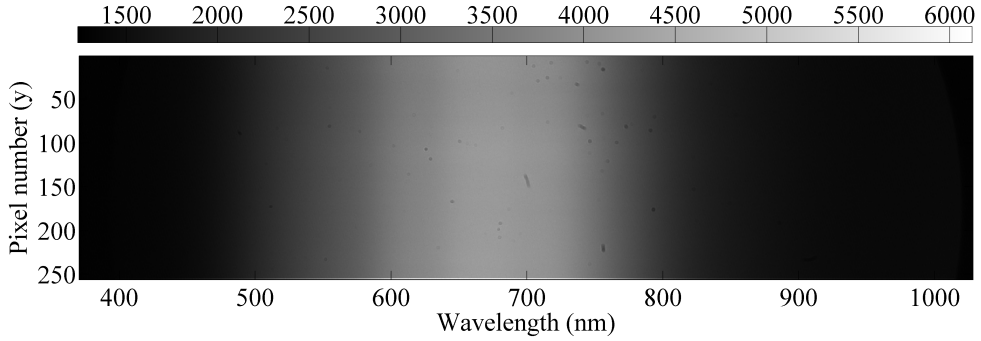

(b)

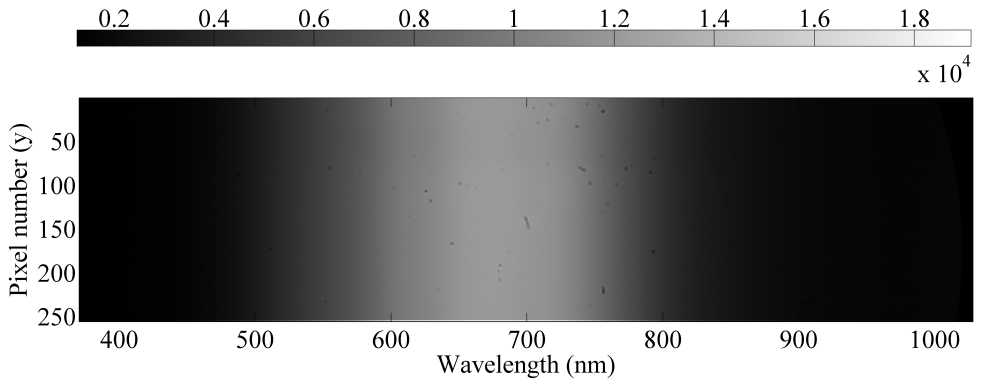

(c)

Figure 2.4.7: CCD images of (a) the dark-counts, (b) the background and (c) the lamp spectrum.

The subtraction of the background removes any effect from the substrate. This is described in the numerator of equation 2.4.1 and for the gold discs, the corrected spectra are shown in figure 2.4.8a. The image is divided through by the lamp spectrum to eliminate the wavelength dependence of the source. This final, normalised image is shown in figure 2.4.8b.

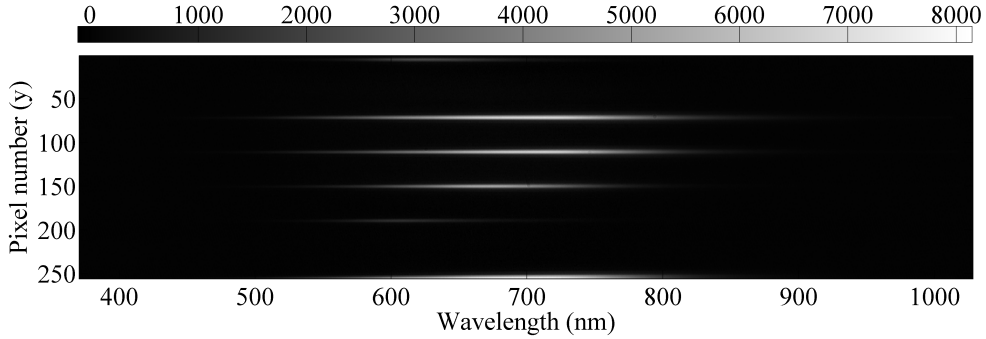

(a)

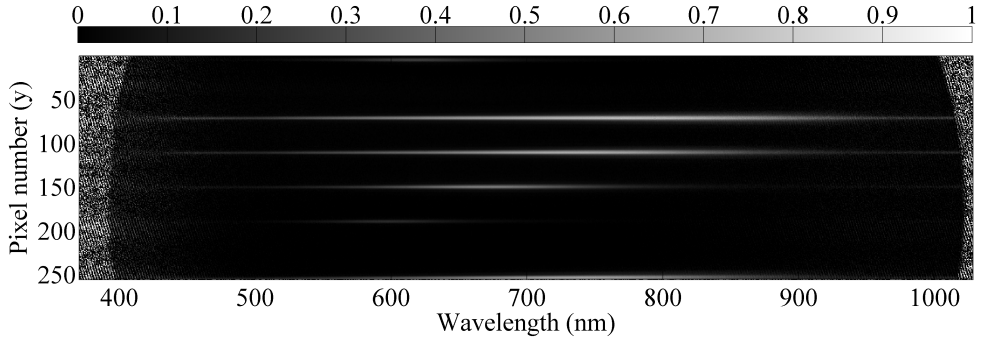

(b)

Figure 2.4.8: CCD images of (a) the background subtracted from the signal and (b) the aforementioned set of spectra divided by the lamp spectrum (with dark-counts subtracted). The range of the colour scale is set manually to improve the clarity of the spectra.

In order to convert this data into line-plots of spectra, a range of rows is specified which completely encompasses one of the spectra, and the rows are simply summed. For the second particle from the bottom in the previous figures, the summed rows produce the following normalised spectrum (figure 2.4.9).

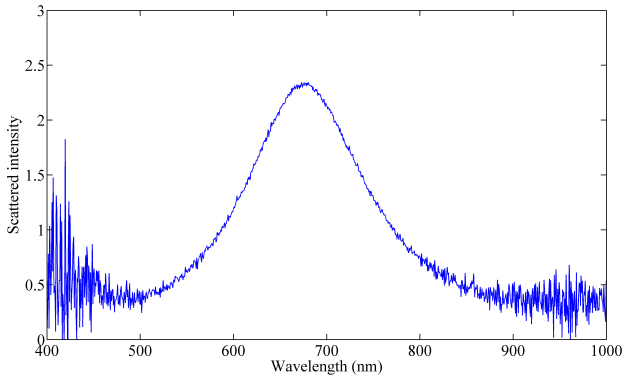

Figure 2.4.9: Spectrum of the second particle from bottom in the previous figures by summing the rows from $y = 140$ to $y = 160$.

It is worth mentioning that the particles must be in focus at all wavelengths. This is difficult in practice due to chromatic aberrations and tilted optical components. If the particles are not in focus, similar spectra may be obtained if the range of pixels over which the integration is carried out is increased. Also, correct alignment of the CCD camera is essential for the accurate measurement of spectra. To achieve this, a calibration lamp is used which emits spectral lines at known wavelengths.

2.4.2 Drawbacks of dark-field spectroscopy

Dark-field spectroscopy has a number of limitations in general, and many of these cannot be addressed easily. Some of the drawbacks discussed here pertain to the specific task of producing comparisons with FEM modelling and some details are specific to the equipment used in this project.

- The incident light has a range of polar angles, the relative intensities of which are unknown.
- The incident light has a range of k-vectors and polarisation states which are also unknown.
- The polarisation states in the substrate are modified by the presence of a glass interface and the angles involved are close to the Brewster angle for an air-glass interface ($\theta_B = \arctan(n_2/n_1) = \arctan(1.5) = 56.3°$).
- The dispersion of the index-matching fluid may not exactly match that of the glass.
- The diffuser results in a change to the lamp spectrum.
- Some of the focussing adjustments are set by eye and hence are somewhat arbitrary and difficult to reproduce exactly.

- Second-order diffraction from the spectrometer grating may affect the measured spectrum at long wavelengths.
- The adjustable numerical aperture of the objective lens used could not be precisely set for numerical apertures between the minimum and maximum values allowed.

2.4.3 Simulated scattering spectra

With FEM modelling, there are certain restrictions when working with single particles. One is the difficulty in including a substrate due to the fact that the external material needs to be specified and it must be the same on both sides of the particle (HFSS v. 11). Therefore, it is possible that reflections may be produced at these interfaces if there is glass on one side and air on the other. For this reason, all FEM calculations are carried out with a homogeneous environment of glass ($n = 1.5$) and all experiments are carried out with index-matching fluid placed on the glass substrate. FEM produces full-wave solutions to the problem, and quantities such as the radiated power can easily be calculated, as can the angle-dependent scattering intensity by implementing a near-field to far-field conversion procedure. It should be noted that the FEM model is carried out for an incident plane wave which has well-defined values of θ and ϕ. For axially symmetric particles the ϕ-dependence is not important in making comparisons with dark-field measurements, but the θ-dependence is (as is the numerical aperture of the collection optics). The experiment could be modified to illuminate the particle over a smaller range of angles, but this significantly reduces the intensity of light collected, especially if the range ϕ of values is similarly reduced. A range of illumination angles $\Delta\theta = \Delta\phi = 1^\circ$ would reduce the intensity by a factor of 7,200 compared to using an unmodified condenser with NA $= 0.85 \rightarrow 0.9$. For these reasons the FEM model is implemented such that the incident θ-value is the mean of the experimental range, i.e. 35.5° in glass and the ϕ value is arbitrary due to the axial symmetry of all the particles considered.

Yet another complication arises from the fact that amongst the various k-vectors illuminating the particle, there is also a large range of polarisation states. Therefore a flat disc will be illuminated by different amounts of s- and p-polarised light at different azimuthal angles (the polarisation states here are defined with respect to the substrate). The intensity will also be reduced by the Fresnel coefficients for the two polarisations at the top surface of the substrate (the particles are fabricated on the 'bottom' face of the substrate in order that they can be indexed matched on that side to the objective lens).

HFSS allows the scattered power to be exported once the far-field conversion is accomplished by internally integrating the scattered power over all angles in θ and ϕ. This power can be converted into an extinction cross-section if the incident intensity is known. In order to mimic dark-field collection in HFSS, the scattered power needs to be integrated over a smaller range of angles, which makes the issue more complicated. From HFSS, a far-field the quantity called rE can be exported. This is simply the magnitude of the electric field multiplied by the radial

distance which can be calculated for any scattered angle. In practice, this can be exported as a table of values over a range of θ and ϕ angles. A numerical integration can then be performed on these values to calculate the intensity collected in the dark-field experiment. This is performed by carrying out the following calculation:

$$I_{collected} = \frac{2\mu_0 c}{4\pi r_{rad}^2} \sum_{n=1}^{n_{max}} \sum_{m=1}^{m_{max}-1} (rE_{m,n})^2 \sin(\theta_{m,n}) \Delta\theta_{m,n} \Delta\phi_{m,n} \tag{2.4.2}$$

where r_{rad} is the radius of the integration sphere in nm. In version 11 of HFSS, there was some discrepancy between the internally calculated integrated power and the equivalent value obtained by preforming a numerical integration over all angles. This was resolved in version 12, and it can therefore be used with some confidence. It is also possible to perform an integration within HFSS over one angle which is desirable as a numerical integration runs into problems because $\sin 0 = \sin \pi = 0$ which, from the above equation, produces an intensity of zero at those angles. For our purposes, $\theta = 180°$ is important because the coordinate system has been chosen such that the collection optics lie along the z-axis. Once the integration over θ has been performed internally, the integration over ϕ can be performed easily in a suitable software environment (taking care not to include the duplicated angle $0° = 180°$). This is carried out for each frequency, and a spectrum can then be produced. The modified expression becomes:

$$I_{collected} = \frac{2\mu_0 c}{4\pi r_{rad}^2} \sum_{m=1}^{m_{max}-1} \int_0^{\pi} (rE(\theta))^2 \sin\theta d\theta \Delta\phi_m \tag{2.4.3}$$

2.5 Results from Mie theory

Mie theory is concerned with the scattering and absorption of spherical objects. Results from this technique will be referred to in subsequent chapters which are concerned with the interaction of two or more nanoparticles.

2.5.1 Cross-sections and the effect of the surrounding index

The extinction spectra from metal spheres can be calculated if the frequency dependent permittivity of the metal is known. To begin with, let us consider a 25nm radius silver sphere surrounded by air. The extinction, scattering and absorption spectra are shown in figure 2.5.1.

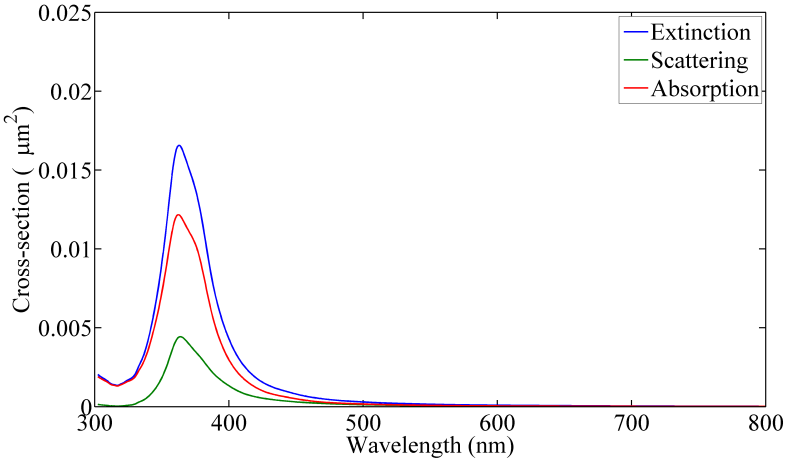

Figure 2.5.1: Extinction, scattering and absorption spectra of a 25nm radius silver sphere surrounded by air.

It can be seen that the three plotted functions have a single resonant feature which is attributable to the plasmonic resonance of the particle. The extinction is primarily dominated by absorption due to the fact that for very small particles there is very little radiative damping. There is an additional feature in the three curves just to the red of the resonance. This is due to a feature in the permittivity of the metal at that frequency (see figure 1.2.3a). The presence of a surrounding dielectric medium (infinite in extent) has a significant effect on the spectral line-shapes[69] and even small changes in refractive index can be sensed.[11] A set of equivalent spectra for an identical particle but surrounded by glass ($n = 1.5$) instead of air is shown in figure 2.5.2.

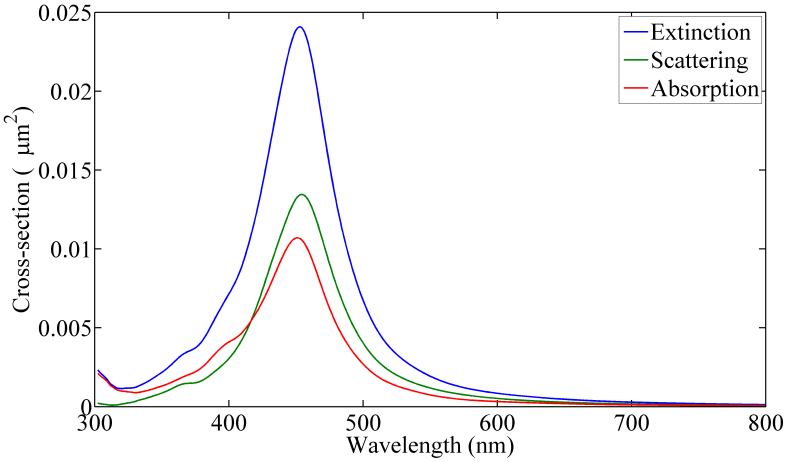

Figure 2.5.2: Extinction, scattering and absorption spectra of a 25nm radius silver sphere surrounded by glass.

It can be seen that the peaks are shifted significantly to the red due to the presence of the surrounding medium (note that the features due to the permittivity do not change position).

The reason for such a marked change in the spectra can be explained by considering a sphere in the electrostatic limit with a field applied (figure 2.5.3).

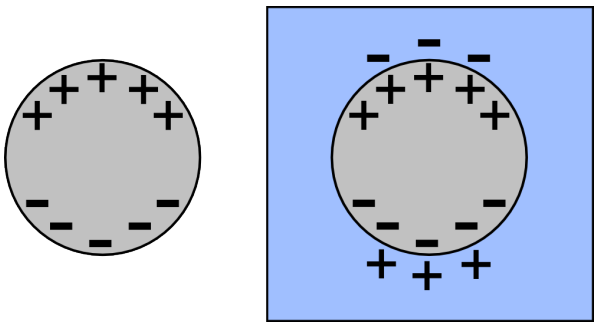

Figure 2.5.3: A metal sphere surrounded by air (left) and glass (right). Bound charge accumulates at the interface between the metal and the dielectric.

When a field is applied to the sphere, a dipole moment is induced and charge accumulates at the surface. When it is placed in a dielectric, the material becomes polarised due to the field within it. This leads to an accumulation of bound charge at the surface of the sphere and of opposite sign to the charge which had accumulated before the addition of the dielectric. This charge acts to reduce the restoring force on the electrons within the sphere (this could be seen as being due to a reduction of the "effective charge" at the interface). The reduction of the restoring force lowers the resonant energy and hence frequency of the system and this is what leads to the red-shift. This is consistent with the Clausius-Mossotti relation (equation 1.3.1). The increase in the extinction cross-section and the fact that the amount of scattered light is more than that absorbed upon the addition of the surrounding dielectric is due to the increased degree of phase retardation across the sample because of the fact that in the dielectric, the wavelength is reduced to $\lambda = \lambda_{air}/n$. The relative strengths in the scattering and absorption cross-sections when the dielectric is introduced is equivalent to that calculated for a similar particle in vacuum whose radius is scaled by the refractive index of the dielectric in the former case (note that the resonance position will still be shifted).

2.5.2 The effect of changing particle size

2.5.2.1 The electrostatic regime

For very small metallic nanospheres ($a \lesssim 10$nm), the size to wavelength ratio is such that there is no significant phase retardation across the particles in the visible range. This means we are in the Clausius-Mossotti regime whereby the resonance position is constant with respect to particle size, and the magnitude of the polarisability is scaled by the volume of the particle. An example of the size-dependence of silver nanospheres surrounded by glass in the small-particle regime is shown in figure 2.5.4.

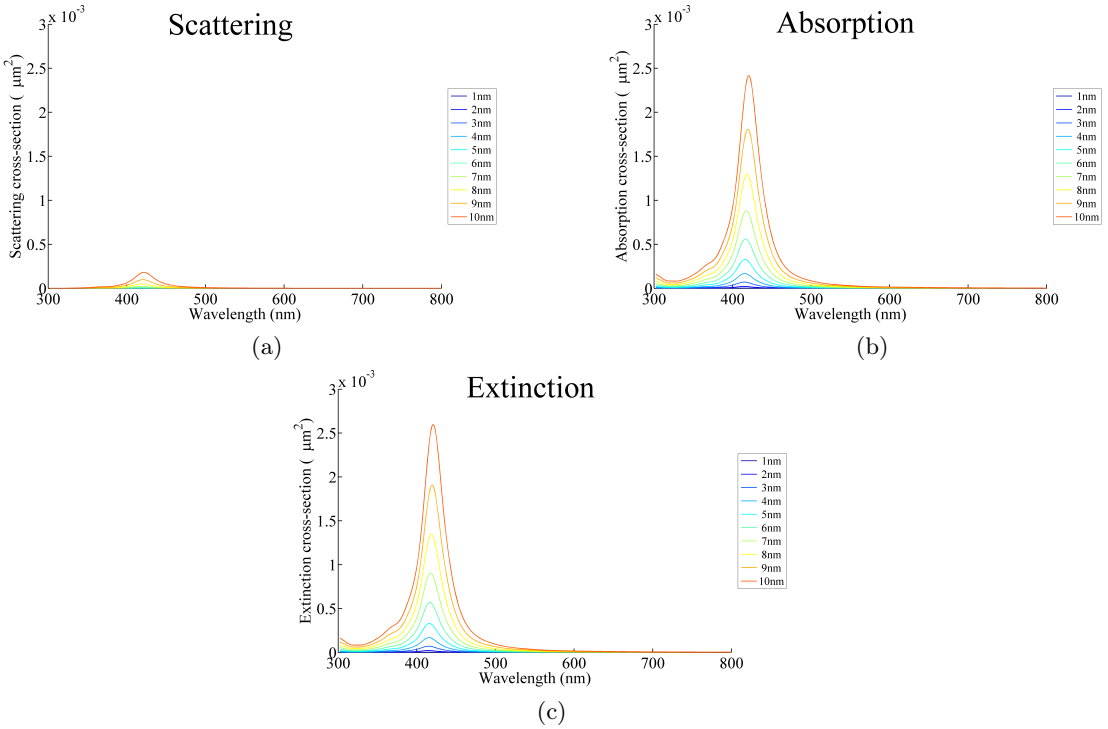

Figure 2.5.4: (a) Scattering, (b) absorption and (c) extinction cross-sections of small silver nanospheres surrounded by glass for a range of radii as calculated by Mie theory.

It can be seen from figure 2.5.4 that the resonance position remains approximately constant for all radii in the range 1 to 10nm. For gold, the same is true, but the resonance wavelength is longer (figure 2.5.5).

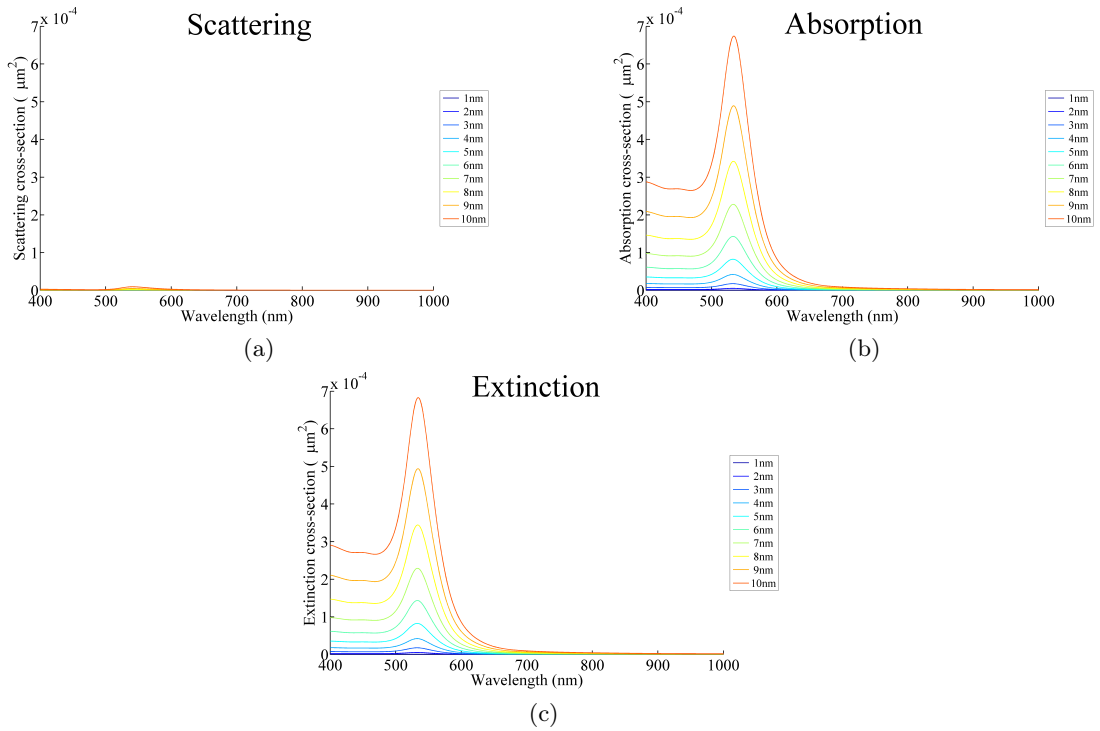

Figure 2.5.5: (a) Scattering, (b) absorption and (c) extinction cross-sections of small gold nanospheres surrounded by glass for a range of radii as calculated by Mie theory.

A noticeable difference between the cross-sections of silver and gold is the presence of a flat band at wavelengths shorter than 500nm for gold. This absorption band is associated with an increased value of the imaginary part of the permittivity in this wavelength range. Another noticeable difference is that the peak wavelengths are to the red of those calculated for silver.

The resonance wavelengths of nanospheres in the small particle regime as calculated by Mie theory are 415nm and 533nm for silver and gold respectively. This can be compared to predictions from the Clausius-Mossotti equation:

$$\alpha = 4\pi a^3 \frac{\epsilon - \epsilon_d}{\epsilon + 2\epsilon_d} \tag{2.5.1}$$

where α is the polarisability, a is the radius of the particle, ϵ is the permittivity of the particle and ϵ_d is the permittivity of the surrounding dielectric. The values of the wavelengths which produce resonances in the expression above are 415nm and 530nm for silver and gold respectively using the same interpolation of the permittivity values which was used to calculate the Mie result. The discrepancy in the values of gold is not fully understood, but it does coincide with large variations in the imaginary part of the permittivity of gold.

2.5.2.2 Larger particles

As the particles are made large enough to exceed the electrostatic limit, significant changes in the spectral line-shapes are observed (figures 2.5.7 and 2.5.8). The first significant change is that the extinction is no longer dominated by absorption. This is due to an increase in radiative damping and is proportional to the volume of the particle. Physically, when the particles are very small, there are not many electrons in the particles, so the amount of scattering is negligible. When the particles are larger, there are significantly more electrons to scatter the light, and eventually this dominates the spectrum, and the absorption becomes negligible[†]. This effect also acts to broaden the spectral line-shape (from equations 1.4.2, 1.4.3 and 1.4.4, the scattering cross-section is proportional to the volume and the absorption cross-section is proportional to the volume squared).

Another significant change is that the resonance becomes red-shifted from the electrostatic resonance position. This is due to 'dynamic depolarisation' which arises from phase retardation across the sample. Put simply, when the phase is constant across the particle, all the electrons act in unison and the resulting dipole moment is the maximum that can be achieved. When the particle is large enough that there is some phase retardation, the result is that the degree of polarisation is reduced in some portions of the particle, and hence the restoring force is reduced. From the discussion above regarding the addition of the surrounding dielectric, this leads to a reduction in the resonance frequency — i.e. a red-shift.

2.5.3 Higher order modes

The most significant change to the spectra of large metallic nanospheres is the appearance of additional peaks at longer wavelengths than those of the electrostatic dipolar resonance.[70,71] These modes are a result of higher order modes being excited. These higher order modes are simply particular modes which are described by spherical harmonics which are supported by the particle and can be coupled to with plane-wave illumination (this is explained in the derivation of Mie theory, appendix D). The cause of the excitation of these higher order modes is that the phase retardation which occurs for larger particles is sufficient that it can drive electrons in different directions in different regions of the particle. The first higher order mode to appear is the quadrupolar mode which is characterised by four equidistant charge accumulations on the surface of the sphere (this has been observed experimentally using scanning near-field optical microscopy (SNOM)[72]). A highly simplified schematic of the excitation of a quadrupolar mode is shown in figure 2.5.6 with the intention of highlighting the role of the phase retardation in exciting such a mode.

[†]Note that as the particles become larger, any absorption features which are due to the permittivity rather than 'plasmonic' effects simply scale with the volume.

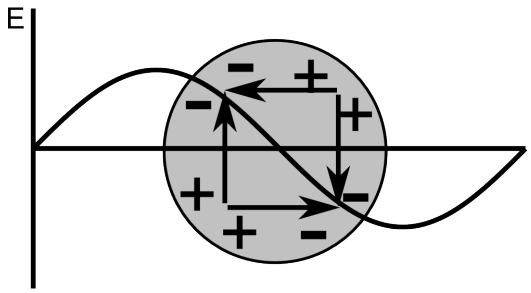

Figure 2.5.6: A simplified schematic of the excitation of a quadrupolar mode of a particle whose size is approximately comparable to the wavelength in the surrounding medium. In reality, for metal spheres the ratio of size to resonance wavelength is dependent on the permittivity of the sphere and the surrounding medium.

When the quadrupolar mode emerges in the spectra, its resonance wavelength initially has the value predicted by the Clausius-Mossotti relation but with the '2 ' in the denominator replaced by $(l+1)/l$ where $l = 2$ for the quadrupolar mode and so on for higher order modes.[53] This condition is based on the radial term of the spherical harmonics which describe the radiation of a spherical multipole in the long wavelength regime. It then continues to grow in strength, to red-shift and to broaden, much like the behaviour of the dipolar mode. Eventually, even higher order modes will emerge. The one after the quadrupolar mode is known as either the hexapolar mode[73] or the octupolar mode.[‡] Here, the term 'octupolar' will be used to be consistent with some of the more recent articles in the literature.[75] The cross-sections of particles in the range $15 \leq a \leq 100$nm have been calculated from Mie theory for silver and gold and are shown in figures 2.5.7 and 2.5.8 respectively.

[‡]The reason for the confusion is the fact that when this mode is excited, charge accumulates in six locations around the surface of the sphere. In terms of multipole theory, however, the mode would be described as an octupole,[74] but with two of the opposite charges being cancelled. This can be thought of as the the charge on the vertices of a cube (with charges arranged in an octupolar distribution) being projected onto a plane in the (1,1,1) direction. The resulting shape is hexagonal, and the spot in the centre consists of both positive and negative charge which cancels.

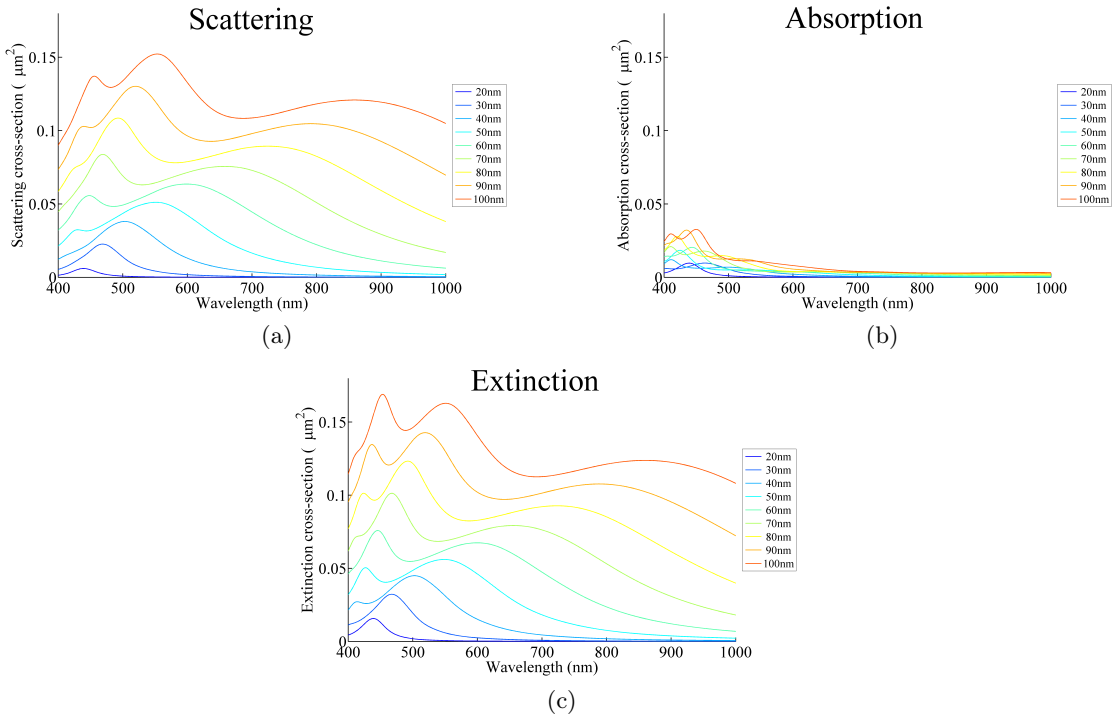

Figure 2.5.7: (a) Scattering, (b) absorption and (c) extinction cross-sections of silver nanospheres with different diameters (larger than figure 2.5.4) surrounded by glass for a range of radii, most of which support higher order modes as calculated by Mie theory.

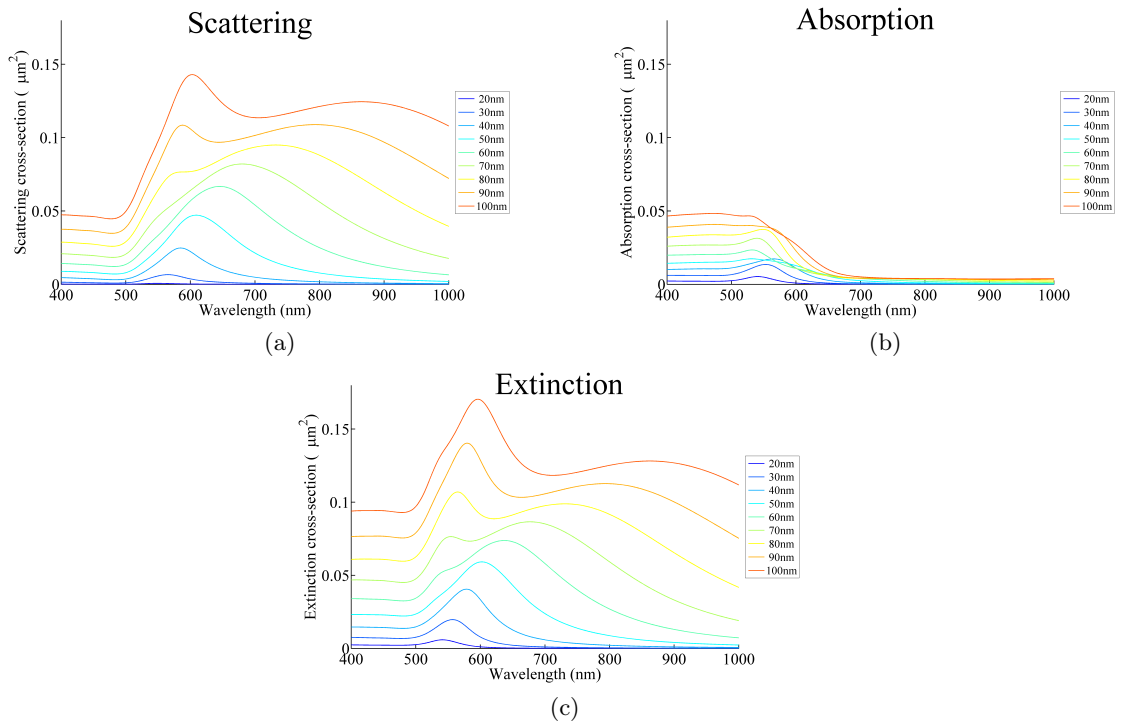

Figure 2.5.8: (a) Scattering, (b) absorption and (c) extinction cross-sections of gold nanospheres with different diameters (larger than figure 2.5.5) surrounded by glass for a range of radii, most of which support higher order modes as calculated by Mie theory.

2.5.4 Modes in isolation

An interesting and useful feature of Mie theory is that its solution takes the form of a summation of spherical harmonics describing the electric and magnetic fields inside and outside the sphere (see appendix). This is normally truncated at a point at which suitable convergence has been obtained,[44,76] but each term in the sum corresponds to a mode of the system. The first term describes the dipolar mode, the second term describes the quadrupolar mode and so on. Therefore, if we wish, we can select one term and neglect all others in order to examine its individual properties.

The dipolar contributions to the cross-sections of silver particles of the same size as those whose spectra are shown in figure 2.5.7 are shown in figure 2.5.9. The quadrupolar contributions are shown in figure 2.5.10 and the octupolar contributions are shown in figure 2.5.11.

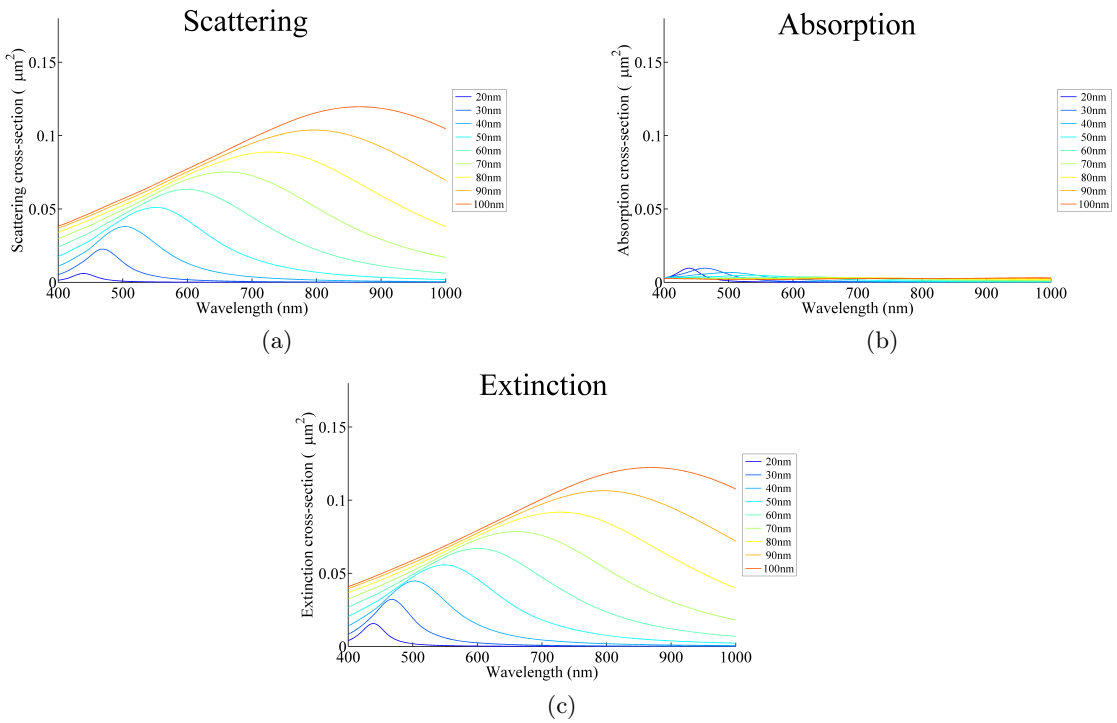

Figure 2.5.9: The dipolar contributions to the (a) scattering, (b) absorption and (c) extinction cross-sections of silver nanospheres surrounded by glass for a range of radii as calculated by Mie theory, most of which support higher order modes.

It can clearly be seen that the dipolar mode significantly broadens and red-shifts as the particle size is increased due to the reasons explained above. It is also clear that apart from the very smallest particles considered here, the extinction spectra are dominated by scattering and absorption is negligible. An explanation for this is that the very small particles are much smaller than the skin depth so a large fraction of the volume can absorb light coherently. For the larger particles, the radius is much larger than the skin depth. Eventually, as we increase the radius, a macroscopic silver sphere will act as an almost perfect spherical mirror — i.e. it will scatter almost all the light and absorb practically nothing.

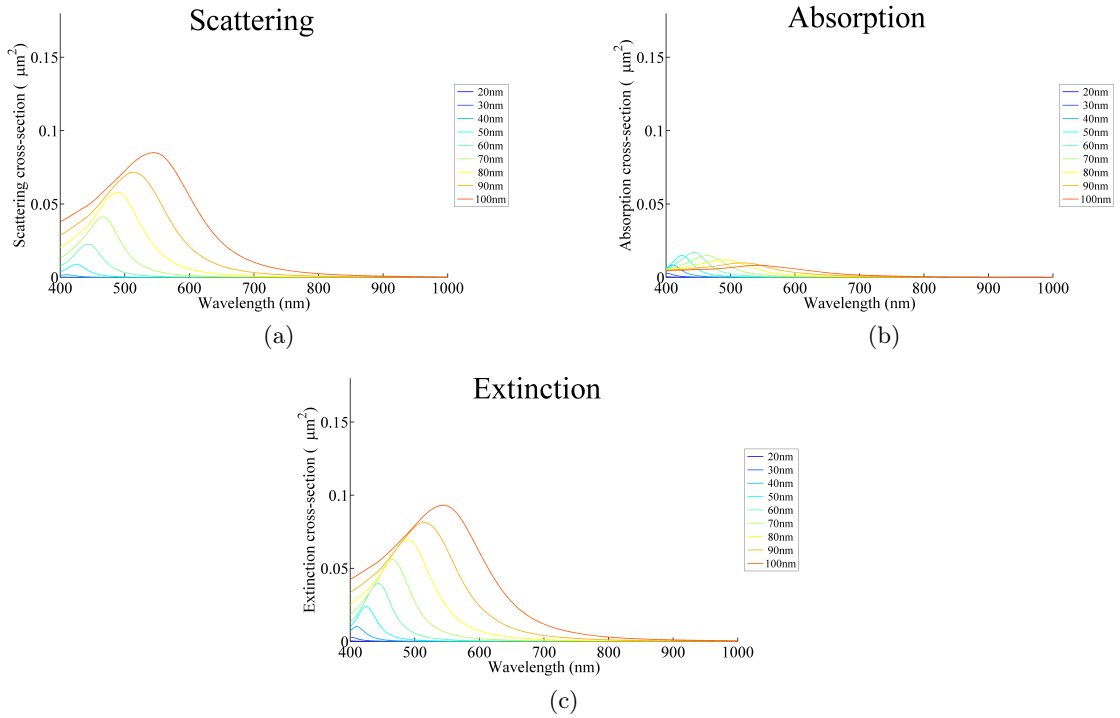

Figure 2.5.10: The quadrupolar contributions to the (a) scattering, (b) absorption and (c) extinction cross-sections of silver nanospheres surrounded by glass for a range of radii, as calculated by Mie theory.

The quadrupolar behaviour is very similar to that of the dipolar mode. An important difference is the wavelength at which the quadrupolar mode first emerges (as mentioned above). The quadrupolar mode is always to the blue of the dipolar mode.

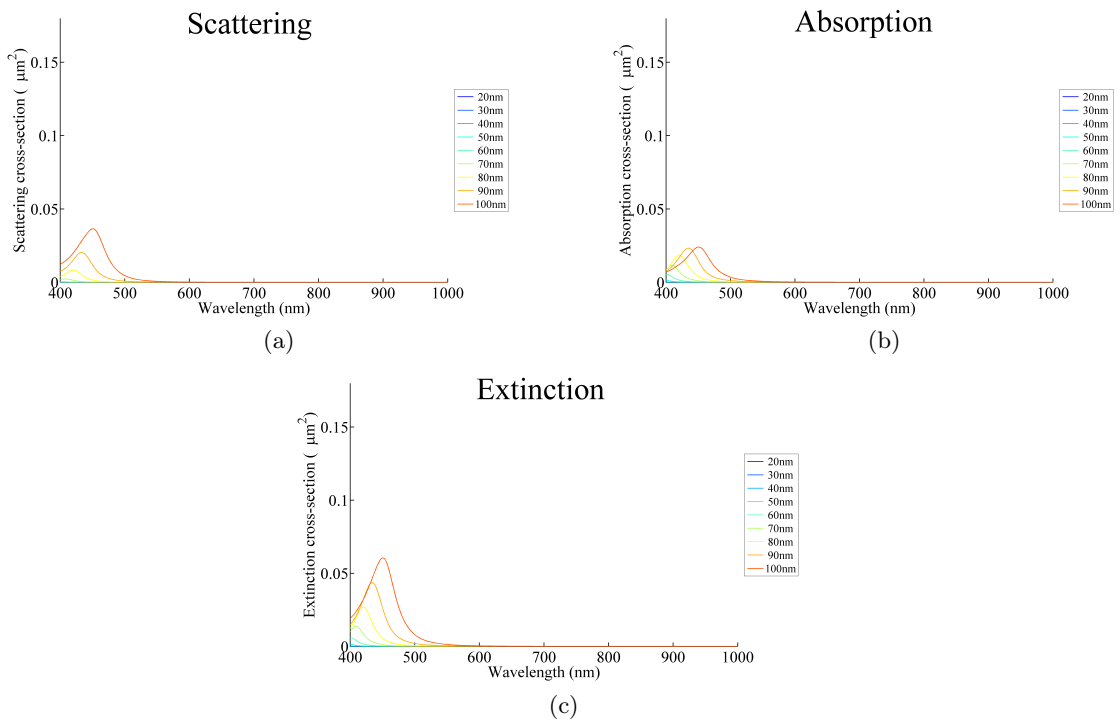

Figure 2.5.11: The octupolar contributions to the (a) scattering, (b) absorption and (c) extinction cross-sections of silver nanospheres surrounded by glass for a range of radii as calculated by Mie theory.

In the spectrum for the total extinction (figure 2.5.7), the strongest peak is from the octupolar mode. We can see from this analysis of the separate modes that it has in fact a relatively small contribution and its apparent strength in the total spectrum, with all modes included, is due to its superposition with the other two significant modes which are considerably broadened by the time the octupolar mode becomes clearly apparent in the total extinction cross-section.

For octupolar modes it can be seen from figure 2.5.11 that even for the largest particles considered, absorption still makes an important contribution to the extinction cross-section due to the fact that the volumes involved with the microscopic dipole moments are small.

The peak extinction wavelengths of silver spheres surrounded by glass have been plotted as a function of particle radius for the first three resonant modes (figure 2.5.12). It can be seen that in the electrostatic regime the peak wavelengths asymptote to well-defined values. These are the same wavelengths as those predicted using $\epsilon = -(l+1)\epsilon_d/l$.

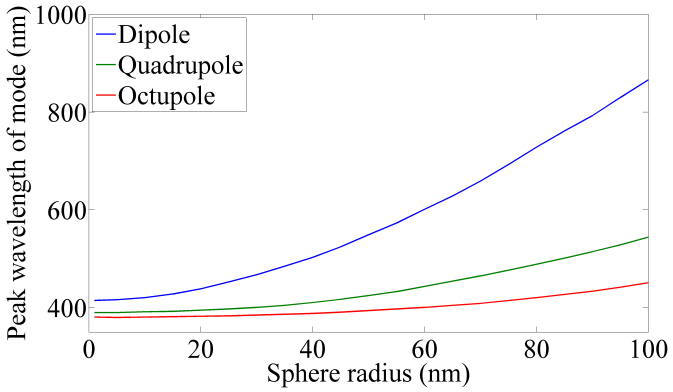

Figure 2.5.12: The peak extinction wavelength as a function of sphere radius for silver spheres surrounded by glass. The peaks for the first three modes are plotted and these can be seen to asymptote in the electrostatic regime.

For spherical particles of this size (i.e. above the electrostatic regime but below the regime of ray optics), the spherical harmonics of the system are the only rigorous way to understand the modes of the system. As the sphere becomes larger there is a new regime which can allow approximate calculations to be carried out.

2.5.5 Very large particles

When the particles are large (order of the wavelength and above), the modes supported by the particle are more like surface modes than volume modes as the radius becomes much larger than the skin depth ($\delta = \sqrt{2\rho/\omega\mu}$ where ρ is the resistivity, ω is the amgular frequency and μ is the magnetic permeability). In other words, their character approaches that of surface plasmon polaritons (SPPs) travelling over the surface of the sphere. As the modes we are considering are resonant, a quantisation of the SPPs needs to be enforced in order to test the validity of a comparison. The form of this quantisation is that there must be an integer number of SPP wavelengths in a distance equal to the circumference of the sphere, i.e.

$$2\pi r = n\lambda_{spp} \tag{2.5.2}$$

The dispersion relation for a surface plasmon on a planar film is given by Raether:[5]

$$k_{spp} = \frac{\omega}{c}\sqrt{\frac{\epsilon\epsilon_d}{\epsilon + \epsilon_d}} \tag{2.5.3}$$

where k_{spp} is the wave number of a SPP, ϵ is the permittivity of the metal and ϵ_d is the permittivity of the dielectric. ω and c are the angular frequency and the speed of light respectively. In order to calculate the quantisations of the system, we need to find the wavelengths

for which the permittivity of the metal allows the equality in equation 2.5.2 to be satisfied. Because experimental values of permittivity are being used, it is impossible to solve this problem by means of an analytical expression. It can be solved numerically, and the results can be compared to the modes calculated by Mie theory. This comparison is easier to perform for silver than gold because for gold the peak wavelengths are at much longer wavelengths and the permittivity values are more difficult to source. In this model, a dipole is described by an SPP whose wavelength is equal to the circumference. This will lead to charge accumulating at two opposite sides of the sphere. If the circumference is equal to two wavelengths, then a quadrupole will be described with alternating charge occurring at four points around the circle, and so on. For a silver sphere surrounded by glass for a range of particle radii, the position of the modes have been calculated by Mie theory and the SPP quantisation approach, and the resonance positions plotted. This is shown in figure 2.5.13.

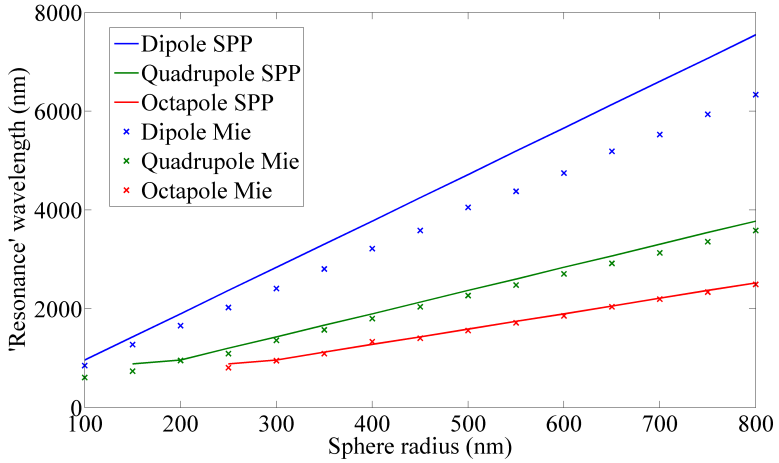

Figure 2.5.13: The resonance positions of the dipole, quadrupole and octupole modes of silver nanospheres surrounded by glass of different radii as calculated by Mie theory and by assuming an integer number of SPPs propagating around the circumference of the sphere.

It is clear from figure 2.5.13 that there is, close correlation for the quadrupolar modes and even closer correlation for the octupolar modes. The agreement is much less well correlated for the dipolar mode though. The higher the order, the shorter the wavelength must be and hence the more planar the surface will appear to the SPP. The dipolar mode can never be represented adequately in this way because the ratio of the radius of curvature to the wavelength will always be such that an approximation to a planar surface is impossible. This analysis, though simplistic, gives some insight into the physical character of the modes for very large particles. It should be noted that for particles of these sizes, many more modes exist, and spectrally they act to produce a flat response which approaches the response of a spherical mirror (figure 2.5.14).

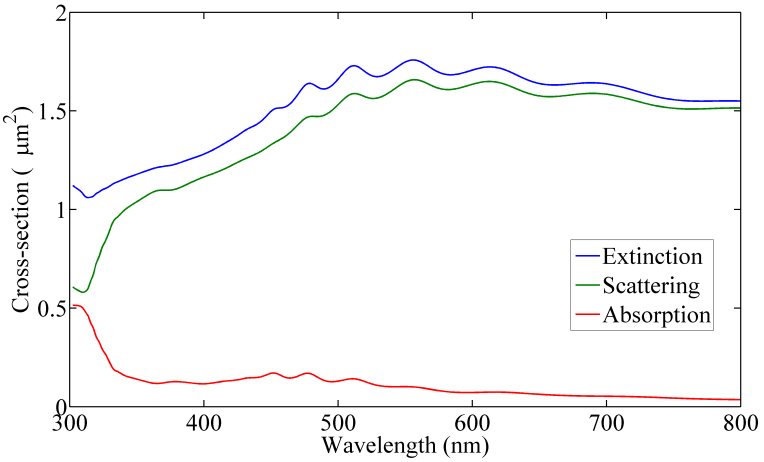

Figure 2.5.14: The cross-sections of a 200nm radius silver sphere surrounded by glass as calculated by Mie theory. There are some fluctuations in the spectra, but they are relatively flat compared to the spectra of smaller particles due to the number of modes which are supported by the sphere.

The planar reflection from bulk silver at an interface with glass is shown in figure 2.5.15.

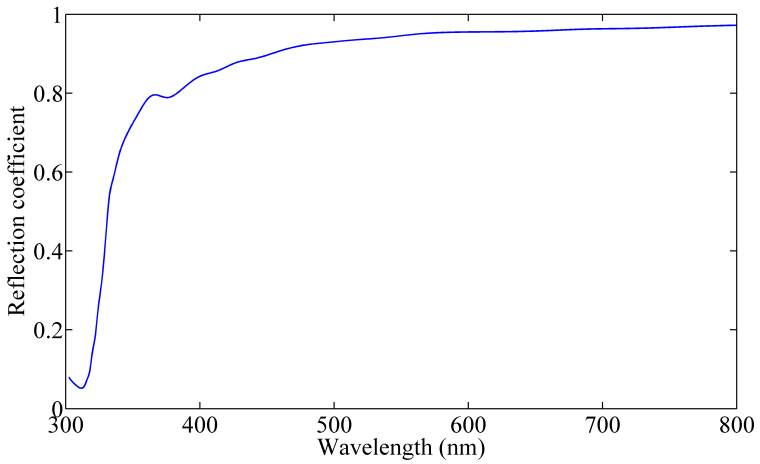

Figure 2.5.15: The Fresnel reflection coefficient of silver at an interface with glass as a function of wavelength at normal incidence.

It can be seen that there are some similarities with the scattering curve in figure 2.5.14, but there is even more similarity with much larger spheres. A similar set of data demonstrate this for a 5μm radius silver sphere in glass (figure 2.5.16).

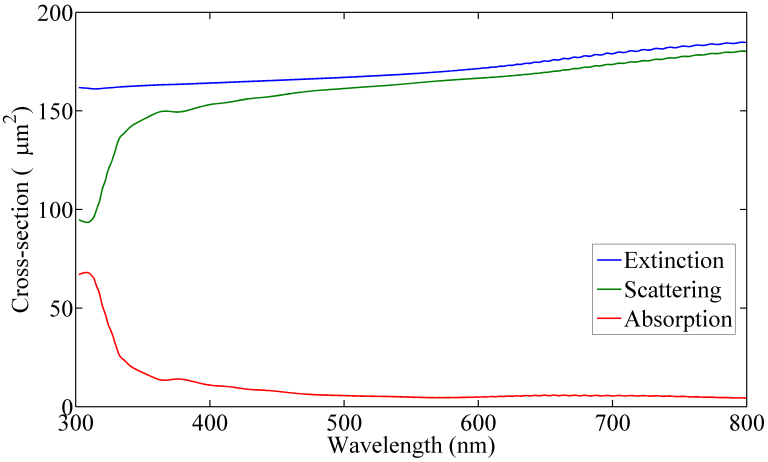

Figure 2.5.16: The cross-sections of a 5000nm radius silver sphere surrounded by glass as calculated by Mie theory. There is broad agreement between the scattering curve shown here and the reflection from planar silver at an interface with glass.

2.6 Angular scattering profiles as calculated by Mie theory

2.6.1 Dipolar mode of a small nanosphere

Once the Mie coefficients have been calculated (see appendix D), it is possible to obtain the field at any point in space. For scattered light we are interested in the far-field regime where $\mathbf{E}_{scatt} \cdot \hat{\mathbf{r}} = 0$, so only the θ and ϕ components of the scattered field remain. The scattered fields are given by:[44]

$$\begin{pmatrix} E_{\theta,s} \\ E_{\phi,s} \end{pmatrix} = \frac{e^{ik(r-z)}}{-ikr} \begin{pmatrix} F_2 & 0 \\ 0 & F_1 \end{pmatrix} \begin{pmatrix} E_0 \\ E_0 \end{pmatrix} \tag{2.6.1}$$

where F_1 and F_2 are functions of θ and ϕ and can be inferred from equations D.8.6 and D.8.7 in the appendix. The scattered intensity as a function of angle is hence given by:

$$I_{Scatt} = |E_{\theta,s}|^2 + |E_{\phi,s}|^2 \tag{2.6.2}$$

An example of this, an angular scattered intensity profile is shown in figure 2.6.1 for a silver sphere with radius 10nm surrounded by glass for a wavelength of 420nm (i.e. on the dipolar resonance). Both a 2D plot and an equivalent spherical plot are shown.

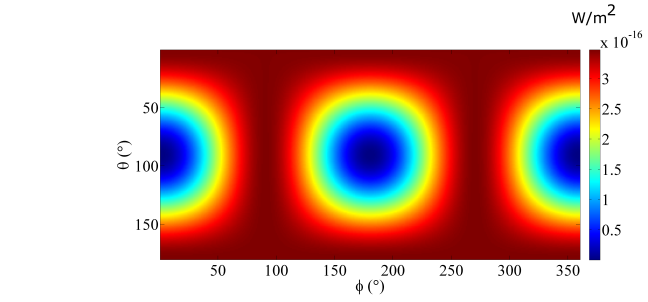

(a)

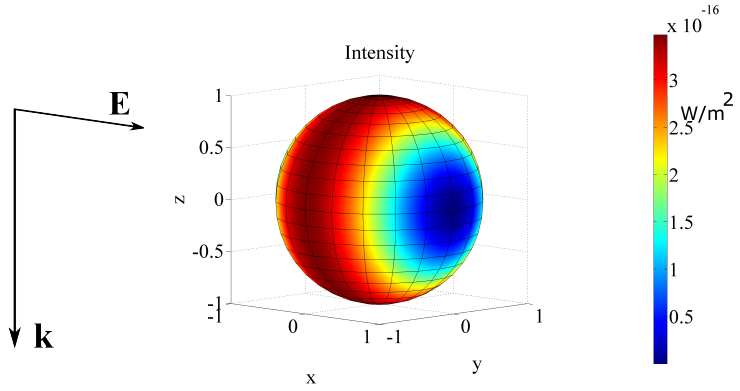

(b)

Figure 2.6.1: Angular distributions of far-field scattered intensity for a silver sphere with radius 10nm surrounded by glass at a wavelength of 420nm as calculated by Mie theory. The incident light is polarised in the x-direction and is propagating in the negative z-direction. The same data are plotted in both (a) and (b).

It can be seen from figure 2.6.1 that the scattered light is strongest for angles which are perpendicular to the polarisation direction. This is a consequence of the factor $\hat{\mathbf{r}} \times (\hat{\mathbf{r}} \times \mathbf{p})$ which appears in the radiative term of the expression for the field of an oscillating electric dipole ($\mathbf{E} = \frac{1}{4\pi\epsilon_0} e^{ikr} \left\{ \frac{1}{r^3} \left(3\mathbf{n}\left(\mathbf{n}\cdot\mathbf{p}\right) - \mathbf{p}\right) - \frac{ik}{r^2}\left(3\mathbf{n}\left(\mathbf{n}\cdot\mathbf{p}\right) - \mathbf{p}\right) - \frac{k^2}{r}\left(\mathbf{n}\times\left(\mathbf{n}\times\mathbf{p}\right)\right)\right\}$). At each angle in 3D space, the electric field has components in the θ and ϕ directions. The absolute value of these components, along with the real part for a given phase and the complex arguments are shown in figure 2.6.2 for the same system as above.

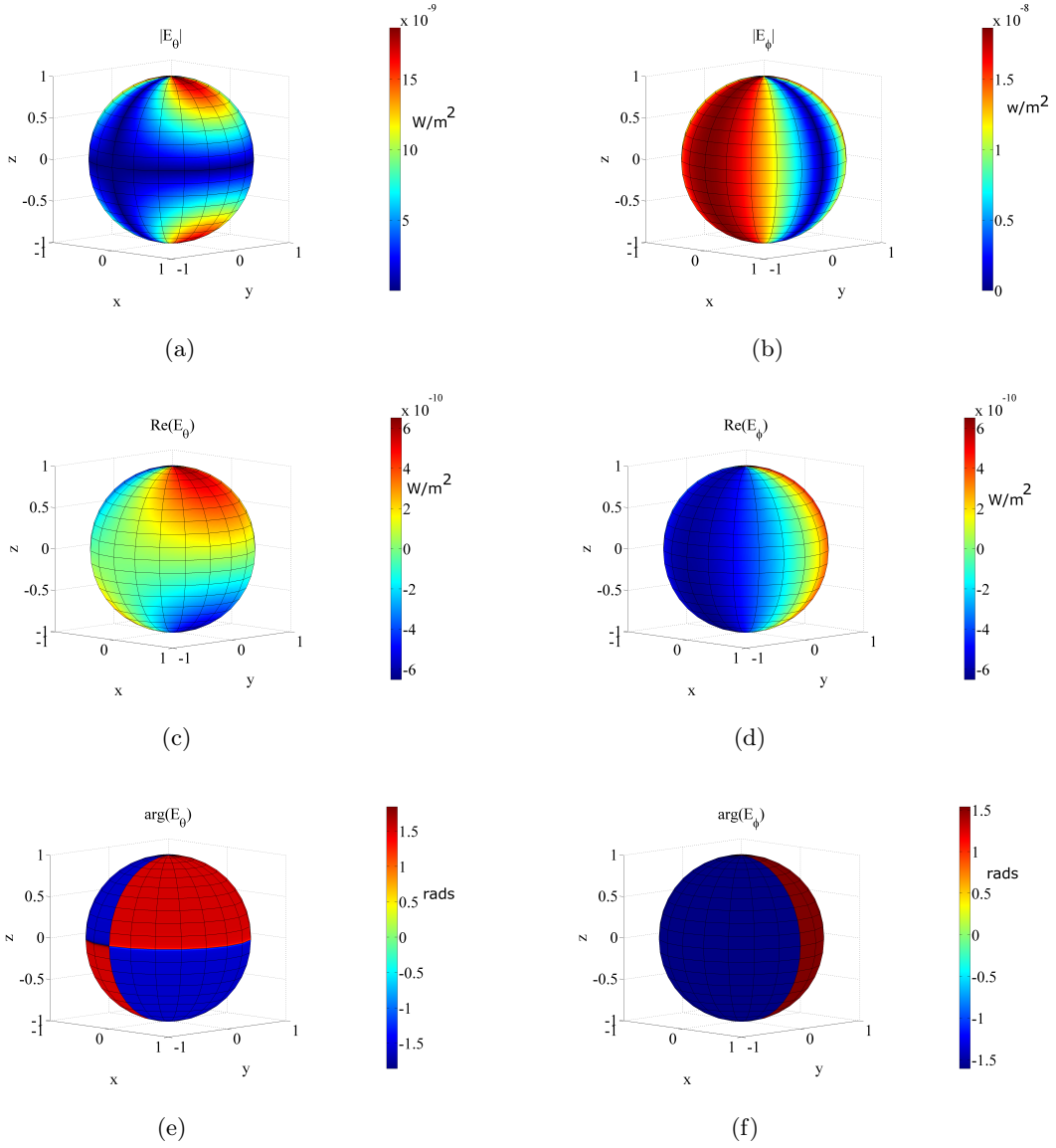

Figure 2.6.2: Angular profiles of both components of the scattered electric field far from a 10nm radius silver sphere surrounded by glass on the wavelength of resonance as calculated by Mie theory. Shown here are, (a) and (b), the absolute values of electric field of the θ and ϕ components respectively, (c) and (d), the real part of the electric field (for phase $\phi = 0$) of the θ and ϕ components respectively, and (e) and (f), the complex argument of the θ and ϕ components of the electric field respectively.

Figure 2.6.2 shows the angular dependence of the separate components of the scattered electric field in the far-field. It is clear from this plot and from physical symmetry considerations that there is no θ-component of the electric field along the y-axis. It is also informative to examine the real parts of the field and the associated phase profiles. These show that at particular angles, the phase suddenly changes by π and at the same angles, the real part of the electric field undergoes a sign change. This is not, however a physical result - it is simply a characteristic of working in a spherical coordinate system as the unit vectors $\hat{\theta}$ and $\hat{\phi}$ are angle dependent

according to the following expressions:

$$\hat{\boldsymbol{\theta}}(\theta,\phi) = \cos\theta\cos\phi\hat{\mathbf{x}} + \cos\theta\sin\phi\hat{\mathbf{y}} - \sin\theta\hat{\mathbf{z}} \tag{2.6.3}$$

$$\hat{\boldsymbol{\phi}}(\theta,\phi) = -\sin\phi\hat{\mathbf{x}} + \cos\phi\hat{\mathbf{y}} \tag{2.6.4}$$

As an example, let us consider the direction defined by $\theta = 0$ and $\phi = 0$. In this direction, the unit vectors become $\hat{\boldsymbol{\theta}}(0,0) = \hat{\mathbf{x}}$ and $\hat{\boldsymbol{\phi}}(0,0) = \hat{\mathbf{y}}$. At $\theta = \pi$ and $\phi = 0$, however, the unit vectors become $\hat{\boldsymbol{\theta}}(\pi,0) = -\hat{\mathbf{x}}$ and $\hat{\boldsymbol{\phi}}(\pi,0) = \hat{\mathbf{y}}$. This is why the oscillating dipole moment, having symmetrical scattering in the forward- and back-scattered directions in a Cartesian system has opposite sign in a spherical system and hence there appears to be a discontinuity in the phase of the scattered light.

2.6.2 Higher order modes of larger spheres

Considering only the dipolar mode in isolation, the scattering profile of larger particles will be qualitatively very similar to that of the small particle considered above, so for the remainder of this discussion, figure 2.6.1 will be referred to when considering the physics of scattering by dipolar modes of spheres.

As discussed above, the individual modes can be considered separately in Mie theory by setting the weighting coefficient of all the other modes to be equal to zero, and this also applies to scattering profiles. The scattering intensity profiles of the dipolar, quadrupolar and octupolar modes of a 50nm radius silver sphere surrounded by glass are shown in figure 2.6.3. These plots are produced at the resonance wavelengths of the respective modes, and the calculation for each mode does not consider any other modes.

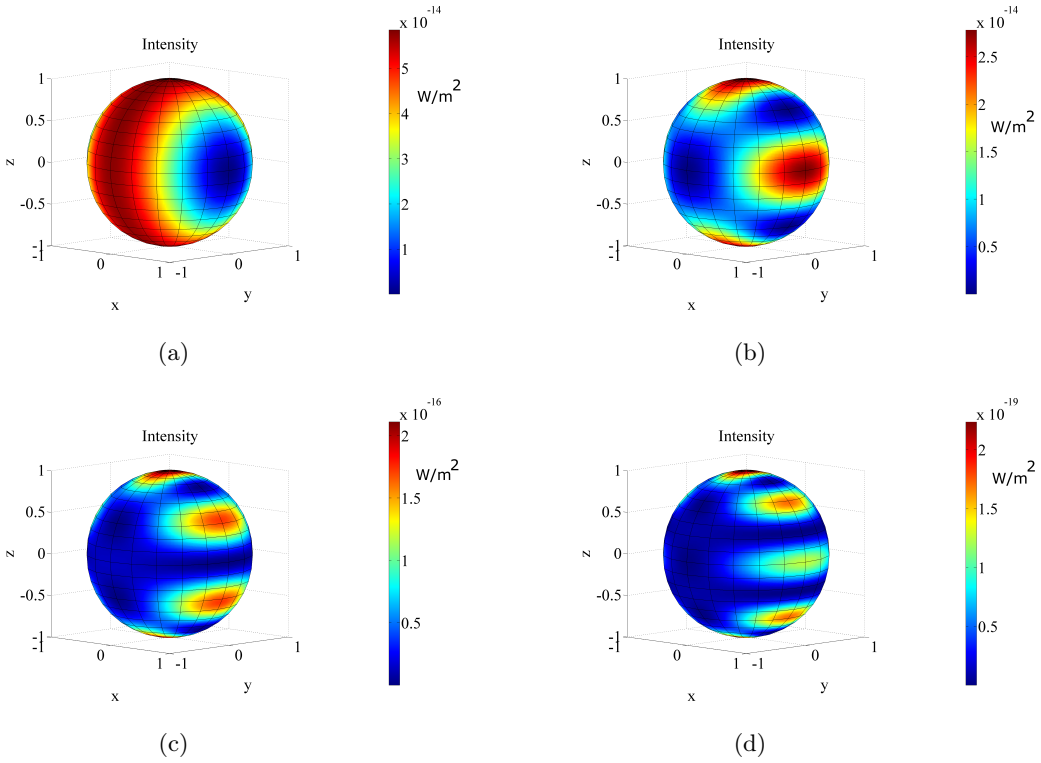

Figure 2.6.3: Scattering profiles of the first four modes ((a) dipole, (b) quadrupole, (c) octupole and (d) hexadecapole) of a 50nm radius silver sphere surrounded by glass as calculated by Mie theory. The profiles of the modes were plotted at the resonant wavelengths of the particular modes, and components from other modes were not included in the calculation.

It can be seen from figure 2.6.3 that while the dipolar mode scatters light in a doughnut-like radiation pattern, the higher order modes scatter strongly into several lobes — the higher the order, the greater the number of lobes. A simplistic, though physically informative picture of cause of these lobes can be inferred from the well-known near-field plots[2,44,54,77] of the electric field calculated for separate modes if it is assumed that the dipole formed between each accumulation of charge is responsible for radiating radially away from the particle (figure 2.6.4).

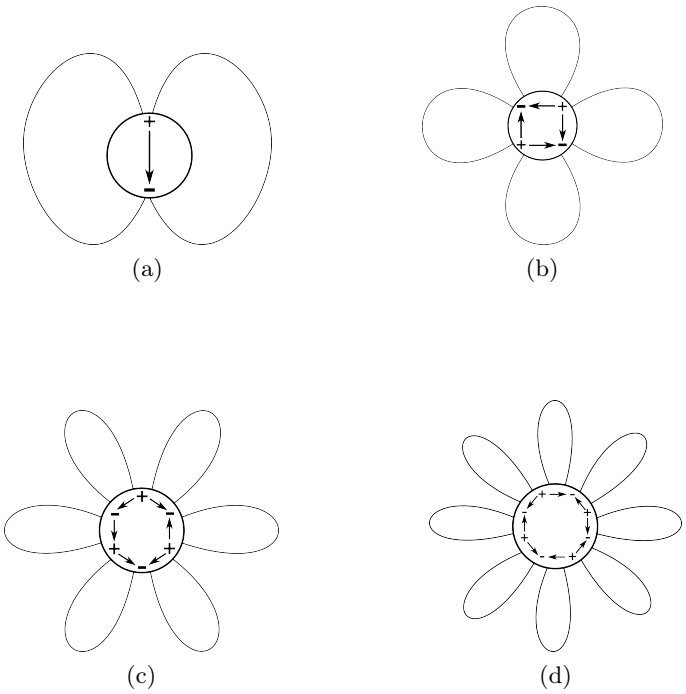

Figure 2.6.4: Schematics showing the far-field scattering lobes of the first four modes and their relation to the oscillating dipole moments on the surface of a sphere. Shown here are (a) the dipolar, (b) quadrupolar, (c) octupolar and (d) hexadecapolar modes of a sphere.

It can be seen in figure 2.6.4 the way in which the near-field charge distribution relates to the location of the scattered lobes. These lobes are equivalent to those seen in the intensity profiles as calculated by Mie theory (figure 2.6.3), and it can clearly be seen that as the order increases, more and more lobes will exist. Interestingly, the dipolar mode is the dominant mode, and its profile is very different to the other modes which can be excited as the dipolar mode can scatter strongly along the axis which is orthogonal to the incident electric field and **k**-vector — all the other modes scatter into lobes which are in the plane containing these vectors because each of the microscopic dipole moments within the particle have oppositely orientated neighbours which cancel their response in the direction orthogonal to the incident electric field and **k**-vector in the far-field.

2.6.3 Superposition of scattered light from several modes

Until now we have only considered the radiation from individual modes in isolation. In reality a very large number of modes are excited on a sphere (up to a limit set by the atomic structure of the metal), but only the first few contribute significantly to the far-field quantities such as extinction and scattering for a metal nanosphere because of the overlap integral between the various modes and the incident field. At a given frequency the light which is scattered in a given direction is a superposition of the fields of several modes, and this can produce markedly different scattering profiles in the forward and backward directions. It is, of course, necessary

to consider the complex field quantities rather than the intensities as there can be a phase difference between the different modes.

Firstly, let us consider a 50nm radius silver sphere surrounded by glass. The response of this nanoparticle is almost entirely described by the dipolar, quadrupolar and octupolar modes. For our purposes we will neglect the effect of the octupolar mode, because its magnitude is much smaller than the two other dominant modes. If we repeat the above analysis of the scattering profiles of these spheres, but take into consideration *all* the important modes, the intensity scattering profiles are somewhat modified. These are shown in figure 2.6.5 for the frequencies of the dipolar and quadrupolar modes.

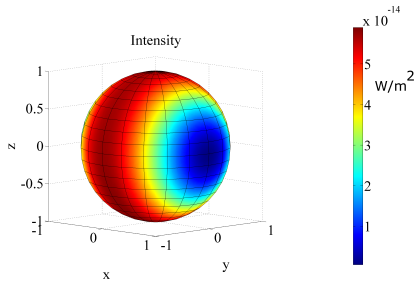

(a)

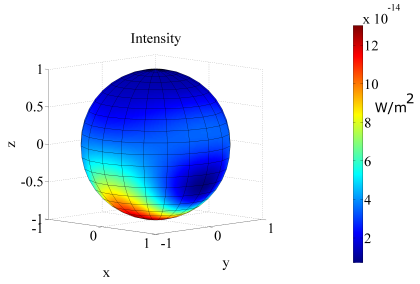

(b)

Figure 2.6.5: Scattering intensity profiles of a 50nm radius silver sphere surrounded by glass at the frequencies of (a) the dipolar mode and (b) the quadrupolar mode. For these profiles, many modes more than the first two were considered in the Mie calculations.

It can be seen from figure 2.6.5 that the intensity profile at the frequency corresponding to the dipolar mode is very similar to the profile when only that mode is considered (figure 2.6.3a). We can hence say that the quadrupolar mode does not have a major effect on the scattering profile at that frequency. This is in agreement with the spectra in figures 2.5.9 and 2.5.10. At the frequency of the quadrupolar resonance, however, the scattering profile is completely different, with most of the light being scattered in the forward direction, and hardly any being back-scattered. This can be explained by examining the complex values of the electric field from both modes which, when squared and summed, form the intensity distribution (figure 2.6.6).

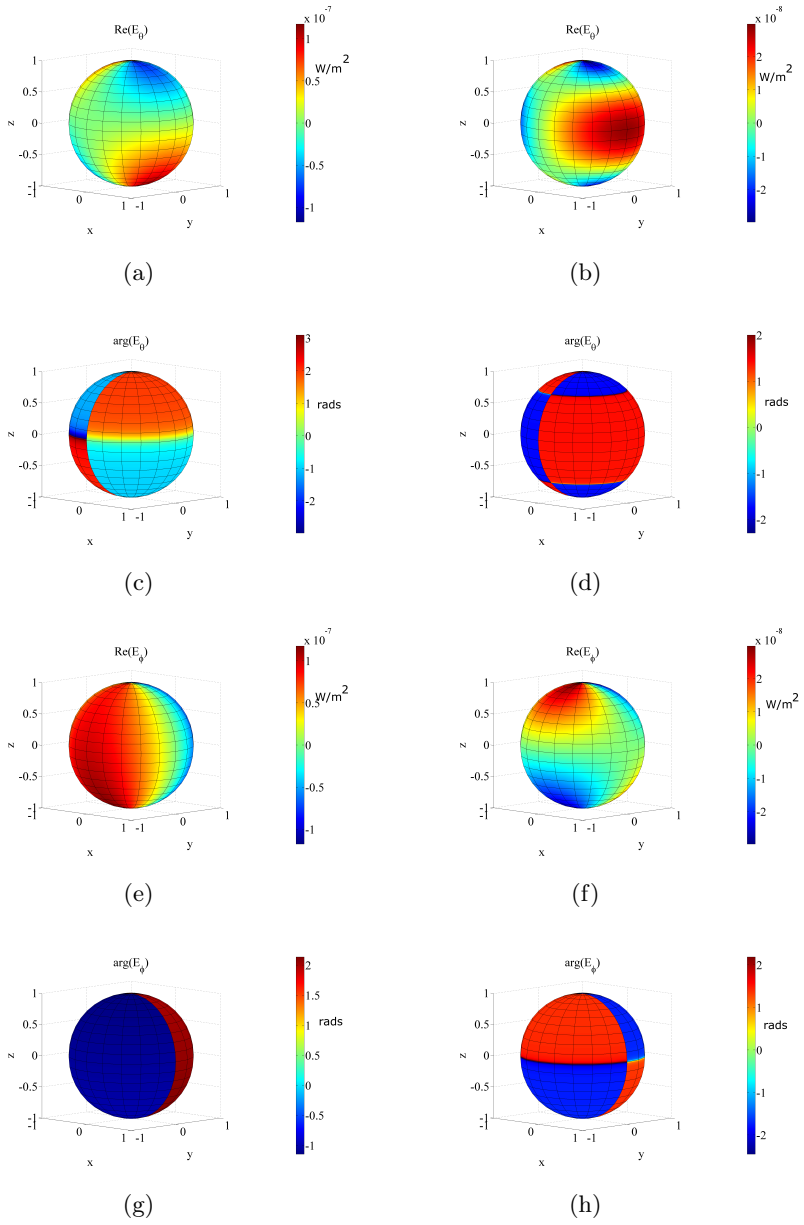

Figure 2.6.6: Angular profiles of the dipolar (a,c,e and g) and quadrupolar (b,d,f and h) contributions of real parts and complex arguments of the two components of the scattered electric field far from a 50nm radius silver sphere surrounded by glass at the wavelength of the quadrupolar mode as calculated by Mie theory.

If a pair of associated plots are considered from figure 2.6.6, it can be seen that when the dipolar contribution is compared directly to the quadrupolar contribution, the mirror symmetry is always opposite between the two modes. Regardless of the coordinate system, with reference to the phase plots, this means that the phase difference between the two modes in the forward and backward directions will be different. A close analysis of the scales in the phase plots indicate that there is a very small phase difference in the forward direction and in the backward direction the phase difference is much closer to 180°. The actual, calculated phase differences

are shown in the table below in degrees.

	Forward	Backward
E_{theta}	40°	145°
E_{phi}	42°	214°

The fact that the phase difference between the two modes in the forward direction is close to 0° ensures that there is significant constructive interference which results in a strong scattered intensity in the forward direction. In the backward direction, the phase difference between the modes is close to 180° so that there is a significant amount of destructive interference which leads to very little back scattered light. This is all despite the fact that the strength of the quadrupolar field is less than half that of the dipolar field at that frequency. The explanation of this is that the modes in isolation are symmetrical, and whenever there is a phase difference between two modes, as shown above, the field increases in one direction and decreases in the other. Once the magnitudes of the fields are squared, the difference is enlarged, and it becomes sufficient to completely dominate the scattering profile.

2.7 Validity of FEM — comparison with Mie theory

Throughout this thesis, FEM is used extensively, so in order to test its validity, the scattering and absorption cross-sections of a sphere were simulated using HFSS (the extinction was calculated as a sum of these values). These results are shown in figure 2.7.1.

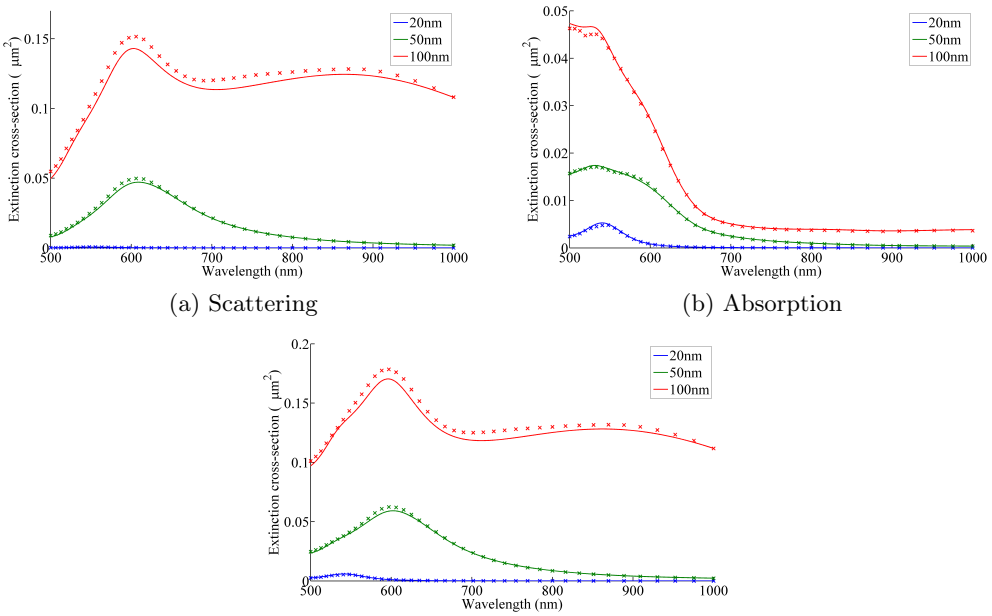

(a) Scattering

(b) Absorption

(c) Extinction

Figure 2.7.1: A comparison between HFSS and Mie theory for gold spheres surrounded by glass for a range of particle radii. The Mie results are shown as line-plots and the HFSS results are shown as crosses.

It can be seen that there is qualitative agreement between HFSS and Mie theory — the shape of the curves and the peak positions are similar, though there are differences in the intensities. This may be due to the fact that in HFSS a sphere is represented by a large number of planar faces, and hence is not strictly spherical.

2.8 Dark-field results

2.8.1 Experimental

Dark field spectra were recorded for 30nm thick gold discs for a range of radii. The discs were fabricated on a glass substrate were index-matched to the objective lens. Even if the polarisation state of the light passing into the condenser lens was known, there would be a large range of polarisations incident on the discs due to the focussing action of the lens. For this reason it was decided to use unpolarised light. The numerical aperture range of the condenser is 0.8-0.95, and the numerical aperture of the objective was set to 0.5 in order that no *incident* light was collected. The scattering spectrum was collected over the range 500-1000nm (figure 2.8.1).

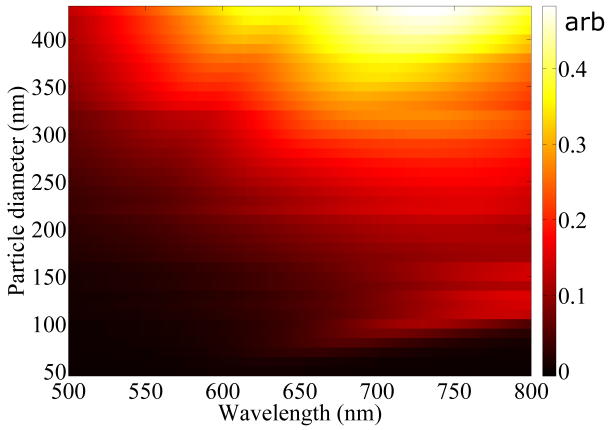

Figure 2.8.1: Dark-field scattering spectra of a number of 30nm thick gold discs surrounded by refractive index $n = 1.5$ with a range of diameters.

It can be seen from figure 2.8.1 that for small diameters, the resonance red-shifts as the diameter is increased, due to radiative damping and dynamic depolarisation. At a diameter of approximately 170nm, the intensity of the mode suddenly drops and two other modes dominate the spectra for all larger diameters. In order to better understand the cause of these features, FEM was used to try to identify the modes.

2.8.2 Modelling

The illumination was set to have a polar angle equal to the mean value produced by the dark-field condenser. The model was solved for 21 different particle diameters in the range 20-440nm, and the edges of all the gold discs were rounded with a radius of curvature of 10nm. The wavelength at which meshing was carried out was 600nm. The scattering spectra for s- and p-polarised light are shown in figure 2.8.2.

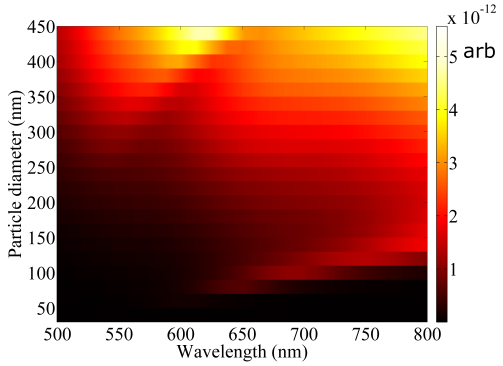

(a)

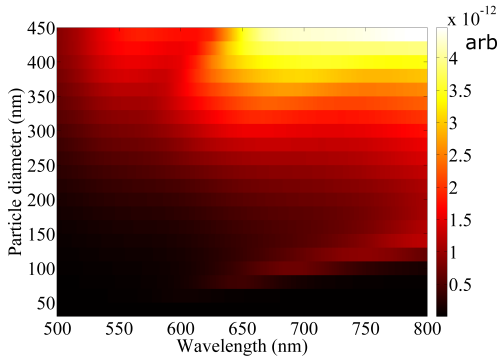

(b)

Figure 2.8.2: Simulated dark-field scattering spectra of 30nm thick gold discs surrounded by refractive index $n = 1.5$ for a range of diameters. Plots are shown for (a) s- and (b) p-polarised incident light.

Before analysing these data, they need to be converted into a form which more closely matches unpolarised light. Because the sample is removed when the spectrum of the lamp is recorded, a different ratio of polarisation intensities exist in the region of the particles compared to the intensity they are normalised to. This is due to the presence of the air-glass interface at the top of the substrate. The two intensities are found using the Fresnel transmission coefficient (figure 2.8.3).

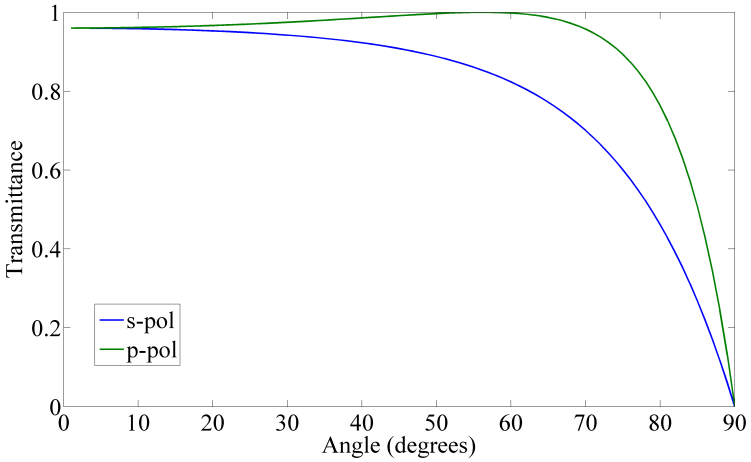

Figure 2.8.3: Fresnel transmission coefficients at an air-glass interface for s- and p-polarised light for all incident angles.

At the incident angle used in the model (35° in glass which is equivalent to 60° in air), the intensity coefficients are ~ 1 for p-polarised light and ~ 0.8 for s-polarised light. The intensities in figure 2.8.2 are scaled by these values in order to produce a combined set of data which approximate unpolarised light for the particular illumination conditions provided by the dark-field condenser when the particles are on the bottom of the substrate (figure 2.8.4).

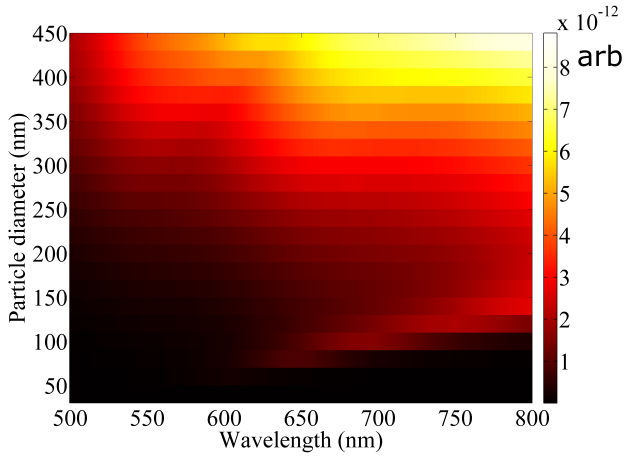

(a)

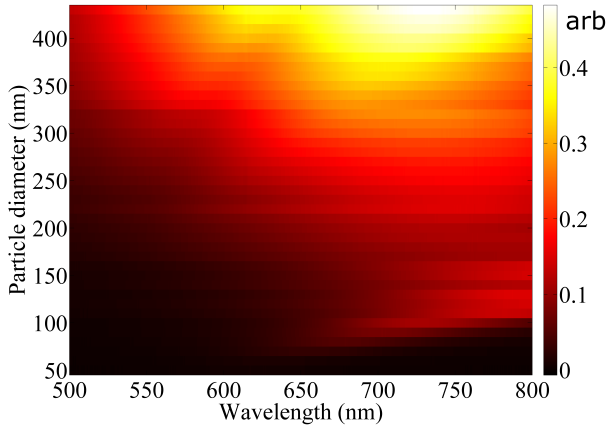

(b)

Figure 2.8.4: Simulated dark-field scattering spectra (a) of a number of 30nm thick gold discs surrounded by refractive index $n = 1.5$ with a range of diameters after correcting for the intensities of the separate polarisations incident on the discs. The equivalent set of experimental data is reproduced here (b).

It can be seen that some agreement exists between the experimental and simulated intensities. Before commenting further on the extent of any agreement, it is worthwhile to examine field profiles from the FEM models in order to identify the modes of the system which are present in the simulated spectra.

2.8.3 Field profiles — identification of modes

The first three modes of the discs have been plotted for s-polarised light (similar plots can be obtained for p-polarised light but the fields are rotated by 90° around the axis normal to the surface of the disc). The total electric fields (incident+scattered) are plotted in figure 2.8.5 for the dipolar, quadrupolar and octupolar modes.

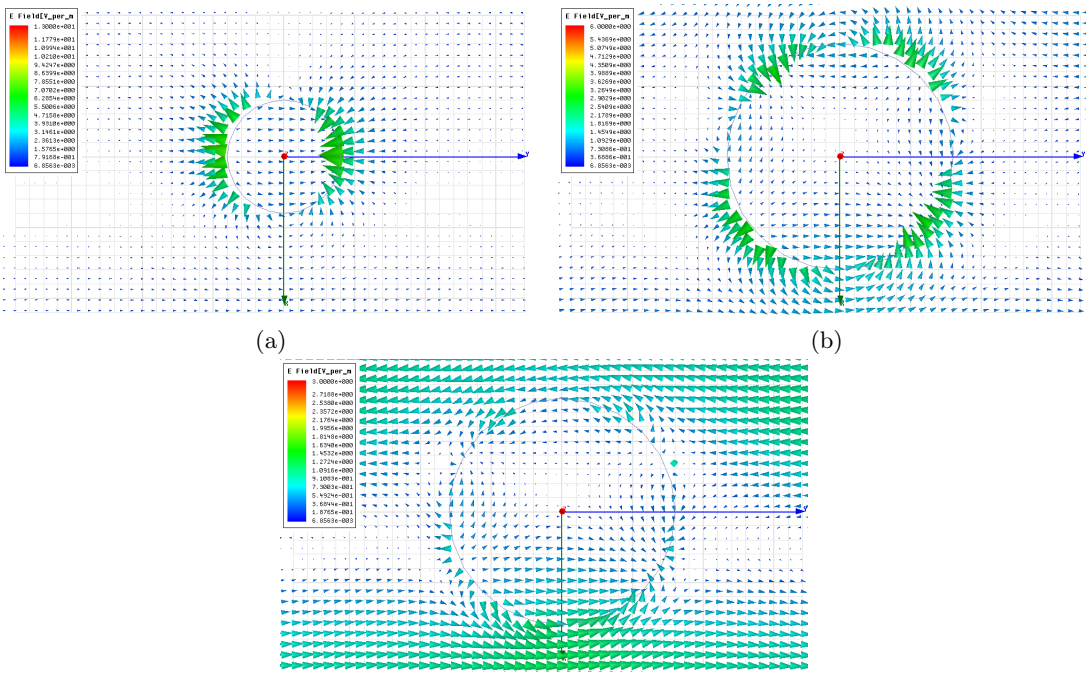

Figure 2.8.5: Simulated electric field plots of (a) a dipolar mode, (b) a quadrupolar mode and (c) an octupolar mode of gold discs. The diameters, wavelengths and phases of these plots were chosen to provide clear indication of the modes. The illumination light is s-polarised (the electric field vector is in the y-direction). The plane for which the fields are plotted passes through the centre of the disc.

It can be seen that the dipolar mode has two charge accumulations, the quadrupolar mode has four and the octupole has six. The wavelengths for which these images were obtained are given in the table below.

Mode	Diameter	Wavelength
Dipolar	160nm	875nm
Quadrupolar	320nm	850nm
Octupolar	320nm	675nm

From this information it is possible to label the modes on figure 2.8.4 (these do not appear distinctly in the plot, but further analysis has confirmed that the modes shift as indicated — figure 2.8.6).

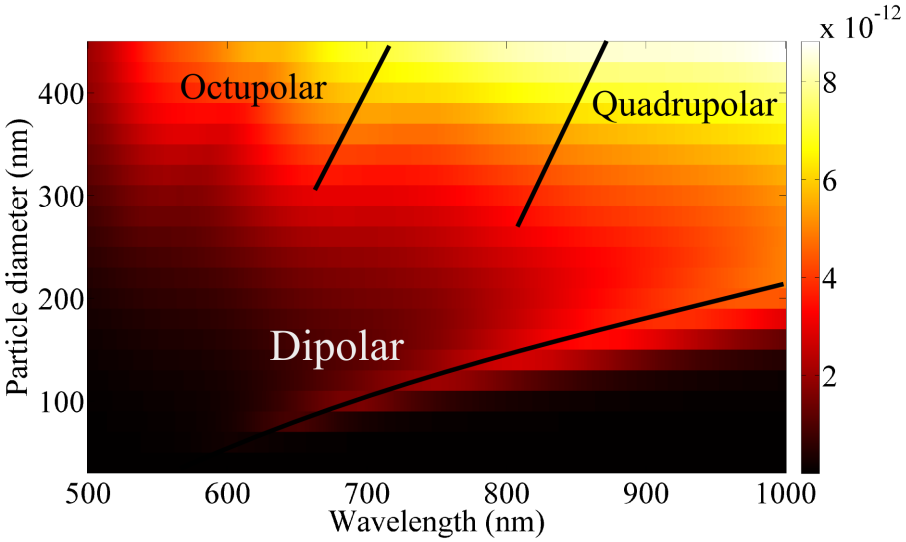

Figure 2.8.6: Simulated dark-field scattering spectra (identical to figure 2.8.4) with the modes labelled.

The peak in intensity which appears at around 550-600nmnm for large discs is stronger for s-polarised light, and is probably the hexadecapolar mode, but it is difficult to identify in the field plots due to the superposition of a number of modes at that wavelength.

The experimental data show good agreement in general at relatively short wavelengths — the red-shift of the dipolar mode is clearly present and both the octupolar and the mode thought to be the hexadecapolar mode match the simulated spectra closely. At long wavelengths, however, (i.e. $\lambda > 800$nm) the agreement is significantly poorer. Instead of high intensities for large particles in this regime due to the effects of the dipolar and quadrupolar modes, the experimental data show a significant drop-off in intensity. Several reasons for this discrepancy have been investigated. The presence of second-order diffraction in the normalisation spectrum could lead to low intensities at long wavelengths, but the drop-off is still present when a long-pass filter in the collection path is used. The possible lack of CCD sensitivity at long wavelengths was discounted due to the lack of noise in the normalised spectrum. Possible absorption by the index matching fluid at long wavelengths has been ruled out by performing a simple transmission experiment across this wavelength range. As a first attempt at checking the spectral sensitivity as a function of the modelled geometry, the effect of rounding the corners was investigated and no significant changes were apparent (a $\sim$ 20nm blue shift was seen when the rounding was introduced). The cause of the discrepancy is still unknown, but it is thought that it could be due to the polarisation states incident on the particle not being fully described by the model or dispersion in the refractive index of the matching fluid at long-wavelengths.

2.9 Summary

In this chapter, the plasmonic response of single particles has been investigated experimentally and theoretically. Mie theory has been used to understand the first few plasmonic modes of spheres, and the scattering patterns of each of the modes have been explored, and the phase relations between the scattering patterns of multiple modes has been used to demonstrate that strong forward scattering can occur at wavelengths when there are significant contributions from the dipolar and quadrupolar modes. In this case, the scattered fields act to interfere constructively in the forward direction and destructively in the backward direction.

The regimes of scattering for metallic spheres have been fully described, from small, sub-wavelength particles, to macroscopic spheres. It has been demonstrated that at intermediate sphere radii, the spectral position of the modes is equivalent to integer numbers of bound surface plasmon-polaritons traversing the surface of the spheres.

A detailed description of dark-field spectroscopy has been provided, and experimental scattering spectra have been compared to results from FEM. The level of agreement has been discussed, and the drawbacks of dark-field illumination have been highlighted.

Chapter 3

Extinction and scattering of metallic nanoparticles in ordered and random arrays

3.1 Introduction

This chapter is concerned with the interaction between plasmonic nanoparticles. Initially, pairs of nanoparticles will be considered in order to establish the different regimes of interaction. Then 2D arrays will be investigated to discover how the different regimes translate into coherent interactions in an infinite, ordered array. Finally, random arrays of nanoparticles will be investigated, and the response will be compared to that of a single particle.

The interaction of pairs of particles (or dimers) has been studied extensively theoretically[78–81] and experimentally.[82,83] Particle pairs continue to be studied carefully; the longevity of such a seemingly simple system is no doubt due to its uses in metamaterial structures,[39,40] sensing[10,84] and local field enhancement.[85] Very recent work by Zuloaga *et al.*[86] even suggests that electron tunnelling may be responsible for the unexpected optical response at separations of less than 1nm.

In the literature, one of the first steps in making the leap from single particles to 2D arrays is to consider chains of particles, and for radiative interactions, most of the physics can be found in this simpler system. Numerical analysis has been applied to chains of spheres,[87] including those that support quadrupolar modes.[88,89] Experimental measurements of chains of discs have also been obtained[90–92]

Experimental reflectance measurements of arrays of metallic rods have been compared to FDTD,[93] and the regimes of interaction described here are consistent with those findings.

A great deal of similar relevant work on nanorods has been carried out in recent years.[94–96] Rods may have very sharp resonances, but they are highly anisotropic, and so discs have been selected to form the basis of this study.

A key paper in the literature regarding plasmonic resonances in metallic nanodiscs is provided by Haynes *et al.*[97] and describes experimental results which clearly demonstrate the regimes of near-field and far-field interactions in arrays of gold discs. Similar trends were reported by Sung *et al.*[98] Nanosphere lithography has been suggested as a useful strategy for producing large arrays of plasmonic particles in hexagonal arrays with the aid of ion beam milling.[99]

A more material-based study on the dispersion of a set of nanodisc chains has been carried out by Yang and Crozier.[100] A solid-state approach has also been applied to the concept of localisation in disordered arrays.[101]

Although some research has been done on disordered arrays,[95,101,102] the modelling of such systems is still being developed.

3.2 Dipole field

Particle pairs (sometimes called dimers) are simply two particles which are investigated simultaneously. These particles are illuminated with light and the extinction or scattering is calculated or measured. When the particles are far apart, they behave independently. However, when they are brought closer together, the light scattered from one particle is able to interact with the other (and *vice versa*), and hence the response is modified. If both particles are identical and both absorb and scatter the light, then some of the light which is scattered by one of the particles falls on the other, and hence some of that light ends up being absorbed as opposed to scattered and hence the absorption of the system increases. In the case of metallic nanoparticles, the interactions can be very strong, particularly when the separation between the particles is of order of the wavelength of the light or less. A good starting point is the equation for the field of an oscillating dipole[77] (ignoring time-dependence):

$$\mathbf{E} = \frac{1}{4\pi\epsilon_0} e^{ikr} \left\{ \frac{1}{r^3} \left(3\mathbf{n}\left(\mathbf{n}\cdot\mathbf{p}\right) - \mathbf{p}\right) - \frac{ik}{r^2} \left(3\mathbf{n}\left(\mathbf{n}\cdot\mathbf{p}\right) - \mathbf{p}\right) - \frac{k^2}{r} \left(\mathbf{n}\times\left(\mathbf{n}\times\mathbf{p}\right)\right) \right\} \tag{3.2.1}$$

Here, $\mathbf{E}$ is the electric field, $\mathbf{p}$ is the dipole moment, $\mathbf{n}$ is a unit vector directed from the dipole towards the observer, r is the distance from the dipole to the observer and k is the wavevector. The first term in the equation above is identical to that of an electrostatic dipole and it dominates in the near-field ($kr \lesssim 1$). The second term is known as the induction term and is related to the amount of energy which is stored by the dipole. The third term is the radiation term and it dominates in the far-field ($kr \gtrsim 1$). The magnitude of this function (including all terms) is plotted in two-dimensions in figure 3.2.1.

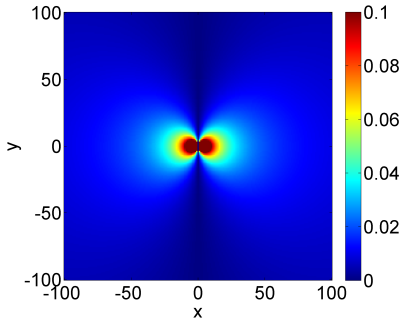

Figure 3.2.1: Electric field magnitude of an oscillating dipole as calculated from the analytical expression (equation 3.2.1) including all components and terms. The dipole moment is oriented along the y-axis, and the magnitudes of both the dipole moment and the k-vector are equal to 1.

In the near-field regime, the field is high close to the ends of the dipole due to the fact that at one of these points, the field from the nearest (say positive) charge is much stronger than the negative charge due to Coulomb's inverse square law. In the far-field, however, the strongest fields are perpendicular to the direction of the dipole moment due to the fact that the oscillating charges radiate orthogonally to their direction of motion. The electric field of a hypothetical oscillating dipole has been calculated, and the electrostatic and radiative terms have been isolated so that their fields can be plotted independently (figures 3.2.2 to 3.2.4). For all the plots shown here, the oscillatory behaviour of the radiation and SI scaling factor have been neglected for clarity (the fields set the amplitude which then should be multiplied by $\frac{1}{4\pi\epsilon_0}e^{ikr}$ for completeness). The electric field components of the near-field term are shown in figure 3.2.2 and the net field amplitude is shown in figure 3.2.3. For the radiative term of the dipolar field, the components are shown in figure 3.2.4 and the field magnitude is shown in figure 3.2.5. In all cases, both the magnitude of the dipole moment and the magnitude of the k-vector are equal to 1.

Figure 3.2.1 shows the well-known profile for dipole radiation (this should be squared to obtain the intensity distribution). It is clear that in the far-field the electric field vanishes quickly along the y-axis (i.e. the direction of the dipole moment). The only term which provides a field of any orientation along the y-axis is the electrostatic term (figure 3.2.2b).

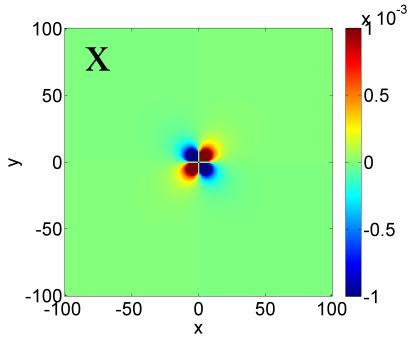

(a)

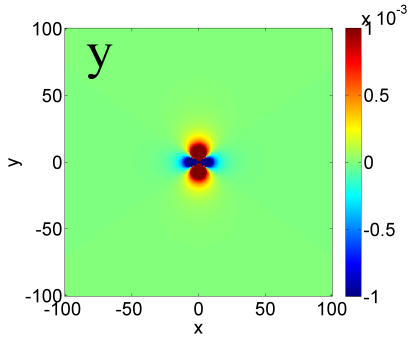

(b)

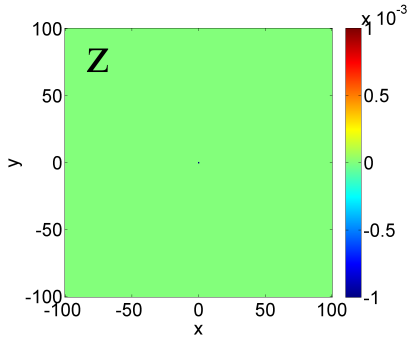

(c)

Figure 3.2.2: Electric field components of the electrostatic term in the expression for dipole radiation. The dipole moment is oriented along the y-axis. The symmetry of the system is such that any plane on which the y-axis lies contains identical fields. The figure shows the (a) x-, (b) y-, and (c) z-components of the electric field. For the z-component, the non-zero value at the origin is spurious and corresponds to a singularity at the position of the dipole. The oscillatory behaviour of the field has been ignored for clarity (i.e. the factor e^{ikr} has been omitted).

The profiles in figure 3.2.2 show the separate components of the electric field term which is dominant close to the dipole. The x-component appears in four lobes. This is due to the fact that no x-component of the field exists along the x-axis due to the cancellation of the fields of the two imaginary charges which constitute the dipole moment. The fields of each of these charges have radial distributions so along the y-axis, there is only a y-component of the field and therefore the x-component is zero. The sign of the fields can be easily understood if a macroscopic dipole is considered.

The y-component of the field is clearly stronger along the y-axis than along the x-axis. This is because along the x-axis, not only do the strengths of the fields decrease due to Coulomb's law (we are also resolving the y-component which is significant very close to the dipole due to the shaping of the field), but it quickly drops off as the fields along the x-axis become more radial.

The z-component is zero everywhere due to the fact that in the x-y plane, symmetry indicates that there can be no net field in the z-direction.

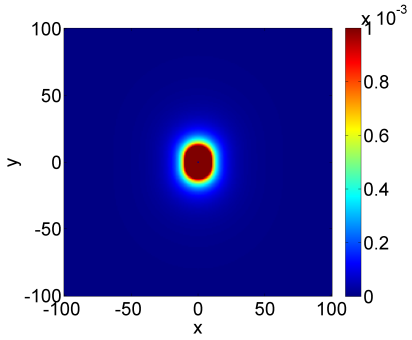

Figure 3.2.3: Electric field magnitude of the electrostatic term of the expression for the field of an oscillating dipole (including all components).

Figure 3.2.3 shows that the total field magnitude of the electrostatic term is stronger along the y-axis than along the x-axis. This result will be used later in the discussion of particle pairs.

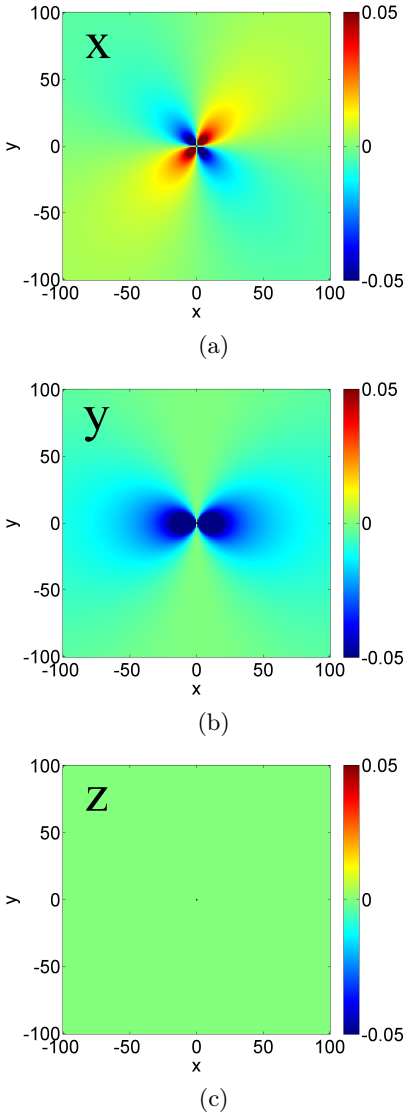

Figure 3.2.4: Electric field components of the radiative term in the expression for dipole radiation. The dipole moment is oriented along the y-axis. The figure shows the (a) x-, (b) y-, and (c) z-components of the electric field (oscillatory behaviour has been omitted for clarity). For (c), the non-zero value at the origin corresponds to a singularity.

Figure 3.2.4 shows the separate electric field components of the radiative term in the expression for dipole radiation. This term dominates in the far-field. The x-component of the field is somewhat similar to the x-component of the near-field term in that four lobes exist with the same sign-changes, but the decay length of the fields is much longer. In this case, the field is zero along the y-axis due to the fact that the field which is generated by accelerating charges (which is the source of the radiation) is parallel to the direction of acceleration. Along the x-axis there is no x-component of the radiation for a similar reason — the field component perpendicular to the dipole moment (which includes the x-axis) has fields which are entirely in the y-direction, hence there can be no x-component.

The y-component of the field is strongest in two lobes centred on the x-axis. These are the

dominant lobes in the far-field of the dipolar radiation profile. These fields are radiative, and hence the radiated light propagates away from the dipole strongly along the x-direction, and along this axis, the field is aligned parallel to the y-axis. It should be noted that the field values are negative everywhere because at a given phase (in this case $\phi = 0$), the radiated light will have a sign which relates to the phase of the dipole moment, and symmetry ensures that the sign is the same everywhere.

The x-component is zero everywhere for the same reasons as discussed above for the electrostatic term.

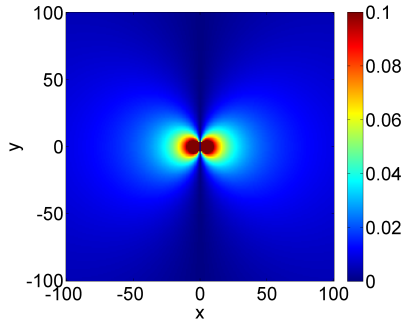

Figure 3.2.5: Electric field magnitude of the radiative term of the expression for the field of an oscillating dipole (including all components).

Figure 3.2.5 shows the total electric field magnitude when all the terms are taken into consideration. This profile is almost identical to the plot of the total field (figure 3.2.1) due to the relatively large value of k which prevents the near-field region from being observed when the radiative term is also plotted.

3.3 Particle pairs

For pairs of nanoparticles which support dipolar modes, the field each particle experiences when illuminated with light is a sum of the field due to the incident light and the field due to the other particle. This can be calculated straightforwardly using a numerical technique known as the coupled dipole approximation (CDA), also known as the discrete dipole approximation (DDA).[49,50] This can, in principle (depending on computational limitations), take into account interactions between very large numbers of particles in a self-consistent manner. A detailed description of the technique is provided in appendix E and details of its implementation here, including a Matlab code is provided in appendix F.

As stated in appendix E, for each pair of particles in the system, there exists a 3×3 interaction matrix which, when multiplied by the dipole moment of particle 1, provides the electric field

contribution particle 1 makes at the site of particle 2*. The interaction sub-matrix is given below:

$$A_{12} = A_{21} = \begin{pmatrix} A_x & 0 & 0 \\ 0 & A_y & 0 \\ 0 & 0 & A_z \end{pmatrix} \tag{3.3.1}$$

where A_x, A_y and A_z are calculated using the dyadic based on the expression for the field of an oscillating dipole. These are given below where r is the distance between the two particles and the unit vectors are either from particle 1 to particle 2 or vice versa — it makes no difference.

$$A_x = \frac{e^{ikr}}{r}\left[\frac{r_x^2}{r^2}\left(\frac{3ik}{r} - \frac{3}{r^2} + k^2\right) - \frac{ik}{r} - \frac{1}{r^2} - k^2\right] \tag{3.3.2}$$

$$A_y = \frac{e^{ikr}}{r}\left[\frac{r_y^2}{r^2}\left(\frac{3ik}{r} - \frac{3}{r^2} + k^2\right) - \frac{ik}{r} - \frac{1}{r^2} - k^2\right] \tag{3.3.3}$$

$$A_z = \frac{e^{ikr}}{r}\left[\frac{r_z^2}{r^2}\left(\frac{3ik}{r} - \frac{3}{r^2} + k^2\right) - \frac{ik}{r} - \frac{1}{r^2} - k^2\right] \tag{3.3.4}$$

The total interaction matrix also needs to provide information as to the response of the particles in isolation. This is provided in the form of the polarisabilities. The sub-matrix is shown here (for two identical particles whose polarisabilities are equal to α):

$$A_{I,I} = A_{II,II} = \begin{pmatrix} \alpha^{-1} & 0 & 0 \\ 0 & \alpha^{-1} & 0 \\ 0 & 0 & \alpha^{-1} \end{pmatrix} \tag{3.3.5}$$

The fact that the values along the diagonal are the same indicate that the particles have a symmetric (i.e. scalar) polarisability. If a non-spherical particle is considered instead, the values along the diagonal will be different. Even more complicated polarisabilities can include 2^{nd} rank terms which would replace the zeros in the sub-matrix. These indicate how, for example, a field polarised along the x-direction can induce a dipole moment in the y- and z-directions.

So the total interaction matrix for the whole system becomes (for two identical particles whose polarisabilities are equal to α):

*There is another identical matrix in this formulation which describes the effect particle 2 has on particle 1.

$$A = \begin{pmatrix} \alpha^{-1} & 0 & 0 & A_x & 0 & 0 \\ 0 & \alpha^{-1} & 0 & 0 & A_y & 0 \\ 0 & 0 & \alpha^{-1} & 0 & 0 & A_z \\ A_x & 0 & 0 & \alpha^{-1} & 0 & 0 \\ 0 & A_y & 0 & 0 & \alpha^{-1} & 0 \\ 0 & 0 & A_z & 0 & 0 & \alpha^{-1} \end{pmatrix} \tag{3.3.6}$$

It is clear from this matrix that the effect particle 1 has on particle 2 is the same as particle 2 has on particle 1 (i.e. there is reciprocity). In order to calculate the dipole moment of the two particles, this matrix must be inverted. Even for the simple case of two particles, the inverse of this matrix is tedious to perform analytically. Thankfully, it is very quick and easy to calculate numerically.

For two 50nm radius gold particles surrounded by glass which lie 100nm apart on the y-axis (where the polarisation direction is along the x-axis and the pair is in resonance), the interaction matrix is computed to be:

$$A = 10^3 \times \begin{pmatrix} 0.25 - 3.17i & 0 & 0 & 1.57 - 1.47i & 0 & 0 \\ 0 & 0.25 - 3.17i & 0 & 0 & -3.14 - 2.00i & 0 \\ 0 & 0 & 0.25 - 3.17i & 0 & 0 & 1.57 - 1.47i \\ 1.57 - 1.47i & 0 & 0 & 0.25 - 3.17i & 0 & 0 \\ 0 & -3.14 - 2.00i & 0 & 0 & 0.25 - 3.17i & 0 \\ 0 & 0 & 1.57 - 1.47i & 0 & 0 & 0.25 - 3.17i \end{pmatrix} \tag{3.3.7}$$

The largest terms in this matrix are those concerning the electric field in the y-direction. This shows that if the dipole moment of one of the particles is oriented in the y-direction, the field experienced by the other particle will be greatest if it lies along an axis parallel to the y-axis and coincident with the first particle. In other words the incident polarisation vector must be parallel to the displacement vector connecting the two particles (we are therefore in the near-field regime).

By inserting this interaction matrix into the full matrix equation $\tilde{\boldsymbol{E}}_{inc} = \tilde{\boldsymbol{A}}\tilde{\boldsymbol{P}}$ (where $\tilde{\boldsymbol{E}}_{inc}$ is a 1D matrix containing the three components of the incident field at the site of each dipole, $\tilde{\boldsymbol{P}}$ is a 1D matrix containing the components of the dipole moments of each particle and $\tilde{\boldsymbol{A}}$ is the interaction matrix), the system of equations can be inverted (using $\tilde{\boldsymbol{E}}_{inc} = \begin{pmatrix} 1 \\ 0 \\ 0 \\ 1 \\ 0 \\ 0 \end{pmatrix}$ for

plane polarised light) to obtain the dipole moments of the two particles:

$$P_I = \begin{pmatrix} -73 - 190i \\ 0 \\ 0 \end{pmatrix} \times 10^{-6} \tag{3.3.8}$$

$$P_{II} = \begin{pmatrix} -73 - 190i \\ 0 \\ 0 \end{pmatrix} \times 10^{-6} \tag{3.3.9}$$

Clearly there is only a component of the dipole moment in the direction of the incident polarisation due to symmetry. The values of $P_{1,x}$ and $P_{2,x}$ change as a function of frequency. The values given here are for the frequency on resonance. If there was no interaction between the particles, the polarisation values would tend to $P_{1,x} = P_{2,x} = \alpha$.

In terms of the far-field optical response, the interaction between the particles can cause very significant changes. For example, the wavelength of peak extinction can be shifted considerably. Let us first consider the regime in which the particles exist along an axis which is perpendicular to both the incident electric field and the k-vector.[83] For a range of vacuum wavelengths the extinction cross-section has been plotted for a number of particle separations (figure 3.3.1). As a reference, the extinction cross-section of two identical non-interacting particles is also shown.

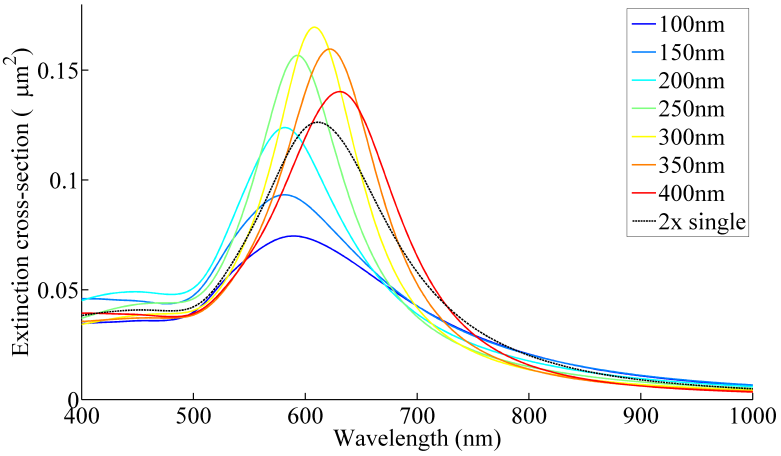

Figure 3.3.1: The extinction cross-section of particle pairs for a range of separations as calculated using the CDA. The particles both lie on an axis which is perpendicular to both the incident electric field and the incident k-vector.

For small separations, a blue-shift is observed. This is due to the radiative term in the expression of the dipolar field whose y-component is plotted in figure 3.2.4b. This field acts to increase the restoring force on the electrons in the particles. Physically, this occurs by the

particles radiating a field such that the field at the point of the neighbouring particle is in the opposite direction to the excitation field (this is why there are negative values of the y-component of the field in figure 3.2.4b). The magnitude of the restoring force is directly related to the energy of the system, and hence the resonant frequency. As was stated above, figures 3.2.2 and 3.2.4 do not display the oscillatory behaviour for clarity, but if this was plotted, it would be seen that the fields oscillate sinusoidally and emanate at the origin. Because this oscillation produces alternating positive and negative values, it is possible that the phase difference between the particles can give rise to a red-shift of the resonance. This is the source of the slight red-shift observed at separations above 300nm. A simplified schematic of the interaction which gives rise to the blue shift is demonstrated in figure 3.3.2. Interactions a and d are repulsive and do not change the dipolar mode, and the interactions c and d act to attract the opposite charge in the neighbouring particles. This has the effect of increasing the restoring force and hence shifts the resonance wavelength to the blue.

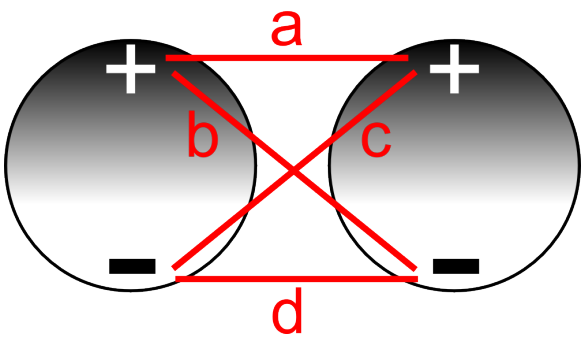

Figure 3.3.2: The interactions between two macroscopic electrostatic dipoles which lie on an axis perpendicular to the direction of the applied field can be described by the four inter-particle interactions above.

Let us now consider the regime in which two particles are brought together along an axis parallel to the polarisation of incident light. The extinction cross-sections have been plotted for a range of separations (figure 3.3.3) and as a reference, the spectrum of two non-interacting particles is also shown.

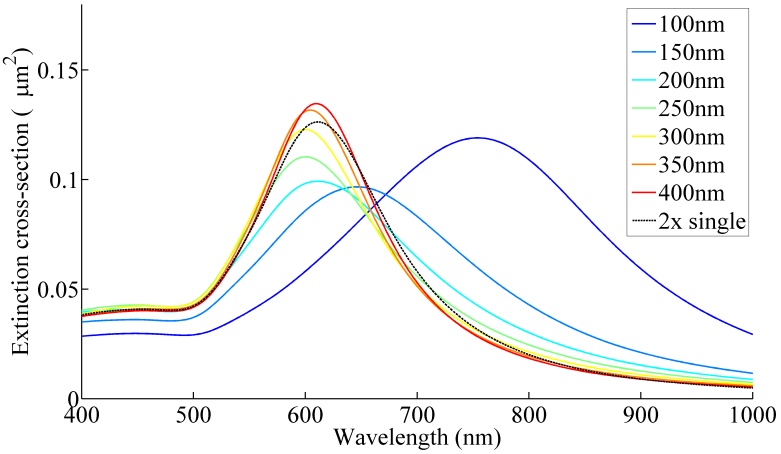

Figure 3.3.3: The extinction cross-section of particle pairs for a range of separations. The particles both lie in an axis which is parallel to the incident electric field.

In figure 3.3.3, for separations between 400 and 200nm, a slight blue-shift is observed due to the fact that phase-difference between the particles is such that the restoring force of the electrons within the particles is increased. For shorter separations, however, the resona1nce wavelength shifts considerably to the red. In order to understand this response it is beneficial to consider macroscopic dipoles again (figure 3.3.4).[83] We are in the electrostatic regime now, and the field is strongest along the axis on which the particles exist, and Coulomb's law tells us that in close proximity to the particles along the axis of symmetry, the dominant interaction is the one labelled b in figure 3.3.4. This interaction acts to attract the opposite charge in the neighbouring particles. Because this interaction dominates in the electrostatic regime, it is a relatively weak feature until the particles are close enough together that the $1/r^2$ term dominates the response, then this interaction rapidly becomes significant in the spectra.

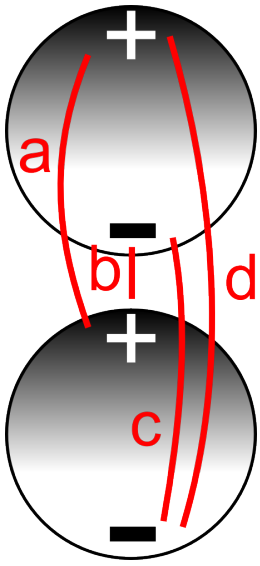

Figure 3.3.4: The interactions between two macroscopic electrostatic dipoles which lie along the same axis as the direction of the applied field can described by the four interactions above.

There are, in fact, antisymmetric modes which the pair of particles can support (see the paper by Markel[103] for a rigorous description of antisymmetric modes using the coupled dipole model). In this situation, the arrangements of the charges on one particle are opposite to those which are illustrated in figures 3.3.2 and 3.3.4. Such modes cannot readily be coupled to if there is no phase difference between the two particles with regards the incident light (i.e. the system and the excitation beam possess the same symmetry). If this symmetry is broken, e.g. by rearranging the particles so that a phase difference exists, then it is possible that the total electric field directions at the locations of the two particles are in opposite directions. This type of mode is sometimes known as a *dark mode* as it cannot be observed with standard illumination[†].

3.4 2D arrays of nanoparticles

When metallic nanoparticles are placed in square arrays, the interaction they experience is a superposition of the effects observed in all the regimes discussed above for particle pairs. The choice of placing the particles in square arrays ensures that the the response of each of the particles is identical for given illumination conditions. This is true for infinite arrays, but for finite arrays, the particles at the edges of the array will have a very different response, but for now this will be ignored. A feature of periodic structures such as square arrays is that they can diffract light (diffraction being a form of coherent scattering), so for large array periods diffraction will be present in the far-field response. Figure 3.4.1 shows the extinction cross-section of finite, square arrays of nanoparticles (50nm radius gold, surrounded by glass) as calculated using the CDA. These square arrays have different array periods, and the total size of the array is as close as possible to $5\mu\text{m} \times 5\mu\text{m}$ without exceeding it. The arrays are illuminated at normal incidence.

[†]The definition of standard illumination is somewhat subjective, so care must be taken when using the term *dark mode* without further details as to the form of the illumination.

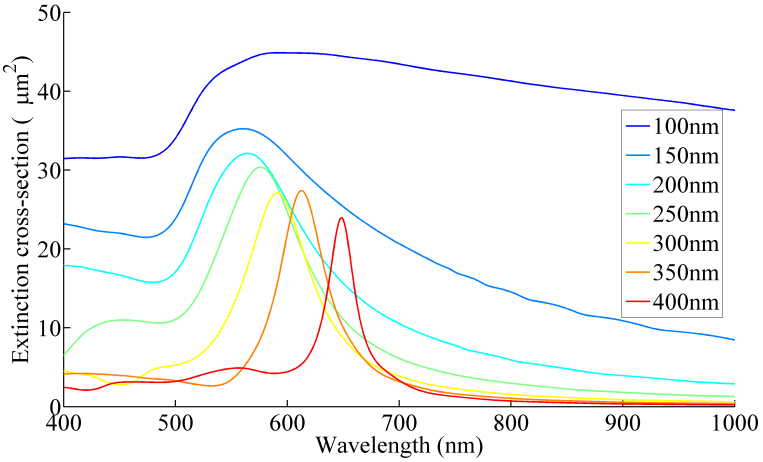

Figure 3.4.1: The extinction cross-section of 5μm $\times$ 5μm square arrays of gold nanoparticles for a range of array periods.

The blue-shift observed as the period is reduced is very strong as a single particle has four nearest neighbours, two of which provide a strong radiative field which produces a blue-shift which is much stronger than that observed for particle pairs. These particles are similarly surrounded by the same number of nearest neighbours, so the responses are collective and the blue shift is made stronger by the presence of many identical particles. For very close separations, the resonance is red-shifted because of the near-field interactions which lie along the axis which is parallel to the incident electric vector (see figure 3.2.2b).[97]

An interesting property of square arrays is that the far-field response in invariant with respect to the azimuthal angle of polarisation when illuminated at normal incidence. This is true of infinite arrays as well as four individual particles arranged at the vertices of a square. This invariance applies to diffractive effects as well as non-diffractive features. The reason is due to the fact that as the polarisation angle is rotated away from one of the lattice vectors, the electric field can be decomposed into its separate components, and, relative to the lattice vectors, both components 'see' the same array as they are resolved along the lattice vectors. When the effects of these two components are summed, the original response is recovered.

3.5 Retrieving the single particle response from an array

Scattering from single particles was discussed in chapter 2. It was highlighted that there are issues with both performing scattering experiments and running simulations to obtain meaningful comparisons between experiment and theory. For the extinction cross-section, however, there are different problems which arise when attempting to measure its value for a single particle experimentally. The main problem is clearly recognised from the optical theorem where the transmitted light is collected on an imaginary screen far from the scatterer

(figure 3.5.1). The screen must be far enough away that the small angle approximation may be applied, and large enough that all the main diffraction peaks are collected.[104]

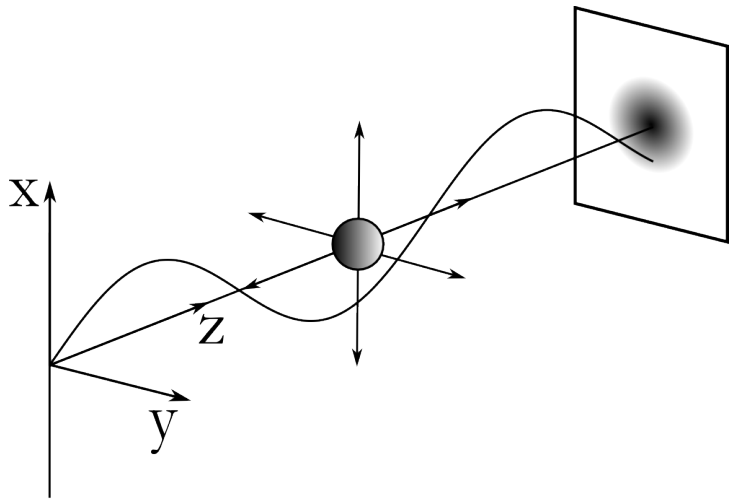

Figure 3.5.1: Schematic showing the intensity on a screen far from a scattering/absorbing particle.

This collected intensity is integrated over a circle (see appendix C for a derivation):

$$\int |\psi|^2 \, dA = \pi R^2 - \frac{4\pi}{k^2} \Im F(0) \tag{3.5.1}$$

Here, ψ is the amplitude at the screen, R is the radius of the screen over which the intensity is integrated, k is the wavevector and $F(0)$ is the scattering amplitude at an angle of 0° from the axis of propagation. The term $\frac{4\pi}{k^2}\Im F(0)$ is the extinction cross-section of the particle. Therefore, if the intensity of incident light is I_0, then the intensity collected will be:

$$I_{collected} = I_0 \left(\pi R^2 - \frac{4\pi}{k^2} \Im F(0) \right) \tag{3.5.2}$$

In an extinction measurement on a single particle this is exactly the light intensity that is collected in the far-field. Once normalised, the extinction becomes:

$$E = 1 - \frac{\pi R^2 - \frac{4\pi}{k^2} \Im F(0)}{\pi R^2} \tag{3.5.3}$$

In real experiments, the collection area is significantly larger than the cross-section of plasmonic particles in the visible regime. This means that regardless of the light intensity, the particle scatters and absorbs a quantity of light which is negligible in comparison to the incident beam and $E \to 0$. Long integration times do not help in practice because fluctuations in the output of the lamp dominate over the relative change in intensity caused by the presence of the

particle. For this reason, we can say that using standard extinction techniques it is impossible to produce reliable measurements on single particles.

One of the aims of the remainder of this chapter is to investigate systems of particles which produce measurable extinction responses whose spectral line-shapes do not differ significantly from the single particle response. Using this technique we aim to *infer* the elusive single particle response from the measurable response of a carefully chosen array (as opposed to using a purely random array and assuming a lack of inter-particle interactions[105]).

3.6 Extinction of ordered arrays

As stated above, the extinction of a single particle is a difficult quantity to measure experimentally. Some suggestions have been made, however which utilise spatial modulation spectroscopy (SMS).[106,107] This requires relatively sophisticated optical equipment. The approach proposed here requires the use of a microscope objective, a slit, and a spectrometer with a CCD camera but relies on the ability to produce particles by a deterministic technique such as EBL.

This approach is based on the principle that dense arrays of particles give clear, measurable values of extinction which a single particle cannot produce. If as a first attempt, we fabricate structures (discs in this case as a prismatic approximation to spheres) by EBL and place the particles in square arrays, the spectral response will be modified significantly due to far-field and near-field coupling of the dipolar mode as stated above. If particles are placed in a dense square array and illuminated with plane-polarised light, the coherent, radiative interactions between neighbouring particles dominate over the near-field response, and the spectral response will be blue-shifted (at very close separations, the near-field response will dominate and a red-shift will be observed). This response can be very different to the single-particle response. A natural thought would be to increase the array period in the hope that the increased separation of the particles would ensure that the radiative modification of the spectral response becomes reduced. Eventually, however, diffraction will feature in the spectra (i.e. when the array period is equal to the wavelength of light in the surrounding medium). Unfortunately for our purposes, the diffraction effect emerges for an array period at which the radiative blue-shift is still a significant feature of the spectral response. Therefore, in a square array, plasmonic particles of this size and composition (50nm radius gold surrounded by glass) will either have their response modified by the blue shift due to radiative interactions or diffractive effects due to the periodic nature of the array. A deviation from the single-particle response is hence unavoidable with this arrangement.

3.7 Introducing random particle positions

An initial attempt at solving this problem of having coherent interactions taking place in square arrays is to eliminate the periodicity in the arrays. This should be accomplished whilst ensuring that the particle density remains approximately the same as in the periodic case, in order to produce a measurable signal. The most extreme approach to reducing the periodicity is to fabricate the particles in random arrays (rather than introduce some dither on the particles' positions in the square array). This is what is attempted here. A computer script was used to generate the 2D coordinates of each of the particles. Each of these coordinates are pseudo-random and are forced to exist within a certain area (e.g. a square of area 25μm^2). This arrangement strongly resembles arrays of particles produced using colloidal solutions,[67,108] but the lithographic technique used here allows flexibility in fabrication which far surpasses that of colloids, where there is no control over the position of individual particles. There is, however, much information in the literature regarding colloidal arrays on substrates and samples prepared by colloidal lithography.[108,109] The blue-shift observed in dense arrays is a consequence of the proximity of the particles and the fact that the radiated fields of each particle extend across a range of angles. In other words, rather than the particles only interacting strongly radiatively when there are neighbours along an axis perpendicular to the incident field, a particle whose local field shares a component with the scattered field of another particle will interact, and this occurs strongly over a range of angles. At any given angle at fixed radius, this field is proportional to $(\hat{\mathbf{r}} \times \mathbf{p}) \times \hat{\mathbf{r}}$ (where $\mathbf{p}$ is the dipole moment and is $\hat{\mathbf{r}}$ the unit vector directed from the dipole to the observer). As stated above, at moderate separations ($d \geq 150nm$) the shift is dominated by this radiative response which is proportional to r^{-1} but at very close separations, the shift is dominated by the near-field interaction (equivalent to the electrostatic dipole field).[97] Despite these spectral shifts, it is possible to reduce the density of the array of particles whilst preserving the randomness to a point at which the array is sparse enough that the particles are no longer interacting strongly, but there is no periodicity to produce diffractive effects. There are two factors which restrict this scheme for reproducing single particle spectra indirectly by fabricating random arrays, and they are (i) although the array is random, neighbouring particles can still be very close together which can shift/broaden any spectral feature, and (ii) particles in an array whose sizes are nominally identical are in fact larger if others are in close proximity due to the nature of EBL — this tends to red-shift and broaden the collective response.

The first factor can be addressed simply by ensuring that when the array is defined, there is a restriction that a minimum separation exists between particles (r_{min}). This can allow the density to remain fixed, but ensure that the particles interact as little as possible by keeping a certain minimum distance between them. As this parameter is increased there is a tendency for the degree of order to increase, so it must be used carefully.

The second factor can be solved by first acknowledging that when the electron beam exposes the PMMA resist, the focused beam is not infinitesimally small. It exhibits a distribution

function centred on the focus (we assume it to be Gaussian). This has the effect of not only exposing the regions desired for the definition of the particles, but also exposes the other parts of the array with a diminishing density of charge. When only one particle is made in isolation this is not an issue but when many particles are close together (i.e. in a dense array) the dose from the tails of the Gaussians of all the other particles sum together and the outcome is that all the particles are over-exposed to an extent which is dependent on the number of neighbouring particles and their proximity (the more they are and the closer they are the greater the dose). The extent of this issue can be reduced by scaling the dose of each particle to allow for the effect of all the other particles in the array (such a scheme is described in appendix A).

Once the array can be fabricated with a degree of confidence as to the size of the particles, the array can be modelled using the coupled dipole approximation (CDA).

3.8 Coupled dipole approximation (CDA) and verification of its accuracy

FEM[110] and other similar techniques are limited to a certain number of meshing points due to computational constraints. This makes it very difficult to model large, random arrays of particles (though it has been attempted for large unit cells containing randomly positioned particles[111]). As discussed above, the CDA allows the dipole moment of each particle to be calculated. From this calculated information the extinction, scattering and absorption cross-sections of the array can be calculated. A limitation of the CDA is that the particles are not finite in size (they are infinitesimally small), in contrast to FEM models. Instead, the polarisability of each particle is given by a particular function which can be different for each of the particles. A function which is commonly used is the polarisability of a small particle with spherical symmetry in the electrostatic approximation. This function is directly analogous to the Clausius-Mossotti function which describes the polarisability of a single molecule in the electrostatic limit. The response of the particles considered in this study cannot be described by a quasi-static field because their size means that there is a significant phase difference from one side of the particle to the other. We therefore turn to an empirical formula by Kuwata *et al.*[45] which takes into account the radiative damping and dynamic depolarisation which occurs in larger particles and shifts the dipolar mode to the red. A comparison between the extinction of single spheres of different diameters embedded in glass as calculated by Mie theory[44,54,77] and with the Kuwata approximation is shown in figure 3.8.1. This shows good agreement for very small particles, and the empirical formula does produce a red-shift and broadening due to radiation damping and retardation effects. The degree of red-shift becomes less accurate for larger particles. The most significant departure from the Mie calculations is the absence of the quadrupolar mode which appears at a shorter wavelength than the dipolar mode for large particles. This limits the applicability of the CDA model to describe interactions

between larger particles, unless only the dipolar mode is of interest. The particles considered in this study for experimental investigation are 50nm in radius, a compromise between ease of fabrication and the ability to compare experimental results with CDA calculations.

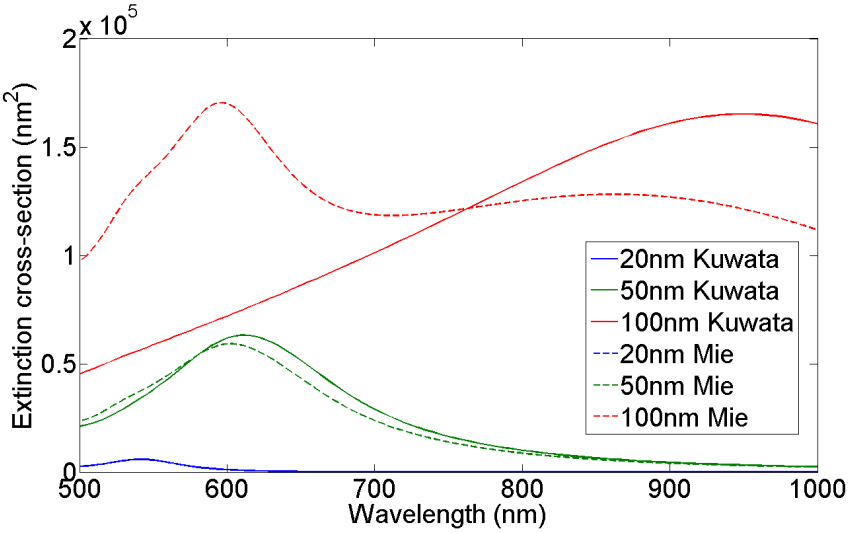

Figure 3.8.1: A comparison between the extinction cross-section of gold spheres of different radii surrounded by glass as calculated by Mie theory and from the Kuwata polarisability function. The quadrupolar mode does not feature in the Kuwata results, and the error in the degree of red-shift increases for larger particles. The permittivity values for gold were taken from Johnson and Christy.[4]

One further important test is to ensure that the interactions between the particles are adequately described. In order to do this a system has been selected which can also be modelled with HFSS. The system chosen is a square array of 50nm radius gold nanospheres surrounded by glass. The CDA results are given in figure 3.8.2b and this should be compared with the results as calculated by HFSS (figure 3.8.2a). The system modelled in HFSS is in fact infinite in its extent in the x-y plane. This is the main deviation from the system modelled by CDA. The results from HFSS were calculated by integrating the total Poynting vector (i.e. incident + scattered) over the bottom of the unit cell to calculate the transmitted light, and dividing it by the incident Poynting vector integrated over the top of the unit cell (see equation 2.2.1). This produced the transmission which can be converted to extinction by $E = 1 - T$. Calculating the extinction cross-section from the CDA model directly uses the calculated values of dipole moment for all the particles in the array. The equation used is based on a form of the optical theorem which is based on the interference between the incident field and the radiation from the dipole (see appendix C for a derivation):

$$\sigma_{ext} = \frac{1}{|E_0|^2}\frac{k}{\epsilon}\sum_{j=1}^{n}\Im\left(\mathbf{E}^*_{inc,j}\cdot\mathbf{p}_j\right) \tag{3.8.1}$$

Here, k is the wave vector, E_0 is the magnitude of the incident electric field, $\mathbf{E}_{inc,j}$ is the

incident electric field calculated at the position of particle j, ϵ is the permittivity of the surrounding medium, n is the number of particles and $\mathbf{p}$ is the dipole moment of particle j as calculated using the CDA method. Clearly the comparison is not perfect between extinction cross-section and integrated extinction, but the trend is clear[‡]. In figure 3.8.2a the separation of 100nm is ignored because in FEM the particles are finite in size, so a gap of $2R$ corresponds to the spheres being in galvanic contact which will produce a completely different response. Also, the number of meshing elements required to define the geometry with touching particles is prohibitively large.

[‡]For an infinite ordered array the conversion is achieved using $E = \sigma_{ext}/A$ for $\sigma_{ext} \leq A$ where A is the area of the unit cell. For $\sigma_{ext} > A$ the extinction is equal to 0. For finite arrays, the particles at the edges of the arrays exhibit a different response and hence a different cross-section so a good comparison is difficult to obtain.

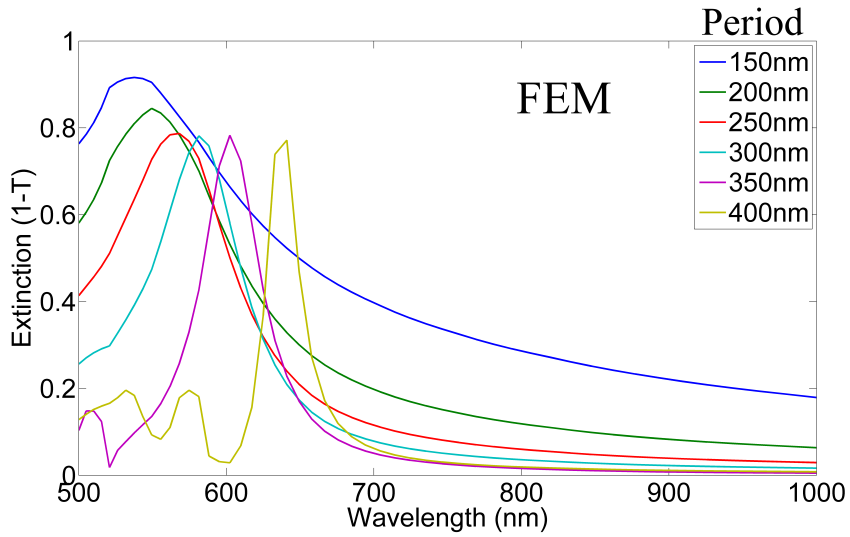

(a)

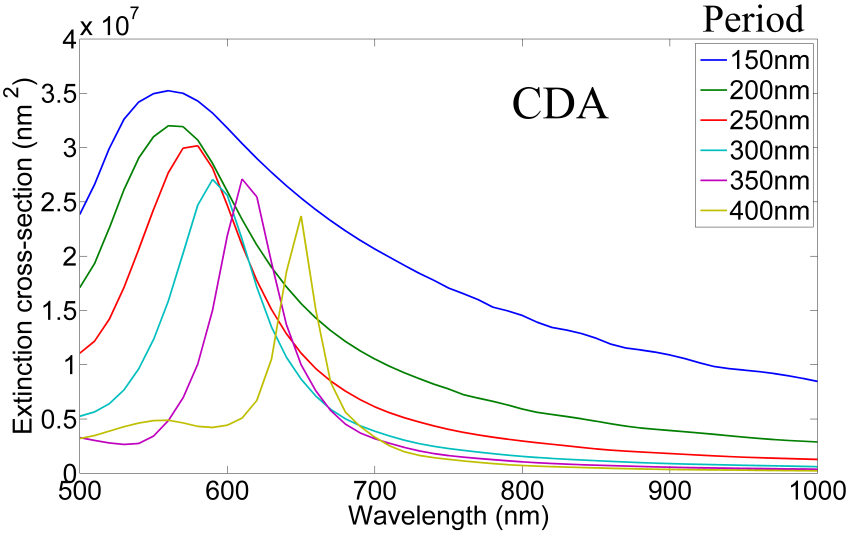

(b)

Figure 3.8.2: A comparison of extinction spectra as calculated by (a) FEM and (b) CDA for 50nm radius gold spheres surrounded by glass positioned in square arrays and illuminated at normal incidence with the polarisation along one of the lattice vectors for a range of array periods. In the FEM model the arrays are infinite, and the extinction is plotted (i.e. $1-T$ where T is the transmittance), and in the CDA model the arrays are finite (approximately $5_{\mu\mathrm{m}} \times 5_{\mu\mathrm{m}}$) and the extinction cross-section of the array is plotted. The trends are the same for both techniques though there are some differences; the peak positions are quite different for close separations due to the fact that the error in the polarisability is compounded due to multiple, strong interactions. Furthermore, the diffraction effects observed for large separations are very different due to the finite size of the array in the CDA model and the inclusion of a component of the diffracted orders in the transmitted light as calculated by HFSS. Furthermore, the difference between the relative heights of the curves based on the two methods is due to different quantities being plotted which do not necessarily have a linear relation.

The peak positions are in good agreement, and the trend of increasing extinction values with increasing particle density is reproduced. There are diffractive features present for the largest

two array periods. The diffraction edge is seen at the wavelength corresponding to the pitch multiplied by array period (e.g. $1.5 \times 400\text{nm} = 600\text{nm}$). In comparisons between FEM and CDA, the diffractive features demonstrate the greatest deviation from good agreement. It is thought that this is due to the manner in which the diffractive orders are handled internally in HFSS. With these caveats, we can proceed to use the CDA for more complex systems which FEM is unable to model.

3.9 Extinction of random arrays

When the particles are placed in random arrays instead of square arrays, the coherent interactions are eliminated (this includes diffraction). The response of a random array is, therefore, a better starting point to find a good approximation of the single particle response. In order to make comparisons with the data for the ordered arrays shown in figure 3.8.2, the CDA model has been used to produce extinction spectra of arrays of particles whose positions are pseudo-random yet have the same areal density as the ordered arrays investigated above (i.e. the same numbers of particles lie within a square of area $25\mu\text{m}^2$, the total area of the square arrays considered above). The additional parameter which is necessary to avoid the overlap of particles is the minimum separation between the particles (r_{min}). This ensures that in the random array, no particle can be closer than r_{min} to any other particle in the array. Even in very sparse arrays, there is a finite probability that two particles may be very close to each other and this needs to be addressed by choosing r_{min} carefully. The reason such care needs to be taken is because such a pair of particles can be close enough to interact strongly and create spectral features which deviate strongly from the single-particle response. By judiciously selecting a value of r_{min} to ensure that as well as having no coherent effects, there are no isolated instances of the kind of very strong inter-particle interactions which could affect the spectra significantly we can begin to approximate the single-particle response. Figure 3.9.1 shows extinction spectra calculated by CDA for random arrays with different particle densities. The value of r_{min} is 100nm for all densities shown in figure 3.9.1.

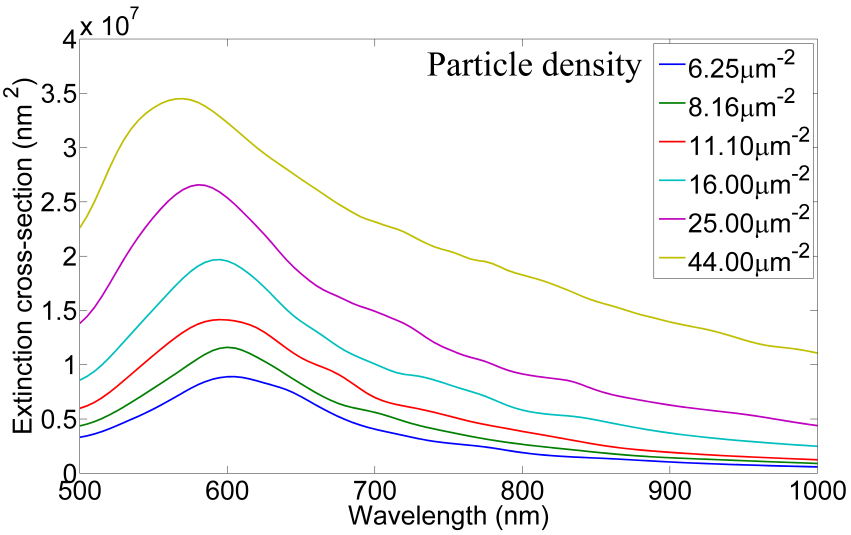

Figure 3.9.1: Extinction spectra of random arrays of 50nm radius gold spheres in glass as calculated using the CDA. The particle density is varied (stated in units of particles per μm^2), and for all densities the minimum separation is r_{min} = 100nm (i.e. the particles would be 'touching' were they real and not parameterised dipole moments). There is a blue shift for higher particle densities, and small fluctuations throughout the spectra are features of the non-periodic array and inhomogeneities between small clusters of particles. It should be noted that there are no diffraction effects in the spectra due to a lack of periodicity. $r_{min} = 100nm$ for all spectra in this figure.

There is a blue-shift as the particles are brought closer together, and the extent of this blue-shift is less than that of the ordered array due to the fact that the interaction is not coherent between all the particles in the array. This suggests, as predicted, that the sparser the array, the closer the response is to the single particle response. There is also some rippling in the spectra which is mostly noticeable at wavelengths longer than the resonance. This is attributed to small agglomerates of particles which have a red-shifted spectrum and produce a small superposition on the otherwise uniform spectra. The presence of these ripples are different for other random arrays which have the same density and r_{min}. If the array was large enough, then the curve would be smoother and the contribution of these agglomerates would result in a broadening of the main peaks.

When the quantity r_{min} is varied for a fixed particle density, the interactions of particles within small clusters can be reduced considerably and hence larger values of r_{min} produce spectra much closer to the single-particle response (figure 3.9.2). With large values of r_{min} the spectra show fewer artifacts which arise from localised interactions between particles within agglomerates as they are prohibited from existing and hence a smoother curve is produced. Also, the level of blue-shift is reduced by increasing the minimum separation. It should be noted that an infinite number of different pseudo-random arrays can be produced, all of which will produce slightly different spectra, and only one specific case is provided here for each set of parameters.

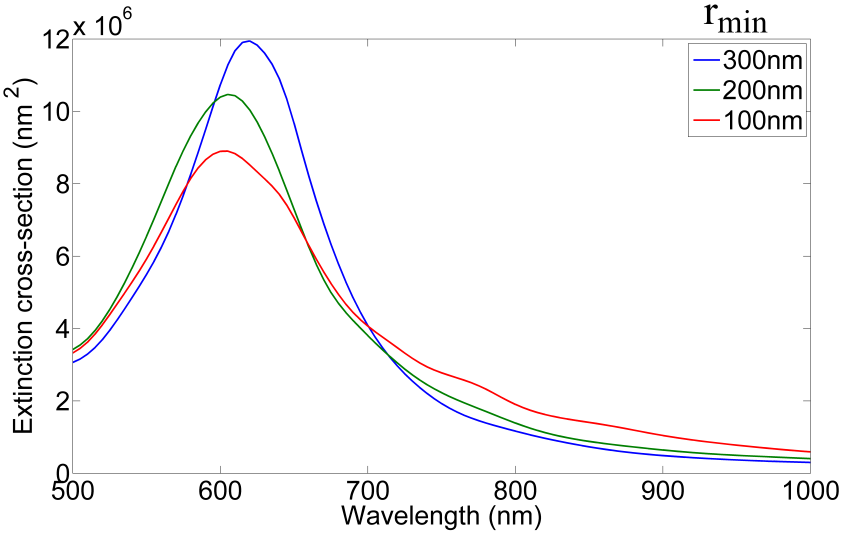

Figure 3.9.2: Extinction spectra of random arrays of 50nm radius gold spheres in glass as calculated using the CDA. The particle density is kept constant ($6.25\mu\text{m}^{-2}$) and r_{min} is varied. As r_{min} is increased, the extinction increases in strength, shifts towards the peak position of a single particle, and becomes smoother (i.e. there are no significant interactions between pairs or small clusters of particles which produce artifacts when r_{min} is small).

A further technique for analysing the manner in which varying r_{min} affects the degree of interaction between particles is to consider the dipole moment of each particle. We take the real part of the complex vector when the phase is $\pi/2$ relative to the incident field. The reason for this that the wavelength at which the dipole moments are calculated for this analysis is the resonance wavelength, and on resonance a $\pi/2$ phase shift occurs, so in order to make the real parts of the dipole moments as large as possible for the purpose of performing a graphical analysis, a phase of $\pi/2$ is used. If the particles are completely non-interacting, the dipole moments will all have the same strength and direction (parallel to the incident electric field). For random arrays, the angular distribution of the radiated dipolar field will have a tendency to rotate the dipole axis of neighbouring particles when $0 < |\hat{\mathbf{p}}_1 \cdot \hat{\mathbf{r}}| < 1$ (where $\mathbf{p}_1$ is the dipole moment of one particle, and $\mathbf{r}$ is the vector to a neighbouring particle). The dipole moments can be visualised either as a plot of dipole moments where the real part of each moment is centred on its associated particle in a 2D map, or as a polar plot of the vectors emanating from the origin. Both forms are shown in figure 3.9.3 for a particle density of $11.1\mu\text{m}^{-2}$ for two different values of r_{min} (100nm and 250nm). For all cases, the fields plotted are for the wavelength at which the extinction cross-section is greatest.

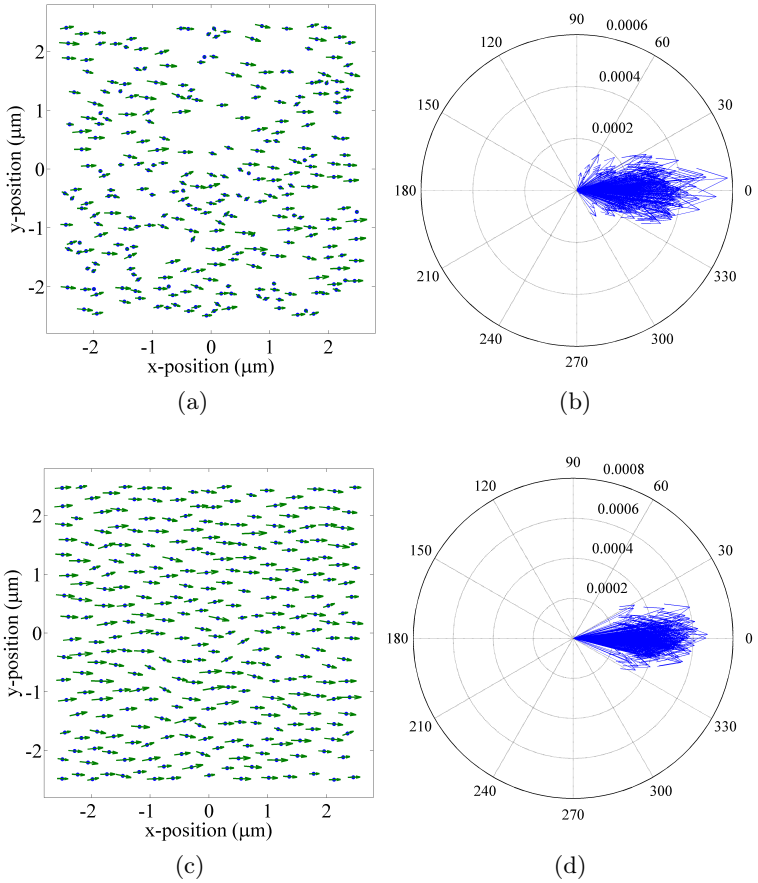

Figure 3.9.3: Orientation and relative magnitude of the dipole moment induced in each of the particles in random arrays of density $11.1\mu\text{m}^{-2}$ when illuminated at normal incidence with the E-field polarised along the x-axis. The minimum separation r_{min} is varied. It is 100nm in (a) and (b), and 250nm in (c) and (d) . (a) and (c) show the real part of the dipole moment vector (at a phase of $\pi/2$ relative to the incident beam) positioned on their associated particles. (b) and (d) show the same vectors emanating from the origin to give a clearer picture of the level of symmetry. Note that the scales are different for the two polar plots.

The angle dependence in figure 3.9.3 is difficult to interpret so for the two cases above, the angles of all the dipole moments have been calculated and then binned into groups in order to see the angular distribution of the dipole moments (figure 3.9.4).

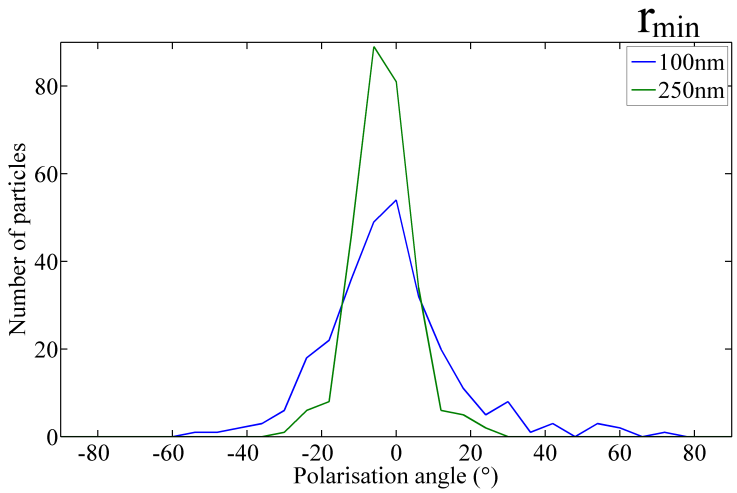

Figure 3.9.4: The polarisation angles have been calculated for two values of r_{min} (100nm and 250nm) for a particle density of $11.1\mu\text{m}^{-2}$. A binning routine was performed on these values, with a bin size of 5°. The number of particles which fall into each bin are plotted here (a line plot was chosen to allow both data-sets to be compared at once).

Figure 3.9.4 demonstrates that the variation in the angle of polarisation is very much reduced when r_{min} is increased. By imposing this more stringent restriction on the particle positions, the standard deviation of the angles has been reduced from 17.8° to 8.0°. The standard deviation of the magnitude of the dipole moment is also reduced by approximately 10%. Histograms of the magnitude are shown in figure 3.9.5.

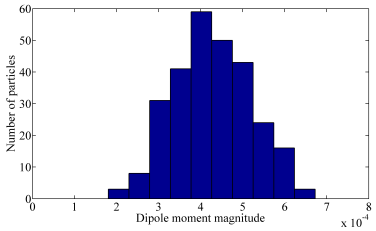

(a) $r_{min} = 100$nm

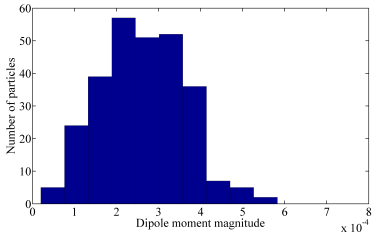

(b) $r_{min} = 250$nm

Figure 3.9.5: The magnitude of the dipole moment has been calculated for all the particles in arrays of particle density $11.1\mu\text{m}^{-2}$ with two values of r_{min}, (a) 100nm and (b) 250nm). A binning routine was performed on these values, with a bin size of 5×10^{-5}Cm. The number of particles which fall into each bin are plotted here as a histogram for each value of r_{min}.

From the derivation of the optical theorem (appendix C) it can be seen that both the orienta-

tion and magnitude of the dipole moment play a part in the overall extinction, so a reduction in the variation of both of these quantities will help to produce a response which is similar to that of a single particle.

3.10 Experimental extinction of ordered arrays

Extinction measurements have been taken from both ordered arrays of gold nanoparticles fabricated by electron-beam lithography (EBL). The EBL process allows the fabrication of nominally prismatic structures, so in order to produce a particle which is comparable to a 100nm diameter sphere, the nominal structures fabricated are cylinders with a height of 100nm and a diameter of 100nm. In reality these structures are somewhat rounded, so the approximation is not as unacceptable as it may appear at first. To improve adhesion to the glass substrate a 2nm layer of chromium was evaporated onto the sample before the gold (the actual amount of gold evaporated was 98nm to make the total metal thickness 100nm).

SEM images show the effect of implementing the dose-scaling correction (figure 3.10.1). The particles in the non-corrected array are in general larger than in the corrected array, and there is a clear increase in the diameter of the particles towards the centre of the array to the extent that some are connected. The corrected sample, on the other hand shows a much weaker trend regarding the increase in diameter towards the centre, though some individual particles are significantly smaller than the nominal size (one is missing completely). The cause of this is currently unknown but could be due to the size of the 'pixels' exposed by the electron beam being comparable to the size of the nominal particles.

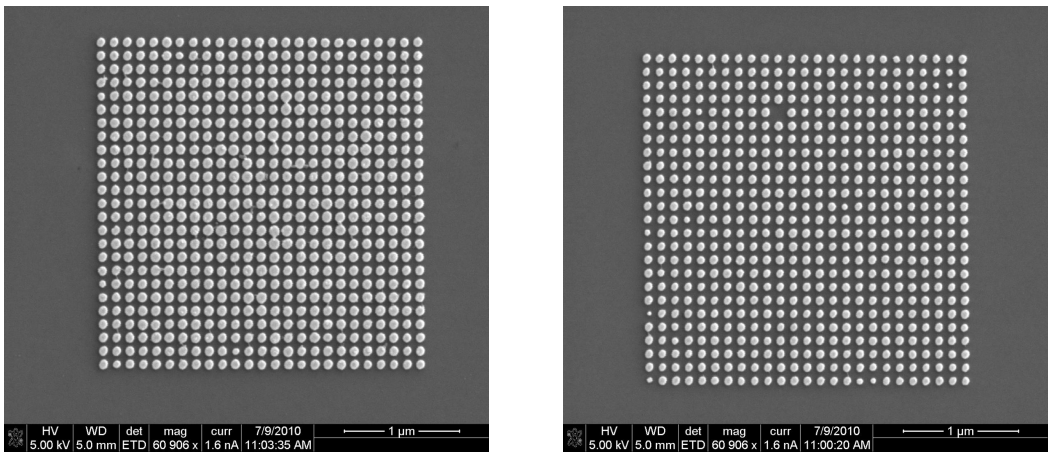

(a) (b)

Figure 3.10.1: SEM images of ordered arrays of nanoparticles with pitch 200nm. The particles are nominally 100nm in diameter. The doses of the particles in (a) are not corrected to account for the proximity effects of fabricating the neighbouring particles and so the particles are larger than the nominal size, particularly at the centre of the array. The particles in (b) have had their doses corrected, and the mean diameter is significantly closer to 100nm (i.e. half the pitch). The increase in diameter towards the centre of the array is less pronounced than in (a), but a number of particles were much smaller than the nominal size, and one particle was missing from the array (possibly due to the lift-off procedure).

Experimental extinction measurements were taken using a Nikon Eclipse TE2000-U microscope and a Princeton Instruments spectrometer with a CCD camera (see schematic in figure 3.10.2). The objective lens used is a 100x oil immersion lens ($n = 1.5$) with a variable numerical aperture which was at the smallest setting (NA = 0.5). The illumination was provided by a tungsten filament lamp with lenses and apertures to provide a 'Kohler' arrangement. The light is polarised along one of the lattice vectors of a square array and along one of the array edges for random arrays (this is consistent with the modelling, though as stated above, the square symmetry negates any effect due of varying incident angle at normal incidence). A slit was used to spatially filter the collected light along one axis so that the light passing through each array is collected, but no more. The intensity of light dispersed across the camera CCD is recorded and the signal from the rows of pixels corresponding to the array are averaged to provide the spectra shown here.

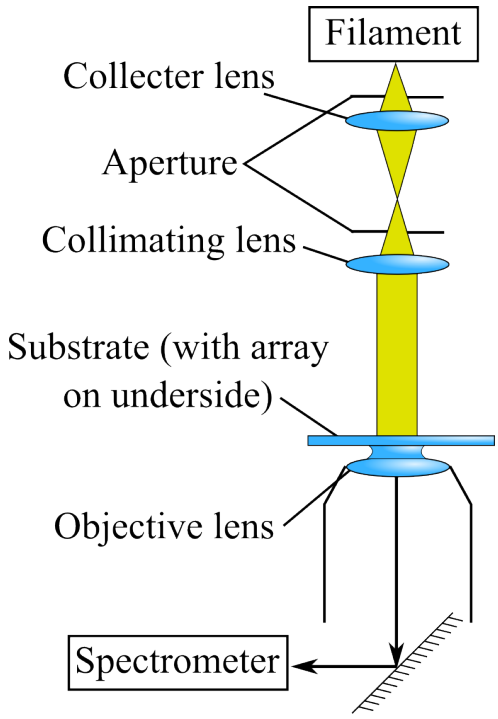

Figure 3.10.2: A schematic of the experimental ("Kohler") arrangement used to obtain extinction spectra. The nanoparticle arrays are placed on the bottom of substrate.

Figure 3.10.3 shows the extinction from ordered arrays of nanoparticles with varying pitch 150nm to 400nm. All the arrays are approximately 5μm on each side. It can be seen that there is qualitative agreement with the results shown in figure 3.8.2 — as the pitch is reduced, the resonance shifts to the blue, and the maximum extinction increases. The diffractive features in the long-pitch spectra show very good agreement with CDA modelling, much better, in fact than FEM. It should be noted that the absolute value of extinction measured here contains a scaling error. This is due to multiple reflections in the optical path of the experiment which could not be eliminated (a new microscope would need to be constructed for this purpose). Also, the increasing extinction at red wavelengths ($\lambda \gtrsim 900$nm) is due to second order diffraction from the spectrometer's grating, and should be ignored. The peak wavelengths are also shifted to the red in comparison to the theory which is likely to be due to the particles having a different geometry in the experiment (i.e. they are non-spherical objects), though this discrepancy is not vital to this discussion.

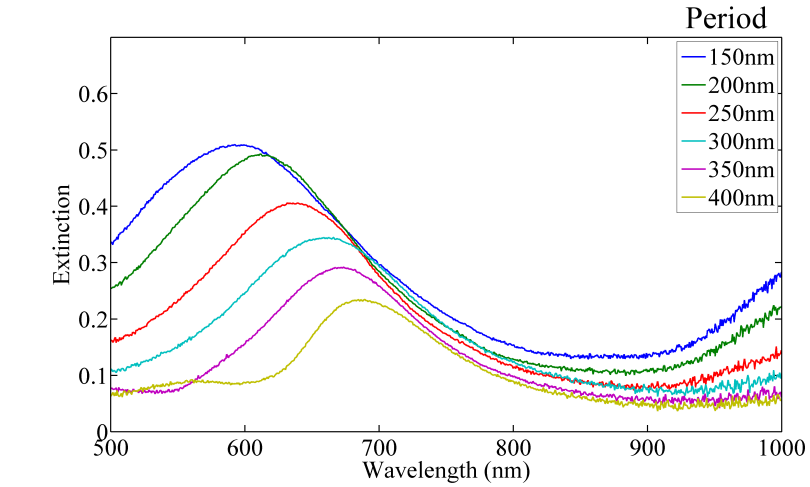

(a)

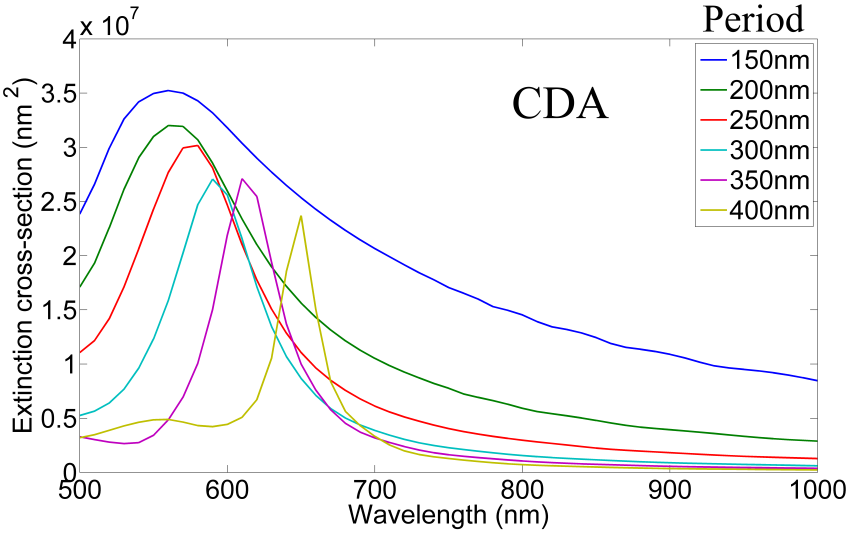

(b)

Figure 3.10.3: Experimental extinction spectra (a) of ordered arrays of nanoparticles for a range of pitches. The arrays are finite in size (approximately $5\mu m^2 \times 5\mu m^2$). For shorter pitches the dipolar resonance shifts to the blue and the level of extinction increases. Diffraction features are also present and in good agreement with the CDA model (b, reproduced here from figure 3.8.2); at 600nm for a pitch of 400nm, and 525nm for a pitch of 350nm. The increase in extinction at long wavelengths is attributable to second order diffraction by the spectrometer grating.

3.11 Experimental extinction of random arrays

The extinction from random arrays has also been measured experimentally for a range of particle densities and values of r_{min}. A great benefit of the technique proposed here is that once the positions of the particles in the random arrays have been defined, this set of positions can be used in the EBL process to expose arrays whose particle positions are identical to those used in CDA calculations. This is what has been done here. Figure 3.11.1 shows the measured

extinction from a set of random arrays whose minimum separation is 150nm.

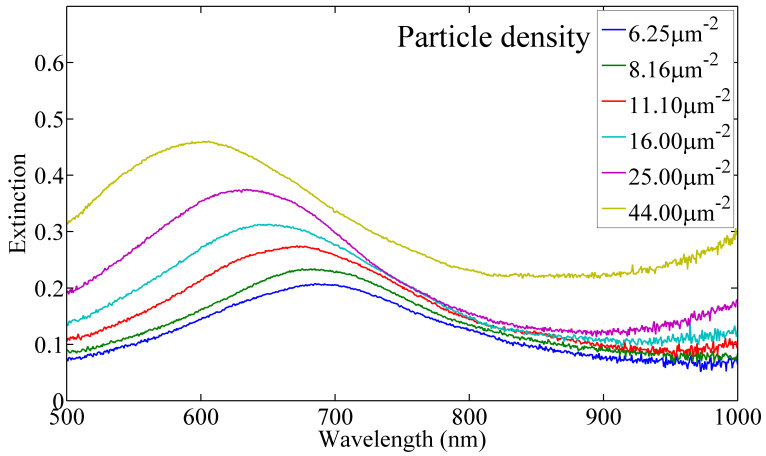

(a)

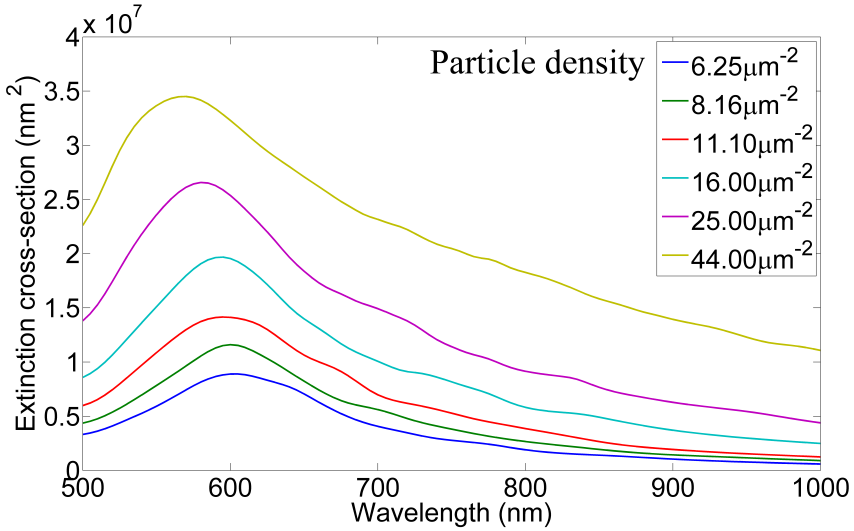

(b)

Figure 3.11.1: Experimental extinction spectra (a) for random arrays of nanoparticles for a range of particle densities. The value of r_{min} is fixed at 150nm for all spectra shown here. CDA results (b) are reproduced from figure 3.9.1.

This set of spectra may be compared to the CDA results in figure 3.9.1 (note that r_{min} has a different value). The figure here shows the blue-shift which is described in the discussion above of the theoretical aspects of the phenomenon. The low density arrays have resonances which are far to the red of the theoretical predictions. This is almost certainly due to the particles being non-spherical. The extent of the blue-shift and broadening is also somewhat stronger than predicted, though this can be explained by the small particles which are present in the SEM images and may be due to the fact that the dose scaling technique is based on a number of assumptions, and the dense, random arrays considered here may push the scheme beyond its reliable capabilities. For the sparser random arrays and ordered arrays, however, the technique works very well.

The effect of changing the minimum separation for a fixed particle density as measured experimentally is shown in figure 3.11.2. The particle density chosen was $6.25\mu m^{-2}$, i.e. the sparsest density in this study. The reason for this is that it is thought that this will give the best approximation to the single-particle response whilst still giving an easily measurable signal.

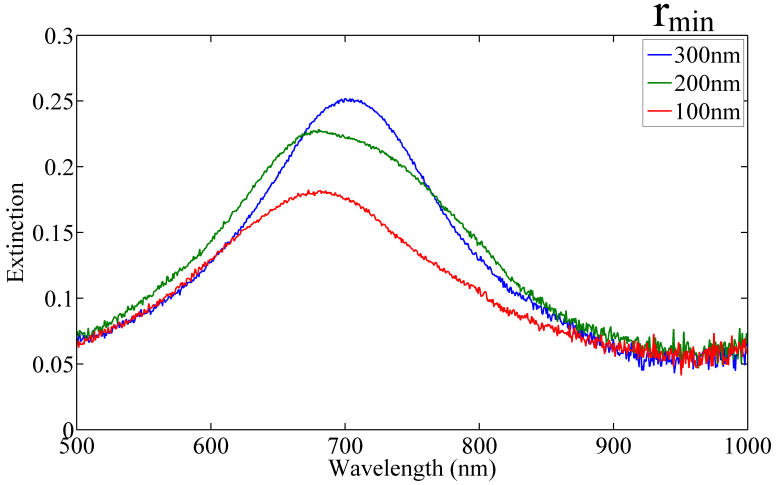

(a)

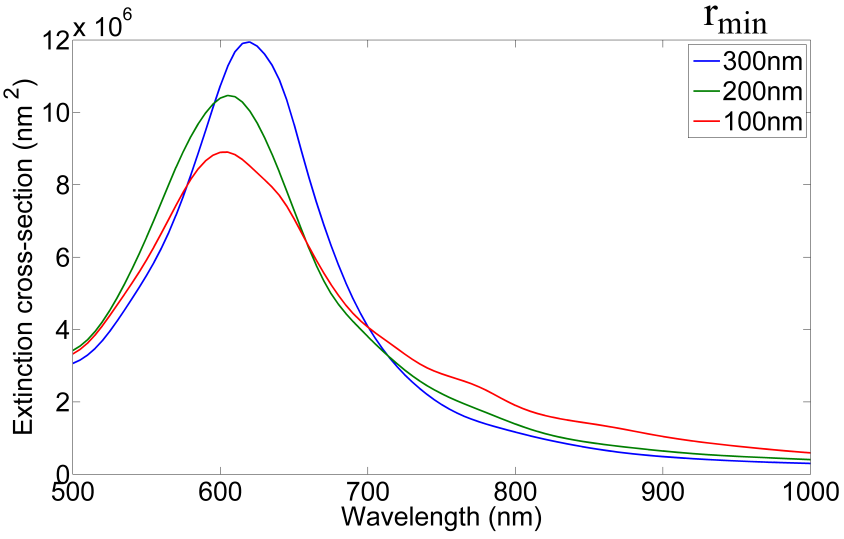

(b)

Figure 3.11.2: Experimental extinction spectra (a) for random arrays of nanoparticles with the value of r_{min} varied. The density is fixed at $6.25\mu m^{-2}$ for all spectra shown here. The CDA results from figure 3.9.2 are reproduced here.

These results agree very well with the CDA calculations plotted in figure 3.9.2 (allowing for the fact that the particle geometry is different and hence the peak position is shifted by 100nm), suggesting that the large value of r_{min} gives a good approximation to the single particle line-shape. Based on this, we can say that the blue curve in figure 3.11.2 represents a spectrum which is close to the line-shape of the extinction of a single particle. The single particle extinction cannot be measured directly, but the results in this chapter show that the single particle response can be approximated by a carefully chosen arrangement of particles in a

random array, and by ensuring that the value of r_{min} is sufficiently large that any interactions between the particles are not significantly strong. Furthermore, we can state that although we have only considered dipolar modes of particles, higher-order modes have fields which decay much more quickly[112] and hence interact to a lesser extent. This suggests that the technique proposed here can be used for particles whose spectra contain features due to higher order modes.

3.12 Summary

We have shown that the coupled diple approximation (CDA) can be used to calculate the extinction spectra of gold nanoparticles (considering only the dipolar mode) both in isolation (directly from the Kuwata polarisability) and in arrays. In square arrays, the nanoparticles interact coherently to produce a blue shift for sub-wavelength period arrays, and diffraction for large periods. In order to retrieve the response of an individual particle, it is necessary to introduce randomness into the array to reduce coherent interactions, and set a minimum separation to eliminate the spectral contribution due to small clusters of nanoparticles. The particle densities discussed here are large enough for their extinction to be measured experimentally, and hence the fabrication technique discussed can be used to produce samples from which it should be possible to determine the response of a single particle indirectly (to a good first approximation). This is achieved by producing the nanoparticles in random arrays in which inter-particle interactions do not play a significant role in the extinction spectra.

Chapter 4

Interaction between particles which support higher order modes

4.1 Introduction

As discussed in the previous chapter, upon illumination, pairs of metallic nanoparticles may experience modification of their plasmonic modes if they are close enough to interact strongly. Depending on the angle of illumination and the polarisation, particle-pairs which are sub-wavelength in separation may experience either a red- or blue-shift of their dipolar modes in comparison with their single-particle spectra. The preceding analysis is sufficient in describing the interactions of particles which are small enough to support only dipolar plasmonic modes, so up to now there has been no discussion regarding higher-order modes of particle in arrays. The study presented here, however, concerns larger particles which may support such modes, and it is the interactions of the modes of such particles which will form the basis of this chapter. The scattering and extinction cross-sections of the type of particle which is considered in this chapter are shown in figure 4.1.1 as calculated by Mie theory (a 50nm radius silver sphere surrounded by glass).

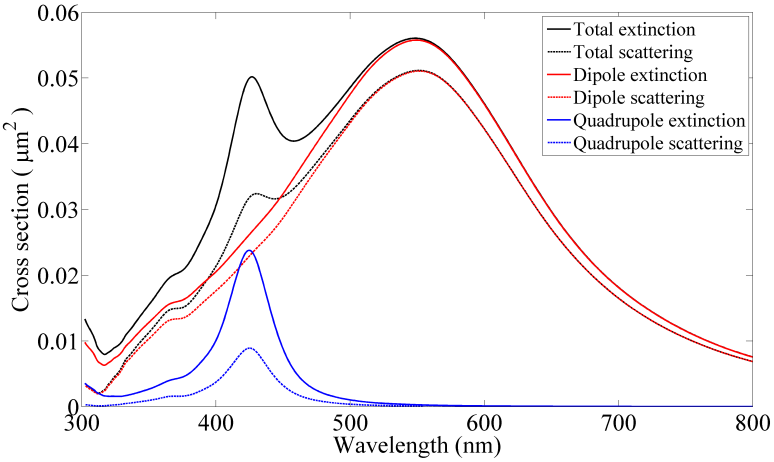

Figure 4.1.1: Spectra calculated using Mie theory showing the extinction and scattering cross-sections of a 50nm radius silver sphere surrounded by glass ($n = 1.5$) (this chapter is almost solely concerned with such particles). Permittivity values for silver were taken from Palik[3] and were interpolated with a cubic spline fit. The spectral features of the dipolar and quadrupolar modes are at 548nm and 427nm respectively. Also shown are the sets of spectra obtained when the calculation is carried out but only considering single modes — the dipolar mode in red and the quadrupolar mode in blue. Additional features in the spectra below 400nm arise from fluctuations in the permittivity values and are not plasmonic effects.

It should be noted that a gold particle of the same size and surrounding medium produces a very different spectrum and the higher order modes are much less prominent in the spectra (figure 2.5.8) due to the fact that the modes occur close to an absorption band.

4.2 Interparticle coupling in 2D arrays of metal spheres

In 2003, Malynych and Chumanov published results which seemingly demonstrated that 50nm radius silver spheres in random arrays exhibit a very large value of optical density (defined as $OD = -\log_{10}(T)$ where T is the transmittance) at a wavelength corresponding to the quadrupolar mode of a single particle, with no discernible spectral feature at the wavelength of the dipolar mode of the single particle.[113] The authors (Malynych and Chumanov[113–115]) attributed this extinction to the in-plane, coherent coupling of the quadrupolar modes of the particles in the array. They proposed that the interactions could be either symmetric or antisymmetric in nature, and would give rise to a "cooperative plasmon mode" (figure 4.2.1). The logic behind this attribution was based on symmetry arguments, thus neglecting the non-periodic nature of the arrays under investigation. It was assumed that for only one spectral feature to exist, all the particles in the array should interact in the same way with their neighbours; dipolar modes could not interact in such a way as along one axis they have large near-fields and no radiative fields, and along the other axis they have weak near-fields and strong radiative fields (see chapter 3). Once these assumptions had been made, only a

short step led to the explanation that the particles' quadrupolar modes must be acting in a coherent, in-plane manner, and thus the "cooperative plasmon mode" produces a single, strong maximum in optical density.

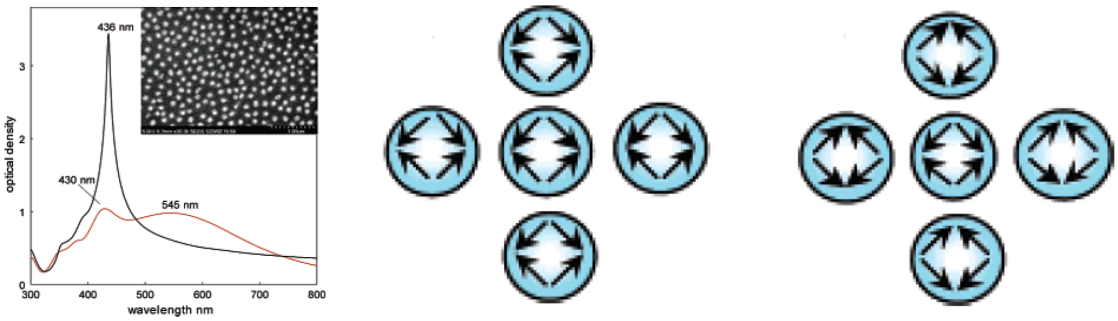

(a) (b) (c)

Figure 4.2.1: Results from Malynych and Chumanov demonstrating what was believed to be a coherent interaction between the quadrupolar modes of all the particles in the system. (a) shows the well-defined peak in optical density and an SEM image of the sample in the inset, (b) and (c) show suggested interactions which might take place and produce the effect seen in (a). These images were reproduced directly from the JACS paper by Malynych and Chumanov.

In this chapter I will provide a more complete description of the interactions in such a system and the reasons that the explanation given by Malynych and Chumanov must be erroneous. Firstly, I will discuss the authors' assumptions in turn, and will then describe the results from modelling which suggest an alternative explanation. In brief, these assumptions are listed below:

1. **All interactions are identical**: In the paper by Malynych and Chumanov, the assumption that all particles must interact in the same way with all other particles makes little sense as their nanoparticles were in dense, colloidal arrays and hence formed a random distribution in which the particles were able to interact with their neighbours, though this assumption may be used as a first approximation (see chapter 3).

2. **A single spectral feature must be due to an interaction which is the same for all nearest neighbours**: Regimes exist in which chains of nanoparticles produce a blue-shifted resonance for particular illumination conditions due to radiative coupling, and when several chains are combined into a large array of rows of particles this spectral response is preserved (again, this is the case in the radiative blue-shift observed in the ordered arrays considered in chapter 3). In other words the particles in each row exhibit one interaction which produces the blue shift, and between the rows there is a very different and weaker interaction and yet there is only one feature in the spectrum. Malynych and Chumanov dismiss such anisotropic interactions as being responsible for the single spectral feature they observed.

3. **The quadrupolar modes must lie in the plane**: In order to excite quadrupolar modes it is essential that there is a phase difference from one side of the particle to the other. At normal incidence (where Malynych and Chumanov observed the strongest effect), there is no phase retardation in the plane and hence an in-plane quadrupolar mode cannot be excited (except where local symmetry is broken).

4.3 Dense, square arrays of metallic nanospheres

In the previous chapter I discussed how the resonant frequency of the dipolar mode of a metallic nanoparticle is modified in the presence of another particle and a number of particles in an array, and it is worth reiterating this briefly here. I demonstrated that head-to-tail interactions lead to a red-shift, and that this effect is only significant at small separations due to the short decay length of the electrostatic dipolar field. On the other hand, when the dipole moments are parallel, yet transversely adjacent, the dipolar plasmonic mode will be blue-shifted due to the radiative fields of the dipolar mode. This effect is observed for much larger separations than for the near-field interactions. The equation for the electric field of an oscillating electric dipole is given below (ignoring the time dependent prefactor $e^{-i\omega t}$):

$$\mathbf{E} = \frac{1}{4\pi\epsilon_0} e^{ikr} \left\{ \frac{1}{r^3} \left(3\mathbf{n}\left(\mathbf{n}\cdot\mathbf{p}\right) - \mathbf{p}\right) - \frac{ik}{r^2} \left(3\mathbf{n}\left(\mathbf{n}\cdot\mathbf{p}\right) - \mathbf{p}\right) - \frac{k^2}{r} \left(\mathbf{n}\times\left(\mathbf{n}\times\mathbf{p}\right)\right) \right\} \tag{4.3.1}$$

where $\mathbf{n}$ is the vector from the point dipole to the observer, $\mathbf{p}$ is the dipole moment, k is the wave number and r is the distance to the observation point. It can be seen that in the electrostatic limit (i.e. when k is very small), only the first term in curly brackets is non-zero and hence this is the electrostatic dipolar field. It can be seen that the field decays as $1/r^3$ and at a given radius it has twice the magnitude along the axis of the dipole as along either orthogonal axis. On the other hand, at large distances from the oscillating dipole, the first two terms will become negligible, allowing the third term to dominate. This corresponds to the radiative field of the dipole and vanishes along the axis of the dipole moment.

From this we can see that along the axis of the dipole ($\boldsymbol{r} \parallel \boldsymbol{p}$), the near-field, electrostatic term will dominate in inter-particle interaction, and from the analysis before, the dipolar mode will be red-shifted. Orthogonal to the dipole moment ($\boldsymbol{r} \perp \boldsymbol{p}$), there are two regimes which could, in principle, dominate — the electrostatic field, and the radiation field, depending on the distance from the dipole. In reality, the induction (i.e. the second term) never dominates the field magnitude — it is always weaker than the dominant term in either of the other two regimes. These two regimes are as follows:

1. Electrostatic regime: the near-field dominates when $r < \frac{1}{k} = \frac{\lambda}{2\pi}$.
2. Radiation regime: the far-field dominates when $r > \frac{1}{k} = \frac{\lambda}{2\pi}$.

When metallic nanoparticles are placed on an infinite square lattice and illuminated at normal incidence with the electric field polarised along one of the lattice vectors of the array (e.g. the x-direction in figure 4.3.1), the electrons in the particles will undergo coherent oscillations and the fields which are produced by each particle will affect all the others in the array. Nearest neighbour interactions will dominate, so, to a first approximation we will begin by considering these interactions.

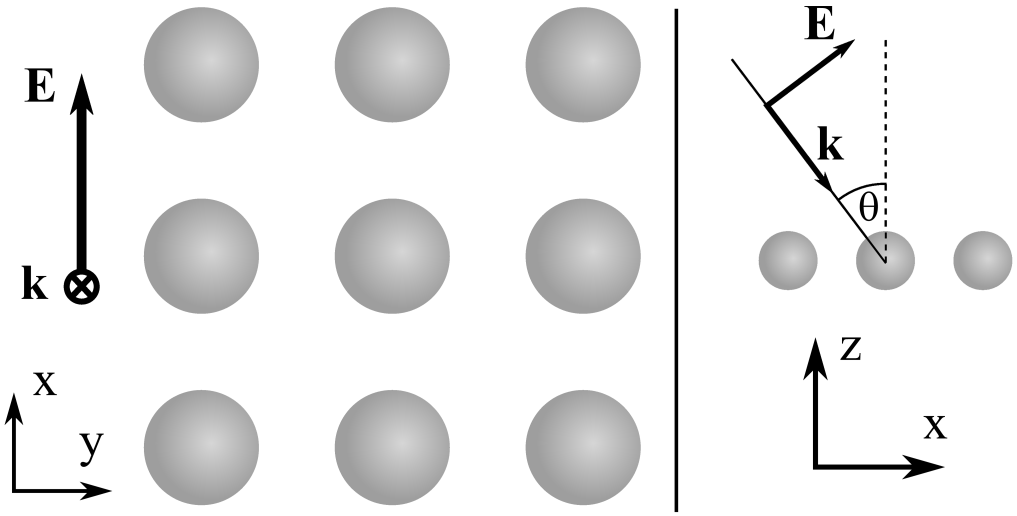

Figure 4.3.1: A schematic showing a small portion of an semi-infinite square array of metal nanoparticles such as those considered in this study. The directions associated with normally incident light are indicated (left), as well as the directions for p-polarised light at oblique incidence to the array (right).

By polarising the light in the x-direction (figure 4.3.1) it can be ensured that the dipole moments of the nanoparticles are aligned with one side of the unit cell. With this arrangement there will be no radiative interaction between a particle and the one above or below it due to the considerations above*. Its interactions along this axis will be dominated by near-field effects whose fields decay as $1/r^3$ and hence the interacting field will be very small at all but very close separations. Therefore we can expect a red-shift of the mode to occur, but only when the particles are close enough together to allow the electrostatic-type field to have a significant effect.

Along the other lattice vector (the y-direction), the radiative fields will dominate at separations greater than the condition stated above, and hence a blue-shift will occur. At smaller separations, as stated above, the near-field interactions will dominate, and in this regime, the red-shift from the head-to-tail interactions in the x-direction will be stronger than the side-to-side interactions in the y-direction.

The discussion so far has been concerned with particles which only exhibit a dipolar mode and largely echoes the discussion in chapter 3, but the spheres used in the study by Malynych and

*Having made this statement, it should be said, however that next-nearest neighbours (in the (1,1) direction) will contribute radiatively, though for now this will be neglected in the discussion.

Chumanov were 50nm in radius and made of silver and hence could easily support higher order modes (see chapter 2 for a detailed analysis of such a particle in isolation). The reason such a particle can support higher order modes whereas an equivalent gold particle could not is due to the permittivity of the metal and the fact that the quasistatic resonance wavelength according to the Clausius-Mossotti relation is at a much shorter wavelength, and with a radius of 50nm, the higher order modes can easily be coupled to. The variation in ϵ dictates the wavelength at which they emerge and according to $\epsilon = -\epsilon_d(l+1)/l$ the difference in wavelengths of successive modes, when emerging, is greater for silver compared to gold.

It is the case that the fields of the quadrupolar mode decay even more rapidly than those of the dipolar mode, so quadrupole interactions only take place when there are very small separations between the particles and so can be neglected[†]. Hence we arrive at the conclusion that at very small separations the spectral response will exhibit a red-shifted dipolar resonance due to the head-to-tail separations and at separations approximately greater than $\lambda/2\pi$ the radiative fields will dominate and tend to blue-shift the resonance. This is, qualitatively, what was observed by Haynes *et al.* who carried out optical experiments on arrays of metallic discs. They observed the blue-shift at relatively large separations and a red-shift at very small separations. It should be noted that the distance at which the electrostatic and radiative fields are balanced in magnitude has previously been calculated for a point dipole (chapter 3), and not an extended nanoparticle, so a direct comparison is not possible with this information (it is still a good approximation). Furthermore, the manner in which the field-strengths translate into absolute shifts in wavelength is beyond the scope of the current discussion. Despite this, the study by Haynes *et al.* is very insightful as it contains much of the physics needed to explain the work by Malynych and Chumanov.

4.4 Method of modelling periodic arrays of nanospheres

A paper by Khlebtsov *et al.* acted as a follow-up to the Malynych paper and analysed numerically the response of small, finite arrays of nanoparticles in both ordered and disordered arrays. They observed that qualitatively, the same spectral features were observed regardless of the degree of positional order in the system. For this reason, it was deemed appropriate to model the response of an infinite square-array in order to approximate the results observed by Malynych and Chumanov.

Modelling was carried out using HFSS version 11. A brief description of the modelling technique will be provided here, highlighting the processes which are specific to the implementation of periodic boundary conditions. A more thorough description of some of the more general aspects is included in chapter 5.

[†]The quadrupolar modes can interact with other dipolar or quadrupolar modes and hence produce hybridised modes if the separations between the particle are small enough.

HFSS provides a graphical user interface and structures may be drawn in three-dimensions, much like computer-aided design. For example, an infinite array of metal spheres surrounded by glass is represented by drawing a sphere at the origin and a cuboidal unit cell around it. To both elements, material parameters are specified (specifically, the real part of the permittivity, where $\epsilon = \epsilon_r + i\epsilon_i$ and the dielectric loss tangent, where loss $= \epsilon_i/\epsilon_r$). If the material is dispersive, a series of frequency-dependent values may be imported. A spline is fit to these values within the software, to allow the model to solve for intermediate frequencies.

In order to avoid the sphere being described by the software as both the material of the sphere and that of the unit cell, a Boolean subtraction is carried out to remove a spherical volume from the centre of the unit cell which is then unambiguously filled with the material attributed to the sphere.

Boundary conditions allow the periodic nature of the array to be specified. For a square lattice, two pairs of 'master' and 'slave' boundaries must be defined (figure 4.4.1). The condition at these boundaries is that the field on the master boundary is the same as the field on its associated slave boundary (each pair of master/slave boundaries are assigned to opposite faces of the unit cell). On the top and bottom of the unit cell, perfectly matched layers (PMLs) are placed at least one wavelength from the origin and they ensure that there are no reflections from the top and bottom of the bounding volume. Once the boundaries are specified, a frequency needs to be specified, for which, the model's mesh is adaptively calculated. Also, the number of adaptive passes which refine the mesh in order to most accurately describe the fields must be set. Also, at this stage, any frequency sweeps are specified and these are usually linear in terms of frequency. Finally, the details of the incident beam must be specified, i.e. the type of wave (plane wave etc.), the direction of propagation and the polarisation including ellipticity if appropriate. Once all these things have been carried out, the model may be run.

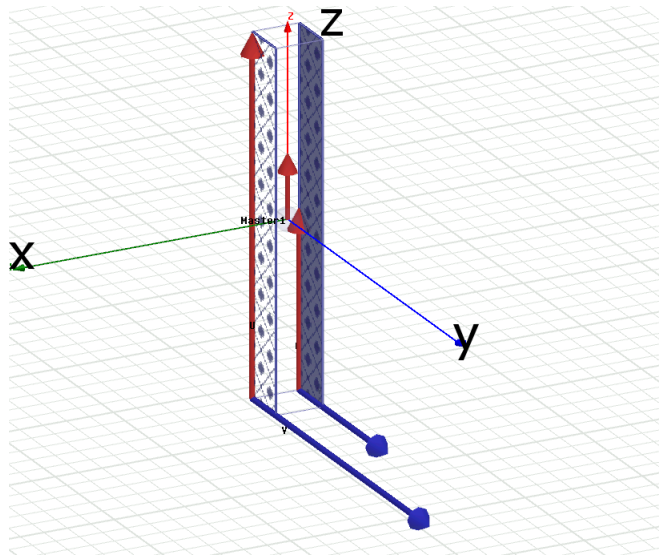

(a)

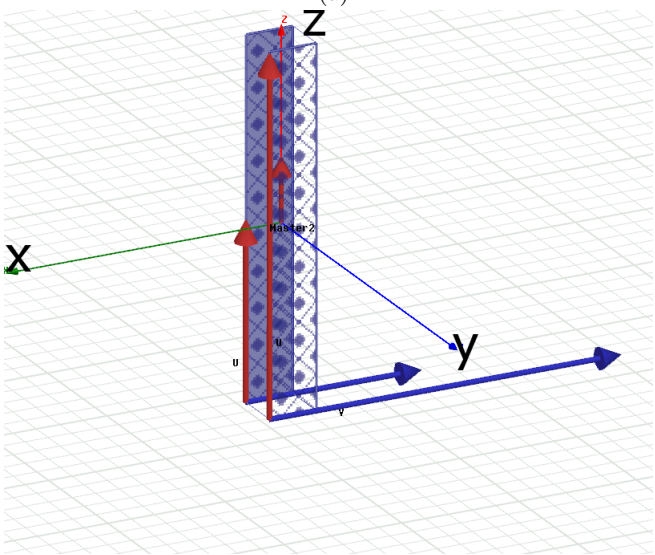

(b)

Figure 4.4.1: Two sets of 'master' and 'slave' boundaries as specified on opposite sides of a unit cells in HFSS.

Upon running the model, the system is split into a number of tetrahedral elements (a process called 'meshing'). The density of the mesh in this initial 'guess' is higher in media with large permittivities to allow for the modified wavelength light of a given frequency will have. From this initial approximation, more tetrahedra are placed in the model in the locations where the spatial variation of the field is greatest. This continues for a specified number of passes. After each new pass, the change in the total energy of the system is calculated ($\Delta U = \frac{1}{2}\left(\int \left(\epsilon E_n^2 + \mu H_n^2\right) dV - \int \left(\epsilon E_{n-1}^2 + \mu H_{n-1}^2\right) dV\right)$) and tends to reduce every time, and at the point where there is no significant change in this value, the model is said to have converged on a solution (from experience, $\Delta U \simeq 10^{-2}$ is a reliable value to use).

Once the model has converged, we make the assumption that this distribution of meshing

points is going to be reasonably accurate in describing the fields of all other frequencies throughout the sweep, so we only have to carry out this adaptive meshing once and the arrangement of tetrahedra is used for all the other frequencies[‡].

4.5 Particle arrays

A clear distinction needs to be made between three types of nanoparticles in the sub-100nm range:

- Very small spherical particles exhibit one mode (the dipolar mode) regardless of illumination angle.
- Larger spherical particles can support higher-order modes whose resonant charge accumulations occur in the plane defined by the incident E-field and k-vector. The modes can be excited at any angle and polarisation but the location of the charge accumulations will be modified according to these parameters.
- Large flat discs are able to support higher order modes but only if there is phase retardation of the incident wave across the plane of the disc. At normal incidence this retardation is not present and hence only a dipolar mode can be excited.

The nanoparticle arrays which were studied by Haynes *et al.*[97] consisted of large discs which could only exhibit dipolar modes at normal incidence, even though the particles were large enough to support quadrupolar modes if they had been illuminated with a component of the incident k-vector in the plane of the discs. The arrays were, however, illuminated at normal incidence so the in-plane quadrupolar mode was not excited. Malynych and Chumanov, in their paper, presented results of extinction measurements from a random array of silver spheres dispersed in a polymer film. These spheres may be classified as "large spheres" using the descriptions above. The authors varied the interparticle separation by means of stretching the elastic film in which the particles were supported. At small particle separations they observed a strong peak in the optical density at the wavelength which corresponds to the quadrupolar mode of the single-particle extinction spectrum. Malynych and Chumanov attributed this large extinction to in-plane, coherent coupling of quadrupolar modes associated with the silver nanospheres in either symmetric or antisymmetric configurations, i.e. as shown in figure 4.2.1b and c respectively. This explanation suggests that the regions of the spheres where the charge should accumulate at certain phases throughout the optical cycle all occur in the plane of the array when a quadrupolar mode is excited at normal incidence. As discussed above, however, the excitation of a quadrupolar mode relies on the existence of phase retardation from one side

[‡]It should be noted that the frequency chosen for meshing is very important as the higher the frequency, generally the greater level of detail, but where a resonance exists, the meshing should be carried out at this point.

of the particle to the other. For normal incidence it is thus impossible to couple to an in-plane quadrupolar mode, and yet it is at normal incidence that Malynych and Chumanov observed their strongest value of optical density. Furthermore, if this in-plane coherent interaction was the cause of the single strong peak observed by Malynych and Chumanov, one would have expected Haynes *et al.* to have observed similar effects in the optical response of their arrays of discs. This is because with regard to in-plane higher-order modes, a large sphere is equivalent to a large disc in that neither support such an excitation, though they can in principle be excited with appropriate illumination. We must, therefore, seek an alternative explanation. In principle, it is possible that in the case of a disordered array, isolated instances of broken symmetry could give rise to the in-plane excitation of a quadrupolar mode. This is due to particles scattering normally incident light into the plane of the array. All dipolar modes will scatter into the plane, but as the array is disordered it is unlikely that this will produce a significant effect. Also, similar spectral features were observed in exact simulations of ordered finite arrays of particles by Khlebtsov *et al.*,[116] demonstrating that the effect is not solely dependent on the presence of disorder.

4.6 Finite element modelling

In order to obtain a more thorough understanding of the physical mechanisms which produce the spectral response of this kind of array, finite-element modelling was carried out which allowed frequency dependent optical density to be calculated, and at the particular frequencies of spectral features of interest, the particles' associated electric field distributions may be studied to provide a better physical insight into the far-field optical response.

As the work by Khlebtsov suggested that the level of disorder was not of primary importance in producing the effect observed by Malynych and Chumanov, we begin by examining ordered, square arrays of nanospheres. Figure 4.6.1 shows the calculated optical density of a square array of 50nm radius silver spheres on a square lattice surrounded by glass for a range of array periods. It can be seen that when the separation is large the spectrum has two distinct peaks which correspond to the dipolar and quadrupolar modes which are similar to those supported by a single particle in isolation. Larger separations can, in principle, be investigated, but at these separations, diffraction becomes apparent in the spectra and it becomes more difficult to thoroughly understand the origin of all the spectral features. For the spectral range used in this investigation (300-800nm), an array period of 200nm is the largest which can be used whilst ensuring that the wavelength corresponding to the diffraction edge is at a shorter wavelength than the blue end of the wavelength range considered here.

The peak which occurs at the longer wavelength, 500nm, corresponds to the dipolar mode whilst the peak at 428nm corresponds to the quadrupolar mode. The dipolar peak is shifted to the blue compared to the single particle extinction spectrum as calculated exactly using Mie theory (figure 4.1.1) due to radiative coupling between the particles (see chapter3). The

wavelength of the quadrupolar mode, however, remains practically unchanged compared to the single-particle case. This is because the radiative decay length of the quadrupolar field is very short compared to that of the dipolar mode,[112] so the frequency of the quadrupolar mode is not significantly perturbed by the presence of neighbouring particles even in an ordered array.

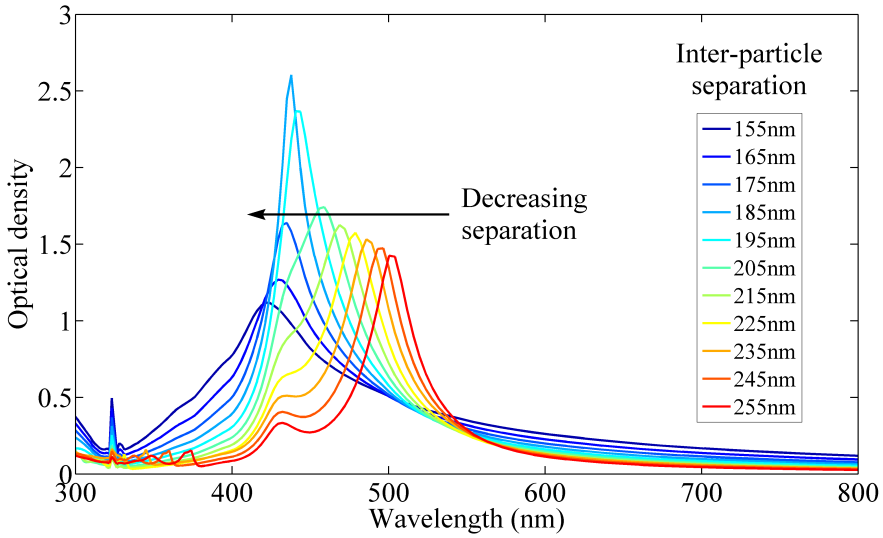

Figure 4.6.1: FEM modelling results showing the optical density spectra of infinite square arrays of silver nanospheres which have a radius of 50nm surrounded by glass for a range of array periods. The arrays with large periods show two distinct features, those of the dipolar and the quadrupolar modes (the dipolar mode being at the longer wavelength). As the interparticle separation is reduced, the dipolar mode is shifted to shorter wavelengths due to coherent radiative interactions between the particles. Closer separations show just one peak. The features below 375nm are mainly due to diffraction effects and features in the permittivity.

Finite-element modelling has allowed us to attribute the two spectral peaks which appear at large separations ($\sim$ 255nm) to be the dipolar and quadrupolar modes by examination of the local electric field distributions inside the spheres. The field profiles shown here are plotted in the x-z plane (figure 4.6.2), i.e. the plane which contains both the incident E-field and k-vector. The dipolar mode appears in the spectra (figure 4.6.1) at a longer wavelength than the quadrupolar mode at these relatively large separations. Time averaged field magnitudes provide sufficient information to be able to identify the modes, but animations (or snapshots at different phases) of the field vectors are able to provide a clearer illustration of the nature of these modes (figure 4.6.2).

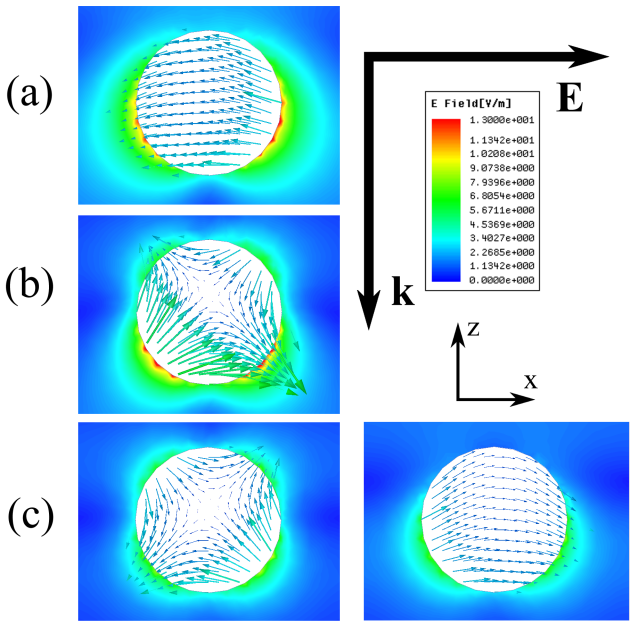

Figure 4.6.2: Electric field profiles for 50nm radius silver spheres in infinite square arrays surrounded by glass as calculated by FEM. Shown in each field-plot is the norm of the real part of the total electric field in the glass surrounding the sphere at a single phase in the x-z plane, and arrows showing the direction and strength of the total electric field inside the sphere. These plots are for (a) an array period of 255nm calculated at a wavelength of 500nm which corresponds to the dipolar mode, (b) a 255nm array period at a wavelength of 428nm which corresponds to the quadrupolar mode, and (c) a 185nm array period at a wavelength of 436nm which corresponds to the single spectral feature of such an array. (c) shows the instantaneous electric field profile for two different phases of the optical cycle separated by 180° (the colour scales are the same for all field plots).

At large separations (i.e. 255nm) the simulated field plots show purely dipolar character at the wavelength of the spectral peak which exists at the longer wavelength (figure 4.6.2a), and purely quadrupolar character at the wavelength corresponding to the spectral peak at the shorter wavelength (figure 4.6.2b). The modes, therefore are distinct from each other as there is very little dipolar character in the field-plot of the particle at the wavelength corresponding to the quadrupolar mode and *vice versa*. This is true for all phases throughout the optical cycle, though only two phases have been presented here. This distinctness is to be expected from consideration of the relative strengths of the two peaks in the corresponding optical density spectrum — at the wavelength of one of the resonances, any contribution from the other mode is extremely weak in comparison.

As the particle separation is reduced, the spectral feature which corresponds to the dipolar mode shifts to the blue due to radiative coupling between neighbouring particles which are perpendicular to the incident electric field. Eventually as the separation is reduced even more, this dipolar resonance begins to overlap with the quadrupolar mode whose resonance wavelength is approximately 430nm (and shifts very little from this wavelength throughout the set of spectra shown in figure 4.6.1). The extent of this overlap continues to increase until

there is only one spectral feature present, i.e. when the array period is 185nm. The dual-mode characteristic of this feature can be seen in the plots of the electric field vectors within the spheres which show both dipolar and quadrupolar character in the x-z plane at two different phases of the optical cycle 180° apart. For separations less than 185nm, the optical density falls and the peak shifts further to the blue. The investigation of separations below 155nm was complicated by what appear to be near-field interactions between the particles. It should be noted that these field plots (figure 4.6.2) are in the plane containing the incident k-vector and incident E-field. The plane which was previously thought to contain the quadrupolar mode according to Malynch and Chumanov, (i.e. the x-y plane) shows a purely dipolar character as the lack of phase retardation in this plane does not allow the quadrupolar modes to be excited as discussed above (figure 4.6.3).

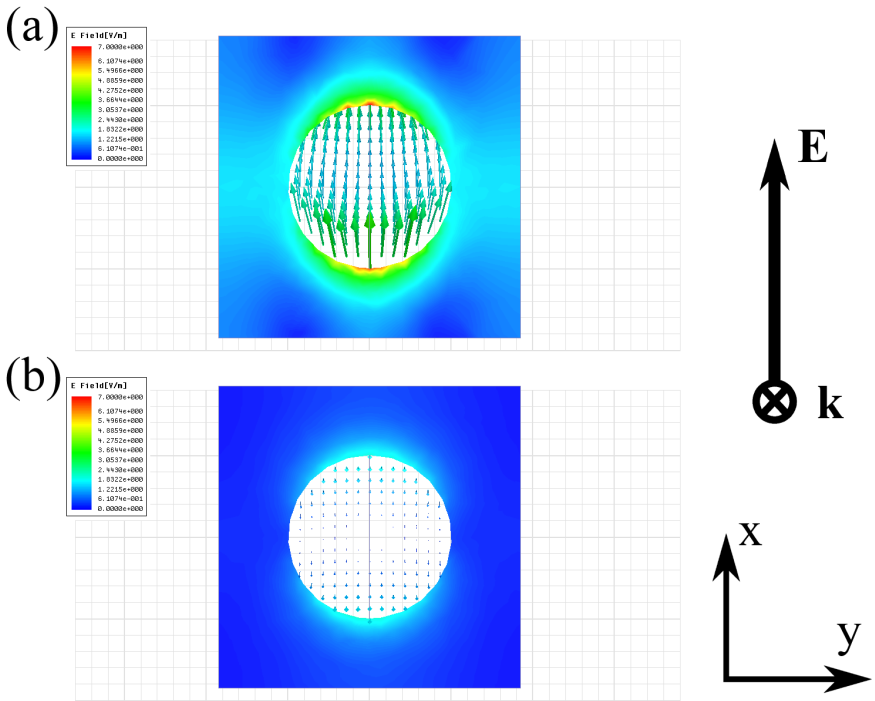

Figure 4.6.3: Electric field profiles for 50nm radius silver spheres in infinite square arrays surrounded by glass as calculated by FEM. Shown in each field-plot is the norm of the real part of the total electric field in the glass surrounding the sphere at a single phase (up to the limits of the unit cell), and arrows showing the direction and strength of the total electric field inside the sphere in the x-y plane (which contains the incident electric field vector, and no component of the incident k-vector). These plots are for a 185nm array period at a wavelength of 436nm which corresponds to the single spectral feature of the short-period system at two different phases of the optical cycle separated by 180° ((a) and (b)).

Figure 4.6.3 demonstrates that there is no in-plane "cooperative plasmon mode" excited at this wavelength. The physical reason for the single peak in optical density may instead be attributed to the overlap between the dipolar and quadrupolar modes. We have, of course, only considered ordered arrays, but we base our assumption that this explanation is valid for random arrays based on the paper by Khlebtsov *et al.* and also the results given in chapter

3 which show that the blue-shift still occurs for random arrays as calculated by the coupled dipole approximation.

4.7 Varying the incident angle

When a dense, ordered array of metal nanoparticles, such as those studied here, is excited optically, its optical response is strongly dependent on the incident illumination conditions. The local field configuration is directly responsible for all aspects of the system's response and the incident field is directly responsible for a significant proportion of this local field. One illumination parameter of particular interest here is the angle of incidence. When an array like those discussed in this chapter is illuminated at an oblique angle the optical response is modified when compared to the response when the array is illuminated at normal incidence. Furthermore, at an arbitrary oblique angle of incidence the optical response is markedly different for p- and s-polarised light due to the completely different field configurations. This is in contrast to normal incidence where polarisation makes no difference in square arrays and, in principle, no difference in random arrays.

The angle dependence of the optical response of the ordered arrays modelled above have been numerically investigated using FEM modelling. The square array of 100nm silver spheres have an array period of 185nm which is the period which produced the best agreement with the results from Malynych and Chumanov. These particles are embedded in a medium with a refractive index of 1.41. This is the refractive index of PDMS which is the material used by Malynych and Chumanov in their angle-dependent investigations. The value of refractive index is taken from a paper by Vezenov *et al.*[117]

This infinite array was simulated with PDMS filling the lower half-space, just covering the entire sphere. The upper half-space was set to be vacuum. The permittivity values for silver were taken from Palik[3] and interpolated using a cubic spline. The height of the unit cell was 1μm and the other two dimensions were varied in order to accommodate changes in the lattice spacing. The top and bottom faces of the unit cell were specified as perfectly matched layers (PMLs) and the global medium was set to be vacuum. The mesh was refined over a number of adaptive passes for a fixed wavelength (400nm) until the model reached convergence. Typically convergence was obtained for between 30,000 and 50,000 tetrahedral elements, the exact number depending on the lattice spacing, polarisation and incident angle. For each lattice spacing and incident angle the mesh from the converged solution at the wavelength of 400nm was used to calculate the fields for all other wavelengths. When the model had solved, the transmittance was evaluated via the appropriate S-parameter (S_{21}).[57]

The optical density of this system has been calculated as a function of incident angle for both polarisations (with one of the lattice vectors lying in the plane of incidence). At normal incidence, the interaction is coherent and acts to shift the dipolar resonance towards the blue,

as stated above. At oblique angles of incidence, however, the response is very different for the two polarisation states.

In the case of s-polarised illumination, the incident E-field is always in the y-direction (see figure 4.3.1 for the schematic) for all angles of incidence, so there is significant dipolar scattering in the x-z plane. Which would tend to retain the blue-shift, but as the angle of incidence is increased, however, there will be de-phasing of the incident field in the x-direction, which is the direction in which the radiative interactions take place, and hence these interactions will no longer be coherent and so will be weakened. They will also be weakened due to the factor $(\hat{\mathbf{r}} \times \mathbf{p}) \times \hat{\mathbf{r}}$ in the expression for the dipolar field. Therefore the magnitude of the blue-shift of the dipolar mode will be reduced. The spectra in figure 4.7.1 demonstrate this, as at higher angles of incidence, the single spectral peak which exists at normal incidence splits into the two separate peaks of the dipolar and quadrupolar modes in a similar way to that observed when the arrays which were illuminated at normal incidence had their array periods increased (figure 4.6.1).

For p-polarised light the incident field configuration produces a markedly different optical response. For all angles of incidence the incident E-field is in the x-z plane, and so for all angles, the dipolar mode scatters light strongly in the direction of the nearest neighbours in the y-direction (again, this is the radiative term in the expression for the dipolar field). It should be made clear that in the y-direction there is no far-field effect due to de-phasing. This is due to the fact that along a given row of particles which is parallel to the y-axis (and for which the radiative interaction will be strongest), the incident k-vector has no component in this direction and so the incident field will have the same phase at the site of each particle in the same row. Along this axis, for all incident angles, the lack of de-phasing allows strong radiative coupling for all the rows of particles despite the fact that each row is subject to incident radiation of a different phase. Therefore for all angles of incidence only one spectral peak is seen — the blue-shift of the dipolar mode is hence preserved for all angles of incidence (figure 4.7.1). Note that the effect of changing the polarisation is very different to the experimental measurements reported by Malynych and Chumanov whose data show the opposite behaviour. Perhaps this was a labelling error, and at any event Malynych and Chumanov provided an incorrect explanation of the phenomenon. They state that s-polarised light allows only the "cooperative plasmon mode" to be excited because the incident electric field vector is always in the plane of the array, and that the presence of a second peak for p-polarised light is due to the excitation of an out-of-plane dipole resonance. If this were the case, the second peak would still be visible at normal incidence as the neighbouring dipoles would still interact in largely the same manner.

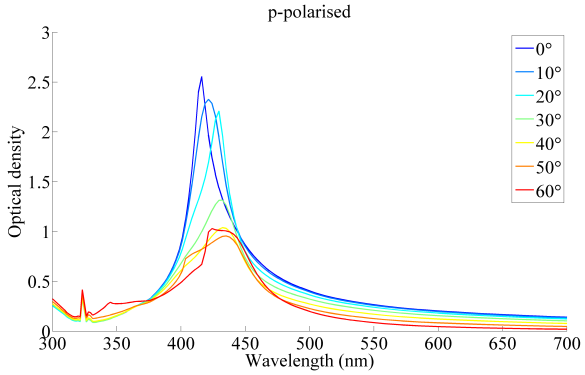

(a)

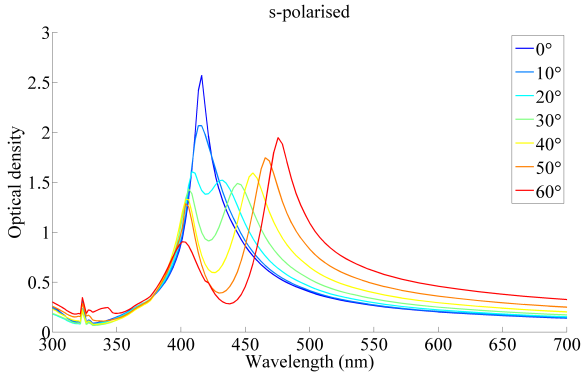

(b)

Figure 4.7.1: Optical density of a square array of 50nm radius silver nanospheres embedded in PDMS ($n = 1.41$) for a range of incident angles as calculated by finite element modelling for both p- and s-polarised light ((a) and (b) respectively). When the light is p-polarised, there is significant radiative coupling between neighbouring particles which keeps the frequency of the dipolar mode blue-shifted relative to the single-particle case. For s-polarised light, there is significantly less interparticle coupling due to the phase retardation of incident light across the array. This effect is more significant at higher angles, and the two peaks corresponding to the dipole and quadrupolar modes are recovered.

4.8 Summary

In this chapter it has been shown that the collective behaviour of a square array of 50nm radius silver nanospheres (which support both dipolar and quadrupolar modes) surrounded by glass can differ strongly from the behaviour of individual nanospheres. Rather than two distinct modes in the extinction spectrum (as seen for single particles) corresponding to the dipolar and quadrupolar modes, there is just one peak in the optical density of a square array with an array period of 185nm. This single peak is due to the dipolar and quadrupolar modes occurring at very similar frequencies. The mechanism which gives rise to this effect is that the neighbouring plasmonic particles radiatively couple together and this coupling perturbs the collective dipolar mode of the array and upon reducing the period of the array, this collective dipolar mode shifts to the blue until it overlaps with the quadrupolar mode. The

mechanism for this interaction is the in-plane radiative dipolar field. The single spectral peak observed in the study of arrays illuminated at normal incidence is in good agreement with experimental data in the literature,[113] yet the field plots presented here suggest an alternative explanation for the existence of the single peak. It is proposed here that for a particular particle separation the dipolar and quadrupolar modes occur at approximately the same frequency and the contributions of the two modes sum to produce the strong response as opposed to the suggestion by Malynych and Chumanov whereby the response is due to an in-plane "cooperative plasmon mode". It should be noted that the electric currents primarily associated with the quadrupolar mode occur in a plane normal to the plane of the array rather than in the plane of the array as suggested in the literature.[113] This study has been extended to show that our explanation of the single spectral feature observed at normal incidence can easily be extended to describe the features in the spectra at oblique incidence for both polarisations. The results presented here show that higher order modes can significantly modify the optical response of metal nanoparticle arrays. As arrays of metallic nanostructures are now being considered for a range of metal-based plasmonic metamaterials, the role of higher order modes may play an important role, especially the electric quadrupolar mode.[118,119]

Chapter 5

Near-field fluorescence enhancement

5.1 Introduction

Electromagnetic field enhancement, in this context, is the phenomenon whereby the local field is stronger than the incident field. An example of field enhancement is using a lens to focus a collimated beam — at the focus the local field is much stronger than in the light incident on the lens. A lens, of course, is limited in its focussing ability by the diffraction limit, so if this limit can be overcome it should be possible to produce an even stronger field in a given volume. Plasmonics enables this to be achieved

Metallic nanoparticles have resonance wavelengths that are much larger than their physical size (in the visible regime), and if a particle is illuminated on resonance, the local near-fields of the particle will not extend very far from the particle, and so the fields will be concentrated in a small, sub-wavelength volume. The fact that these particles have free conduction electrons means that they can be very strongly polarised by incident fields, and hence they are ideal for producing near-field enhancements. Presented here are experimental and theoretical results concerning several novel structures which exhibit strong field enhancements.

Electromagnetic enhancement is measured experimentally by coating the samples with a fluorescent* dye which absorbs strongly at a laser wavelength. The extent to which these dye molecules fluoresce is dependent on the local field intensity. Here, the intensity of fluorescence from small volumes of dye is measured and this gives an indication as to the strength of the local electric field enhancement.

This chapter contains work carried out in collaboration with a group at the University of Manchester led by Sasha Grigorenko (including Vasyl Kravets, Frederik Schedin and Andre Geim). The team at Manchester was responsible for the fabrication of the initial 'tower'

*Fluorescence is the process whereby a molecule can absorb light at a certain wavelength and re-emit it (i.e. fluoresce) at a longer wavelength.

structures but all experimental measurements were performed in Exeter by myself, George Zoriniants (from Exeter) and Sasha Grigorenko from Manchester. GZ was heavily involved in preparing the fluorescence samples, and analysing the experimental data. All the modelling presented here was carried out by myself. Where appropriate I have highlighted any occasion where work was carried out by people other than myself.

5.1.1 Two-tier structures

The near-field enhancement of individual nanoparticles and particle dimers is well-known,[85] but here we are interested in a type of structure which comprises two metallic discs of different sizes, one on top of the other. This geometry was first fabricated serendipitously, but gave rise to strong enhancement of the local electric field, so it was studied further. This type of structure we call the 'tower' structure, and a similar structure whose geometry is more controllable was also studied called a 'pagoda' structure.

5.2 Tower and pagoda structures

Both the tower and pagoda structures were fabricated using electron-beam lithography, but by different processes. The fabrication details of each structure are described in appendix A.

5.2.1 Tower

The tower structure is shown in figure 5.2.1 and was fabricated by collaborators at the University of Manchester:

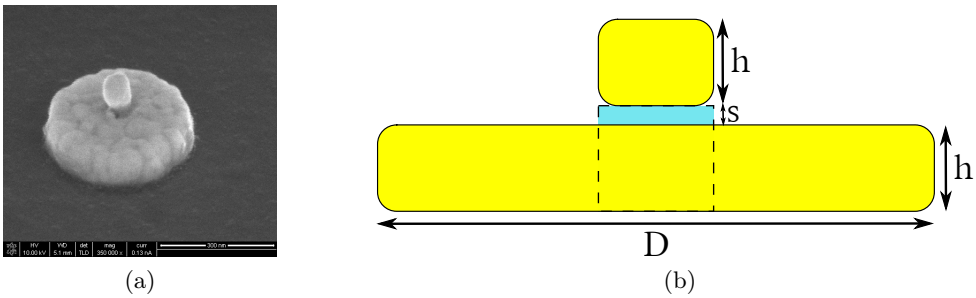

(a) (b)

Figure 5.2.1: An SEM of a tower structure (a) and (b) a diagram of a cross-section through a 'tower' structure (the yellow regions represent gold and the blue represents overexposed PMMA. The PMMA column extends through the centre of the large disc as a cylindrical pillar.

An important factor in producing the tower is that the PMMA pillar is slightly higher than the thickness of gold evaporated, and the result is that the small disc on top of the pillar

is electrically isolated from the larger disc. The large disc is, in fact, a ring as the PMMA column extends through its centre — this has been confirmed by using FIB to mill a cross-section through one of the structures.

5.2.2 Pagoda

The pagoda structure is shown in figure 5.2.2. It was fabricated by the author and colleague (GZ) with two EBL exposures.

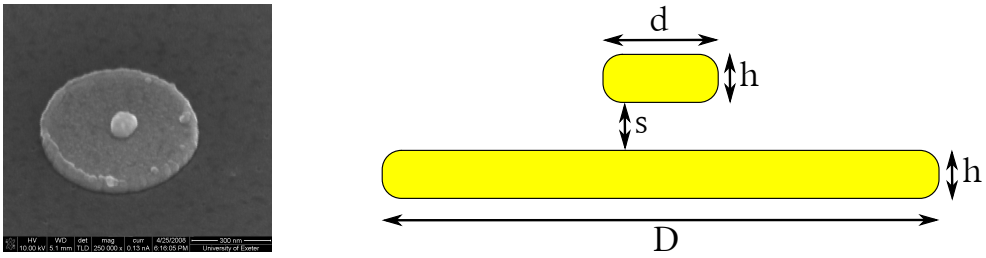

(a) (b)

Figure 5.2.2: An SEM of a 'pagoda structure' (a) and (b) a diagram of a cross-section through a 'pagoda' structure (the yellow regions represent gold).

The dielectric spacer layer was spin-coated to a thickness of 100nm. It was thought that reducing the thickness of the spacer would improve enhancement, but this was not observed experimentally, possibly due to electrical contact through pinholes in the dielectric spacer. This dependence will be discussed later in this chapter.

5.3 Characterisation of sample morphology

The geometries of the metallic nanostructures were investigated using scanning electron microscopy (SEM) and atomic force microscopy (AFM). SEM has the advantage of being able to probe the sample at oblique incidence, and AFM has the ability to measure thickness with good accuracy. SEM images are shown in figures 5.9.2 and 5.9.3. This characterisation has shown that the gold in the tower structure was 90nm thick and the overexposed PMMA column was 110nm thick. The diameter of the large disc was approximately 590nm and the diameter of the small disc was approximately 110nm. For the pagoda structure, the gold thickness was 40nm and the large disc had a diameter of 300nm and the small disc had a diameter of 100nm. The dielectric spacer was 100nm

5.4 Fluorescence preparation

The fluorescence experiment was carried out by spin-coating a fluorescent dye across the whole of each sample to a thickness of approximately 30nm (figure 5.4.1). The dye (oxazine 1 perchlorate) was dissolved in anisole and chlorobenzene (1:1 by volume) and PMMA (495kD) was added to it to act as a host (1% by weight). It was spun at 4000rpm for 90s to achieve the desired thickness. The concentration of the dye in the film was chosen to be 2% by weight.

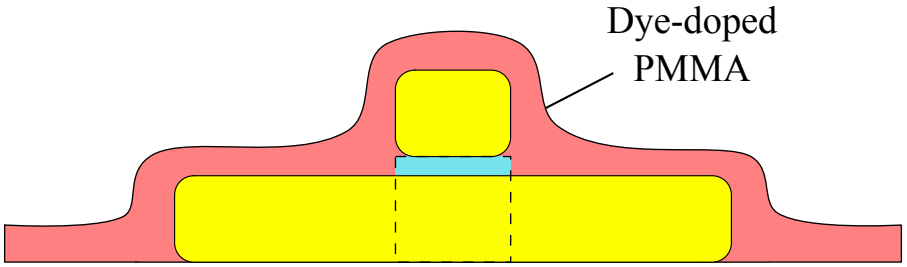

Figure 5.4.1: A 'tower' structure coated with a layer of fluorescent dye-doped PMMA. This representation is approximate as the exact topology is unknown.

5.5 Fluorescence confocal microscopy

In order to probe the near-fields of the sample, a confocal microscope (Leica TCS SP5) was used to measure the fluorescence emission from a small volume of a sample. A 633nm HeNe laser was focussed to a small, diffraction-limited volume by a 63x objective lens. The fluorescence emission was collected from the same volume by the same lens used for excitation. A pinhole below the lens ensures that the collected light is from the same volume as that which is illuminated by the excitation beam. The emission light is dispersed by a prism over the entrance to a photomultiplier tube (PMT) which can accept light over a customisable range of wavelengths. For this experiment, the range was set to 650 - 800nm so that no light from the excitation beam is measured; only fluoresced light. The numerical aperture of the objective lens is NA = 1.4 which produces a Gaussian beam waist of $w > \frac{\lambda}{\pi \cdot NA} \simeq 140$nm. The Gaussian beam profile is given by the following equation, where z is the distance along the beam axis, E_0 is the intensity of the field, w is the beam waist (expressed as a radius), ϕ is the phase and ρ is a the distance to a point in the plane perpendicular to the beam axis for a given value of z.[120]

$$E(\rho, z) = E_0 \frac{w}{w(z)} \exp\left(-\frac{\rho^2}{w(z)^2}\right) \exp(i\phi(\rho, z)) \tag{5.5.1}$$

The beam width (radius) is given by the following formula where λ is the wavelength:

$$w(z) = w\sqrt{1 + \left(\frac{z\lambda}{\pi w^2}\right)^2} \tag{5.5.2}$$

For reasons specific to the particular lens used for this experiment, the Gaussian waist was in fact approximately 200nm according to the manufacturer's notes.

The resolution of the collection optics is also important and was investigated by observing very small metallic particles (fabricated by EBL) and measuring the fluorescence profile. In the limit of an infinitesimally small particle, the profile will produce the resolution of the collection optics. The profile was observed (by GZ) to be approximately a Gaussian superimposed on a uniform background:

$$I = I_0 + A\exp\left(-\frac{|\boldsymbol{r} - \boldsymbol{r}_0|^2}{2\sigma^2}\right) \tag{5.5.3}$$

where $\boldsymbol{r}$ and $\boldsymbol{r}_0$ are two-dimensional vectors in the image plane. $\boldsymbol{r}$ is the position at which the intensity is measured, and $\boldsymbol{r}_0$ is the position of the particle. I_0 is the background intensity, A is the amplitude of the Gaussian profile and σ is the Gaussian width. A 100nm particle gave a value of $\sigma \simeq 230$nm and a 600nm particle produced $\sigma \simeq 370$nm. By extrapolating these values to produce a sigma value for an infinitesimally small particle, we obtain a value of $\sigma \simeq 200$nm.

Index matching fluid was used (with an index $n = n_{glass} = 1.5$) so that the system can be regarded as existing in a homogeneous environment, and hence the effect of the substrate has been neglected.

5.6 Experimental far-field fluorescence enhancement by metallic nanostructures

In order to measure the fluorescence enhancement experimentally, we used the Gaussian beam to scan the sample, and at each position of the beam the fluoresced light intensity was collected with a photomultiplier tube (PMT). This measured signal along with internal synchronisation pulses within the microscope allows an image to be constructed of fluoresced intensity as a function of position across the sample. Once normalised, this data can be converted into fluorescence enhancement. It should be noted that the point at which fluorescence is collected is, in fact, the position of the focus of the incident Gaussian beam, and hence (due to the confocal arrangement) the focus of the collection optics. The resulting image is a two-dimensional representation of fluorescence intensities, and hence bright regions represent strong fluorescence enhancement. Figure 5.6.1 (prepared by GZ) shows SEM images, fluorescence images, and a

plot of fluorescence intensities along a line of the image for a single particle, a large ring and a tower structure. It can be seen that the single particle produces a small enhancement of order 1.6 (where an enhancement of 1 represents the baseline of no enhancement), the large ring produces slight degradation (~ 0.9), and the tower structure produces very large fluorescence enhancement (approximately 23).

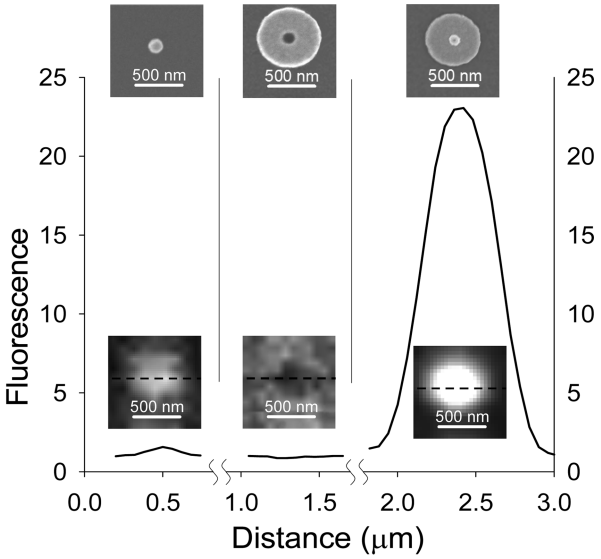

Figure 5.6.1: SEM images, fluorescence confocal images and plots of fluorescence intensity as a function of focus position along a line shown in the fluorescence images for the 'tower' structure and its constituent particles. These quantities are shown for (l-r) a single small particle, a single large ring and a 'tower' structure (the small disc and the ring have the same size as those which constitute the tower structure).

Figure 5.6.2 (also prepared by GZ) shows an equivalent set of results for the pagoda-type structure. It can be seen that the small disc, the large disc and the pagoda all enhance the fluorescence emission but enhancement due to the pagoda is significantly stronger than its constituent elements, though the maximum enhancement is significantly smaller than that observed for the tower structure.

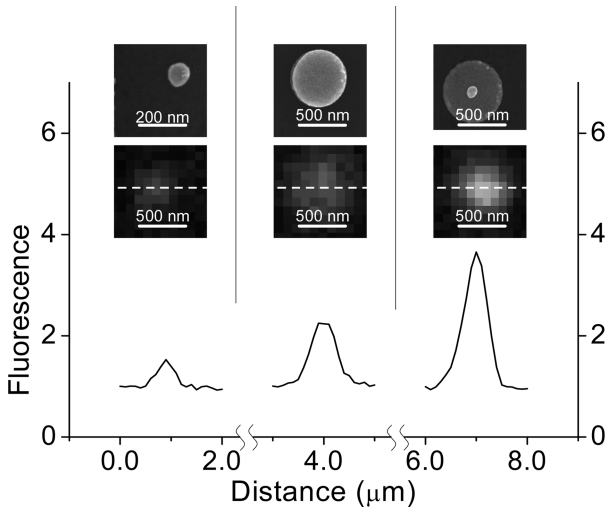

Figure 5.6.2: SEM images, fluorescence confocal images and plots of fluorescence intensity as a function of focus position along a line shown in the fluorescence images for the 'pagoda' structure and its constituent particles. These quantities are shown for (l-r) a single small particle, a single large disc and a 'pagoda' structure (the small disc and the large disc have the same size as those which constitute the pagoda structure).

The enhancement due to the small disc is caused by the well-known phenomenon of field confinement due to localised surface plasmon resonances. Light of a given wavelength can excite a resonance in a particle that is much smaller than the wavelength of light. As discussed previously, the oscillating dipole moment associated with the resonance has strong fields which occur in very small volumes. If a fluorescent dye molecule is in the vicinity of the high fields, its fluorescence increases in proportion to the intensity (i.e. $|\mathbf{E}|^2$)[†]. Therefore, our 2D image of fluorescence enhancement approximates to a map of the near-fields in the region in which the dye is present (assuming a uniform distribution of dye molecules).

In this study, one of the single, small discs is approximately in resonance with the excitation wavelength. The large ring, while not in resonance still supports a plasmon resonance but the coupling strength is not as great. For the large disc in the pagoda system, the fluorescence enhancement is actually stronger than the small particle even though it is far from being in resonance with the incident light. The explanation is that the large disc acts as a mirror and the dye region is raised from the disc's surface into a region which overlaps with an anti-node in the standing-wave produced by the mirror-like disc. Even more counter-intuitive is the effect observed for the isolated ring (part of the tower structure) where the enhancement is actually less than that of the background (the substrate coated with dye). An explanation for this effect is that in contrast to the pagoda case, the tower structure does not have a spacer layer of dielectric covering the large ring, so the dye-doped PMMA is in direct contact with the gold. This lack of a spacer results in quenching of the fluorescence due to direct interactions between the dye molecules and the gold surface.[121]

[†]The fluorescence is also dependent on the quantum efficiency of the dye.

The composite structures, in comparison with the single particles, show greatly enhanced fluorescence emission and this is thought to be due to the interaction between the two metallic elements in each structure. A simplistic, electrostatic picture can demonstrate this effect: when a dipole moment is created in the small particle, it can induce an 'image' of the dipole in the large disc/ring if they are in close enough proximity (i.e. the near-field zone).[122] This induced dipole moment has the opposite orientation to the dipole moment in the small particle and due to the proximity, the field between the separated charges has the potential to become very strong. To investigate this complicated system I employed finite-element modelling which is able to solve the local fields for arbitrary geometries with arbitrary methods of excitation.

5.7 Finite-element modelling technique

5.7.1 Model setup

The systems described above have been replicated using 3D finite-element modelling in HFSS version 11.1. This section contains a fairly complete description of the modelling procedure.

The volume within which the fields were calculated was defined to be spherical. This sphere was specified to have a radius of 1000nm and was set to have the permittivity of glass ($\epsilon_{glass} = 2.25 + 0i$). Although fields are not calculated in the region outside this volume, it is still assigned the material parameters of glass to avoid reflections. A 'radiation boundary' at the interface between the simulation volume and the space beyond attempts to absorb all out-going radiation.

Inside the sphere, close to the centre, the discs are created which form the plasmonic structure. The permittivity values are taken from spectroscopic ellipsometry measurements at a wavelength of 633 nm by collaborators at Manchester. For the tower structure, a tall disc-shaped column was created which passed through the centre of the large disc and supported the small disc. The PMMA and chromium permittivities was also measured using spectroscopic ellipsometry at Manchester. Here is a table of the values used:

Material	Permittivity
Gold	$-12.2 + 0.77i$
PMMA	$2.19 + 0i$
Chromium	$-5.7 + 29.9i$
Glass	$2.25 + 0i$

For the pagoda structure, the small disc was simply placed above the large disc by the thickness of the deposited dielectric (which was assumed to have the same permittivity as glass. SEM

imaging reveals that although the gold elements are nominally 'discs', they are in fact considerably rounded at their edges. If the model contained unrealistically sharp edges, the values of electric field close to them could be much larger than in the real system. For this reason the edges of all gold structures were rounded (filleted) in the model with a radius of curvature of 20nm. When gold structures are created within glass, the material in the region of the gold is not uniquely defined, so to eliminate this problem, the volumes of gold are subtracted from the volume of glass (the same applies to all other materials). The excitation was set to be a Gaussian beam centred at the top of the large disc. The Gaussian width[‡] was set to be 200nm, the k-vector was set to be along the negative-z-direction and the electric field was polarised in the x-direction throughout (though the choice of the x-direction is arbitrary). The frequency of the excitation was set to be the equivalent of a wavelength of 633nm in air (i.e. the laser wavelength). The model was then solved, during which time the mesh was refined over seven adaptive passes (figure 5.7.1) until there were approximately 150,000 tetrahedral elements in the model (no user-defined meshing operations were defined in order to avoid bias). At this point it was observed that the model's solution had converged and any further adaptive passes would not have improved the model's accuracy significantly.

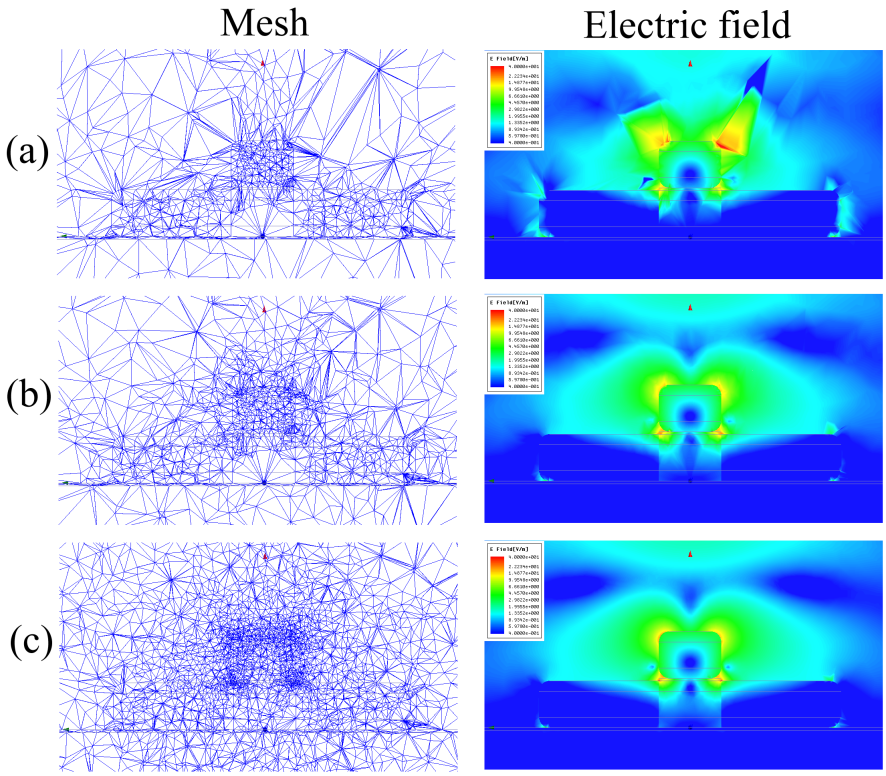

Figure 5.7.1: The mesh-grid and corresponding electric field profile as produced by HFSS for a tower structure after (a) one pass, (b) two passes and (c) seven passes.

The parameter which signifies the degree of convergence is the change in the magnitude of the

[‡]There are many definitions of Gaussian 'width', and the one used here is "the full-width diameter at half-height of the magnitude of the *electric field*".

total energy of the system between passes (figure 5.7.2). If it is of the order 10^{-2} the convergence is judged to be acceptable and further passes are likely to be prohibitively intensive, computationally, and yield little improvement to the accuracy of the field distribution. This optimum balance between computational time and accuracy is based on the convergence of physical quantities generated from previously solved simulations.

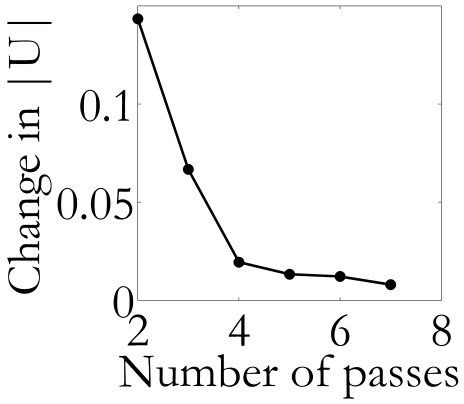

Figure 5.7.2: The convergence over 7 passes for the system shown in figure 5.7.1. The convergence parameter is $\Delta |U|$ where U is the energy of the system.

5.7.2 Data extraction

Once the model has been solved, it is possible to extract data (such as the electric field) for further analysis. For this system, we are primarily interested in the intensity integrated over a volume containing fluorescent dye. It is possible to carry out this procedure within HFSS, but the dye-doped volume must be specified before the model is solved and the meshing elements are forced to be aligned with the bounding surface even though they are composed of the same material (the dye-doped PMMA is assumed to have the same refractive index as glass to simplify the calculations). A result of this is that the number of meshing points within the model increases dramatically as the additional curved surfaces require a high density of points to provide an accurate representation of the geometry. As we are already working at the limits of our computational capabilities, this approach leads to a lower density of tetrahedra in the regions of main interest (i.e. close to the metal surfaces) and hence the degree of convergence is compromised. To avoid this potential loss of accuracy, the dye-layer is not specified in the model, and the raw data is exported from HFSS for post-processing.

The electric field magnitude can be mapped to a cubic grid and exported with an indexed list of coordinates. The element size used here is 25nm^2 and the total exported volume is $960 \times 960 \times 230\text{nm}$ and hence the number of elements is $192 \times 192 \times 46 = 1.7 \times 10^6$ (figure 5.7.3).

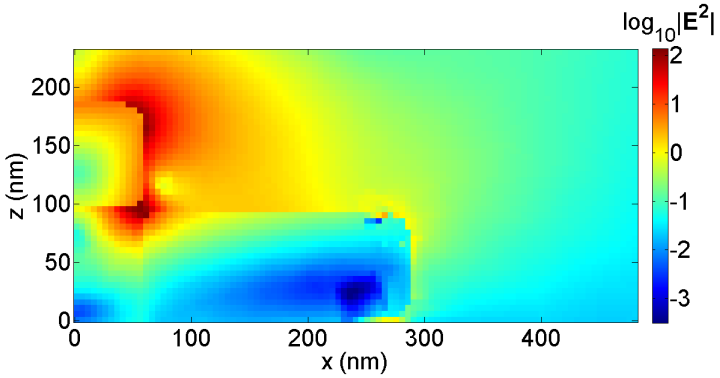

Figure 5.7.3: Cross section of intensity ($|\mathbf{E}|^2$) through centre of exported 3D cubic array.

The value of each point is taken to be the average value of $|\mathbf{E}|^2$ throughout the 25nm^2 volume associated with the point. We are interested solely in the intensity in the dye region, so it is necessary to specify which points are within this volume. This is specified as follows using Matlab. Initially a 2D array is generated with logical values specifying where dye is present in a cross-section through the centre of the structure (a plane containing the z-axis). This is achieved by specifying parameters and the rules regarding where the dye exists as defined by these parameters. Loops are then performed over the whole array to set each element to be a logical '1' if dye is present and '0' if no dye is present (figure 5.7.4). The array is specified to comprise 97×46 elements to ensure compatibility with the data exported from HFSS. Note that due to mirror symmetry, only half of the points in the cross-section need to be calculated to completely describe the cross section (all points with a radius of greater than 480nm are outside the range of the collection optics and hence are ignored).

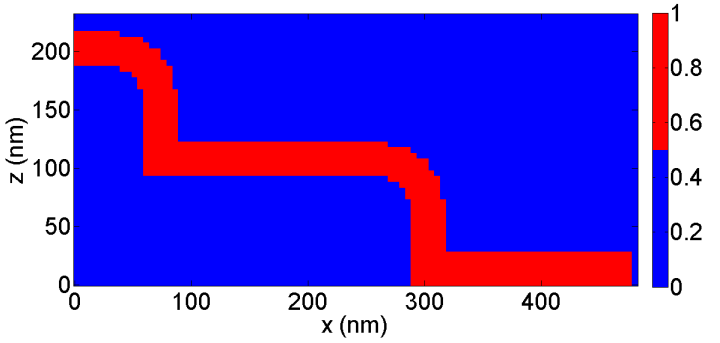

Figure 5.7.4: Logical array showing regions where dye exists.

Furthermore, the rotational symmetry of the system means that the complete 3D structure can be completely described by this array. Using this information, a loop can be specified in a computer program to sweep this 2D array through 360° in order to generate a 3D matrix

whose geometry is congruent with that exported from HFSS and whose elements have the same logical meaning as in the 2D case. This enables a direct matrix operation to be carried out whereby a new matrix of the same dimensions as the other two is created which contains the values of intensity ($|\mathbf{E}|^2$) at all points whose equivalent points in the logical matrix (which is converted into integer values) are equal to 1. Mathematically this can be represented as $M(i,j,k) = I(i,j,k) \times L(i,j,k)$ where M is the intensity which can, in principle, be measured, I is the intensity output directly from HFSS and L is the logical matrix (which has been converted to an integer) which defines the dye volume (figure 5.7.5).

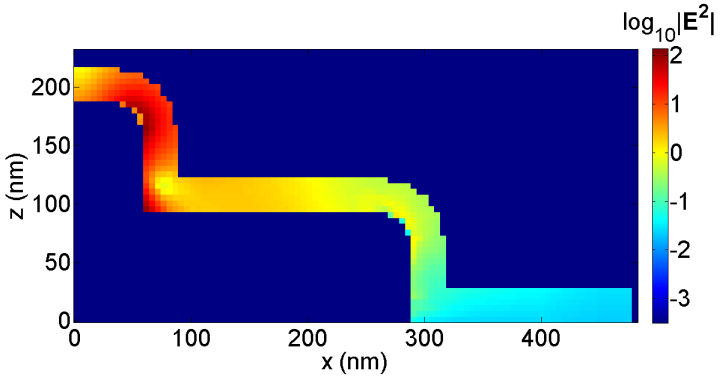

Figure 5.7.5: The intensity in selected dye regions.

It should be remembered that the figures shown here are only 2D slices through 3D arrays of numbers which specify the dye volume.

If we then assume that the fluorescent dye is distributed uniformly throughout the selected volume, it is reasonable to accept that the fluorescence intensity produced at each point is proportional to the actual excitation intensity at that point. Hence, when the structure is illuminated with the particular focus described here, the light fluorescently emitted from the dye region is collected via the PMT and is proportional to the near-field intensity. Therefore, in order to calculate the total fluorescence intensity (assuming a quantum yield of 1), we can simply sum all the elements in the 3D matrix of measured intensities: $F_{total} = \sum_{i,j,k} M(i,j,k)$.

5.7.3 Scanning beam

The preceding discussion was for the case of an incident Gaussian beam focussed at the centre of the structure and at the height of the centre of the small particle when it is a part of a composite structure. In reality, the beam scans across the sample, and so the structure is illuminated differently for each position of the beam. Due to the confocal arrangement of the microscope, the area of the sample over which light is collected is the same as that of the illuminated area. So, in order to accurately replicate the scanning of the beam in the modelling, the model must be solved for Gaussian foci in a number of positions, and for each

of these models, the data extraction procedure needs to be modified accordingly (i.e. a new logical matrix of elements must be created for illumination which is off-centre from the axis of the sample, figure 5.7.6)[§]. Once this is carried out for a number of points and the intensity for each point of focus is calculated by summing the elements in the 3D array 'M', we can fill in the elements of a 2D array with the quantity $F_{total}(x, y)$ which is analogous to an image from a scanning confocal microscope. To perform a quantitative comparison between experiment and theory, the experimentally-produced image of fluorescence enhancement from a single structure is integrated up to a radius of 480nm where the intensity approaches that of the background (memory restrictions were also taken into consideration when deciding on this value). This is calculated by assuming $F(r)$ is comprised of trapezoidal elements, each of which can be represented by a linear function. These linear functions are integrated independently over each radius interval using the following expression to produce a solid of revolution.

$$\begin{aligned} S &= 2\pi \int_a^b rF(r)dr \\ &= \left[2\pi \frac{m}{3}\left(b^3 - a^3\right) + \frac{c}{2}\left(b^2 - a^2\right)\right] \end{aligned} \tag{5.7.1}$$

where a and b are the limits of r for each trapezoidal element, $F(r)$ is the integrated intensity as a function of scanning beam position (a linear function in each region) and m and c are the gradient and intercept of the linear function (this trapezoidal approach was proposed by GZ).

This calculates the integrated intensity for the discrete, concentric radius ranges which are set by the points exported from the finite-element model. These are simply summed to produce the total integrated intensity which is equivalent to the total integrated intensity measured experimentally. The same procedure is carried out for the theoretical results and the numbers are compared. This procedure has been carried out for the following structures:

Tower	Pagoda
Composite	Composite
Large	Large
Small	Small
Background	

For each of these structures a different array needs to be designed to accurately replicate the dye region. For the background, the dye region was a uniform layer which was scanned up to a radius of 480nm. This is the value that the other models will tend towards as the Gaussian focus is moved away from the structure.

[§]We assume (based on confocal observations) a similar response for the beam scanning in the directions of the incident electric and magnetic fields in order to reduce computational time by a factor of approximately 6.

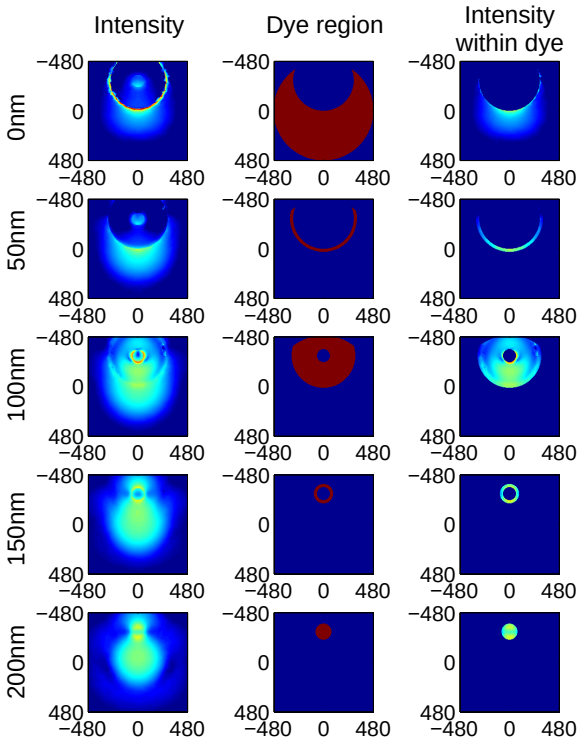

Figure 5.7.6: The three columns demonstrate the manner in which the intensities in the dye regions are selected for the specific case of a tower structure illuminated 290nm from the centre of the structure. The first column shows the modelled intensity plotted on a logarithmic colour scale of cross sections in the x-y plane at a number of positions on the z-axis (these heights are indicated). The second column shows the regions where dye exists (calculated using the algorithm discussed above), and the third column shows the intensities in those regions where dye exists with zero intensity elsewhere.

For the tower structure, the integrated intensities as a function of focus position (radial position from the centre of the structure) is shown in figure 5.7.7.

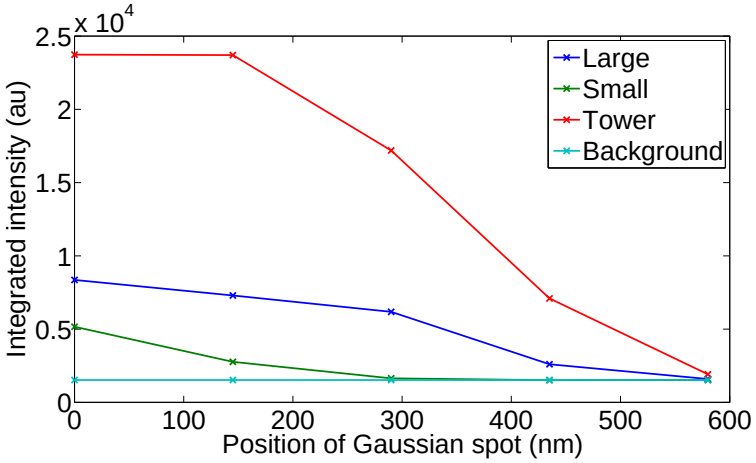

Figure 5.7.7: Simulated integrated intensity as a function of radial position of Gaussian beam with respect to the centre of the structure for a tower structure.

When these lines are used to calculate 2D conical integrals for the tower structure and its constituents the following results are obtained:

Structure	Conical integral
Large	4.20×10^9
Small	1.88×10^9
Tower	11.5×10^9
Background	1.61×10^9

This clearly demonstrates that the composite structure produces near fields, which, when integrated over the dye-volume are considerably stronger than the constituent elements when studied separately.

Here we define several quantities which are used in order to better understand the enhancement quantitatively.

5.8 Enhancement factors (experimental and simulated):

The background intensity (where there are no metal structures) is given by:

$$S_B = 2\pi \int_0^R rF(r)dr = qI_0\pi R_0^2 \tag{5.8.1}$$

where $F(r)$ is the measured signal, q is the quantum yield (i.e. the probability of an absorbed photon producing a fluoresced photon), I_0 is the uniform intensity of the background and R_0

is the integration radius. For the small disc the intensity can be approximated as a top hat function (this analysis was carried out in collaboration with GZ):

$$S_S = q\left(I_S \pi r^2 + I_0 \pi \left(R_0^2 - r^2\right)\right) \tag{5.8.2}$$

were I_S is the uniform intensity at a point directly above the centre of the small disc and r is the radius of the top hat function (i.e. the radius of the small disc). We can normalise this fluorescence as follows:

$$\Sigma_S = \frac{S_S - S_B}{S_B} \tag{5.8.3}$$

and the enhancement factor is:

$$G_S = \frac{I_S}{I_0} = \Sigma_S \frac{R_0^2}{r^2} + 1 \tag{5.8.4}$$

Although this enhancement factor can easily take very large values, there is the potential for large errors due to the assumption of a top-hat functional form of the intensity of the small disc.

Similarly, for a large disc on its own, the fluorescence signal is:

$$\Sigma_L = \frac{S_L - S_B}{S_B} \tag{5.8.5}$$

and the enhancement factor is therefore:

$$G_L = \frac{I_L}{I_0} = \Sigma_S \frac{R_0^2}{R^2} + 1 \tag{5.8.6}$$

where R is the radius of the large disc ($R \simeq D/2 \simeq 300$nm), and hence its associated top-hat function. It should be noted that the top-hat approximation is more accurate for large discs than small discs as we are closer to the regime of ray-optics.

The enhancement of the composite nanostructure is shown below in terms of the measured fluorescence signals for the large disc and the nanostructure.

$$G_{NS} = \frac{R_0^2}{r^2}\left(\Sigma_{NS} + \Sigma_L\left(\frac{r^2}{R^2} - 1\right)\right) + 1 \tag{5.8.7}$$

These quantities can now be calculated from experimental data using the top-hat approximation, and from simulated results using the method of conical integrals. The main results are listed in the table below:

Enhancement factor	Experimental	Simulated
G_S	29.7	17.8
G_L	0.4	5.5
G_{NS}	885.5	458.9
G_{casc}	29.8	25.8

The quantity G_{casc} is the "cascaded" enhancement and is simply $G_{casc} = G_{NS}/G_S$. These values have been plotted on a logarithmic scale (figure 5.8.1). It can be seen that there are discrepancies between the modelling and experiment, particularly for the enhancement factor for the large structure, but as discussed before this is likely to be due to fluorescence quenching by the dye's close proximity to the metal.

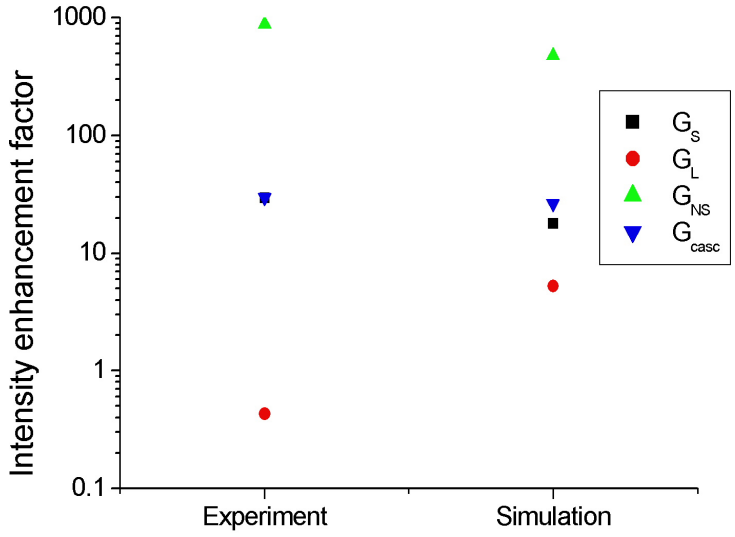

Figure 5.8.1: Intensity enhancement factors for the tower structure. Values are shown for both experiment and modelling.

Figure 5.8.2 shows the intensity ($|\mathbf{E}|^2$) profiles for the tower structure with the small and large particles aligned concentrically and its two constituents. The field is plotted on a logarithmic colour scale to retain detail over several orders of magnitude.

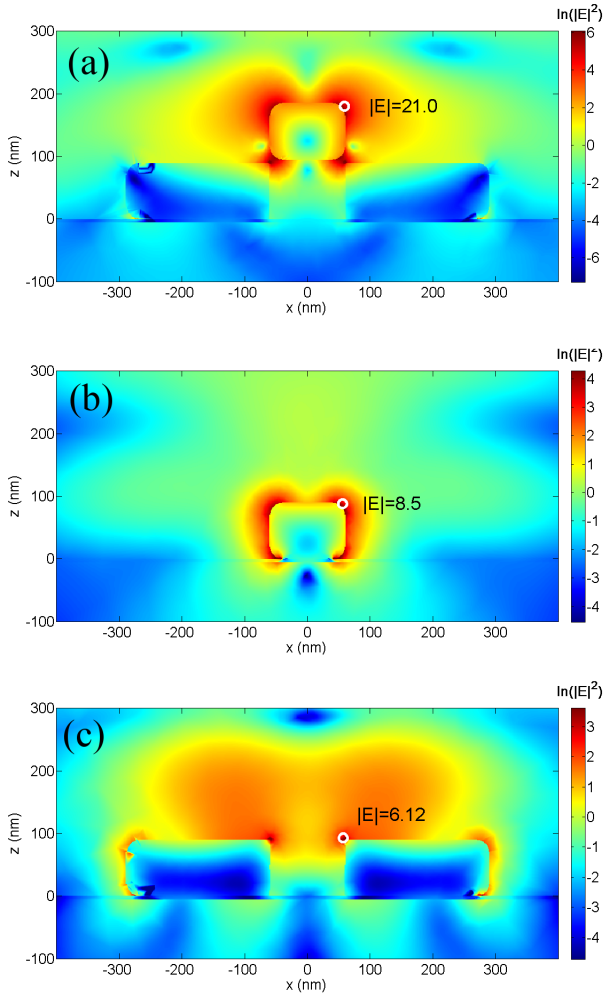

Figure 5.8.2: Intensity profiles ($|\mathbf{E}|^2$) in a cross section through the centre of (a) the tower structure, (b) a small disk and (c) a large disk with a hole through the middle. The plane of the cross-section is the plane containing the incident E-field and k-vector. Each logarithmic colour scale is normalised to the maximum and minimum intensities in its particular plot, and all the numerical values are normalised to the incident Gaussian beam. The positions of the maximum intensities are also indicated and their associated field strengths labelled.

5.9 Pagoda structures

A similar study was carried out for the pagoda structure and the final enhancements are shown in figure 5.9.1.

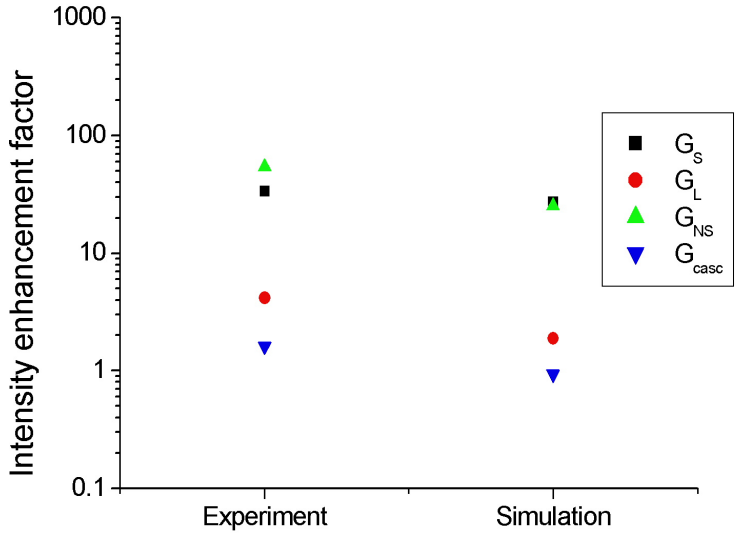

Figure 5.9.1: Intensity enhancement factors for the pagoda structure. Values are shown for both experiment and modelling.

Although the enhancements are not as high as those of the tower, the fabrication technique allows variables to be adjusted relatively easily. One variable we varied was the centre-to-centre distance between the small and large discs. In order to investigate this system with one sample, we designed a moiré pattern whereby an array of large discs was fabricated in a square array, and the small discs were produced on top but with a slightly different lattice spacing so that in one corner of the grid the two discs are coincident, and in the other corner they are perfectly misaligned. This enables us to study the enhancement of the single discs, aligned structures and every position in between. The fluorescence confocal microscopy image of this sample is shown in figure 5.9.2 along with SEMs of the structures (this was carried out in collaboration with GZ).

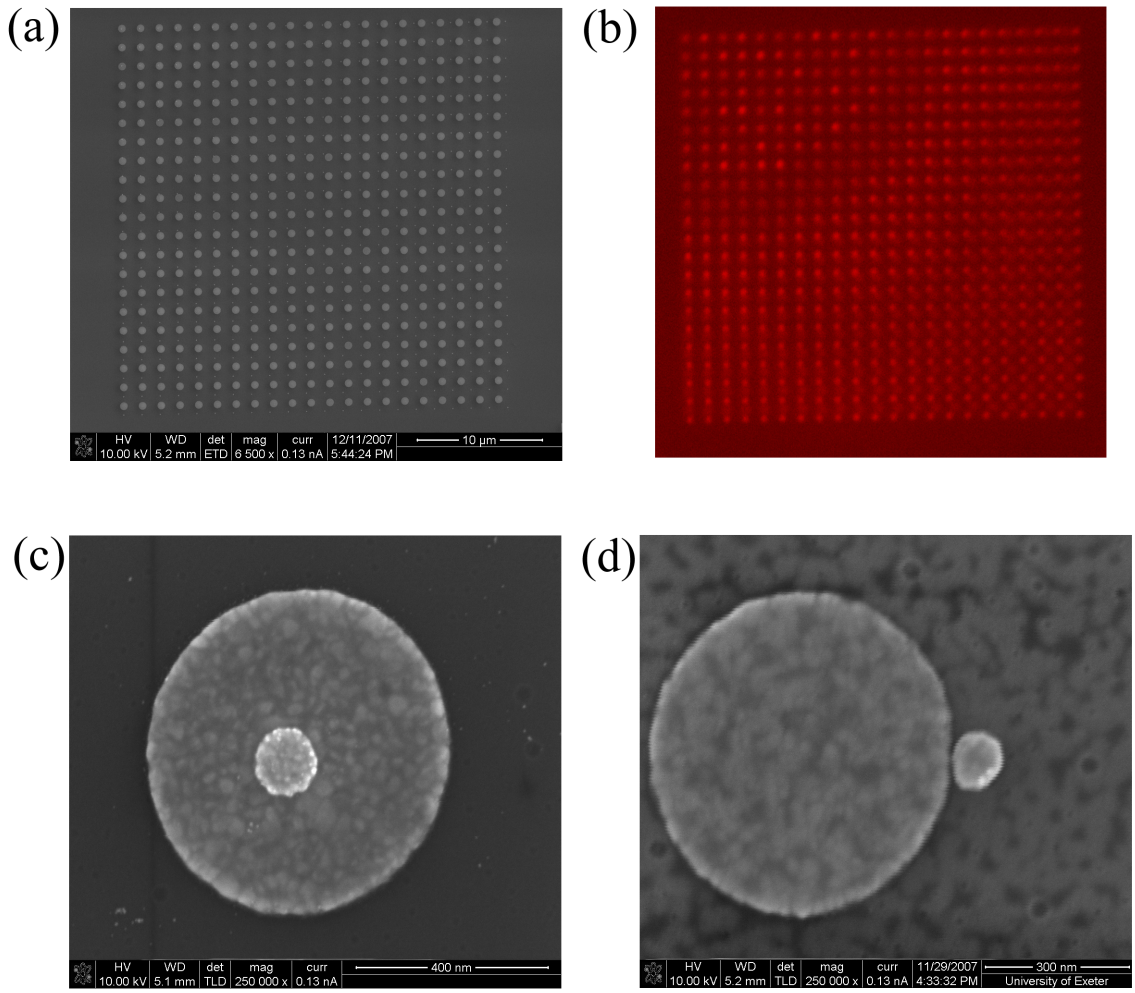

Figure 5.9.2: (a) an SEM image of a moiré pattern consisting of large discs (r = 300nm) and small discs (r = 100nm) with slightly different lattice vectors. When the two discs are concentric, the pagoda structure is constructed. The size of the array is approximately 40μm and the two lattice vectors were carefully chosen so that in the top left corner the particles are directly overlapping, and in the bottom right they are perfectly misaligned. (b) shows a fluorescence confocal microscope image of the moiré structure. (c) shows a pagoda structure whose small particle is nominally aligned with the centre of the large one. (d) shows the very close separation which can be achieved using a two-stage lithography procedure with a dielectric layer.

It can be seen by comparing the SEMs with the confocal images in figure 5.9.2 that when the particles are completely misaligned the enhancement of the small particle is much stronger than the large one (i.e. in the bottom right corner — this is clearer on screen than when printed). It should be noted that the metal thickness is less than the tower structure and there is a dielectric layer on top of the large disc which prevents the fluorescence quenching which was seen in the tower case. As the particles are brought closer together, the fluorescence intensity increases considerably and then suddenly drops off. The exact mechanism which causes this effect is not known, but it occurs when the particles are slightly overlapping, so it could be that the resonant frequency of the system is shifted due to the proximity and hence moved

away from the laser wavelength. Also, the geometry of the small disc is likely to be very different (see figure 5.9.3) as it will have been formed on a non-planar surface (i.e. on the edge of the large disc). Once the small disc is close to being directly above the large disc the field enhancement can reach its maximum but it can be seen in figure 5.9.2b that there is a lot of variation in the top left region of the array. It is likely that this variation is simply due to a combination of the error in the actual position of the small discs relative to the large discs and the likelihood of this position being able to produce interactions which produce strong near-fields. This variation highlights the need for a number of structures to be analysed and an average taken. This was carried out for all the data shown in the previous section (the fluorescence intensity from 36 nominally identical particles was measured and averaged).

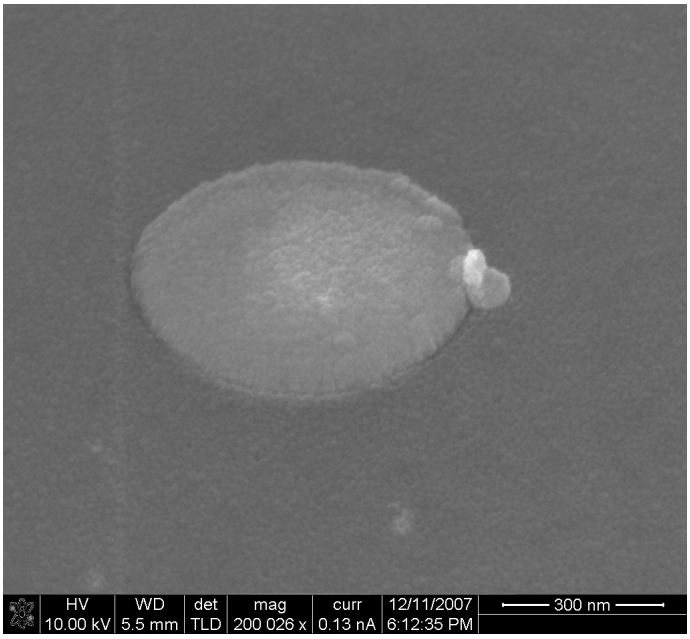

Figure 5.9.3: An SEM image of a small disc created on the edge of a small disc (separated by a dielectric layer). The geometry of the small disc is highly modified. This SEM image was taken with a tilted stage in order to view the structure at oblique incidence.

The field profiles were calculated in exactly the same way as for the tower case. These are shown in figure 5.9.4 with the maximum values of $|\mathbf{E}|$ indicated.

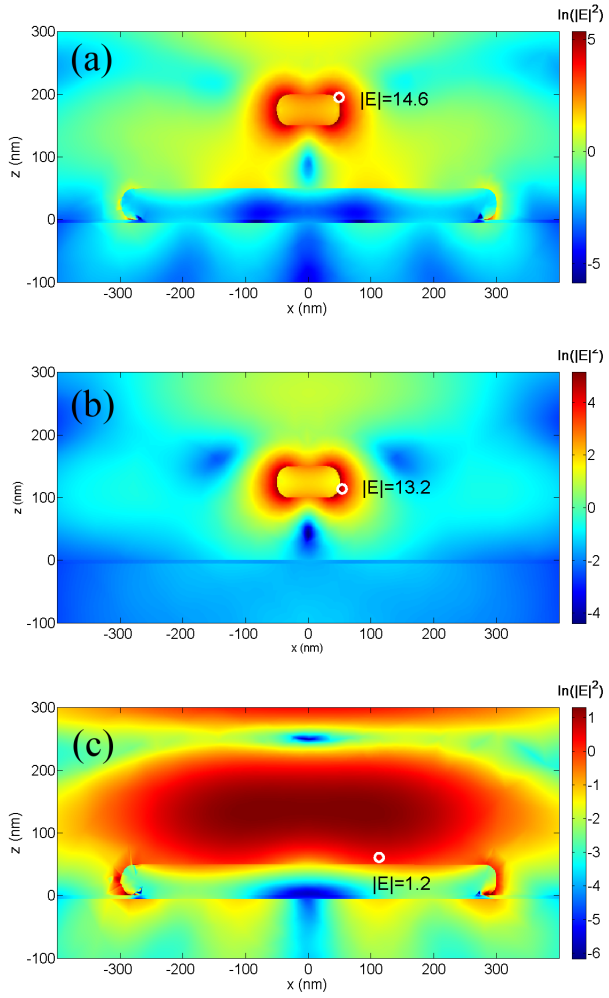

Figure 5.9.4: Intensity profiles ($|\mathbf{E}|^2$) in a cross section through the centre of the pagoda structure, a small disc and a large disc. The plane of the cross-section is the plane containing the incident E-field and k-vector. Each logarithmic colour scale is normalised to the maximum and minimum intensities in its particular plot, and all the numerical values are normalised to the incident Gaussian beam. The positions of the maximum fields are also indicated

5.10 Triple structures

As a starting point in attempting to produce even stronger field enhancements, it was decided that it would be desirable to first clarify a point regarding the *cascaded* enhancement (i.e. the enhanced fields of one particle excite another and so on) of the two-tier system. Although our initial work was based on a concept proposed by Li *et al.*,[27] using two tier structures does not address the question of whether the enhancement is really cascaded as there is only one cascade in the system. To see whether the effect iscascaded, rather than simply a two-particle interaction, three-tier structures were produced. These are very similar to the tower structures, but they have a very small particle on top of the smaller disc of the two-tier structure, separated by a thin dielectric spacer layer. The first two layers were fabricated by

collaborators in Manchester in the same way as a tower structure, but the third and smallest disc was fabricated by a further EBL procedure, thus producing a 30nm diameter particle on top of the middle disc (which previously was the small one). This new small disc is supported on a layer of HfO_2 which has a thickness of $\sim$ 7nm. The size of this smallest disc is close to the grain-size of thermally evaporated gold, so experimentally it only approximates to a disc, but as the EBL process makes nominally prismatic structures the term 'disc' will continue to to be used.

This structure was probed experimentally using conventional fluorescence microscopy and surface enhanced Raman spectroscopy[¶] by our collaborators in Manchester working in conjunction with Philipp Klar and Cinzia Casiraghi at the Free University of Berlin. Raman spectroscopy is extremely sensitive to high fields (the Raman enhancement is approximately proportional to $|\mathbf{E}|^4$).[12] The enhancement in SERS is due to the structure producing very high local fields. The fields are even stronger for the case for the triple structure than the double structure. Only the triple structure produces a distinct Raman spectrum, indicating that the extra cascade is important in the overall enhancement.

In contrast to measuring the integrated fluorescence enhancement, modelling for Raman enhancement is concerned with the field at the point at which the molecule is located. As we do not know the exact positions of all the molecules, we instead assume in this thesis that there is one molecule at the position of the highest field, so therefore we calculate the highest field in the region at which the Raman molecule resides. It was realised that there is a very sensitive dependence of the field enhancement on the thickness of the spacer layer underneath the smallest particle. Electric field plots of the triple-structure are shown in figure 5.10.1 for a range of spacer thicknesses t (the plane shown is a cross-section through the centre of the structure and contains the incident electric field and $\mathbf{k}$-vector).

[¶]This is where the vibrational and rotational modes of molecules are observed in an emission spectrum and the emission due to these modes is greatly enhanced by the presence of metal structures.

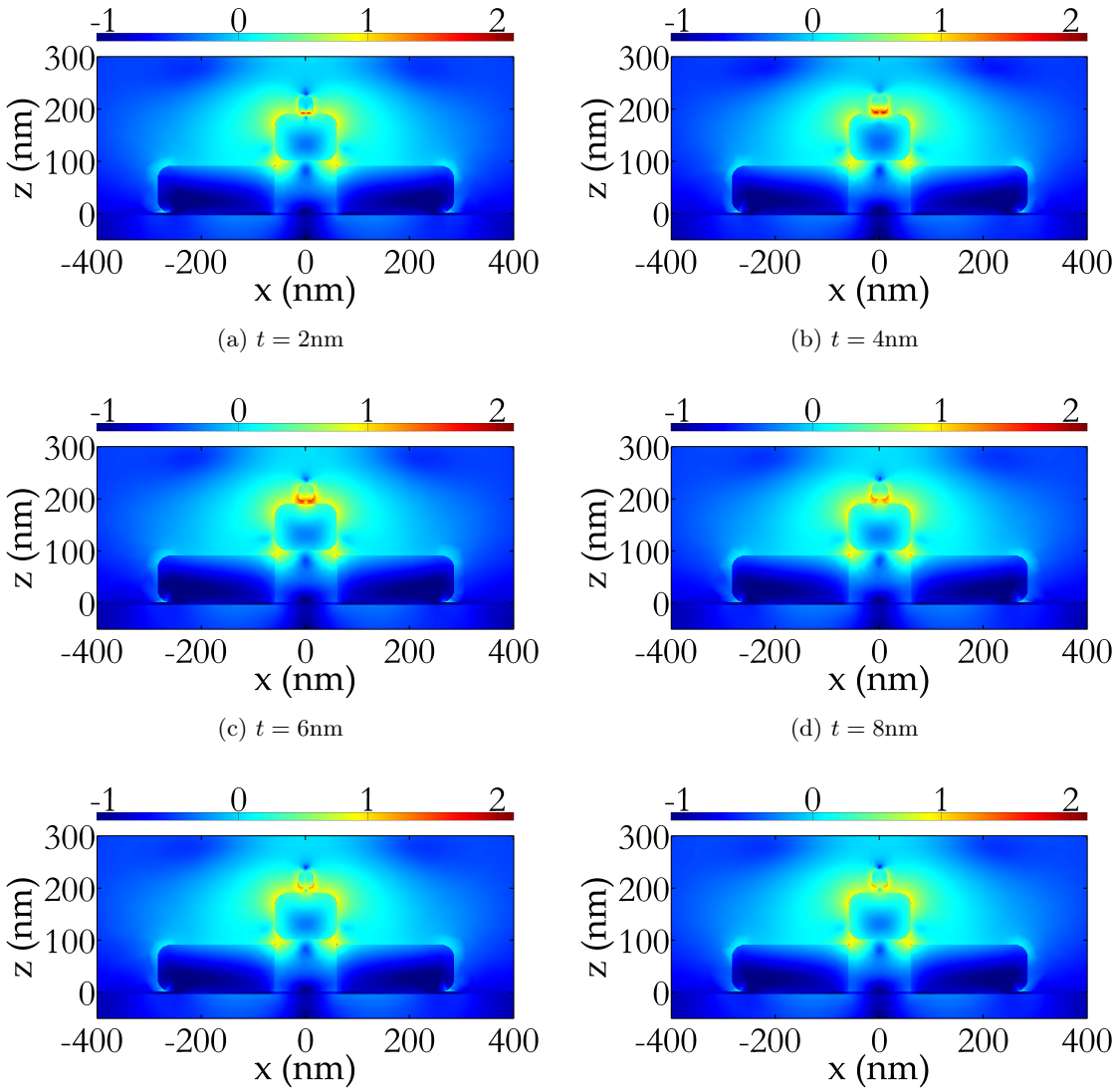

(a) $t = 2$nm

(b) $t = 4$nm

(c) $t = 6$nm

(d) $t = 8$nm

(e) $t = 10$nm

(f) $t = 12$nm

Figure 5.10.1: Simulated electric field plots ($\log_{10} |\mathbf{E}|$) of triple-structures for a range of thicknesses of the spacer layer underneath the smallest particle. It can be seen that the strongest fields occur when the spacer thickness is between 4 and 6nm.

In order to quantify the maximum field enhancement, the field magnitudes are averaged over a spatial region 1nm in extent, and the maximum value of this averaged field (which occurs in a region where the dye can physically exist) is stated here as the maximum field enhancement. For the plots shown in figure 5.10.1 (and a number of others), the maximum field enhancements have been plotted to demonstrate the dependence on the spacer thickness (figure 5.10.2)

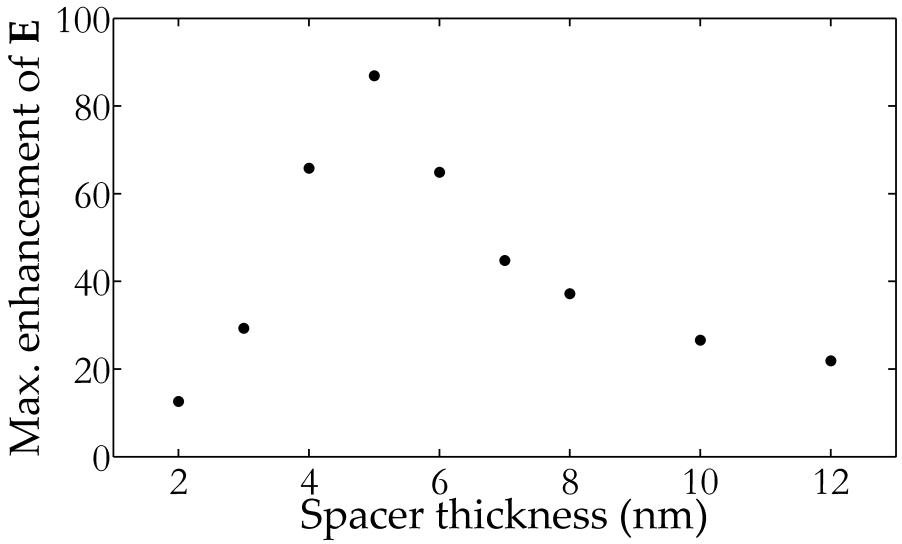

Figure 5.10.2: The dependence of the maximum field enhancement on the thickness of the HfO_2 spacer layer. The peak occurs for a thickness of 5nm.

This shows considerable sensitivity in the thickness and calls into question the validity of the models in describing real, fabricated structures. For example, in a real experiment there could be rough spikes of metal at the bottom of the small particle which could increase the intensity still further. Having said this, these models have been designed to be as realistic as possible (within the confines of computational power). It is hoped that the values of maximum enhancement these models produce correlate with experiment. All metallic edges in the models are rounded and all extracted fields are averaged over small volumes to avoid numerical noise which could lead to an over-estimate of the local field.

At the optimum spacer thickness (t = 5nm), the profile of the electric field magnitude has been plotted

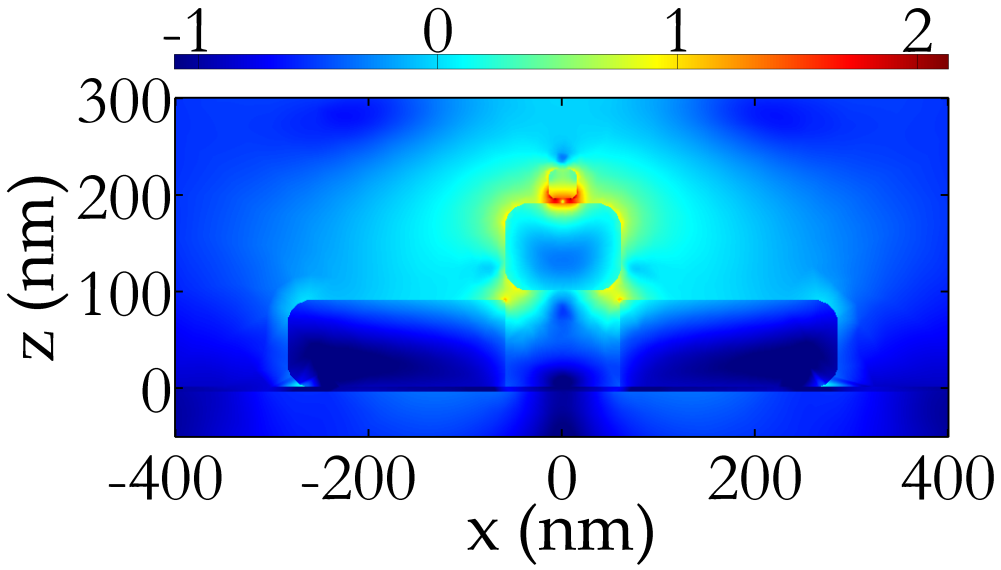

Figure 5.10.3: A simulated electric field plot ($\log_{10}|\mathbf{E}|$) of a triple-structure with optimum thickness of the spacer layer underneath the smallest particle. The highest fields are in the vicinity of the smallest particle.

It can be seen that very high fields exist in the region under the small particle, and it is suspected that the dye molecules are close to that location in order to produce a measurable Raman signal.

In order to further demonstrate the cascaded nature of this enhancement, the near-fields of the constituent structures have also been modelled. These fields are shown in figure 5.10.4.

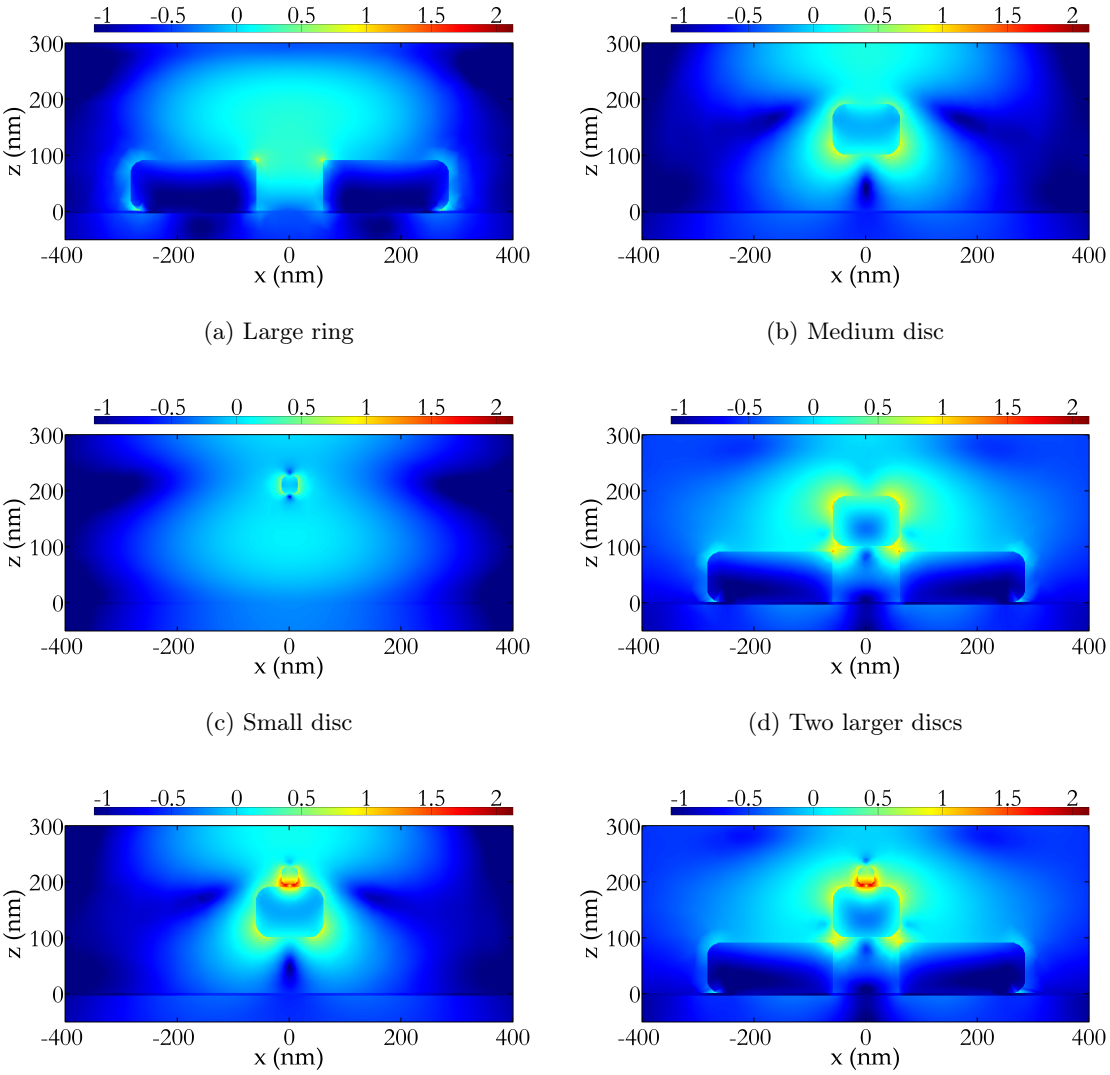

(a) Large ring

(b) Medium disc

(c) Small disc

(d) Two larger discs

(e) Two smallest discs

(f) Triple structure

Figure 5.10.4: Simulated electric field ($\log_{10} |\mathbf{E}|$) plots of the constituents of the triple structure as a comparison. The thickness of the spacer layer under the smallest particle is 5nm.

The maximum fields in the regions outside of the gold, HfO_2 and overexposed PMMA for the structures shown in figure 5.10.4 are summarised in the table below:

Structure	Maximum field enhancement
Large ring	6.5
Medium disc	8.8
Small disc	4.9
Two largest discs	16.7
Two smallest discs	71.8
Triple structure	86.9

It can be seen that the majority of the enhancement of the triple structure is due to the interaction of the two smallest discs (probably they are being excited close to resonance). The next natural progression following on from this is to simulate the response of a quadruple structure — the same as the triple structure but with an even smaller particle placed on top (again separated by a dielectric, though thinner than before). The electric fields of such a structure are shown in figure 5.10.5, where the smallest particle has a radius of 5nm and is separated from the next-smallest particle by a 1nm layer of HfO_2.

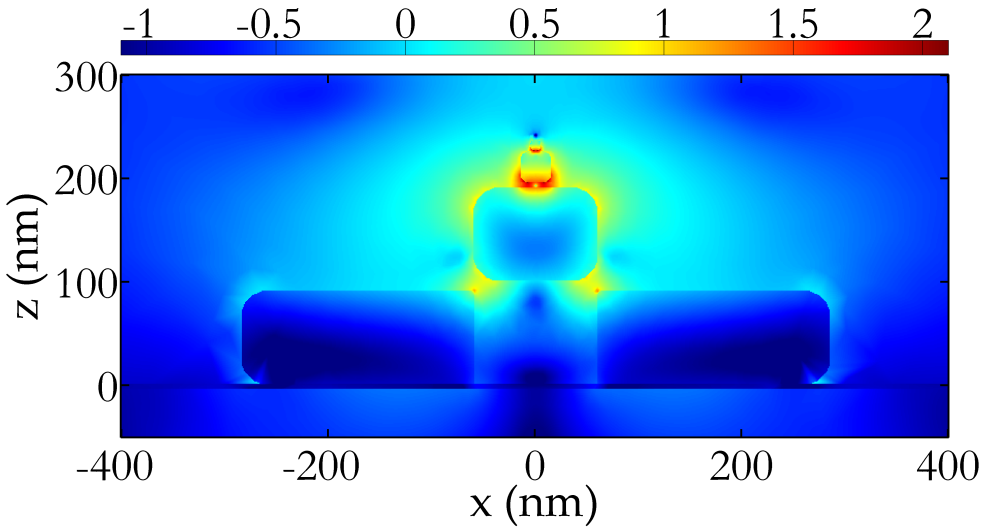

Figure 5.10.5: A simulated electric field plot ($\log_{10}|\mathbf{E}|$) of a quadruple-structure with a 1nm spacer layer underneath the smallest particle, which has a radius of 5nm.

Although preliminary modelling does not show an increase in the maximum field from such a structure, it is comparable, and with further optimisation, this field could be increased further. The field averaging procedure may also need to be modified, as the curvature of the smallest disc is such that the $1nm^2$ area intersects the metal, in which the field is much smaller, and hence reduces the averaged value. This will hopefully lead the way to a more optimised representation of the effect predicted by Li *et al.*

5.11 Summary

In this chapter, it has been shown that composite nanostructures comprising metallic discs and dielectrics can produce strong local fields when illuminated with light. These strong near-fields have been probed experimentally by measuring the integrated fluorescence enhancement from a dye-doped PMMA film which is coated on the structures, and a novel procedure has been utilised to perform numerical calculation and extract the data in order to best represent the experimental conditions. Although the 'tower' structure provided a stronger field enhancement

that the 'pagoda', the pagoda provides a flexible method for producing new, 3D structures. The distance dependence of the two discs in the pagoda structure has been probed experimentally, and this has demonstrated regimes in which the field enhancement is greatest.

Finally, the local fields of triple structures have been calculated in order to demonstrate that the fields are stronger than the double-structures, and hence has led to the experimental observation of a strong Raman signal.

Chapter 6

Conclusions and future work

6.1 Conclusions

In this thesis, original work has been presented which has been the result of investigations into the optical response of metallic nanoparticles in isolation, in arrays, and in composite metal-dielectric structures, with particular attention paid to resonant plasmonic modes of nanoparticles, modes that can be modified in the presence of other nanoparticles.

In the consideration of the optical response of individual metallic nanoparticles, Mie theory has been used to better understand not only the dipolar plasmonic mode of metal spheres, but the higher-order modes, particularly the quadrupolar modes. The effects of changing the particle size, material and surrounding medium have been investigated with a view to applying this knowledge to other geometries which have similarities in their response, for example, discs. Gold discs have been fabricated for this study by electron-beam lithography (EBL), and their scattering spectra have been acquired for a range of disc radii for a fixed thickness using dark-field spectroscopy. It has been shown that the plasmonic modes of these discs can be qualitatively understood by comparison with finite-element method (FEM) modelling which has allowed field plots to be used in order to identify the modes which correspond to the peaks in the scattering spectra.

Due to the later use of several numerical techniques, these techniques have had their validity tested against Mie theory. For spheres similar to those used throughout this work, the absorption, scattering an extinction have been plotted as calculated by finite-element modelling, an empirical polarisability function and Mie theory. It is seen that FEM provides a reasonable agreement with Mie theory for the particles chosen across the spectral range considered. The Kuwata polarisability function suffers from the fact that it only describes the dipolar mode and hence higher order modes are simply not present in the spectra. Also, large spheres ($r > 50$nm) are not accurately described due to limitations of the implementation of dynamic depolarisation and damping effects in the empirical function.

It has been demonstrated that the resonance wavelengths of higher order modes are comparable to an integer number of wavelengths of surface plasmon polaritons (SPPs) which can oscillate around the circumference of a sphere. This analysis was carried out by calculating the surface plasmon wavelength using the dispersion relation and plotting the incident wavelengths which would excite continuous standing waves on the surface of the sphere. This representation is analogous to the Bohr model of the atom. When compared to the analytical results from Mie theory, the agreement is good for higher-order modes, but poor for the dipolar mode due to the curvature of the surface.

A regime of strong forward scattering has been observed for metallic spheres which can support both dipolar and quadrupolar modes, for example a 100nm diameter silver sphere surrounded by glass. In this regime, at the frequency of the quadrupolar mode, there is still a contribution to the scattering spectrum from the dipolar mode. It has been shown that while the dipolar and quadrupolar modes both scatter strongly in the forward and backward directions, the phase relation between them is such that there is constructive interference in the forward direction and destructive interference in the backward direction, which leads to very strong forward scattering and weak backward scattering.

For the work presented here, a new code has been prepared in order to implement the coupled dipole approximation (CDA) with the intention of modelling non-periodic arrays of nanoparticles which support only dipolar modes. As a test of its accuracy, a comparison was made with FEM which demonstrated broad agreement with the exception of the diffractive features in the spectra of arrays with large array periods. Following this agreement, the technique was used to investigate arrays which cannot be modelled by FEM, namely random arrays of nanoparticles.

The random positions of particles were generated numerically with a parameter r_{min} which controlled the minimum separation between the particles. These positions and the empirical polarisability function were used to calculate the dipole moments of the particles in the random arrays and these calculated dipole moments have been used to calculate the extinction, scattering and absorption of the arrays. A script was written to place the random positions of the particles into a file which is readable by the EBL software used here (Raith's Elphy Quantum). By this method, a sample can be produced where the positions of the particles are nominally identical to those analysed by the CDA. In comparing experiment and CDA results, ordered arrays were also fabricated as references. Qualitative agreement was achieved in comparing the ordered arrays (a blue shift for smaller particle separations was observed), and the diffractive features seen experimentally were better described by the CDA than FEM. For random arrays, both the particle density and r_{min} were varied and generally speaking a blue shift was observed when the particles were closer together, combined with spectral broadening. It was seen that for fairly sparse arrays (particle density $6.25\mu\text{m}^{-2}$), an increase in the value of r_{min} provided a sample whose spectra are measurable, but the interactions between the particles are weak and incoherent. This led to the possibility that the extinction of a single

particle (which cannot be measured using conventional optical systems) can be inferred from a carefully specified pseudo-random array of identical nanoparticles which produce a measurable signal.

As well as optical far-field quantities, the dipole moments can also be plotted onto a 2D map of the sample, thereby showing the strength and direction of the dipole moment of each particle at that particle's position. This has been animated and the time-resolved dipole interactions can be observed.

In producing arrays of particles where the density is relatively high, it has been observed that the particles at the centre of the arrays are larger than those at the edges due to the broad Gaussian profile of the electron beam contributing to the exposure of regions of the resist other than those it is actually writing. This issue has been mitigated somewhat by a scheme in which the exposure of each particle in an array (random or ordered) is initially calculated and then a dose-scaling factor is calculated for each particle by inverting the interaction matrix. This scheme neglects the finite size of the particles and the sensitivity of the resist and it is necessary to know the Gaussian width, but it works to a first approximation with limited success.

Experimental data in the literature provided an interesting result regarding the interaction of colloidal silver spheres which supported quadrupolar modes. It was observed by Malynych and Chumanov that, for certain particle densities, the optical density exhibited a single, strong peak at the wavelength of the quadrupolar mode. This was attributed to in-plane coherent interactions between the quadrupolar modes which produce a "cooperative plasmon mode". This explanation was based on symmetry arguments. Modelling carried out as a part of this thesis along with clear physical arguments demonstrate that the explanation proposed by the authors of the experimental work is erroneous. FEM modelling has demonstrated that the same far-field response can be produced by a square-array of identical spheres. Further investigations into the near-field profiles of the spheres demonstrate that no quadrupolar mode exists in the plane of the array due to a lack of phase retardation in this plane (this agrees with the discussion of single particles). It is also demonstrated that as the array period is reduced so that it approaches the particle density in the experimental work, the dipolar mode shifts to the blue, but the quadrupolar mode does not shift at all (at least any shift is not detectable). Eventually, there is a superposition of the spectral features of the two modes and the optical density increases considerably. This leads to the conclusion that the dipolar mode is blue-shifted to the point that it overlaps with the quadrupolar mode and hence only a single peak is observed, and it is significantly stronger than either peak before they became overlapped. Further attention was paid to the experimental results concerning the angle-dependent response of a similar array for both polarisations. FEM modelling has demonstrated a similar response, and the physical descriptions which were successfully applied to the sample when illuminated at normal incidence have been applied to oblique angles of incidence as well, though it was noticed that a labelling error may have been apparent in the experimental work which led to the wrong analysis of the two polarisation states.

Finally, the near-field response of composite structures has been analysed with the purpose of producing strong local fields which can be used for fluorescence enhancement measurements and surface enhanced Raman spectroscopy (SERS). This work was carried out in collaboration with colleagues here at Exeter and at the University of Manchester. The samples investigated here are large metallic discs with small discs concentrically above them and separated by a dielectric spacer. Variations on this geometry have also been investigated (all are fabricated using novel extensions of EBL). The samples produced large fluorescence enhancement when probed using fluorescence confocal microscopy. Modelling this system poses problems because the illumination is Gaussian in nature but the beam scans across the sample. Furthermore, the dye exists in a layer whose exact topology is not known. The topology is estimated, and once the model is solved, the total intensity is integrated throughout this volume to provide an indication of the intensity of the fluoresced intensity with the beam in that position. The model is also run for other positions of the Gaussian focus, and a further integration technique is used to approximate the spot observed in the image produced by the scanning confocal beam. Good agreement with the experimental data was produced and in cases where agreement was lacking, physical explanations were able to explain the discrepancy (e.g. fluorescence quenching near a metal surface which cannot be modelled classically). A further study of a tower structure comprising three discs, fabricated by collaborators, examined the high fields that led to a strong Raman signal. The enhancement required to observe the phenomenon experimentally was in broad agreement with calculations performed using FEM.

6.2 Future work

There are a number of aspects of this work which could form the bases of new investigations. On the technical side, I have highlighted the difficulties associated with dark-field spectroscopy, and I would like to propose that an alternative, optical arrangement would produce more flexibility in the illumination conditions available and would enable models to more accurately represent the experimental configuration. This suggestion is to collimate the beam emerging from a fibre,and use this light to illuminate the sample at any angle and with any polarisation. This way, even though the collection optics will remain largely unchanged, there is ultimate flexibility in illumination which is simply not possible with a fixed dark-field condenser lens. Furthermore, a very basic optical arrangement should be used to avoid the light-leakage problems which have resulted in errors in transmission measurements using a microscope.

It is hoped that the technique proposed to infer single-particle extinction spectra from pseudo-random arrays will be applicable to more exotic geometries such as metamaterial elements (e.g. split-ring resonators) as once the extinction spectrum of one element is known, it is far simpler to use that element to deterministically construct new materials.

Details have been given regarding the preferential forward-scattering of single nanoparticles which can support quadrupolar modes. It is conceivable that such particles could improve the

efficiency of solar cells if they were placed on top of the semiconductor (plasmonic enhancement of solar cells has, so far, been achieved using different methods,[123–126] though the use of the quadrupolar mode has been suggested[127]). Furthermore, in order to cover a broader wavelength band, a unit cell could be used which contains four particles of two different sizes. Each size of particle could produce a scattering cross-section which on resonance is as large as the unit cell. Therefore, the two particles which have different resonant frequencies will scatter the light as efficiently as possible at two separate wavelengths. Clearly from the discussion above, this type of dense array will act to shift the resonances, so the particle sizes and geometries will have to be carefully selected.

An interesting phenomenon was discovered serendipitously when an array of silver nanoparticles was fabricated and, during the lift-off procedure, a number of nanoparticles were accidentally removed from the substrate. Upon imaging this array under dark-field illumination, it was seen that the regions where the particles were missing produced very strong scattering (see figure 6.2.1). It should be noted that the sample was prepared for SEM imaging before the dark-field image was obtained. This involved a 1nm Au-Pd film being sputtered onto the sample to make it conductive. Similar dark-field images have also been produced where no conductive layer was present so the Au-Pd film was not thought to be a cause of the effect. Without the defects, all the plasmons in the array (with the exception of the edges) are oscillating coherently and hence there is no scattering* When one particle is removed, however, this coherence is interrupted and the modification to the local field configuration is transferred to the far-field in the form of strong scattering. A possible future experiment could be to produce scattering spectra from the defects and observe changes in the spectral shape as a function of particle separation. This should enable the experimenter to determine whether the spectral response can be modified in new ways.

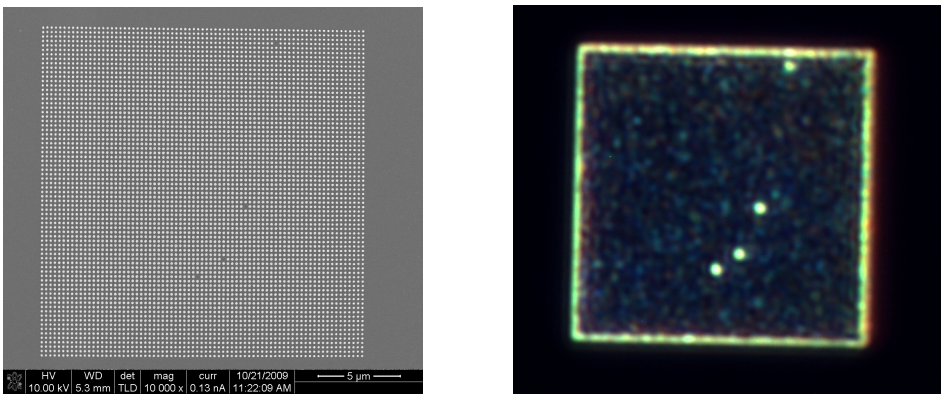

(a) (b)

Figure 6.2.1: Arrays of metal nanoparticles with missing particle exhibit strong scattering at the site of the vacancy. The missing silver nanoparticles in the array shown in the SEM (a) produce the scattering shown in the dark-field image (b). The nanoparticles are silver discs and have a thickness of 100nm and a nominal diameter of 100nm. Note that similar arrays of thinner discs (30nm) did not show such strong scattering.

*In reality, there is some scattering and this is due to inhomogeneities in the geometries of the particles.

The use of the CDA in conjunction with electron-beam lithography could provide a direct comparison of experiment and modelling for *aperiodic* arrays similar to the work carried out by L. Dal Negro and colleagues.[128,129]

It is hoped that the multiple exposure EBL procedure could produce very small dielectric gaps between metal nanostructures which could produce even stronger near-fields in planar structures than could be achieved with a single lithography run.

Finally, the analysis of the near-fields of composite structures has prompted new ideas of directions in which such structures may be taken. One such structure is based on work by Maier *et al.* and involves placing a small disc on top of a large disc (with a dielectric spacer) and varying the lateral position of the smaller disc in order to break the symmetry. This can facilitate the excitation of quadrupolar modes in the larger disc (FEM data not presented here). Furthermore, placing two smaller discs on top of the large disc (diametrically opposite each other) it might be possible to produce a metamaterial element whereby an obliquely incident beam excites the quadrupolar mode of the disc, and near-field interactions excite opposite dipole moments in the two smaller particles. This can allow an oscillating magnetic field to be generated in the region between the two smaller discs, which could provide the permeability required in metamaterial structures. Broken symmetry and the excitation of Fano[130] resonances in plasmonic structures are rapidly growing areas within plasmonics.[118,131–138]

6.3 Presentations

6.3.1 Publications

- Cascaded optical field enhancement in composite plasmonic nanostructures
  V.G. Kravets, G. Zoriniants, C.P. Burrows, F. Schedin, C. Casiraghi, P. Klar, A.K. Geim, W.L. Barnes, and A.N. Grigorenko
  Physical Review Letters **105** 246806 (2010)

- Extinction and scattering of metallic nanoparticles in ordered and random arrays
  C.P. Burrows and W.L. Barnes
  Proceedings of SPIE Vol. **7757**, 77572I (2010)

- A comparison of techniques used to simulate the scattering of electromagnetic radiation by metallic nanostructures
  J. Parsons, C. P. Burrows, J. R. Samble and, W. L. Barnes
  Journal of Modern Optics **57** 356 (2010)

- Composite Au nanostructures for fluorescence studies in visible light
  V.G. Kravets, G. Zoriniants, C.P. Burrows, F. Schedin, A.K. Geim, W.L. Barnes, and A.N. Grigorenko
  Nano Letters **10** 874 (2010)

- Large spectral extinction due to overlap of dipolar and quadrupolar plasmonic modes of metallic nanoparticles in arrays
  C.P. Burrows and W.L. Barnes
  Optics Express **18** 3187 (2010)

- Localised surface plasmon resonances in periodic non-diffracting metallic nanoparticle and nanohole arrays
  J. Parsons, E. Hendry, C.P. Burrows, B. Auguie, J.R. Sambles and W.L. Barnes
  Physical Review B **79** 073412 (2009)

6.3.2 Conferences

- Extinction and scattering of metallic nanoparticles in ordered and random arrays
  C.P. Burrows and W.L. Barnes
  Poster presentation at SPIE Optics+Photonics, San Diego, USA, August 2010.

- Simultaneous excitation of dipolar and quadrupolar plasmon modes of metal nanoparticles
  C.P. Burrows and W.L. Barnes
  Oral presentation at the CMMP (Condensed Matter and Material Physics) conference. University of Warwick, UK, December 2009.

- Plasmonics and light trapping in photovoltaic cells
  C.P Burrows, C.R. Lawrence and W.L. Barnes
  Poster presentation at Thin Film Photovoltaics, Institute of Physics, London, September 2009.

- Large spectral extinction due to the overlap of dipolar and quadrupolar plasmonic modes of nanoparticles in arrays
  C.P. Burrows and W.L. Barnes
  Poster presentation at Nanometa, Seefeld, Austria, January 2009.

Appendix A

Electron Beam Lithography

Introduction

The study of the plasmonic properties of metallic nanoparticles has accelerated enormously in recent years, and a significant contribution to this progress can be ascribed to developments in nanofabrication. Two main technologies for producing customised arrays of nanoparticles are electron beam lithography (EBL) and focussed ion-beam milling (FIB). Both of these techniques are possible with a modified FEI Nova 600 system which is used throughout this project. EBL is generally used to fabricate particles on substrates, and FIB tends to be used for milling holes in planar films, though either process can in principle be used to achieve both results. Electron beam lithography comprises a number of steps that allow tailor-made samples to be made — these are summarised below, with more details to follow:

1. A glass substrate is thoroughly cleaned to remove dust and contaminants..
2. A photo-resist (PMMA) is spin-coated onto the substrate. This will form the EBL mask.
3. A thin metal layer is evaporated onto the PMMA to make it conductive.
4. The electron beam of a scanning electron microscope (SEM) is used to expose a chosen geometry (which is drawn using a computer) onto the sample. The electron beam breaks the polymer chains in those regions exposed to it, making them more soluble than the unexposed PMMA*.
5. The exposed sample has the silver removed by wet-etching.
6. The sample is developed i.e. the exposed PMMA is removed by dissolving with a suitable solvent.

*A 'negative resist' undergoes cross-linking of the molecules when exposed, and hence produced the inverse pattern upon developing.

7. The metal which is to form the particles is evaporated onto the sample to the correct thickness[†].

8. The remaining PMMA and metal film is removed by gently boiling the sample in acetone.

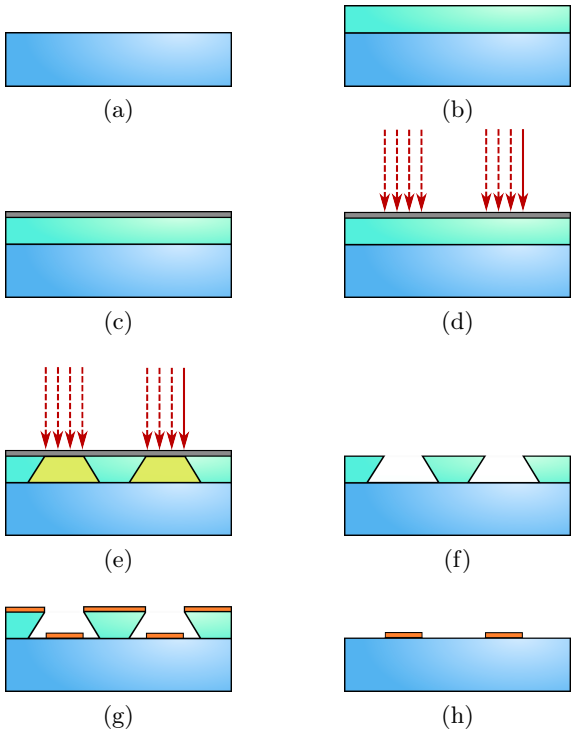

Figure A.0.1: Schematic showing the EBL process. (a) a glass substrate is cleaned, (b) a PMMA layer is spin-coated onto the substrate, (c) a thin layer of metal is evaporated onto the PMMA, (d) the sample is exposed by an electron beam in the regions where the particles are needed, (e) this breaks the polymer chains in those regions, (f) the metal and exposed PMMA are removed chemically, (g) metal is evaporated onto the sample and (h) the remaining PMMA and metal film are removed with acetone and the nanostructures are left behind.

I will now describe each process in more detail.

A.1 Sample cleaning

Glass substrates are cleaned as follows:

1. The substrate is cleaned using cotton buds and acetone to remove any large pieces of dust which may be on the surface. The acetone evaporates quickly so there is no need to dry the sample. This is the only stage which uses cotton buds as they can introduce fibres to the substrate.

[†]For details regarding the effect of different conditions on the quality of the evaporated film see the paper by Liu *et al.*[139]

2. The substrate is then placed in a custom-made PTFE sample-holder which supports the substrate vertically and makes contact with the substrate at the edges only. This sample holder is then immersed in a beaker of nitric acid for approximately 10 minutes.
3. The sample and sample-holder are rinsed several times with ultra-pure water (18MΩcm) to remove all traces of acid.
4. The sample (in its holder) is placed in a beaker of acetone and is sonicated for approximately 10 minutes.
5. The sample is then removed quickly and placed in a beaker of isopropyl alcohol (IPA) in order that the acetone does not evaporate while the sample is exposed to the air.
6. Once sonication in IPA is complete (again, approximately 10 minutes), the sample is quickly dried with nitrogen so that the IPA is not allowed to evaporate and leave drying marks.
7. The sample is placed in a clean perspex box and is put in a vacuum desiccator for storage if it is not required immediately.

A.2 Spin-coating of PMMA

PMMA is available in solid (powdered) form or in a liquid solution. The liquid solution is available in a range of concentrations; 'A2' is 2% concentration, 'A4' is 4% etc.. To produce a thin film of required thickness, we use the technique of spin-coating. This involves placing a few drops of PMMA solution (dissolved in the solvent anisole) on a glass substrate, and spinning it at a particular angular frequency. The spin-coater consisted of a 22mm diameter rotating metal turntable with a hole in the centre through which a vacuum is applied by a rotary pump. This vacuum holds the sample in place throughout the procedure. The spinning motion throws solution from the substrate and an equilibrium is reached at which the cohesive and adhesive forces in the liquid and at the interface balance the outward 'force' due to the rotation, and hence no more material leaves the substrate, and the thickness of the film remains constant. Tables of film thickness are consulted in order to set the correct speed for the desired thickness. There are different tables for each concentration of PMMA — the more viscous, the thicker the film for a given angular velocity. For a thickness of 200nm, a rotational speed of 4,000 rpm is used for PMMA A4. As long as equilibrium is reached, the duration of the spinning is irrelevant. During spinning, Newton's rings can be seen to change as the thickness falls until there is no change in the thickness and the pattern becomes static and hence equilibrium has been reached. This takes less than one minute, but spinning continues for a full 90 seconds in order to ensure uniformity.

After spin coating, the sample is placed on a hot plate at 180°C for approximately 10 minutes to evaporate any remaining solvent in the film and to soften the film for improved surface smoothness.

A.3 Evaporation of metallic over-layer

In order to accurately expose the sample with the electron beam, it is essential that no charge is allowed to build up on the sample when it is in the SEM. If the sample is electrically insulating, then the electrons from the beam will accumulate on the surface, and hence will act to deflect the beam. This is overcome by evaporating a layer of silver or gold onto the surface of the PMMA, and a metal clamp ensures that this surface is earthed.

The process of thermal evaporation is as follows:

1. The sample is placed face-down at the top of a vacuum chamber.
2. At the bottom of the chamber, the metal is placed in a boat or filament which is relatively inert and has a very high melting point (usually tungsten or molybdenum).
3. The system is evacuated to approximately 6×10^{-6}mbar by means of a rotary pump and either a turbo-molecular or oil diffusion pump.
4. A current is passed through the boat or filament, the metal melts and begins to evaporate. This evaporation is almost radially uniform, and hence only a small fraction of the evaporated metal is actually deposited on the sample.
5. Close to the sample a piezoelectric crystal measures the mass that has been deposited, and this information is converted into a thickness by a control unit which is programmed with the density of the metal.
6. Once the required thickness has been obtained, the system is allowed to cool for 30 minutes, and then atmospheric pressure is restored, and the sample removed. If the chamber is opened while the sample is hot it could react with the atmosphere.

If the metal is too thick, few electrons will be transmitted through this film, and those that do will be significantly scattered, leading to a loss of resolution. On the other hand, if the film is too thin, it will be islandised, and hence will not conduct DC from the electron beam. Generally, 20-25nm is a good compromise.

A.4 Electron-beam exposure

Software (Elphy Quantum by Raith) is used to design geometries which can then be exposed by the electron beam. In principle any geometry can be designed, but for disc-shaped particles, simple circles are drawn. The exposed area for each array is known as the 'writefield' and a commonly used size is 50μm $\times$ 50μm. It is possible to expose several arrays on the same sample using a 'position list' which sets the position at which each array will be exposed. A

very important parameter which needs to be set is the electron dose (measured in $\mu C\,cm^{-2}$) and determines the amount of charge which a unit area will be subjected to. It is dependent on a number of parameters; the beam current, the dwell time, and the step size (effectively the 'pixel' size). The dose has an optimum value for each particular geometry to be exposed. The reason for this is that the beam profile at the focus has a Gaussian distribution, and hence regions are exposed which are not at the centre of the focussed beam. When large areas are exposed, each 'pixel' acquires a certain dose from all other particles according to the Gaussian rule (see chapter 3). Therefore the area dose needs to be reduced for large areas.

In terms of setting up the SEM, a procedure is followed:

1. The sample is placed on an x-y-z translation stage in the SEM chamber.
2. The chamber is evacuated (to less than 10^{-5}mbar).
3. The scanning directions of the electron beam are calibrated using a self-similar chess-board sample. The chess-board sample is used to align the x- and y- directions of the stage movement in a local coordinate system.
4. The sample is raised to the working distance (5mm from the final condenser lens) and is brought to a good focus (using a 'contamination spot'[‡] and made non-astigmatic).
5. The centre of the sample is aligned with the focus of the beam (being careful not to expose the sample too soon), and exposure of the chosen areas begins.

A.5 Removal of metallic over-layer

The conducting metal layer needs to be removed in order for the developer to act on the exposed PMMA underneath. This is achieved by immersing the sample (suspended it in a PTFE sample holder) in a 1:1 mixture of gold etchant (potassium iodide) and ultra-pure water. The etching should take 5-10 seconds, and inspection should reveal that no gold/silver remains on the sample. The sample is immediately rinsed in ultra-pure water to remove all traces of gold etchant.

A.6 Developing

Immediately, the sample should be immersed in a beaker of developer (IPA and water, 9:1) for 60 seconds. This will dissolve the exposed PMMA and gentle agitation will ensure complete removal of this polymer from the surface.

[‡]A contamination spot is produced by allowing the electron beam to dwell at a single point for $1s < t < 180s$. This has the effect of sputtering contaminants within the chamber onto that spot and hence a small bright square is produced which can aid focussing (it will be elliptical if the beam is astigmatic).

The sample should be briefly rinsed with a slow jet of ultra-pure water, and then immersed in ultra-pure water for a further 60 seconds. Following the immersion in water, the sample is dried with nitrogen.

A.7 Evaporation of metal film to produce structures

A metallic film is produced in the same way as described above (i.e. by thermal evaporation). For this step it is essential that the sample is orthogonal to the evaporation direction in order that the resulting particles have the same geometry as the exposed holes. It is also important that there is no metal connecting the particles to the metal film which sits on top of the unexposed PMMA. If this happens, it is likely that during lift-off, the particles will be removed with the film.

The rate of evaporation is approximately 1-2Ås^{-1}.

A.8 Lift-off

After evaporation, the sample has a metal film coating all the remaining PMMA and has metal in the holes which will form the particles. In order to remove the remaining PMMA and the metal film with it, the sample is immersed in a beaker of acetone which dissolves the PMMA and allows the metal film to lift away from the sample. This can be carried out at room temperature or it can be boiled. At room temperature, the beaker should be covered to avoid the acetone evaporating, and it should be left overnight. When boiled (at $T > 56°$C), the film can lift off in 30 minutes, though the turbulent acetone can lead to particles being removed unintentionally and the film may disintegrate into small pieces which could remain on the sample. If possible, the metal film is removed from the beaker with tweezers as soon as it is no longer attached to the sample. Even when this is carried out in cold acetone, it can be beneficial to heat the acetone slightly to remove any final traces of PMMA which may be on the surface of the glass.

The sample should then be immersed in IPA very quickly so that the acetone does not evaporate from the surface of the sample. The IPA is less volatile than acetone so it is possible to remove it from the surface of the sample using pressurised nitrogen which avoids drying marks.

A.9 Dose-scaling technique

As stated in chapter 3, when exposing a small region of resist with an electron beam, the rest of the array is subject to a small additional dose due to the Gaussian profile of the beam at

its focus. Described here is an initial attempt at resolving this discrepancy in arbitrary arrays of point-like particles.

Consider an array of n identical particles. Each particle receives the dose intended for itself plus dose from all the other $n-1$ particles in the array. Assuming the particles to be infinitesimally small, the total intensity received by the particles when each is exposed nominally to a beam with a peak intensity of 1 is $d_{1\ldots n}$ which can be calculated using the following matrix notation as a system of linear equations.

$$\begin{pmatrix} 1 & Z_{2,1} & \cdots & Z_{n,1} \\ Z_{1,2} & 1 & \cdots & Z_{n,2} \\ \vdots & \vdots & \ddots & \vdots \\ Z_{1,n} & Z_{2,n} & \cdots & 1 \end{pmatrix} \begin{pmatrix} 1 \\ 1 \\ \vdots \\ 1 \end{pmatrix} = \begin{pmatrix} d_1 \\ d_2 \\ \vdots \\ d_n \end{pmatrix} \tag{A.9.1}$$

Using the following definition for the matrix elements:

$$Z_{p,q} = \exp\left(-\frac{|\mathbf{r}_p - \mathbf{r}_q|^2}{2c^2}\right) \tag{A.9.2}$$

When point p is exposed with a certain dose and some of this dose is incident on particle q, $Z_{p,q}$ is the factor by which the initial dose is scaled as experienced by particle q, where c is the width of the Gaussian distribution. This matrix equation can be modified in order that the incident intensity for each particle is the unknown quantity (the interaction matrix remains unchanged as it is purely a geometrical quantity):

$$\begin{pmatrix} 1 & Z_{2,1} & \cdots & Z_{n,1} \\ Z_{1,2} & 1 & \cdots & Z_{n,2} \\ \vdots & \vdots & \ddots & \vdots \\ Z_{1,n} & Z_{2,n} & \cdots & 1 \end{pmatrix} \begin{pmatrix} k_1 \\ k_2 \\ \vdots \\ k_n \end{pmatrix} = \begin{pmatrix} 1 \\ 1 \\ \vdots \\ 1 \end{pmatrix} \tag{A.9.3}$$

This can be solved by simply inverting the matrix, then the resulting values of $k_{1\ldots n}$ represent the factor by which the incident intensity needs to be modified in order that all the particles are exposed with the same net intensity. This method is liable to produce non-physical results in the form of negative solutions and therefore for some random arrays this technique cannot be implemented. In these cases, however, a minimum dose factor can be set (e.g. k_p must be > 0.5) which, although it will not produce a mathematically correct solution to the matrix equation, it will suggest physical dose factors which provide a significantly improved uniformity of particle sizes. This has been checked by entering the calculated dose scaling factors back into the left-hand-side equation A.9.3 and examining how close the actual doses are to 1 (they are usually within 10% but arrays which produce a greater error are discarded in favour of random arrays which allow the actual doses to be closer to 1).

A.10 Fabrication of the tower and pagoda structures

The tower and pagoda structures are fabricated as follows:

A.10.1 Tower

The tower structure was fabricated as follows by collaborators at the University of Manchester:

1. A 5nm chromium layer was evaporated onto a glass substrate to make it conductive for electron-beam lithography.
2. 70nm of 495kD PMMA was spin-coated onto the chromium.
3. 50nm of 950kD PMMA was spin-coated on top of the bottom PMMA layer (the two layers were used to improve the success of the lift-off).
4. The electron beam scanned a large circle on the sample, thus exposing, and breaking the polymer chains.
5. Following this, the electron beam exposed a smaller circle the centre of the large circle with a higher dose in order to overexpose, i.e. cross-link the PMMA, and make it insoluble.
6. The sample was developed (removing the polymer with broken chains) and a pillar of cross-linked PMMA was left behind at the centre.
7. 90nm of gold was thermally evaporated onto the sample.
8. Acetone was used to remove the un-exposed PMMA.

A.10.2 Pagoda

Fabrication of the pagoda structure is a longer process, but it is ultimately more flexible.

1. A 5nm chromium layer was evaporated onto a glass substrate to make it conductive for electron-beam lithography.
2. 100nm of 950kD PMMA was spin-coated on top of the chromium layer.
3. The electron beam scanned a large circle on the sample, thus exposing, and breaking the polymer chains. Also, on this sample, alignment marks were exposed in order that the second layer could be exposed with good precision (these took the from of four crosses at the corners of 40μm squares which contained the structures).

4. The sample was developed (removing the polymer with broken chains), thus leaving a circular hole.
5. 50nm of gold was thermally evaporated onto the sample.
6. Acetone was used to remove the un-exposed PMMA.
7. A 100nm thickness of a commercial dielectric (Wide 15 by Brewer Science inc.) was used as a spacer layer. It was spin-coated and then baked.
8. A new 100nm layer of PMMA was spin-coated onto the sample.
9. The alignment marks were used to carefully align the electron beam without exposing the region where the existing structures are.
10. The smaller disc was exposed in a position which was accurate to within 20nm.
11. The PMMA was developed.
12. A 50nm gold film was evaporated onto the sample.
13. Lift-off in acetone removed the remaining PMMA and metal film.

Appendix B

Polarisability

The expression known as the Clausius- Mossotti equation describes the polarisability of a molecule inside a polarisable dielectric. The same result is found when considering a polarised sphere such as a nanosphere in the electrostatic regime. Deriving this expression for a polarised sphere within a dielectric is the aim of this appendix, with emphasis on physical understanding. The logic is largely derived from Purcell,[140] but the inclusion of a surrounding medium has been added here.

B.1 Origin of the permittivity

Imagine a charged sphere at the origin. Surround the sphere by a polarisable, but electrically neutral material which extends to infinity. How is the electric field modified at a distance r from the charge?

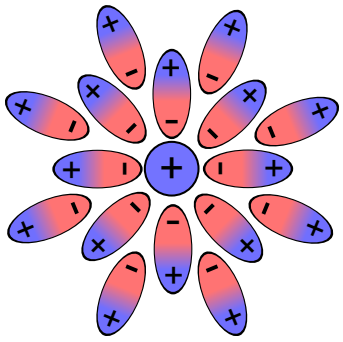

Figure B.1.1: The radial polarisation of molecules in a dielectric when a free charge is present.

The electric field from the charge on the sphere alone is:

$$\mathbf{E}_{free} = \frac{Q_{free}}{4\pi\epsilon_0 r^2}\hat{\mathbf{r}} \tag{B.1.1}$$

The charge on the sphere is referred to as free charge to distinguish it from charge generated by polarising dielectrics. When the new surrounding medium is present, the polarisable molecules will align themselves radially, and hence a quantity of charge will build up at the surface of the charged sphere and will have opposite sign. This new charge is referred to as *bound charge* and the field it produces is:

$$\mathbf{E}_{bound} = \frac{Q_{bound}}{4\pi\epsilon_0 r^2}\hat{\mathbf{r}} \tag{B.1.2}$$

so, the total field from the two sources of charge is:

$$\mathbf{E}_{total} = \frac{1}{4\pi\epsilon_0 r^2}(Q_{free} + Q_{bound})\hat{\mathbf{r}} \tag{B.1.3}$$

It is reasonable to assume that the amount of bound charge is directly proportional to the amount of free charge ($Q_{bound} = CQ_{free}$ where C is a negative constant). So, now we have:

$$\mathbf{E}_{total} = \frac{Q_{free}}{4\pi\epsilon_0 r^2}(1 + C)\hat{\mathbf{r}} \tag{B.1.4}$$

Clearly, the presence of the medium introduces a factor by which the original field is modified. As stated above, for our situation the medium acts to reduce the field, so we shall rewrite our equation with a new factor in the denominator ($\epsilon = 1/(1 + C)$):

$$E = \frac{Q_{free}}{4\pi\epsilon\epsilon_0 r^2} \tag{B.1.5}$$

In order to obtain some clearer meaning of the value of ϵ, we shall rewrite it as follows:

$$\epsilon = \frac{1}{1 + C} = \frac{1}{1 + \frac{Q_{bound}}{Q_{free}}} = \frac{Q_{free}}{Q_{free} + Q_{bound}} \tag{B.1.6}$$

From equations B.1.1 and B.1.2 we can rewrite this as:

$$\epsilon = \frac{E_{free}}{E_{free} + E_{bound}} = \frac{E_{free}}{E_{total}} \tag{B.1.7}$$

This is the relative permittivity, and is simply the field when no material is present divided by the field when it is present.

B.2 The capacitor

Another geometry for which all field lines are parallel is a capacitor. By constructing a Gaussian pillbox over one of the plates and making it very thin, the field is calculated as follows:

$$\int \mathbf{E} \cdot d\mathbf{S} = \frac{1}{\epsilon_0} \int \sigma \, dS \tag{B.2.1}$$

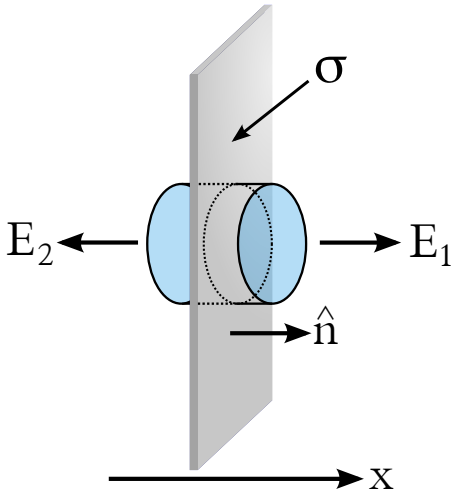

Figure B.2.1: Gaussian pillbox over a sheet of charge.

The magnitudes of the fields on each side of one of the capacitor plates are given as follows ($\hat{\mathbf{n}}$ is the unit vector in the x-direction, i.e. perpendicular to the plate):

$$\mathbf{E}_1 = \frac{\sigma}{2\epsilon_0}\hat{\mathbf{n}} \qquad \mathbf{E}_2 = -\frac{\sigma}{2\epsilon_0}\hat{\mathbf{n}} \tag{B.2.2}$$

Where the indices 1 and 2 indicate the fields in the half-spaces in the positive and negative directions of x relative to the plate. When another parallel plate carrying opposite charge is placed next to it (in the negative x-direction), the field outside the plates becomes zero due to the positive and negative charge cancelling, and inside, the field is the sum of the contributions from the two plates (i.e. double):

$$\mathbf{E}_{between} = -\frac{\sigma}{\epsilon_0}\hat{\mathbf{n}} \tag{B.2.3}$$

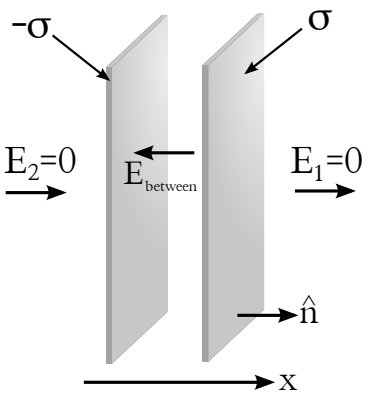

Figure B.2.2: The field between two plates of a capacitor.

B.3 A slab of material

When a medium is polarised, the bulk of the material is electrically neutral, but the surfaces hold charge which makes it analogous to a capacitor. When a thin slab of material is placed in an electric field, charge builds up on the opposite surfaces and this charge acts to reduce the field inside (it acts in the opposite direction and hence is negative).

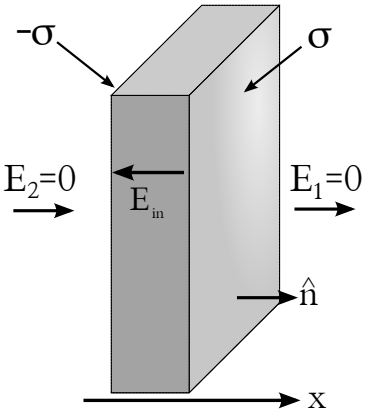

Figure B.3.1: The field inside a polarised dielectric is equivalent to a capacitor (σnow represents the charge density on the surface of the dielectric).

The field inside is given by:

$$\mathbf{E}_{in} = \mathbf{E}_{out} + \mathbf{E}_{pol} \tag{B.3.1}$$

E_{pol} is simply the amount of surface charge divided by the permittivity of free space as in equation B.2.3 (σnow represents the charge density on the surface of the dielectric):

$$\mathbf{E}_{in} = \mathbf{E}_0 - \frac{\sigma}{\epsilon_0}\hat{\mathbf{n}} \tag{B.3.2}$$

This is a very general equation, and it assumes that the field inside the material is due to surface charge which exists independently of the applied field. If we now suppose that the amount of surface charge on the dielectric is proportional to the internal field (assuming the applied field is in the $\hat{\mathbf{n}}$ direction in order to avoid the vector notation), we now have:

$$E_{in} = E_0 - \chi E_{in} \tag{B.3.3}$$

Where $\chi E_{in} = \frac{\sigma}{\epsilon_0}$. So, χ is the factor which determines the amount of surface charge generated per unit field and is known as the *susceptibility*. From this and equation B.1.7 we can derive an expression for ϵ (it is the factor by which the incident field in vacuum is reduced when the dielectric is present):

$$\epsilon = \frac{E_0}{E_{in}} = (1 + \chi) \tag{B.3.4}$$

We can now introduce the quantity P which is the *polarisation* of the material. It is defined as:

$$P = \epsilon_0 \chi E_{in} = \epsilon_0(\epsilon - 1)E_{in} \tag{B.3.5}$$

If the slab is surrounded by another material with permittivity ϵ_d, the polarisation is modified as follows:

$$P = \epsilon_0(\epsilon - \epsilon_d)E_{in} \tag{B.3.6}$$

This notation adds no new physics to the discussion at this stage. We could continue to use E_{pol} at all times and not introduce P. Still, this is the convention (it will become of some use later), and we are still avoiding the unnecessary introduction of the displacement vector. We will however state that the polarisation vector could be written as follows by substituting equations B.3.1 and B.3.3.

$$P = \epsilon_0(E_0 - E_{in}) = -\epsilon_0 E_{pol} \tag{B.3.7}$$

Where E_{pol} is the field due to the accumulated surface charge. The total field in a capacitor is now:

$$E_{in} = E_0 - \frac{P}{\epsilon_0} \tag{B.3.8}$$

From this it is clear that the degree of polarisation P is identical to the surface charge density σ in this arrangement (equation B.3.2).

B.4 Physical interpretation of the permittivity

When a material has an external field applied, the polarisable molecules align so as to reduce the field. The factor by which the field is reduced is the permittivity. When relating the polarisation field to the external field, we need to use the following equation:

$$E_{pol} = \frac{\epsilon - \epsilon_d}{\epsilon} E_0 \tag{B.4.1}$$

If a polarisable dielectric is placed in the field, E_{pol}will be the amount by which the internal field is reduced compared to the applied field. Let us consider four regimes:

1. It is trivial, but worthwhile to show that when $\epsilon = 1$, there is no polarisation field.
2. Water has a permittivity of $\epsilon = 81$ in the electrostatic limit. Therefore the polarising field in water is almost 99% of the strength of the applied field.
3. Metals have negative permittivities and can in fact produce internal fields much stronger than non-metals as they have large reserves of free electrons which can move to the surfaces to provide the surface charge which forms the polarising field. For example if a metal had a permittivity of $\epsilon = -10$, the polarising field would be $E_{pol} = 1.1E_0$. As $\epsilon \to -\infty$ the strength of the polarising field tends to the strength of the applied field.
4. When $\epsilon = 0$, the polarising field becomes infinite. This corresponds to a bulk plasmon.

B.5 An arbitrary rod

Imagine a long thin rod of material which is polarised along its axis (the z-direction). If the rod is split into a series of units, the dipole moment of each unit will be:

$$\mathbf{p} = \mathbf{P} dV = \mathbf{P}\, dA\, dz \tag{B.5.1}$$

where A is the cross-sectional area of the rod, and dz is the length of the element in the z-direction. If we try to find the potential at a distance from this rod, we must integrate the potential from all of the dipole moments. The expression for a single dipole moment is:

$$\phi = \frac{1}{4\pi\epsilon_0}\frac{p\cos\theta}{r^2} \tag{B.5.2}$$

If we integrate this along the length of the rod (from z_1 to z_2), we have

$$\phi_{total} = \frac{1}{4\pi\epsilon_0}\int_{z_1}^{z_2}\frac{P\cos\theta\, dA\, dz}{r^2} = \frac{PdA}{4\pi\epsilon_0}\int_{z_1}^{z_2}\frac{\cos\theta\, dz}{r^2} \tag{B.5.3}$$

Now, if we substitute $dz\,\cos\theta = dr$ (i.e. dr is the amount by which r is modified in traversing the length element), so

$$\phi_{total} = \frac{PdA}{4\pi\epsilon_0}\int_{z_1}^{z_2}\frac{dr}{r^2} = -\frac{PdA}{4\pi\epsilon_0}\int_{z_1}^{z_2}\frac{d}{dr}\left(\frac{1}{r}\right)dr = -\frac{PdA}{4\pi\epsilon_0}\frac{d}{dr}\int_{r_1/\cos\theta_1}^{r_2/\cos\theta_2}\left(\frac{1}{r}\right)dr \tag{B.5.4}$$

By substituting $z_1 = r_1\cos\theta_1$ and $z_2 = r_2\cos\theta_2$ and expanding the resulting logarithms, we end up with :

$$\phi_{total} = \frac{PdA}{4\pi\epsilon_0}\left(\frac{1}{r_1} - \frac{1}{r_2}\right) \tag{B.5.5}$$

This is simply the the potential two charges of magnitude PdA with different sign at r_1 and r_2. In other words, the potential of the rod measured in the far-field depends only on the charge at either end and does not depend at all on the dipole moments in between (i.e. they cancel).

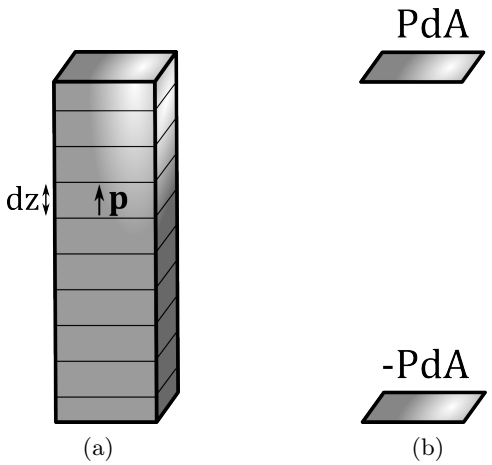

Figure B.5.1: (a) a stack of polarised elements with dipole moment $\mathbf{p}$ which, in the far-field, is equivalent to (b) a dipole comprised of two separated charges.

If we extend this geometry to an assembly of rods, we can produce a slab whose surface charge is $\sigma = P$.

B.6 The sphere

A sphere may also be described by an assembly of rods (figure B.6.1), but of course, the surfaces will no longer necessarily be orthogonal to the rod axes. The surface charge density is hence reduced when the top and bottom surfaces are at greater angles (i.e. the charge is spread over a larger area). If $\theta$is the polar angle (along the rod, $\theta = 0$), then the surface charge density will be modified from the slab case as follows:

$$\sigma = P\cos\theta \tag{B.6.1}$$

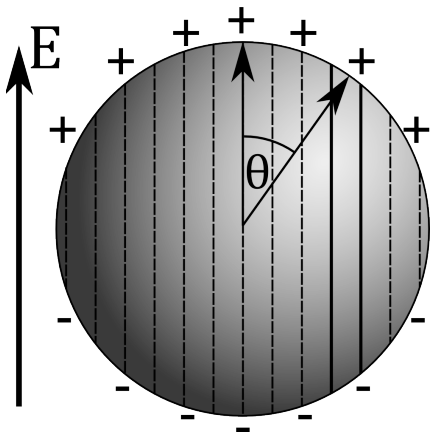

Figure B.6.1: A sphere comprised of a series of rods.

Now, when a sphere is polarised, its charges are displaced with axial symmetry, and, from the multipole expansion, the external potential of an arbitrary spherical distribution of charge is exactly equivalent to infinitesimal multipoles at the origin. In our case, the sphere has only a dipole contribution. If we imagine that all the negatively charged electrons are displaced a distance s, and the positive ions remain stationary, and both sets of charges remain spherical in shape, the field outside the sphere will be equivalent to the sum of a single positive charge Q at the centre of the positive sphere, and a single negative charge $-Q$ at the centre of the negative sphere. Therefore the dipole moment will be $p = Qs$. If we now relate this to the individual charges we obtain

$$p = Qs = \frac{4}{3}\pi r^3 Nqs = \frac{4}{3}\pi r^3 P \tag{B.6.2}$$

where N is the density of electrons involved in the polarisation, r is the radius of the sphere and q is the electronic charge. We have managed to get rid of Q and s which do not have any meaningful significance (and certainly are not measurable), and we are left with a value of the dipole moment which, when placed at the origin, produces the same external potential as the

polarised sphere. In order to calculate the internal field, we first need to know the potential at the surface of the sphere (radius r_0):

$$\phi = \frac{p\cos\theta}{4\pi\epsilon_0\epsilon_d r_0^2} = \frac{1}{3}Pr_0\cos\theta \tag{B.6.3}$$

We know that $r_0\cos\theta = z$, so

$$\phi = \frac{1}{3\epsilon_0\epsilon_d}Pz \tag{B.6.4}$$

This shows us that the potential at the surface depends only on the z-coordinate, which is obvious to an extent as we have previously stated that the charge distribution must be axially symmetrical. The potential at the surface satisfies Laplace's equation inside the sphere, so we can now calculate the field inside:

$$E_z = -\frac{\partial\phi_{pol}}{\partial z} = -\frac{\partial}{\partial z}\left[\frac{1}{3\epsilon_d}Pz\right] = -\frac{1}{3\epsilon_d}P \tag{B.6.5}$$

As the electric field only has components in the z-direction, it can be re-written as

$$\mathbf{E}_{surf.} = -\frac{1}{3\epsilon_d}P\hat{\mathbf{z}} \tag{B.6.6}$$

We now know the field at the boundary, but the field within the sphere is still yet to be found. The potential inside the sphere is a solution of Laplace's equation:

$$\nabla^2\phi = \frac{\partial^2\phi}{\partial x^2} + \frac{\partial^2\phi}{\partial y^2} + \frac{\partial^2\phi}{\partial z^2} \tag{B.6.7}$$

The internal potential must, from the boundary condition at the surface, be equal to $\frac{1}{3\epsilon_d}Pz$. The potential which solves Laplace's equation whilst complying with the boundary condition at the surface is simply the same potential plus an unknown constant — $\phi = \frac{1}{3\epsilon_d}Pz + C^*$. The electric field inside the sphere can now be written as:

$$\mathbf{E}_{pol} = -\nabla\phi = -\frac{1}{3\epsilon_d}P\hat{\mathbf{z}} \tag{B.6.8}$$

This field is calculated for a given charge distribution, but so far we have not discussed the manner in which this polarisation is induced. The total field is the sum of the incident field and the polarisation field:

*This constant is, in fact equal to zero from the uniqueness theorem.

$$\mathbf{E}_{total} = \mathbf{E}_0 + \mathbf{E}_{pol} = \mathbf{E}_0 - \frac{1}{3\epsilon_d} P\hat{\mathbf{z}} \tag{B.6.9}$$

Ignoring the vectorial notation and using equation B.3.6 , we can write:

$$E_{total} = E_0 - \frac{\epsilon_0(\epsilon - \epsilon_d)}{3\epsilon_0\epsilon_d} E_{total} \tag{B.6.10}$$

In terms of E_{total} we now have:

$$E_{total} = \left(\frac{3\epsilon_d}{\epsilon + 2\epsilon_d}\right) E_0 \tag{B.6.11}$$

The polarisation can now be written as:

$$P = \epsilon_0(\epsilon - \epsilon_d)E_{total} = \epsilon_0 3\epsilon_d \left(\frac{\epsilon - \epsilon_d}{\epsilon + 2\epsilon_d}\right) E_0 \tag{B.6.12}$$

If this is now converted to the polarisability, we obtain

$$\alpha = \frac{PV}{\epsilon_0\epsilon_d E_0} = 4\pi a^3 \left(\frac{\epsilon - \epsilon_d}{\epsilon + 2\epsilon_d}\right) \tag{B.6.13}$$

Appendix C

The Optical Theorem

The optical theorem relates the extinction cross-section to the polarisability of a particle and is used several times in this thesis in different forms. Because a great deal of understanding can be gained from deriving the theorem (which is hidden in such a simple expression), a derivation is provided here.

This derivation was produced by examining several independent derivations, and selecting the aspects of each which provide a physical, rather than mathematical derivation of a deceptively simple expression.

The physical approach regarding scalar waves incident on a particle with a screen in the far-field was described by Newton[104] and forms the core of this derivation. The conversion to vector waves was performed by myself with the help of books[42,44,74] and papers, notably a paper by Berg *et al.*[141] which clearly describes the counter-intuitive solution that the extinction cross-section is dependent on the scattered power in the forward direction *only*. The conversion into the final form (which is identical to that used by Draine[49,50]) was performed by myself.

C.1 Hypothetical extinction experiment

Let us consider an experimental arrangement much like figure 3.5.1 with an incident wave illuminating a scattering object, and a screen far away from the object. At this screen the light intensity is reduced by the presence of the particle and the amount by which the intensity is decreased is dictated by the optical theorem.

The total field is the sum of the incident and scattered field where $\mathbf{F}(\theta, \phi)$ is the angle-dependent vector scattering amplitude

$$\begin{aligned} \mathbf{E} &= \mathbf{E}_{inc} + \mathbf{E}_{scatt} && \text{(C.1.1)} \\ &= E_0 \left[e^{ik\hat{\mathbf{z}}\cdot\mathbf{r}}\hat{\mathbf{x}} + \frac{1}{kr}\mathbf{F}(\theta,\phi)e^{ikr} \right] && \text{(C.1.2)} \end{aligned}$$

Use the binomial theorem to substitute for r:

$$r = \sqrt{x^2+y^2+z^2} \simeq z + \frac{x^2+y^2}{2z} \tag{C.1.3}$$

Now consider the intensity and make the substitution for $\mathbf{r}$ assuming that the scattered wave-vector is radial and the incident wave is propagating along the z-direction:

$$|\mathbf{E}|^2 = E_0^2 \left| e^{ikz}\hat{\mathbf{x}} + \frac{1}{kr}\mathbf{F}(\theta,\phi)e^{ikz}e^{ik(x^2+y^2)/2z} \right|^2 \tag{C.1.4}$$

This can be expanded as (approximating r to z in the denominator):

$$|\mathbf{E}|^2 = E_0^2 \left[1 + \frac{1}{kz}F_x^*(\theta,\phi)e^{-ik(x^2+y^2)/2z} + \frac{1}{kz}F_x(\theta,\phi)e^{ik(x^2+y^2)/2z} + \frac{1}{k^2z^2}\mathbf{F}(\theta,\phi)\mathbf{F}^*(\theta,\phi) \right] \tag{C.1.5}$$

The final term is comparatively small, so can be dropped. We can also use the complex identity $Z + Z^* = 2\Re(Z)$:

$$|\mathbf{E}|^2 = E_0^2 \left[1 + 2\Re\left(\frac{1}{kz}F_x(\theta,\phi)e^{ik(x^2+y^2)/2z} \right) \right] \tag{C.1.6}$$

If this intensity is now integrated over a screen whose normal is parallel to the direction of propagation of the incident wave and is far enough away to use the small-angle approximation, we have (assuming that $F_x(\theta,\phi) \to F_x(0)$):

$$\int |\mathbf{E}|^2 \, dA = E_0^2 \left[A + 2\Re\left(\frac{F_x(0)}{kz} \int_{-\infty}^{\infty} e^{ikx^2/2z} dx \int_{-\infty}^{\infty} e^{iky^2/2z} dy \right) \right] \tag{C.1.7}$$

Integrating from $-\infty$ to ∞ we are assuming that the sheet is large enough to collect all the light, and the integral can be carried out as a Gaussian. This produces:

$$\int |\mathbf{E}|^2 \, dA = E_0^2 \left[A + 2\Re \left(\frac{F_x(0)}{kz} \frac{2iz\pi}{k} \right) \right] = E_0^2 \left[A + \frac{4\pi}{k^2} \Re \left(iF_x(0) \right) \right] \tag{C.1.8}$$

This can be rewritten in the familiar form:

$$\int |\mathbf{E}|^2 \, dA = E_0^2 \left[A - \frac{4\pi}{k^2} \Im \left(F_x(0) \right) \right] \tag{C.1.9}$$

where the extinction cross-section is:

$$\sigma_{ext} = \frac{4\pi}{k^2} \Im \left(F_x(0) \right) \tag{C.1.10}$$

where our generic scattered field is described by:

$$\mathbf{E}_{scatt} = E_0 \frac{1}{kr} \mathbf{F}(\theta, \phi) e^{ikr} \tag{C.1.11}$$

C.2 Extinction of a particle with known polarisability

If we turn to the specific case of the scattered field of a dipole (taking just the radiative part), we have:

$$\mathbf{E}_{dipole} = -\frac{1}{4\pi\epsilon} \frac{k^2}{r} \left(\hat{\mathbf{r}} \times \left(\hat{\mathbf{r}} \times \mathbf{p} \right) \right) e^{ikr} \tag{C.2.1}$$

When $\mathbf{p} = \epsilon\alpha\mathbf{E}_0$, we obtain (when the incident field is oriented along the x-axis):

$$\mathbf{E}_{dipole} = -E_0 \alpha \frac{1}{4\pi} \frac{k^2}{r} \left(\hat{\mathbf{r}} \times \left(\hat{\mathbf{r}} \times \hat{\mathbf{x}} \right) \right) e^{ikr} \tag{C.2.2}$$

Relating this back to the expression for the generic scattered field, we find that $\mathbf{F}$ can be written as:

$$\mathbf{F} = -\alpha \frac{1}{4\pi} k^3 \left(\hat{\mathbf{r}} \times \left(\hat{\mathbf{r}} \times \hat{\mathbf{x}} \right) \right) \tag{C.2.3}$$

The $x-$component of $\mathbf{F}$ in the forward direction is now:

$$F_x = \alpha \frac{1}{4\pi} k^3 \tag{C.2.4}$$

The extinction cross-section of a dipole can therefore be written in the following simple form:

$$\sigma_{ext} = k\Im\left(\alpha\right) \tag{C.2.5}$$

C.3 Extinction of a particle with known dipole moment

In the formalism of the coupled dipole model, however, the net dipole moment of the particle is modified by the presence of other particles, and as the dipole moment is the calculated quantity from the model we shall rewrite equation C.2.5 in terms of the actual dipole moment rather than the polarisability. Starting from equation C.2.1, we can resolve the two far-field coordinates of $\mathbf{E}_{dip}$ in the forward-scattered direction labelled r'.

$$\mathbf{E}_{dipole} = -\frac{1}{4\pi\epsilon}\frac{k^2}{r'}e^{ikr'}\left[\frac{1}{|\mathbf{E}_{in}|}\left(\left(\hat{\mathbf{r}'}\times\left(\hat{\mathbf{r}'}\times\mathbf{p}\right)\right)\cdot\mathbf{E}_{in}\right)\frac{\mathbf{E}_{in}}{|\mathbf{E}_{in}|}\right.$$
$$\left. + \frac{1}{|\mathbf{E}_{in}|}\left(\left(\hat{\mathbf{r}'}\times\left(\hat{\mathbf{r}'}\times\mathbf{p}\right)\right)\cdot\left(\hat{\mathbf{r}'}\times\mathbf{E}_{in}\right)\right)\frac{\left(\hat{\mathbf{r}'}\times\mathbf{E}_{in}\right)}{|\mathbf{E}_{in}|}\right] \tag{C.3.1}$$

The corresponding value of $\mathbf{F}$ is:

$$\mathbf{F}_{dipole} = -\frac{1}{4\pi\epsilon}k^3\left[\frac{1}{|\mathbf{E}_{in}|^2}\left(\left(\hat{\mathbf{r}'}\times\left(\hat{\mathbf{r}'}\times\mathbf{p}\right)\right)\cdot\mathbf{E}_{in}\right)\frac{\mathbf{E}_{in}}{|\mathbf{E}_{in}|}\right.$$
$$\left. + \frac{1}{|\mathbf{E}_{in}|^2}\left(\left(\hat{\mathbf{r}'}\times\left(\hat{\mathbf{r}'}\times\mathbf{p}\right)\right)\cdot\left(\hat{\mathbf{r}'}\times\mathbf{E}_{in}\right)\right)\frac{\left(\hat{\mathbf{r}'}\times\mathbf{E}_{in}\right)}{|\mathbf{E}_{in}|}\right] \tag{C.3.2}$$

According to the preceding analysis, the only component of $\mathbf{F}$ which contributes to the extinction cross-section is the component which is parallel to the incident field (see equation C.1.5). For the dipole considered here, the component along the direction of $\mathbf{E}_{in}$ is:

$$F_{dipole,\,E_{in}} = -\frac{1}{4\pi\epsilon}\frac{1}{|\mathbf{E}_{in}|^2}k^3\left(\hat{\mathbf{r}'}\times\left(\hat{\mathbf{r}'}\times\mathbf{p}\right)\right)\cdot\mathbf{E}_{in}^* \tag{C.3.3}$$

Where we have used the complex conjugate to ensure that the magnitude of the scattering function is calculated. If we now use the vector identity $\mathbf{A}\times\left(\mathbf{B}\times\mathbf{C}\right) = \left(\mathbf{A}\cdot\mathbf{C}\right)\mathbf{B} - \left(\mathbf{A}\cdot\mathbf{B}\right)\mathbf{C}$, we obtain:

$$F_{dipole,\,E_{in}} = -\frac{1}{4\pi\epsilon}\frac{1}{|\mathbf{E}_{in}|^2}k^3\left(\left(\hat{\mathbf{r}'}\cdot\mathbf{p}\right)\hat{\mathbf{r}'} - \left(\hat{\mathbf{r}'}\cdot\hat{\mathbf{r}'}\right)\mathbf{p}\right)\cdot\mathbf{E}^*_{in} \tag{C.3.4}$$

From the way in which the direction of forward-scattering was defined, we know that $\hat{\mathbf{r}'}\cdot\mathbf{E}_{in} = 0$, so we now have:

$$F_{dipole,\,E_{in}} = \frac{1}{4\pi\epsilon}\frac{1}{|\mathbf{E}_{in}|^2}k^3\left(\mathbf{p}\cdot\mathbf{E}^*_{in}\right) \tag{C.3.5}$$

Finally, this can be inserted into equation C.1.10 to obtain:

$$\sigma_{ext} = \frac{k}{\epsilon\,|\mathbf{E}_{in}|^2}\Im\left(\mathbf{p}\cdot\mathbf{E}^*_{in}\right) \tag{C.3.6}$$

This function can be used to calculate the extinction cross-section of particles when the dipole moment has been calculated and the direction, magnitude and phase of the incident light at the position of the dipole is known. This is the case in the coupled dipole approximation and that is how the extinction cross-section is computed using the codes provided in appendixF.

Appendix D

Mie Theory

D.1 Motivation

Mie theory is an exact, electrodynamic analysis of the absorption and scattering of light by a sphere. It was first solved by Gustav Mie[54] in 1908 and since then similar approaches have been used to arrive at the same solution. The variables in Mie theory are the sphere radius, the wavelength of light and the complex refractive indices of the sphere and the surrounding medium.

Although Mie theory has been derived in a number of books, most are very mathematical at the expense of physical descriptions. Despite this there are often many steps skipped which makes complete understanding time consuming as reference to other texts or independent verification of the algebra is often needed. Presented in this appendix is a derivation which presents no new information, but takes inspiration from a number of sources and seeks to provide a complete (rather than brief) derivation of Mie theory which should be understandable by anyone who can solve a partial differential equation by the method of separation of variables — no detailed knowledge of spherical Bessel functions or the associated Legendre polynomials is assumed. Standard vector identities have been used without derivation and a few other identities regarding Bessel functions have been omitted (their inclusion would lead to unnecessary complication and diversion from the main goal). The method is based heavily on the approach and notation of Bohren and Huffman[44] as that text is both modern and widespread in use. This approach was strongly influenced by Stratton[77] who proposed an alternative derivation which was less abstract than Mie's original paper. Further books by Van De Hulst,[42] Jackson,[112] Tricker[1] and Born and Wolf[2] provided additional descriptions which make up this complete derivation. Finally, Boas's book on mathematical techniques[142] has largely been used as a source for the more mathematical parts of the derivation.

By virtue of the fact that this is a complete derivation and assumes very little, it is very mathematical and at times no physical insight can be obtained from the equations and this,

unfortunately, is unavoidable. It is hoped that the examples and physical descriptions at the end of the derivation will make up for the rather abstract derivation.

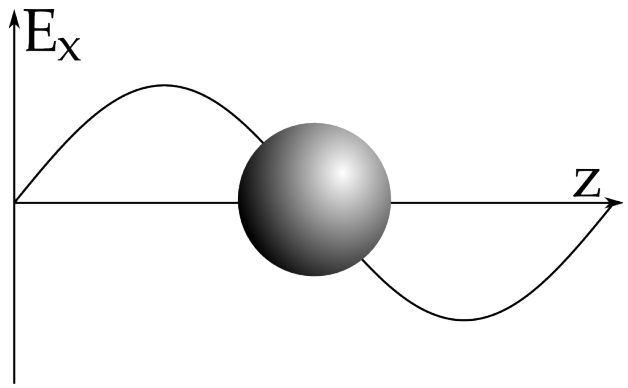

Figure D.1.1: Schematic showing the coordinate system of a sphere illuminated by a plane wave.

D.2 Introduction

The approach of Mie theory is as follows. A set of orthogonal basis vectors is selected so that a weighted sum of them is able to accurately represent any electromagnetic vector field. These vectors can usefully be written in terms of a scalar function, and when expressed as a wave equation, the condition for satisfying the vector wave equation becomes equivalent to the condition for satisfying the scalar wave equation — a much easier task. This wave equation is effectively the Helmholtz equation in spherical polar coordinates, and its solutions have radial, azimuthal and polar character (i.e. Bessel functions, trigonometric functions and associated Legendre polynomials respectively). This scalar field can then be used to reconstruct the vector fields. Orthogonality relations are used to ensure that the vectors are appropriate for representing all possible vector fields. Further orthogonality relations are considered between the basis vectors and the incident field, the scattered field and the internal field, and they specify which of the basis vectors should be used to describe the various electromagnetic fields. The expression for the incident field is derived by calculating the overlap between the incident field and the various basis vectors to test for any overlap. In order to derive expressions for the internal and scattered fields, boundary conditions at the surface must be applied along with physical arguments. This simply produces a set of four linear equations with four unknown variables (i.e. the weighting coefficients). Once solved, the fields are completely described and quantities such as the cross-sections can be calculated.

D.3 Electromagnetic fields

First, assume that the field is time-harmonic in a linear, isotropic, homogeneous medium.

$$\mathbf{E} = \mathbf{E}_0 \exp(i(\mathbf{k}\cdot\mathbf{r} - \omega t)) \tag{D.3.1}$$

$$\mathbf{H} = \mathbf{H}_0 \exp(i(\mathbf{k}\cdot\mathbf{r} - \omega t)) \tag{D.3.2}$$

If we then apply the vector-Laplacian operator (this form comes from Lagrange's formula for the vector-triple-product),

$$\nabla^2\mathbf{A} = \nabla(\nabla\cdot\mathbf{A}) - \nabla\times(\nabla\times\mathbf{A}) \tag{D.3.3}$$

to the electric and magnetic fields, remembering that the divergence of a plane wave is zero:

$$\nabla\cdot\mathbf{E} = 0 \tag{D.3.4}$$

$$\nabla\cdot\mathbf{H} = 0 \tag{D.3.5}$$

we obtain the Helmholtz wave-equations for $\mathbf{E}$ and $\mathbf{H}$:

$$\nabla^2\mathbf{E} + k^2\mathbf{E} = 0 \tag{D.3.6}$$

$$\nabla^2\mathbf{H} + k^2\mathbf{H} = 0 \tag{D.3.7}$$

From Maxwell's equations in free space,

$$\nabla\times\mathbf{E} = -\mu\frac{\partial\mathbf{H}}{\partial t} \tag{D.3.8}$$

$$\nabla\times\mathbf{H} = \epsilon\frac{\partial\mathbf{E}}{\partial t} \tag{D.3.9}$$

we know that the electric and magnetic fields (equations D.3.1 and D.3.2) are dependent on each other via:

$$\nabla\times\mathbf{E} = i\omega\mu\mathbf{H} \tag{D.3.10}$$

$$\nabla\times\mathbf{H} = -i\omega\epsilon\mathbf{E} \tag{D.3.11}$$

D.4 Definition of basis vectors

It is the electric and magnetic fields that we want to represent in terms of basis vectors in spherical coordinates. These are just another set of orthogonal vectors which can specify all fields completely. So let us begin by constructing a new vector $\mathbf{M}$ which will form the foundation of the new basis:

$$\mathbf{M} = \nabla \times (\mathbf{c}\psi) \tag{D.4.1}$$

Here, c is a "constant vector" which has unit length. Later, this will define an axis on which the basis is constructed, and ψ is a scalar field (which will become very important and useful shortly).

We know that the divergence of the curl of any vector is zero, so the divergence of equation D.4.1 becomes:

$$\nabla \cdot \mathbf{M} = 0 \tag{D.4.2}$$

If we take the wave-vector of the field described by $\mathbf{M}$ to be $\mathbf{k}$, then we can write the vector wave equation for $\mathbf{M}$ in the same way we did for $\mathbf{E}$ and $\mathbf{H}$:

$$\nabla^2\mathbf{M} + k^2\mathbf{M} = 0 \tag{D.4.3}$$

We can make a substitution to introduce the scalar field ψ into the wave equation. First we need to apply Lagrange's formula and use the fact that the divergence of $\mathbf{M}$ is zero:

$$\nabla^2\mathbf{M} = \nabla(\nabla \cdot \mathbf{M}) - \nabla \times (\nabla \times \mathbf{M}) = -\nabla \times (\nabla \times \mathbf{M}) \tag{D.4.4}$$

Now we can substitute in equation D.4.1:

$$\nabla^2\mathbf{M} = -\nabla \times (\nabla \times (\nabla \times (\mathbf{c}\psi))) \tag{D.4.5}$$

We can now apply the rule for the curl of a product of a scalar and a vector remembering that the vector $\mathbf{c}$ is constant and hence has no curl:

$$\nabla \times (\mathbf{c}\psi) = \psi\nabla \times \mathbf{c} - \mathbf{c} \times \nabla\psi = -\mathbf{c} \times \nabla\psi \tag{D.4.6}$$

This gives:

$$\nabla^2\mathbf{M} = \nabla \times (\nabla \times (\mathbf{c} \times \nabla\psi)) \tag{D.4.7}$$

The following vector identities (equations D.4.8, D.4.9 and D.4.10) are used in the order written (the first is used on the outer curl in equation D.4.8). The identities are used conjunction with equation D.4.2 and the fact that the divergence of a constant vector is 0 in order to cancel all but the first term:

$$\nabla \times (\mathbf{A} \times \mathbf{B}) = \mathbf{A}(\nabla \cdot \mathbf{B}) - \mathbf{B}(\nabla \cdot \mathbf{A}) + (\mathbf{B} \cdot \nabla)\mathbf{A} - (\mathbf{A} \cdot \nabla)\mathbf{B} \tag{D.4.8}$$

$$\nabla(\mathbf{A} \cdot \mathbf{B}) = (\mathbf{A} \cdot \nabla)\mathbf{B} + (\mathbf{B} \cdot \nabla)\mathbf{A} + \mathbf{A} \times (\nabla \times \mathbf{B}) + \mathbf{B} \times (\nabla \times \mathbf{A}) \tag{D.4.9}$$

$$\nabla \cdot (\nabla\psi) = 0 \tag{D.4.10}$$

The many cancellations result in the following simple equation:

$$\nabla^2\mathbf{M} = \nabla \times (\mathbf{c}\nabla^2\psi) \tag{D.4.11}$$

Once this is substituted into equation D.4.3 along with the definition of $\mathbf{M}$ (equation D.4.1), the vector wave equation becomes:

$$\nabla^2\mathbf{M} + k^2\mathbf{M} = \nabla \times \left[\mathbf{c}\left(\nabla^2\psi + k^2\psi\right)\right] = 0 \tag{D.4.12}$$

This is a very important result as it shows that we can find a solution to the vector wave equation by solving the scalar wave equation first which is much simpler.

The electromagnetic wave is comprised of both electric and magnetic components, so our basis needs to account for this. We shall define another vector $\mathbf{N}$ which will form a pair, along with $\mathbf{M}$ which will be able to completely describe both the electric and magnetic fields. $\mathbf{N}$ is defined as follows:

$$\mathbf{N} = \frac{\nabla \times \mathbf{M}}{k} \tag{D.4.13}$$

This equation, along with the following expression demonstrate that the basis vectors **M** and **N** have the necessary properties needed to describe an electromagnetic wave; they each are proportional to the curl of the other variable (just like the electric and magnetic fields).

$$\nabla \times \mathbf{N} = k\mathbf{M} \tag{D.4.14}$$

This field also has zero divergence and satisfies the Helmholtz equation

$$\nabla^2\mathbf{N} + k^2\mathbf{N} = 0 \tag{D.4.15}$$

These waves are ideal for our basis: they have a divergence of zero, the curl of one field is proportional to the other, and they both satisfy the wave equation. We will be solving the scalar wave equation in spherical coordinates, and then use equations D.4.1 and D.4.13 to recover the vector fields. Because of our choice of coordinate system it is convenient to take our constant vector to be the radial vector **r**. This has the effect of making sure the field **M** is always normal to the sphere radius at a particular point.

D.5 Solution of the scalar wave equation (separation of variables)

The scalar wave equation in spherical polar coordinates is:

$$\frac{1}{r^2}\frac{\partial}{\partial r}\left(r^2\frac{\partial\psi}{\partial r}\right) + \frac{1}{r^2\sin\theta}\frac{\partial}{\partial\theta}\left(\sin\theta\frac{\partial\psi}{\partial\theta}\right) + \frac{1}{r^2\sin^2\theta}\frac{\partial^2\psi}{\partial\phi^2} + k^2\psi = 0 \tag{D.5.1}$$

To solve this we use the method of separation of variables, assuming a solution of the form:

$$\psi(r,\theta,\phi) = R(r)\Theta(\theta)\Phi(\phi) \tag{D.5.2}$$

We can substitute this into the wave equation and obtain the following three differential equations for the three variables (the exact from of these equations requires a certain degree of foresight):

$$\frac{d^2\Phi}{d\phi^2} + m^2\Phi = 0 \tag{D.5.3}$$

$$\frac{1}{\sin\theta}\frac{d}{d\theta}\left(\sin\theta\frac{d\Theta}{d\theta}\right) + \left[k^2 - \frac{m^2}{\sin^2\theta}\right]\Theta = 0 \tag{D.5.4}$$

$$\frac{d}{dr}\left(r^2\frac{dR}{dr}\right) + \left[k^2r^2 - n(n+1)\right]R = 0 \tag{D.5.5}$$

D.5.1 Azimuthal part

The first equation (equation D.5.3), for the azimuthal part of the field is straightforward to solve, and it has two solutions, one even, and the other odd (even though these functions are familiar they are plotted in figure D.5.1 as reference will be made to their symmetry later):

$$\Phi_e = \cos(m\phi) \tag{D.5.6}$$

$$\Phi_o = \sin(m\phi) \tag{D.5.7}$$

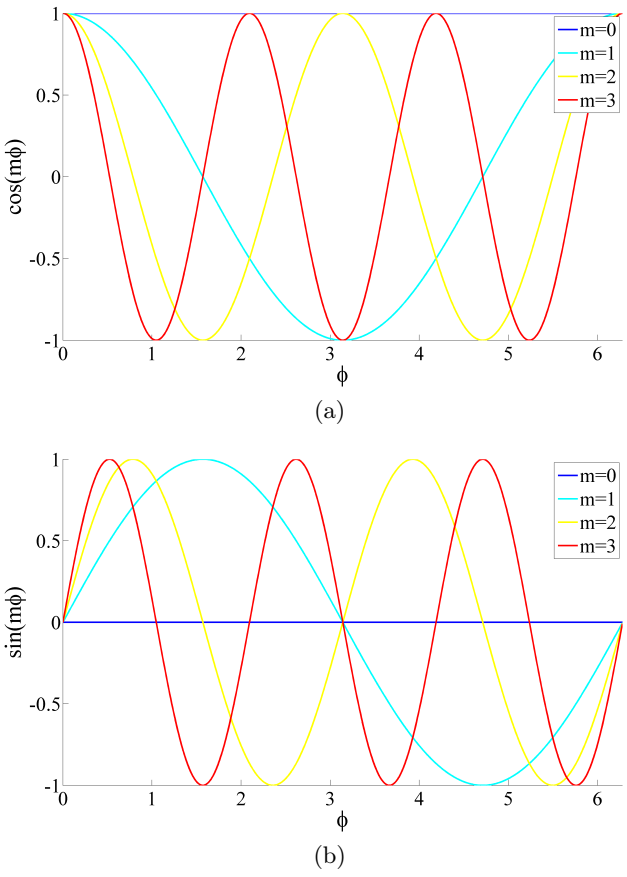

Figure D.5.1: Even (a) and odd (b) solutions to the azimuthal part of the Helmholtz equation.

Here, m is an integer or zero in order that the function is periodic in ϕ and continuous (i.e. $\Phi(\phi) = \Phi(\phi + 2\pi)$).

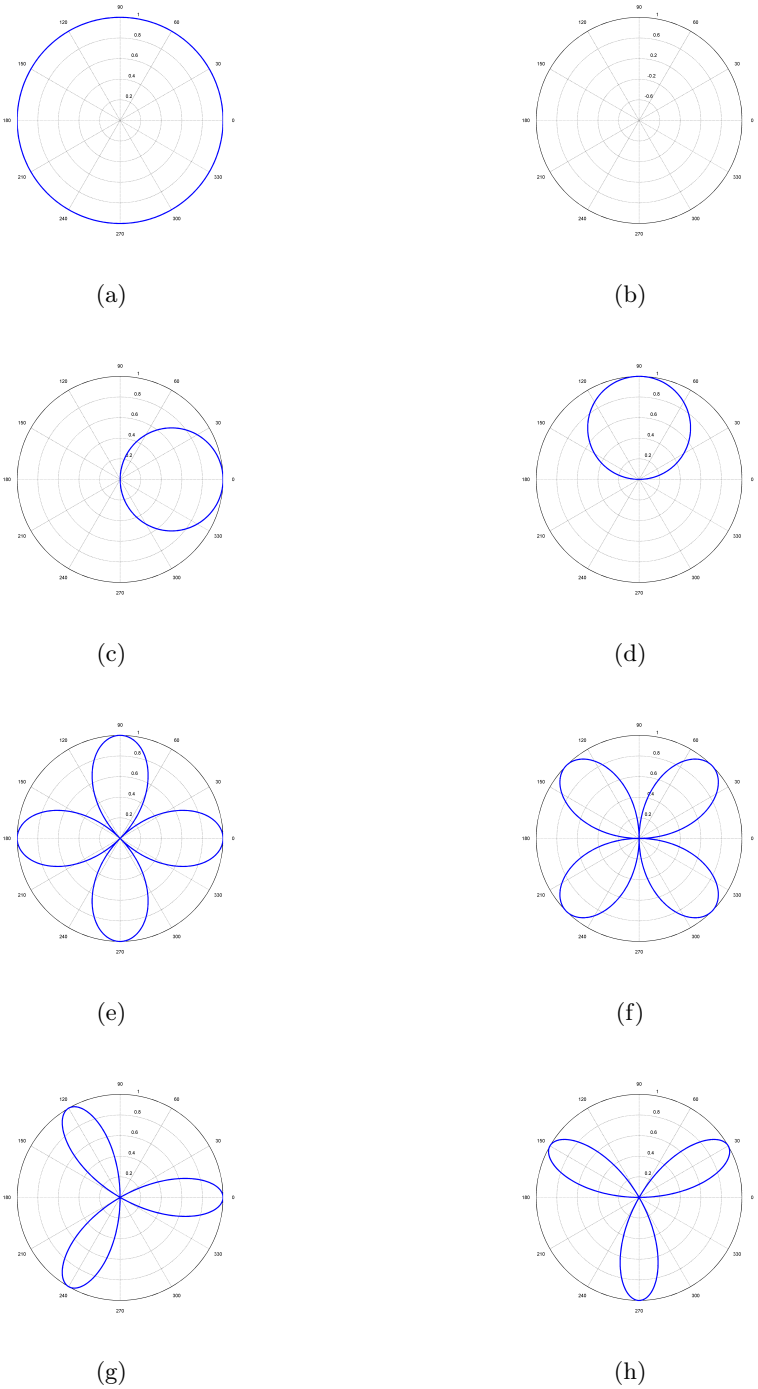

(a) (b) (c) (d) (e) (f) (g) (h)

Figure D.5.2: The first four even (a, c, e, g) and odd (b, d, f, h) solutions to the azimuthal part of the Helmholtz equation (equation D.5.3). Negative values exist, and these are plotted at opposite angles, hence leading to overlap for the odd modes. The magnitudes of these functions are plotted in figure D.5.3.

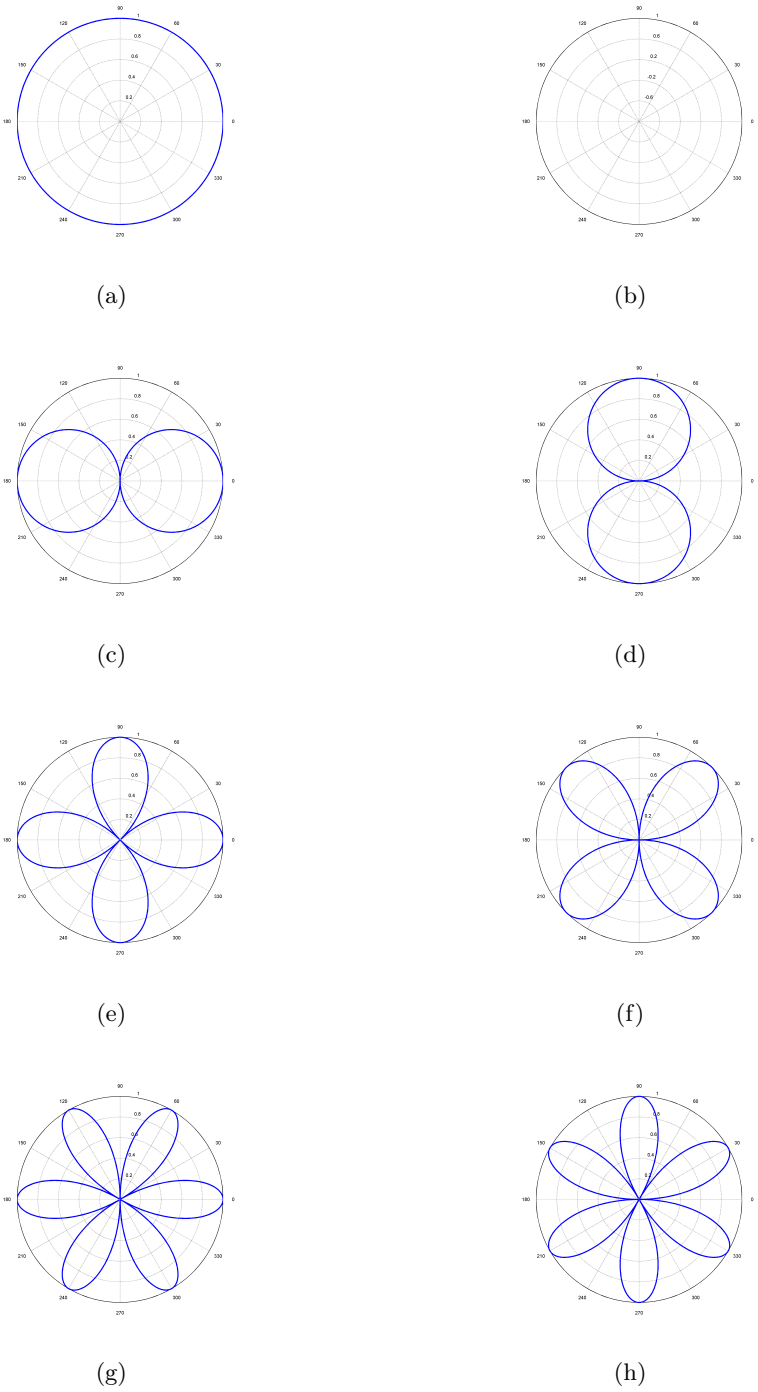

(a) (b) (c) (d) (e) (f) (g) (h)

Figure D.5.3: The magnitudes of the first four even (a, c, e, g) and odd (b, d, f, h) solutions to the azimuthal part of the Helmholtz equation (equation D.5.3). Negative values exist, and these are plotted at opposite angles, hence leading to overlap for the odd modes.

D.5.2 Polar part

The polar equation (equation D.5.4)is more difficult to solve, and we have anticipated the solution by letting the separation variable $k^2 = n(n+1)$ in order for the solution to be finite

at $\theta = 0$ or π (i.e. the polynomial series will converge).

$$\frac{1}{\sin\theta}\frac{d}{d\theta}\left(\sin\theta\frac{d\Theta}{d\theta}\right) + \left[n(n+1) - \frac{m^2}{\sin^2\theta}\right]\Theta = 0 \tag{D.5.8}$$

In order to solve the equation it is useful to make the substitution:

$$x = \cos\theta \tag{D.5.9}$$

This transforms the equation to:

$$(1-x^2)\frac{d^2\Theta}{dx^2} - 2x\frac{d\Theta}{dx} + \left[n(n+1) - \frac{m^2}{1-x^2}\right]\Theta = 0 \tag{D.5.10}$$

This is known as the "associated Legendre equation" and its solutions are in the form of a series of polynomials. To find these solutions we must first substitute:

$$\Theta = (1-x^2)^{m/2}u \tag{D.5.11}$$

This transforms equation D.5.10 into:

$$(1-x^2)\frac{d^2u}{dx^2} - 2(m+1)x\frac{du}{dx} + [n(n+1) - m(m+1)]\,u = 0 \tag{D.5.12}$$

When $m = 0$, this equation is simply known as "Legendre's equation" and solving this first will make solving equation D.5.12 easier:

$$(1-x^2)\frac{d^2u}{dx^2} - 2x\frac{du}{dx} + n(n+1)u = 0 \tag{D.5.13}$$

We now assume the solution to equation D.5.13 to be a series of polynomials:

$$u = a_0 + a_1x + a_2x^2 + a_3x^3 + \cdots + a_lx^l + \ldots \tag{D.5.14}$$

This can be differentiated several times in order to make the necessary substitutions in equation D.5.12:

$$\frac{du}{dx} = a_1 + 2a_2x + 3a_3x^2 + 4a_4x^3 + \ldots + la_lx^{l-1} + \ldots \tag{D.5.15}$$

$$\frac{d^2u}{dx^2} = 2a_3 + 6a_3x + 12a_4x^2 + 20a_5x^3 \ldots + l(l+1)a_l x^{l-2} + \ldots \tag{D.5.16}$$

Once the substitution is made, we are able to collect the coefficients of the various powers of x and make them equal to zero. We are able to do this because we know that any function has only one series expansion, so the equation can be factorised into the various powers of x and then each expression can be set to zero.

So, up to the second power of x we have:

- Constants:

$$2a_2 + n(n+1)a_0 = 0 \tag{D.5.17}$$

- First power of x:

$$6a_3 + (n^2 + n - 2)a_1 = 0 \tag{D.5.18}$$

- Second power of x:

$$12a_4 + (n^2 + n - 6)a_2 = 0 \tag{D.5.19}$$

- The n^{th} power gives:

$$(l+2)(l+1)a_{l+2} + (n^2 + n - l^2 - l)a_l = 0 \tag{D.5.20}$$

The coefficient of a_n can be factorised to give:

$$n^2 + n - l^2 - l = (n+l)(n-l) + (n-l) = (n-l)(n+l+1) \tag{D.5.21}$$

This gives the general expression which can be used to generate subsequent terms in the expansion:

$$a_{l+2} = \frac{(n-l)(n+l+1)}{(l+2)(l+1)}a_l \tag{D.5.22}$$

The equations given above (D.5.17-D.5.19) are included within this new formula. We can now use this general expression to give a complete expression for u, with two constants a_0 and a_1 to be determined by initial conditions (in fact only once these two terms are known is it possible to calculate the other terms in the series):

$$u = a_0 \left[1 - \frac{n(n+1)}{2!}x^2 + \frac{n(n+1)(n-2)(n+3)}{4!}x^4 - \dots\right] + a_1 \left[x - \frac{(n-1)(n+2)}{3!}x^2 + \frac{(n-1)(n+2)(n-3)(n+4)}{5!}x^5 - \dots\right] \quad \text{(D.5.23)}$$

These two series converge for $x^2 < 1$, but don't for $x^2 = 1$. This is a problem as our problem is spherical in nature and we have already made the substitution $x = \cos\theta$. This means that as θ varies from 0 to π, so x varies from -1 to 1 and the series may diverge at those extrema. We now need to consider the effect of setting $n = 0, 1, 2, 3, \dots$ to see if this problem can be eliminated.

When $n = 0$, the a_1 term diverges, but the a_0 term becomes:

$$u = a_0 \quad \text{(D.5.24)}$$

When $n = 1$, the a_0 series diverges, but the a_1 series is zero after the first term (due to $(1-1)$ in the numerator):

$$u = a_1 x \quad \text{(D.5.25)}$$

When $n = 2$, the a_1 series diverges, but the a_0 series is zero after the second term (due to $(2-2)$ in the numerator):

$$u = a_0(1 - 3x^2) \quad \text{(D.5.26)}$$

This process can be continued, and each time, one series will diverge and the other will be truncated after a number of terms. These expressions for u evaluated for different values of n are known as the Legendre polynomials (P_n) and are the solutions to Legendre's equation. Note that here the value of a_0 or a_1 is selected so that $u = 1$ when $x = 1$. This is acceptable as they are still solutions to Legendre's equation, and any scaling factors can be added later which are specific to the particular problem. The first three Legendre polynomials are:

$$P_0 = 1 \quad \text{(D.5.27)}$$

$$P_1 = x \quad \text{(D.5.28)}$$

$$P_2 = \frac{1}{2}(3x^2 - 1) \quad \text{(D.5.29)}$$

Returning now to equation D.5.12, if we differentiate it we obtain:

$$(1-x^2)\frac{d^2}{dx^2}\left(\frac{du}{dx}\right) - 2\left[(m+1)+1\right]x\frac{d}{dx}\left(\frac{du}{dx}\right) + \left[n(n+1)-(m+1)(m+2)\right]\frac{du}{dx} = 0 \tag{D.5.30}$$

This is exactly the same as the equation we started with (equation D.5.12) but with du/dx instead of u, and $(m+1)$ instead of m. In other words, $u = P_n(x)$ is a solution of equation D.5.12 when $m = 0$, $u = \frac{d}{dx}P_n(x)$ is a solution when $m = 1$, $u = \frac{d^2}{dx^2}P_n(x)$ is a solution when $m = 2$ etc., so in general the solution to equation D.5.10 in terms of Θ is:

$$\Theta = (1-x^2)^{m/2}\frac{d^m}{dx^m}P_n(x) \tag{D.5.31}$$

We can therefore write the solutions as a polynomial, much like the unassociated Legendre polynomials:

$$P_n^m(x) = (1-x^2)^{m/2}\frac{d^m}{dx^m}P_n(x) \tag{D.5.32}$$

The functions are known as the 'associated Legendre polynomials' and describe the polar part of the solution to the spherical wave equation. In terms of θthis is written as:

$$P_n^m(x) = \sin^m\theta\frac{d^m}{d(\cos\theta)^m}P_n(\cos\theta) \tag{D.5.33}$$

The first few associated Legendre polynomials in terms of x and $\cos\theta$ are shown below and plotted in figure D.5.4 (for just $m = 1$, looking ahead slightly):

$$P_1^1 = (1-x^2)^{1/2} = \sin\theta \tag{D.5.34}$$

$$P_2^1 = 3x(1-x^2)^{1/2} = 3\cos\theta\sin\theta \tag{D.5.35}$$

$$P_3^1 = \frac{3}{2}(5x^2-1)(1-x^2)^{1/2} = \frac{3}{2}(5\cos^2\theta-1)\sin\theta \tag{D.5.36}$$

$$P_4^1 = \frac{5}{2}(7x^3-3x)(1-x^2)^{1/2} = \frac{5}{2}(7\cos^3\theta-3\cos\theta)\sin\theta \tag{D.5.37}$$

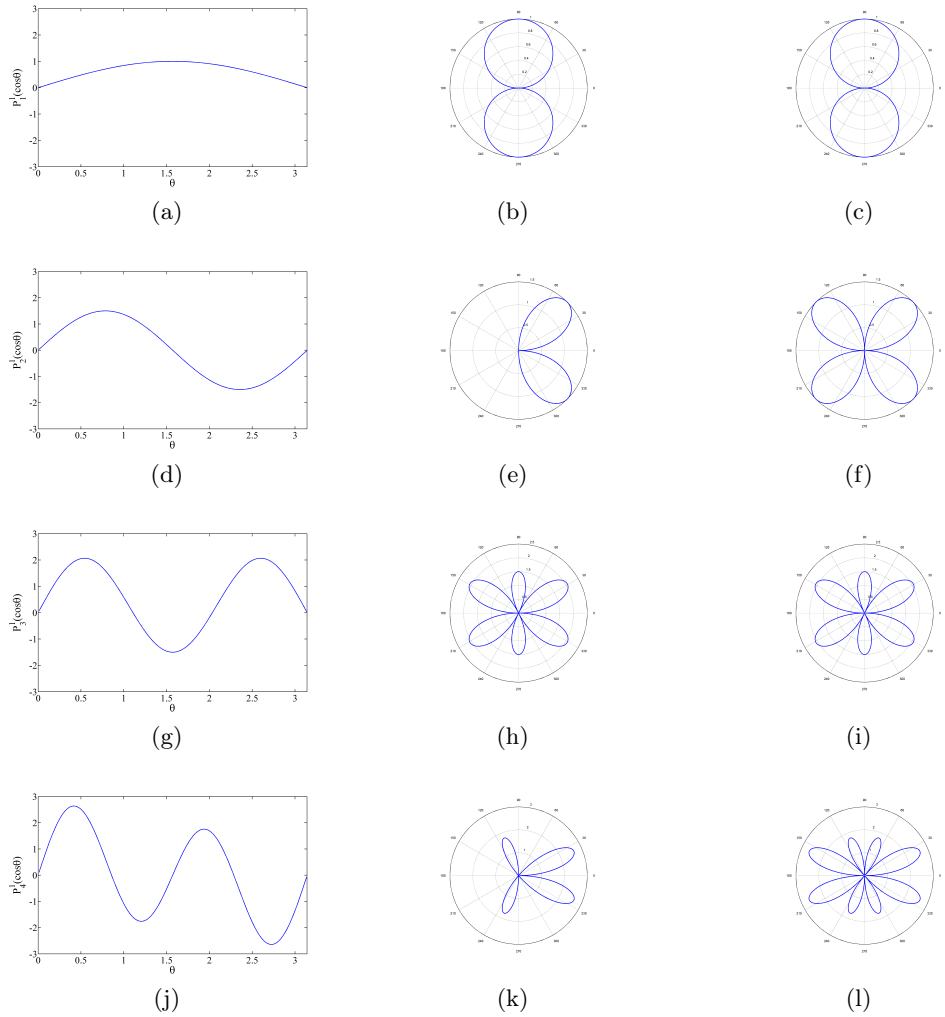

Figure D.5.4: The first four associated Legendre polynomials (equations D.5.34 to D.5.37) with $m = 1$. Line plots against θ are shown (a, d, g, j) as well as the polar plots of the same functions (b, e, h, k) and polar plots of the magnitudes (c, f, i, l) to highlight the symmetry differences between the odd and even polynomials.

D.5.3 Radial part:

If we introduce the following variables into the radial part of the separated equation (equation D.5.5),

$$\begin{aligned} \rho &= kr \\ Z &= R\sqrt{\rho} \end{aligned} \tag{D.5.38}$$

we obtain

$$\rho\frac{d}{d\rho}\left(\rho\frac{dZ}{d\rho}\right)+\left[\rho^2-(n+1/2)^2\right]Z=0 \tag{D.5.39}$$

Let's make the substitution $p=n+1/2$ to simplify the following workings:

$$\rho\frac{d}{d\rho}\left(\rho\frac{dZ}{d\rho}\right)+\left[\rho^2-p^2\right]Z=0 \tag{D.5.40}$$

This is Bessel's equation and can be solved in a similar way as we did for Legendre's equation, i.e. by assuming a series solution of polynomials. Only considering the general terms in the series, we have:

$$Z=\sum_{n=0}^{\infty}a_n\rho^{n+s} \tag{D.5.41}$$

$$\frac{dZ}{d\rho}=\sum_{n=0}^{\infty}a_n(n+s)\rho^{n+s-1} \tag{D.5.42}$$

$$\rho\frac{dZ}{d\rho}=\sum_{n=0}^{\infty}a_n(n+s)\rho^{n+s} \tag{D.5.43}$$

$$\frac{d}{d\rho}\left(\rho\frac{dZ}{d\rho}\right)=\sum_{n=0}^{\infty}a_n(n+s)^2\rho^{n+s-1} \tag{D.5.44}$$

$$\rho\frac{d}{d\rho}\left(\rho\frac{dZ}{d\rho}\right)=\sum_{n=0}^{\infty}a_n(n+s)^2\rho^{n+s} \tag{D.5.45}$$

Here, s is a number to be found.

When these terms are entered into equation D.5.40, we can equate coefficients for powers of ρ (in s, $s+1$, $s+2$ etc.) much like we did for the Legendre polynomials:

For ρ^s:

$$s^2a_0=p^2a_0 \tag{D.5.46}$$

So,

$$s=\pm p \tag{D.5.47}$$

For $\rho^{(s+1)}$:

$$(1+s)^2 a_1 = p^2 a_1 \tag{D.5.48}$$

Using equation D.5.47, we are forced to say that equation D.5.48 can only be satisfied if $a_1 = 0$.

And so on. We will now skip to the general expression for $\rho^{(s+n)}$:

$$\left[(n+s)^2 - p^2\right] a_n + a_{n-2} = 0 \tag{D.5.49}$$

Rewritten in a more useful form, we have:

$$a_n = -\frac{a_{n-2}}{(n+s)^2 - p^2} \tag{D.5.50}$$

When $s = p$ (one of the solutions of equation D.5.47), the coefficients are:

$$a_n = -\frac{a_{n-2}}{n(n+2p)} \tag{D.5.51}$$

Because $a_1 = 0$, all odd terms will also be zero. We can replace n with $2n$ to ensure we have an expression purely for odd a's:

$$a_{2n} = -\frac{a_{2n-2}}{2n(2n+2p)} \tag{D.5.52}$$

These formulae can be simplified by using the gamma function. The gamma function is defined as:

$$\Gamma(p) = \int_0^\infty x^{p-1} e^{-x} dx \tag{D.5.53}$$

(for $p > 0$).

The recursion relation which can generate the values is as follows:

$$\Gamma(p+1) = p\Gamma(p) \tag{D.5.54}$$

So, we have that:

$$\Gamma(p+1) = p\Gamma(p) \tag{D.5.55}$$

$$\Gamma(p+2) = \Gamma(p+2) = (p+1)\Gamma(p+1) \tag{D.5.56}$$

$$\Gamma(p+3) = (p+2)\Gamma(p+2) = (p+2)(p+1)\Gamma(p+1) \tag{D.5.57}$$

And so on. We can now rewrite our coefficients in terms of gamma functions:

$$a_2 = -\frac{a_0}{2(2+2p)} = -\frac{a_0}{2^2(1+p)} = -\frac{a_0}{2^2}\frac{\Gamma(1+p)}{\Gamma(2+p)} \tag{D.5.58}$$

$$a_4 = -\frac{a_2}{2^3(2+p)} = -\frac{a_0}{2!2^4(1+p)(2+p)} = -\frac{a_0}{2!2^4}\frac{\Gamma(1+p)}{\Gamma(3+p)} \tag{D.5.59}$$

$$a_6 = -\frac{a_0}{3!2^6}\frac{\Gamma(1+p)}{\Gamma(4+p)} \tag{D.5.60}$$

For large values of n it is clear that the Γ functions make the expressions a lot tidier (this will lead to simpler computations later on).

The series solution is now:

$$Z = \sum_{n=0}^{\infty} a_n \rho^{n+s} = a_0 \rho^p \Gamma(1+p)\left[\frac{1}{\Gamma(1+p)} - \frac{1}{\Gamma(2+p)}\left(\frac{\rho}{2}\right)^2 + \right.$$
$$\left. + \frac{1}{2!\Gamma(3+p)}\left(\frac{\rho}{2}\right)^4 - \frac{1}{3!\Gamma(4+p)}\left(\frac{\rho}{2}\right)^6 + \ldots\right] \tag{D.5.61}$$

$$Z = a_0 2^p \left(\frac{\rho}{2}\right)^p \rho^p \Gamma(1+p)\left[\frac{1}{\Gamma(1)\Gamma(1+p)} - \frac{1}{\Gamma(2)\Gamma(2+p)}\left(\frac{\rho}{2}\right)^2 + \right.$$
$$\left. + \frac{1}{\Gamma(3)\Gamma(3+p)}\left(\frac{\rho}{2}\right)^4 - \frac{1}{\Gamma(4)\Gamma(4+p)}\left(\frac{\rho}{2}\right)^6 + \ldots\right] \tag{D.5.62}$$

In the last step we have inserted $\Gamma(1)$ and $\Gamma(2)$ for symmetry (both are equal to 1). Also, we have made the substitution $\rho^p = 2^2(\rho/2)^p$. If we use our expression for a_0 having taken $s = p$:

$$a_0 = \frac{1}{2^p\Gamma(1+p)} \tag{D.5.63}$$

Then the solution to Z (equation D.5.62) becomes the "Bessel function of the first kind of order p". This is written (using the new symbol $J_p(\rho)$):

$$J_p(\rho) = \sum_{n=0}^{\infty} \frac{(-1)^n}{\Gamma(n+1)\Gamma(n+p+1)} \left(\frac{\rho}{2}\right)^{2n+p} \tag{D.5.64}$$

The Bessel function of the second kind is the same, but with $s = -p$. This function takes the following form (using the new symbol $Y_p(\rho)$):

$$Y_p(\rho) = \sum_{n=0}^{\infty} \frac{(-1)^n}{\Gamma(n+1)\Gamma(n-p+1)} \left(\frac{\rho}{2}\right)^{2n-p} \tag{D.5.65}$$

Finally, in our initial version of Bessel's equation, our p was equal to $n + 1/2$. When this substitution is made, the resulting functions are known as the spherical Bessel functions and take the following form (and have lower-case symbols):

$$j_n(\rho) = \sqrt{\frac{\pi}{2\rho}} J_{(2n+1)/2}(\rho) \tag{D.5.66}$$

$$y_n(\rho) = \sqrt{\frac{\pi}{2\rho}} Y_{(2n+1)/2}(\rho) \tag{D.5.67}$$

These spherical Bessel functions are plotted in figure for $n = 0,\ 2, \ldots 5$.

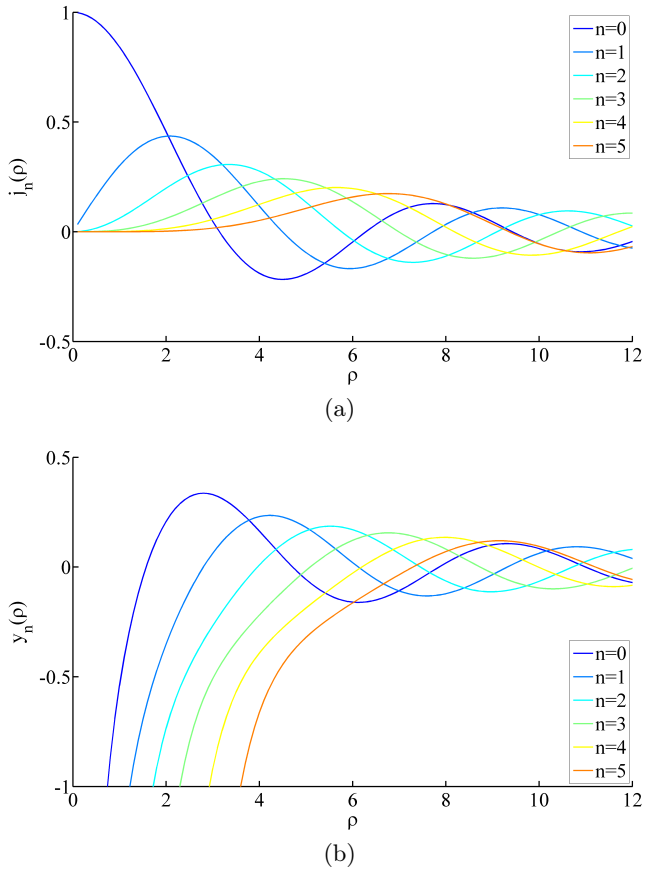

Figure D.5.5: The first six spherical Bessel functions $j_n(\rho)$ and $y_n(\rho)$.

It is also worth mentioning at this point, that any linear combination of Bessel functions also satisfies Bessel's equation, including those with complex coefficients. One such example which will be particularly useful in the derivation of Mie theory is known as the Hankel function (or sometimes Bessel function of the third kind). There are two forms of Hankel functions, and again we are only interested in the "spherical" Hankel functions:

$$\begin{aligned} h_n^{(1)}(\rho) &= j_n(\rho) + iy_n(\rho) \\ h_n^{(2)}(\rho) &= j_n(\rho) - iy_n(\rho) \end{aligned} \tag{D.5.68}$$

Note that from now on z_n will denote any arbitrary spherical Bessel function which is yet to be decided.

D.6 Rewriting the solutions

Now we have solutions for the radial, polar and azimuthal parts of the solution to the scalar wave equation. For the radial component, we have the spherical Bessel functions, for the polar part we have the associated Legendre polynomials, and for the azimuthal part we have the periodic trigonometric functions. Because there is a choice of the even or odd function in the azimuthal part, the scalar wave can be written in two forms:

$$\psi_{emn} = \cos(m\phi)P_n^m(\cos\theta)z_n(kr) \tag{D.6.1}$$

$$\psi_{omn} = \sin(m\phi)P_n^m(\cos\theta)z_n(kr) \tag{D.6.2}$$

Where 'e' stands for even and 'o' stands for odd.

From these scalar equations, we can find the expression for the *vector* spherical harmonics from:

$$\mathbf{M}_{emn} = \nabla \times (\mathbf{r}\psi_{emn}) \tag{D.6.3}$$

$$\mathbf{N}_{emn} = \frac{\nabla \times \mathbf{M}_{emn}}{\mathbf{k}} \tag{D.6.4}$$

$$\mathbf{M}_{omn} = \nabla \times (\mathbf{r}\psi_{omn}) \tag{D.6.5}$$

$$\mathbf{N}_{omn} = \frac{\nabla \times \mathbf{M}_{omn}}{\mathbf{k}} \tag{D.6.6}$$

In terms of their components in spherical coordinates (i.e. by substituting equations D.6.1), we have:

$$\begin{aligned}\mathbf{M}_{emn} =& -\frac{m}{\sin\theta}\sin(m\phi)P_n^m(\cos\theta)z_n(\rho)\hat{\mathbf{e}}_\theta \\ & -\cos(m\phi)\frac{d}{d\theta}P_n^m(\cos\theta)z_n(\rho)\hat{\mathbf{e}}_\phi\end{aligned} \tag{D.6.7}$$

$$\begin{aligned}\mathbf{M}_{omn} =& \frac{m}{\sin\theta}\cos(m\phi)P_n^m(\cos\theta)z_n(\rho)\hat{\mathbf{e}}_\theta \\ & -\sin(m\phi)\frac{d}{d\theta}P_n^m(\cos\theta)z_n(\rho)\hat{\mathbf{e}}_\phi\end{aligned} \tag{D.6.8}$$

$$\begin{aligned}\mathbf{N}_{emn} =& \frac{z_n(\rho)}{\rho}\cos(m\phi)n(n+1)P_n^m(\cos\theta)\hat{\mathbf{e}}_r \\ & +\cos(m\phi)\frac{d}{d\theta}P_n^m(\cos\theta)\frac{1}{\rho}\frac{1}{d\rho}\left[\rho z_n(\rho)\right]\hat{\mathbf{e}}_\theta \\ & -m\sin(m\phi)\frac{P_n^m(\cos\theta)}{\sin\theta}\frac{1}{\rho}\frac{d}{d\rho}\left[\rho z_n(\rho)\right]\hat{\mathbf{e}}_\phi\end{aligned} \tag{D.6.9}$$

$$\begin{aligned}\mathbf{N}_{omn} =& \frac{z_n(\rho)}{\rho}\sin(m\phi)n(n+1)P_n^m(\cos\theta)\hat{\mathbf{e}}_r \\ & +\sin(m\phi)\frac{d}{d\theta}P_n^m(\cos\theta)\frac{1}{\rho}\frac{1}{d\rho}\left[\rho z_n(\rho)\right]\hat{\mathbf{e}}_\theta \\ & +m\cos(m\phi)\frac{P_n^m(\cos\theta)}{\sin\theta}\frac{1}{\rho}\frac{d}{d\rho}\left[\rho z_n(\rho)\right]\hat{\mathbf{e}}_\phi\end{aligned} \tag{D.6.10}$$

These equations represent the vector spherical harmonics and are our new set of basis vectors. They can be used to describe any wave, but clearly they are at most home when describing spherically symmetrical waves, or waves with angular periodicity. Our incident wave is a plane-wave and, unfortunately, it is awkward to express such a wave in terms of spherical harmonics. It is, however, possible and this will be demonstrated in the next section.

D.7 Expansion of a plane wave in spherical harmonics

Our incident plane wave, polarised in the x-direction (figure D.1.1) can simply be written as:

$$\mathbf{E}_i = \mathbf{E}_0 e^{ikr\cos\theta}\hat{\mathbf{e}}_x \tag{D.7.1}$$

The unit vector may be written in spherical coordinates as follows:

$$\hat{\mathbf{e}}_x = \sin\theta\cos\phi\hat{\mathbf{e}}_r + \cos\theta\cos\phi\hat{\mathbf{e}}_\theta - \sin\phi\hat{\mathbf{e}}_\phi \tag{D.7.2}$$

We need to expand $\mathbf{E}_i$in terms of spherical harmonics:

$$\mathbf{E}_i = \sum_{m=0}^{\infty}\sum_{n=0}^{\infty}\left(B_{emn}\mathbf{M}_{emn} + B_{omn}\mathbf{M}_{omn} + A_{emn}\mathbf{N}_{emn} + A_{omn}\mathbf{N}_{omn}\right) \tag{D.7.3}$$

The weighting coefficients A_{emn}, A_{omn}, B_{emn} and B_{omn} are very important as they describe the degree to which each of the spherical harmonics are present in a given field configuration.

In order to describe a plane wave we need to be sure that the various expressions for the vector spherical harmonics are orthogonal. First, we can show that $\sin(m\phi)$ and $\cos(m'\phi)$ are orthogonal for all values of m and m':

$$\int_0^{2\pi} \sin(m\phi)\cos(m'\phi) = 0 \tag{D.7.4}$$

From this it is clear that $\mathbf{M}_{emn}$ and $\mathbf{M}_{omn}$ (from equations D.6.7 and D.6.8) are orthogonal as where cos appears in one equation, sin appears in the other, so:

$$\int_0^{2\pi}\int_0^{\pi} \mathbf{M}_{em'n'} \cdot \mathbf{M}_{omn} \sin\theta d\theta d\phi = 0 \tag{D.7.5}$$

By the same logic, $(\mathbf{N}_{omn}, \mathbf{N}_{emn})$, $(\mathbf{M}_{omn}, \mathbf{N}_{omn})$ and $(\mathbf{M}_{emn}, \mathbf{N}_{emn})$ are all orthogonal pairs of functions. There are two more pairs of functions which we need to check — these are $(\mathbf{M}_{emn}, \mathbf{N}_{omn})$ and $(\mathbf{N}_{emn}, \mathbf{M}_{omn})$. Considerations of factors containing ϕ cannot prove the orthogonality, so we will now turn to θ. We need to show that the following equation becomes zero for all n and n' (this is found by 'dotting' either of these pairs and considering only the factors containing Legendre polynomials):

$$m\int_0^{\pi}\left(P_n^m\frac{dP_{n'}^m}{d\theta} + P_{n'}^m\frac{dP_n^m}{d\theta}\right)d\theta = P_n^m P_{n'}^m|_0^{\pi} \tag{D.7.6}$$

We can re-write things slightly by transforming the associated Legendre function into the m^{th} derivative of the corresponding Legendre polynomial using this relation:

$$P_n^m(\mu) = (1-\mu^2)^{m/2}\frac{d^m P_n(\mu)}{d\mu^m} \tag{D.7.7}$$

where $\mu = \cos\theta$, so for $\theta = 0$ and $\theta = \pi$, P_n^m vanishes, except when $m = 0$. From this we can see that equation D.7.6 vanishes for all m, n and n', so these two pairs of functions are also orthogonal.

Finally, we need to check that the functions are orthogonal with each other for different degrees (i.e. n). We need to show that:

$$\int_0^{2\pi}\int_0^{\pi} \mathbf{M}_{emn} \cdot \mathbf{M}_{emn'} \sin\theta d\theta d\phi = 0 \tag{D.7.8}$$

$$\int_0^{2\pi}\int_0^{\pi} \mathbf{M}_{omn} \cdot \mathbf{M}_{omn'} \sin\theta d\theta d\phi = 0 \tag{D.7.9}$$

$$\int_0^{2\pi}\int_0^{\pi} \mathbf{N}_{emn} \cdot \mathbf{N}_{emn'} \sin\theta d\theta d\phi = 0 \tag{D.7.10}$$

$$\int_0^{2\pi}\int_0^{\pi} \mathbf{N}_{omn} \cdot \mathbf{N}_{omn'} \sin\theta d\theta d\phi = 0 \tag{D.7.11}$$

Let's first only consider the case when $m \neq 0$. Similarly to before, we need to show that:

$$\int_0^{\pi} \left(\frac{dP_n^m}{d\theta}\frac{dP_{n'}^m}{d\theta} + m^2 \frac{P_n^m P_{n'}^m}{\sin^2\theta} \right) \sin\theta d\theta d\phi = 0 \tag{D.7.12}$$

We know that P_n^m and $P_{n'}^m$ satisfy the polar part of the solution to the Helmholtz equation (and hence so does their sum), so, using this we can write:

$$\begin{aligned} 2\sin\theta \left(\frac{dP_n^m}{d\theta}\frac{dP_{n'}^m}{d\theta} + m^2 \frac{P_n^m P_{n'}^m}{\sin^2\theta} \right) = \left\{ n(n+1) + n'(n'+1) \right\} P_n^m P_{n'}^m \sin\theta \\ + \frac{d}{d\theta}\left(\sin\theta \frac{dP_{n'}^m}{d\theta} P_n^m + \sin\theta \frac{dP_n^m}{d\theta} P_{n'}^m \right) \end{aligned} \tag{D.7.13}$$

So, orthogonality is proven as the left-hand-side of equation D.7.13 is equal to the integrand of equation D.7.12 which is equal to zero from the Helmholtz equation.

For the case of a plane wave, we now need actual expressions for A_{emn}, A_{omn}, B_{emn} and B_{omn} in order to express the plane wave in terms of spherical harmonics. The weighting coefficients are effectively the overlap integrals between the spherical harmonics and the field which they are describing. Only the expression for B_{emn} is given here but the others can be written similarly:

$$B_{emn} = \frac{\int_0^{2\pi}\int_0^{\pi} \mathbf{E}_i \cdot \mathbf{M}_{emn} \sin\theta \, d\theta \, d\phi}{\int_0^{2\pi}\int_0^{\pi} |\mathbf{M}_{emn}|^2 \sin\theta \, d\theta \, d\phi} \tag{D.7.14}$$

Vectorially, the orthogonality between the incident field and the separate spherical harmonics (i.e. equations D.6.7-D.6.10 and equation D.7.2) means that both B_{emn} and A_{omn} are equal to 0 (i.e. once the dot product is calculated, the products of sines and cosines vanish when integrated over all angles). Furthermore, the other two coefficients are zero unless $m = 1$. The main physical reason for this orthogonality is that the incident field is a polarised plane wave so the field must not have any variation perpendicular to direction of the k-vector.

This important result means that the incident wave can now be written as:

$$\mathrm{E}_i = \sum_{n=1}^{\infty} \left(B_{o1n}\mathbf{M}_{o1n} + A_{e1n}\mathbf{N}_{e1n} \right) \tag{D.7.15}$$

We can even go one step further and eliminate one of the radial solutions — the expression $y_p(\rho)$ is not finite at the origin so is useless for representing a plane wave. We therefore only take the solutions generated by $j_n(\rho)$. In terms of the notation, we will use a superscript (1) to indicate that the vector spherical harmonics are generated from the scalar function which includes $j_n(\rho)$ alone:

$$\mathrm{E}_i = \sum_{n=1}^{\infty} \left(B_{o1n}\mathbf{M}^{(1)}_{o1n} + A_{e1n}\mathbf{N}^{(1)}_{e1n} \right) \tag{D.7.16}$$

The denominator of equation D.7.14 needs to be evaluated. It is a simple integral to perform using equation D.7.13. A change of variable to $x = \cos\theta$ allows the following definition:

$$\int_{-1}^{1} \left(P_n^m(x)\right)^2 dx = \frac{2}{2n+1}\frac{(n+m)!}{(n-m)!} \tag{D.7.17}$$

This makes the denominator equal to

$$j_n^2 \pi n(n+1)\frac{2}{2n+1}\frac{(n+m)!}{(n-m)!} \tag{D.7.18}$$

The numerator is a bit more tricky to integrate. The integral can be simplified so that it contains

$$\int_0^{\pi} \frac{d}{d\theta}(\sin\theta P_n^1) e^{i\rho\cos\theta} d\theta \tag{D.7.19}$$

We can rewrite this in terms of the non-associated Legendre polynomials using equation D.7.7:

$$\int_0^{\pi} \frac{d}{d\theta}\left(-\sin\theta \frac{P_n}{d\theta} \right) e^{i\rho\cos\theta} d\theta \tag{D.7.20}$$

This can be simplified even further using equation D.5.4 to make D.7.7 proportional to:

$$\int_0^\pi e^{i\rho\cos\theta} P_n \sin\theta d\theta \tag{D.7.21}$$

By coincidence, this is part of an expression for the spherical Bessel function of the first kind:

$$j_n(\rho) = \frac{i^{-n}}{2} \int_0^\pi e^{i\rho\cos\theta} P_n \sin\theta d\theta \tag{D.7.22}$$

The coefficient B_{o1n} can now be written down:

$$B_{o1m} = i^n E_0 \frac{2n+1}{n(n+1)} \tag{D.7.23}$$

Although calculating B_{o1n} was difficult, A_{emn} poses even more problems, but these can be be solved by using the methods above and integrating the integral in the denominator by parts. This leads to:

$$A_{e1n} = -iE_0 i^n \frac{2n+1}{n(n+1)} \tag{D.7.24}$$

The plane wave can now be written completely as:

$$\mathbf{E}_i = E_0 \sum_{n=1}^{\infty} i^n \frac{2n+1}{n(n+1)} (\mathbf{M}_{o1n}^{(1)} - i\mathbf{N}_{e1n}^{(1)}) \tag{D.7.25}$$

D.8 The internal and external fields

So far we have only considered the incident radiation. We can now proceed to examine the modes supported by the spherical object. In addition to the incident field $\mathbf{E}_i$ we can define the internal field $\mathbf{E}_1$ and the external, scattered field $\mathbf{E}_s$. An important boundary condition is:

$$(\mathbf{E}_i + \mathbf{E}_s - \mathbf{E}_1) \times \hat{\mathbf{e}}_r = (\mathbf{H}_i + \mathbf{H}_s - \mathbf{H}_1) \times \hat{\mathbf{e}}_r = 0 \tag{D.8.1}$$

where the magnetic fields are calculated by taking curls of the electric fields. The fields inside the sphere are:

$$\mathbf{E}_1 = E_0 \sum_{n=1}^{\infty} i^n \frac{2n+1}{n(n+1)} (c_n \mathbf{M}_{o1n}^{(1)} - i d_n \mathbf{N}_{e1n}^{(1)}) \tag{D.8.2}$$

$$\mathbf{H}_1 = \frac{-k_1}{\omega \mu_1} E_0 \sum_{n=1}^{\infty} i^n \frac{2n+1}{n(n+1)} (d_n \mathbf{M}_{e1n}^{(1)} - i c_n \mathbf{N}_{o1n}^{(1)}) \tag{D.8.3}$$

where $\mu_1$is the permittivity of the sphere and k_1 is the wave-number inside the sphere and c_n and d_n are coefficients to be found. To arrive at equation D.8.2 we recognised that although the sphere can support modes whose electric fields are described by $\mathbf{M}_{emn}$ and $\mathbf{N}_{omn}$, if it is illuminated by a plane wave, orthogonal modes could not be supported, so we keep the same form of the field. We also ensure that the same spherical Bessel functions are used in order to avoid infinities at the origin.

The Bessel function we have been avoiding so far is suitable to describe the fields outside the sphere as it only becomes infinite at the origin. As mentioned above, Hankel functions are combinations of $j_n(\rho)$ and $y_n(\rho)$ and are reproduced below:

$$h_n^{(1)}(\rho) = j_n(\rho) + i y_n(\rho) \tag{D.8.4}$$

$$h_n^{(2)}(\rho) = j_n(\rho) - i y_n(\rho) \tag{D.8.5}$$

These two expressions are analogous to $e^{\pm x} = \cos x \pm i \sin x$, one of which corresponding to a forward propagating wave, and the other corresponding to a backward propagating wave. From this analogy (which is in agreement with a more rigorous treatment) we take only the solutions $h_n^{(1)}$ because it is unphysical for a scattered field to be propagating towards the scatterer. The scattered fields are calculated from the boundary condition above and are hence written as:

$$\mathbf{E}_s = E_0 \sum_{n=1}^{\infty} i^n \frac{2n+1}{n(n+1)} (i a_n \mathbf{N}_{e1n}^{(3)} - b_n \mathbf{M}_{o1n}^{(3)}) \tag{D.8.6}$$

$$\mathbf{H}_s = \frac{k_1}{\omega \mu_1} E_0 \sum_{n=1}^{\infty} i^n \frac{2n+1}{n(n+1)} (i b_n \mathbf{N}_{o1n}^{(3)} - a_n \mathbf{M}_{e1n}^{(3)}) \tag{D.8.7}$$

where the superscript (3) is used to define Hankel functions of the first kind ($h_n^{(1)}(\rho)$).

D.9 Angular dependence

Computations can be made simpler if the following angle dependent functions are defined:

$$\pi_n = \frac{P_n^1}{\sin\theta} \tag{D.9.1}$$

$$\tau_n = \frac{dP_n^1}{d\theta} \tag{D.9.2}$$

Polar plots of π_n and τ_n are shown for $n = 1, 2 \ldots 5$ in figures D.9.1 and D.9.2 with the magnitude of the function plotted alongside the actual values.

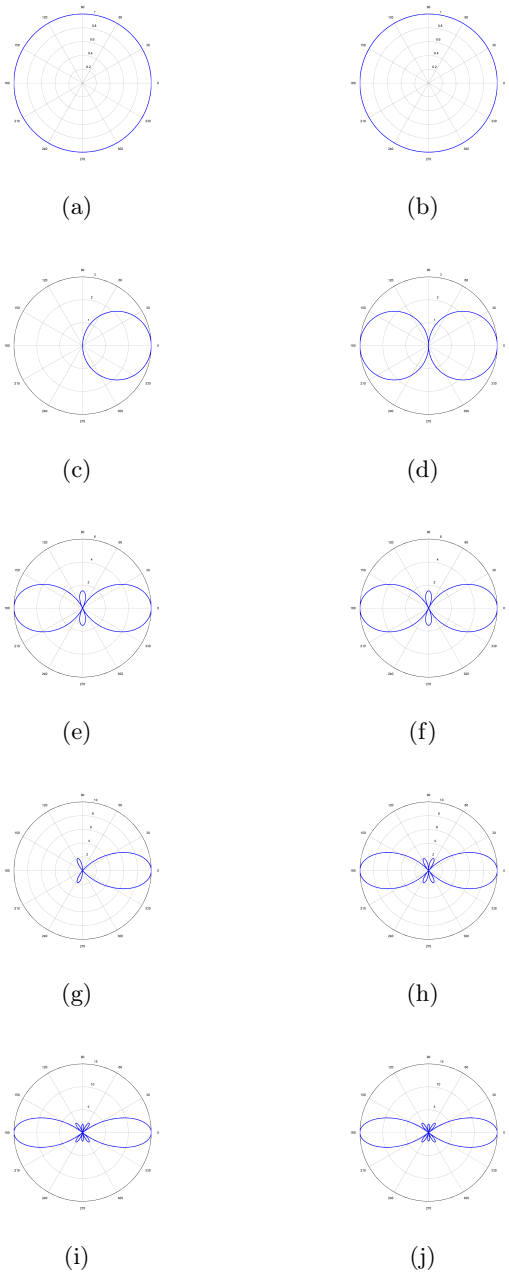

(a) (b)

(c) (d)

(e) (f)

(g) (h)

(i) (j)

Figure D.9.1: The first five functions π_n where $n = 1, 2 \ldots 5$. Shown here are the actual values with negative values hidden for odd functions (a, c, e, g, i) and their corresponding magnitudes (b, d, f, h, j)

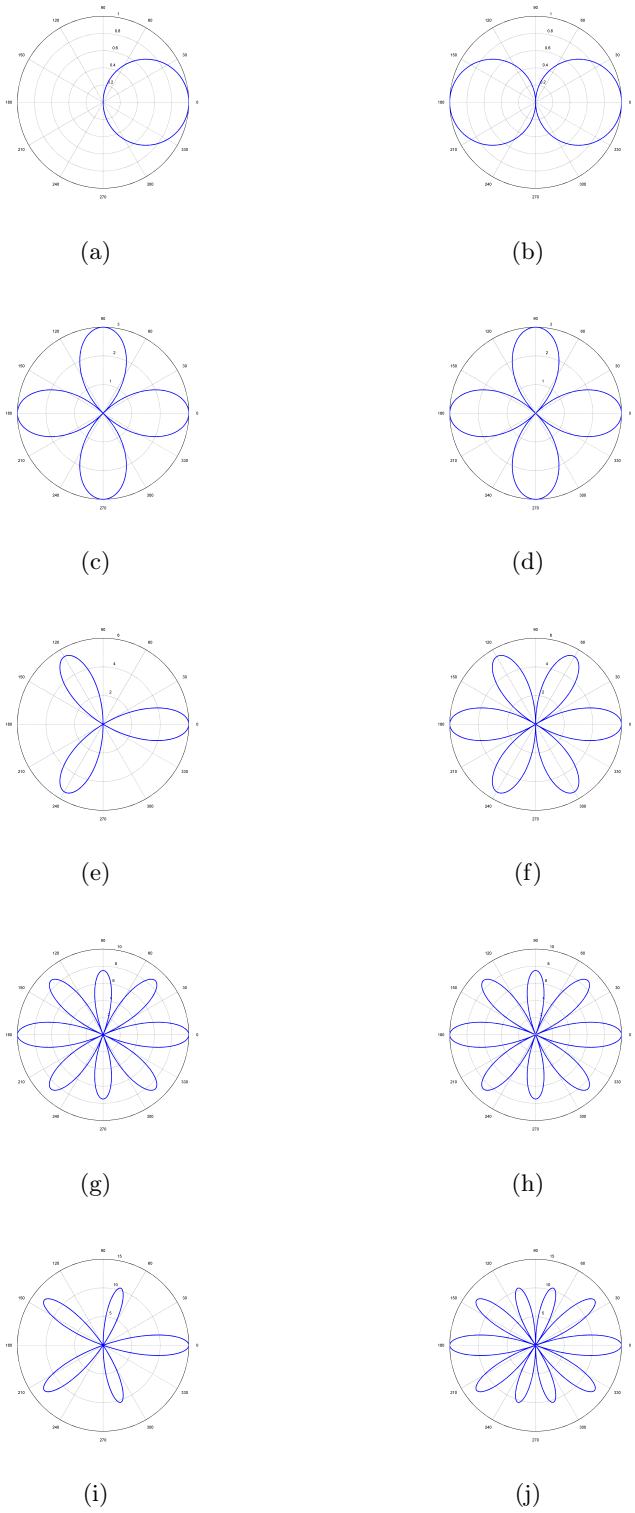

(a) (b) (c) (d) (e) (f) (g) (h) (i) (j)

Figure D.9.2: The first five functions τ_n where $n = 1, 2 \ldots 5$. Shown here are the actual values with negative values hidden for odd functions (a, c, e, g, i) and their corresponding magnitudes (b, d, f, h, j)

These can be generated from the recurrence relations with $\mu = \cos\theta$:

$$\pi_n = \frac{2n+1}{n-1}\mu\pi_{n-1} - \frac{n}{n-1}\pi_{n-2} \tag{D.9.3}$$

$$\tau_n = n\mu\pi_n - (n+1)\pi_{n-1} \tag{D.9.4}$$

and the starting conditions are $\pi_0 = 0$ and $\pi_1 = 1$. The vector spherical harmonics can now be rewritten with these angular dependent functions:

$$\mathbf{M}_{e1n} = -\sin\phi\pi_n(\cos\theta)z_n(\rho)\hat{\mathbf{e}}_\theta - \cos\phi\tau_n(\cos\theta)z_n(\rho)\hat{\mathbf{e}}_\phi \tag{D.9.5}$$

$$\mathbf{M}_{o1n} = \cos\phi\pi_n(\cos\theta)z_n(\rho)\hat{\mathbf{e}}_\theta - \sin\phi\tau_n(\cos\theta)z_n\hat{\mathbf{e}}_\phi \tag{D.9.6}$$

$$\begin{aligned}\mathbf{N}_{e1n} =& \frac{z_n(\rho)}{\rho}\cos\phi n(n+1)\sin\theta\pi_n(\cos\theta)\hat{\mathbf{e}}_r \\ &+ \cos\phi\tau_n(\cos\theta)\frac{[\rho z_n(\rho)]'}{\rho}\hat{\mathbf{e}}_\theta \\ &- \sin\phi\pi_n(\cos\theta)\frac{[\rho z_n(\rho)]'}{\rho}\hat{\mathbf{e}}_\phi\end{aligned} \tag{D.9.7}$$

$$\begin{aligned}\mathbf{N}_{o1n} =& \frac{z_n(\rho)}{\rho}\sin\phi n(n+1)\sin\theta\pi_n(\cos\theta)\hat{\mathbf{e}}_r \\ &+ \sin\phi\tau_n(\cos\theta)\frac{[\rho z_n(\rho)]'}{\rho}\hat{\mathbf{e}}_\theta \\ &+ \cos\phi\pi_n\frac{[\rho z_n(\rho)]'}{\rho}\hat{\mathbf{e}}_\phi\end{aligned} \tag{D.9.8}$$

We have omitted superscripts which indicate the exact Bessel function which should be used, but they will be added later with (1) denoting $j_n(k_1 r)$ and (3) denoting $h_n^{(1)}(kr)$. These equations only contain π_n, τ_n and associated Legendre polynomials, so it is useful to know the form these functions take. These are shown in figures D.5.4, D.9.1 and D.9.2.

It should be noted that some of the angular values are not shown because they are negative and overlap with symmetrical portions of the plotted functions. This demonstrates that there is often a phase difference of π between forward- and back-scattered radiation depending on the mode which is excited.

When it comes to describing the modes which can be supported by spheres, it is possible to split them into two groups — transverse magnetic modes (where there is no radial magnetic component) and transverse electric modes (where there is no radial electric field component).

It is a combination of these modes which describe the scattered field entirely (equations D.8.6 and D.8.7).

These modes, though well defined mathematically, are not easy to understand physically, so we will proceed to calculate some physical quantities before returning to the physics in more detail.

D.10 Mie coefficients

As shown in equations D.8.6 and D.8.7, the scattered field is specified by a weighted series of spherical harmonics. The weighting coefficients a_n and b_n must be found in order that the scattered field can be calculated explicitly. Similarly, c_n and b_n need to be calculated to specify the internal field unambiguously.

For each mode the following boundary conditions apply at the surface of the sphere:

$$E_{i\theta} + E_{s\theta} = E_{1\theta} \tag{D.10.1}$$
$$E_{i\phi} + E_{s\phi} = E_{1\phi} \tag{D.10.2}$$
$$H_{i\theta} + H_{s\theta} = H_{1\theta} \tag{D.10.3}$$
$$H_{i\phi} + H_{s\phi} = H_{1\phi} \tag{D.10.4}$$

We can use the expressions for the incident field (equation D.7.25 and its associated magnetic field), the internal field (equations D.8.2 and D.8.3) and the scattered field (equations D.8.6 and D.8.7) along with the boundary conditions above (equations D.10.1 to D.10.4), the orthogonality of $\sin\phi$ and $\cos\phi$, the orthogonality of $\tau_n + \pi_n$ and $\tau_n - \pi_n$ and the vector spherical harmonics (equations D.9.5-D.9.8) in order to obtain a set of linear equations in terms of the Mie coefficients (a lot of tedious algebra):

$$j_n(mx)c_n + h_n^{(1)}(x)b_n = j_n(x) \tag{D.10.5}$$
$$\mu\left[mxj_n(mx)\right]' c_n + \mu_1\left[xh_n^{(1)}(x)\right]' b_n = \mu_1\left[xj_n(x)\right]' \tag{D.10.6}$$
$$\mu m j_n(mx)d_n + \mu_1 h_n^{(1)}(x)a_n = \mu_1 j_n(x) \tag{D.10.7}$$
$$\left[mxj_n(mx)\right]' d_n + m\left[xh_n^{(1)}(x)\right]' a_n = m\left[xj_n(x)\right]' \tag{D.10.8}$$

Here we have used $x = ka$ (a is the radius and k is the wave-number) and $m = N_1/N$ (where N_1 is the refractive index of the sphere and N is the refractive index of the surrounding medium). These equations are solved straightforwardly:

$$a_n = \frac{\mu m^2 j_n(mx)[xj_n(x)]' - \mu_1 j_n(x)[mxj_n(mx)]'}{\mu m^2 j_n(mx)[xh_n^{(1)}(x)]' - \mu_1 h_n^{(1)}(x)[mxj_n(mx)]'} \quad \text{(D.10.9)}$$

$$b_n = \frac{\mu_1 j_n(mx)[xj_n(x)]' - \mu j_n(x)[mxj_n(mx)]'}{\mu_1 j_n(mx)[xh_n^{(1)}(x)]' - \mu h_n^{(1)}(x)[mxj_n(mx)]'} \quad \text{(D.10.10)}$$

$$c_n = \frac{\mu_1 j_n(x)[xh_n^{(1)}(x)]' - \mu_1 h_n(x)[xj_n(mx)]'}{\mu_1 j_n(mx)[xh_n^{(1)}(x)]' - \mu h_n^{(1)}(x)[mxj_n(mx)]'} \quad \text{(D.10.11)}$$

$$d_n = \frac{\mu_1 m j_n(x)[xh_n^{(1)}(x)]' - \mu_1 m h_n^{(1)}(x)[xj_n(x)]'}{\mu m^2 j_n(mx)[xh_n^{(1)}(x)]' - \mu_1 h_n^{(1)}(x)[mxj_n(mx)]'} \quad \text{(D.10.12)}$$

The dominant coefficient will be the one with the smallest (i.e. zero) denominator. This will not be discussed in detail because the resulting resonant frequency is complex and does not aid the physical understanding of the problem.

The scattering coefficients (equations D.10.9 and D.10.10) can be re-written in a slightly simpler form using the Riccati- Bessel functions:

$$\psi_n(\rho) = \rho j_n(\rho) \quad \text{(D.10.13)}$$

$$\xi_n(\rho) = \rho h_n(\rho) \quad \text{(D.10.14)}$$

Assuming the sphere and the surrounding medium to be non-magnetic ($\mu = \mu_1 = 1$), we now have:

$$a_n = \frac{m\psi_n(mx)\psi_n'(x) - \psi_n(x)\psi_n'(mx)}{m\psi_n(mx)\xi_n'(x) - \xi_n(x)\psi_n'(mx)} \quad \text{(D.10.15)}$$

$$b_n = \frac{\psi_n(mx)\psi_n'(x) - m\psi_n(x)\psi_n'(mx)}{\psi_n(mx)\xi_n'(x) - m\xi_n(x)\psi_n'(mx)} \quad \text{(D.10.16)}$$

D.11 Angular scattering profiles and cross-sections

In order to compute the total scattered power (and hence the scattering cross-section) we need to integrate the scattered time-averaged Poynting vector over all angles (where $\hat{\mathbf{n}}$ is the outward surface normal to an arbitrary imaginary sphere which is concentric with the sphere under consideration but larger):

$$W_{scatt} = \int_0^{2\pi}\int_0^{\pi} \bar{\mathbf{S}} \cdot \hat{\mathbf{n}} \sin\theta \, d\theta \, d\phi = \frac{1}{2}\Re \int_0^{2\pi}\int_0^{\pi} (\mathbf{E}_s \times \mathbf{H}_s^*) \cdot \hat{\mathbf{n}} r^2 \sin\theta \, d\theta \, d\phi \quad \text{(D.11.1)}$$

We know that in the far-field there are only θ- and ϕ-components of the fields, so we can ignore radial components. We also know that the electric and magnetic fields are always perpendicular to each other. This allows equation D.11.1 to be expanded to give (by calculating the matrix determinant):

$$W_{scatt} = \frac{1}{2}\Re\int_0^{2\pi}\int_0^{\pi}\left(E_{s,\theta}H^*_{s,\phi} - E_{s,\phi}H^*_{s,\theta}\right)r^2\sin\theta\,d\theta\,d\phi \tag{D.11.2}$$

The spherical symmetry of the problem allows us to assume an arbitrary polarisation state, and the far-field quantities will remain unchanged. Without derivation, we state the alternative form of the Hankel function which describes the scattered field:

$$z_n^{(3)} \quad = h_n^{(1)} \quad = i\rho^n\left(-\frac{1}{\rho}\frac{d}{d\rho}^n\right)\left(\frac{e^{i\rho}}{\rho}\right) \tag{D.11.3}$$

This can be simplified to the following asymptotic value when ρ is large:

$$h_n^{(1)} \simeq \frac{(-i)^n}{i\rho}e^{i\rho} \tag{D.11.4}$$

Furthermore, without derivation (it is based on an identity) we state the asymptotic form of the derivative of this Bessel function:

$$\frac{dh_n^{(1)}}{d\rho} \simeq \frac{(-i)^n}{\rho}e^{i\rho} \tag{D.11.5}$$

If we now return to the components of the scattered field $\mathbf{E}_s$ from equation D.8.6 we have (whose terms are from equations D.9.5 and D.9.8):

$$E_{s,\theta} \simeq E_0\sum_{n=1}^{\infty}i^n\frac{2n+1}{n(n+1)}\left[ia_n\cos\phi\tau_n(\cos\theta)\frac{[\rho z_n(\rho)]'}{\rho} - b_n\cos\phi\pi_n(\cos\theta)z_n(\rho)\right] \tag{D.11.6}$$

$$E_{s,\phi} \simeq E_0\sum_{n=1}^{\infty}i^n\frac{2n+1}{n(n+1)}\left[-ia_n\sin\phi\pi_n(\cos\theta)\frac{[\rho z_n(\rho)]'}{\rho} - b_n\sin\phi\tau_n(\cos\theta)z_n\right] \tag{D.11.7}$$

From this we obtain, using the product rule and the asymptotic version of the spherical Bessel functions and the fact that the series will converge after certain number of terms:

$$E_{s,\theta} \simeq E_0 \sum_{n=1}^{\infty} i^n \frac{2n+1}{n(n+1)} \left[i a_n \cos\phi \tau_n(\cos\theta) \left(\frac{(-i)^n}{\rho} e^{i\rho} + \frac{(-i)^n}{i\rho^2} e^{i\rho} \right) \right.$$
$$\left. - b_n \cos\phi \pi_n(\cos\theta) \frac{(-i)^n}{i\rho} e^{i\rho} \right] \quad \text{(D.11.8)}$$

$$E_{s,\phi} \simeq E_0 \sum_{n=1}^{\infty} i^n \frac{2n+1}{n(n+1)} \left(-i a_n \sin\phi \pi_n(\cos\theta) \left(\frac{(-i)^n}{\rho} e^{i\rho} + \frac{(-i)^n}{i\rho^2} e^{i\rho} \right) \right.$$
$$\left. + b_n \sin\phi \tau_n(\cos\theta) \frac{(-i)^n}{i\rho} e^{i\rho} \right) \quad \text{(D.11.9)}$$

If we now eliminate terms containing ρ^{-2} we have:

$$E_{s,\theta} \simeq E_0 \sum_{n=1}^{\infty} i^n \frac{2n+1}{n(n+1)} \left(i a_n \cos\phi \tau_n(\cos\theta) \frac{(-i)^n}{\rho} e^{i\rho} - b_n \cos\phi \pi_n(\cos\theta) \frac{(-i)^n}{i\rho} e^{i\rho} \right) \quad \text{(D.11.10)}$$

$$E_{s,\phi} \simeq E_0 \sum_{n=1}^{\infty} i^n \frac{2n+1}{n(n+1)} \left(-i a_n \sin\phi \pi_n(\cos\theta) \frac{(-i)^n}{\rho} e^{i\rho} + b_n \sin\phi \tau_n(\cos\theta) \frac{(-i)^n}{i\rho} e^{i\rho} \right) \quad \text{(D.11.11)}$$

Rewriting, dropping the arguments of π_n and τ_n, and using the fact that for integer n, $i^n(-i)^n = 1$ we obtain:

$$E_{s,\theta} \simeq -E_0 \cos\phi \frac{e^{i\rho}}{i\rho} \sum_{n=1}^{\infty} \frac{2n+1}{n(n+1)} \left(a_n \tau_n + b_n \pi_n \right) \quad \text{(D.11.12)}$$

$$E_{s,\phi} \simeq +E_0 \sin\phi \frac{e^{i\rho}}{i\rho} \sum_{n=1}^{\infty} \frac{2n+1}{n(n+1)} \left(a_n \pi_n + b_n \tau_n \right) \quad \text{(D.11.13)}$$

These expressions provide the angular distribution of electric field far from the sphere which we will consider next. We assume that $a_n = 1$ and $b_n = 0$ based on the symmetry of the system considering that we are polarised along the x-direction (the terms governed by b_n simply describe the same modes when the intensity is calculated but the fields are rotated by an azimuthal angle of 90°). This allows us to concentrate on the angular distribution of the

modes which, in the process of a real calculation, will be weighted by the Mie components. We can now plot angle-dependent intensity plots ($I(\theta, \phi) \simeq \tau_n^2 \cos^2\phi + \pi_n^2 \sin^2\phi$) over θ and ϕ. The angular distribution of the first five modes are shown in figure D.11.1.

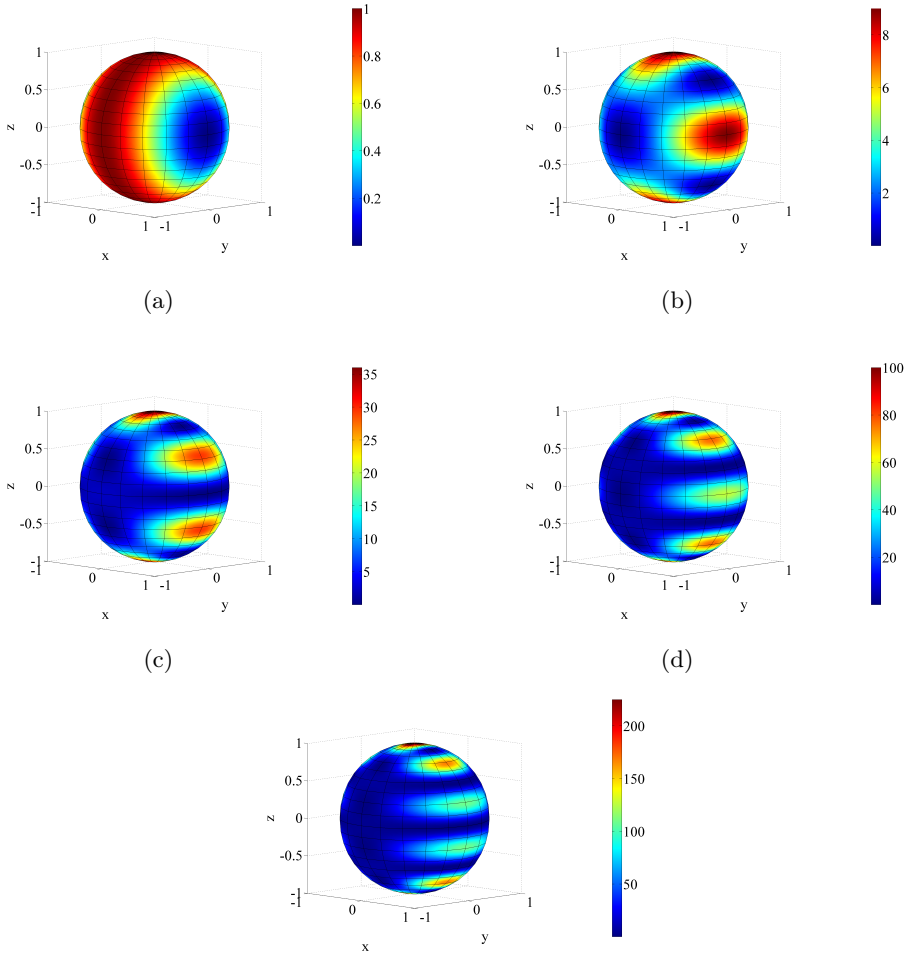

Figure D.11.1: The first five angular scattering profiles. The far-field intensity is plotted against θ and ϕ (all prefactors are omitted and it is assumed that $a_n = 1$ and $b_n = 0$).

In order to calculate the scattering cross-section, the integrated scattered intensity is normalised by the incident intensity. Once the integration is carried out, the final expression is:

$$C_{sca} = \frac{2\pi}{k^2} \sum_{n=1}^{\infty} (2n+1) \left(|a_n|^2 + |b_n|^2 \right) \tag{D.11.14}$$

The extinction cross-section can be calculated using the optical theorem:

$$C_{ext} = \frac{4\pi}{k^2}\Re\left(F\left(0^\circ\right)\right) \tag{D.11.15}$$

The angular functions F for the θ and ϕ components are as follows:

$$F_\theta = \sum_{n=1}^{\infty}\frac{2n+1}{n(n+1)}\left(a_n\tau_n + b_n\pi_n\right) \tag{D.11.16}$$

$$F_\phi = \sum_{n=1}^{\infty}\frac{2n+1}{n(n+1)}\left(a_n\pi_n + b_n\tau_n\right) \tag{D.11.17}$$

From figures D.9.1 and D.9.2 it can be seen that for forward-scattered light ($\theta = 0^\circ$), $\pi_n(\cos(0)) = \tau_n(\cos(0))$, so we can write:

$$F_\theta(0) = F_\phi(0) = \sum_{n=1}^{\infty}\pi_n(\cos(0))\frac{2n+1}{n(n+1)}\left(a_n + b_n\right) \tag{D.11.18}$$

In order to find an expression for $\pi_n(\cos(0))$ we turn to equations D.9.1 and D.9.2 and substitute the expression for τ_n into equation D.7.7 we obtain:

$$\pi_n \quad (\cos(0)) = \tau_n(\cos(0)) = \left.\frac{dP_n}{d(\cos(\theta))}\right|_{\theta=0} \tag{D.11.19}$$

The Legendre polynomials are solutions to equation D.5.13 which we need to rewrite in terms of $x = \cos(\theta)$:

$$\sin^2\theta\frac{d^2P_n}{(d\cos\theta)^2} - 2\cos\theta\frac{dP_n}{d\cos\theta} + n(n+1)P_n = 0 \tag{D.11.20}$$

When $\theta = 0$, we can write this as:

$$\frac{dP_n}{d\cos\theta} = \frac{n(n+1)}{2}P_n = 0 \tag{D.11.21}$$

We know that $P_n(x) = x$, so $P_n(\cos 0) = \cos 0 = 1$, so our expression for π_n and τ_n at $\theta = 0$ becomes:

$$\pi_n(\cos(0)) = \tau_n(\cos(0)) = \frac{n(n+1)}{2} \tag{D.11.22}$$

and hence our expression for the extinction cross-section in the form of the optical theorem can now be written as:

$$C_{ext} = \frac{4\pi}{k^2}\Re\left(\sum_{n=1}^{\infty}(n+1/2)\left(a_n+b_n\right)\right) \tag{D.11.23}$$

Finally, the absorption cross-section can be inferred from the extinction and scattering cross-sections (it can be calculated independently by integrating the total Poynting vector over the surface of the sphere):

$$C_{abs} = \frac{4\pi}{k^2}\Re\left(\sum_{n=1}^{\infty}(n+1/2)\left(a_n+b_n\right)\right) - \frac{2\pi}{k^2}\sum_{n=1}^{\infty}(2n+1)\left(|a_n|^2+|b_n|^2\right) \tag{D.11.24}$$

Appendix E

The coupled dipole approximation (CDA)

The coupled dipole model (CDA), also known as the discrete dipole model (DDA)[49,50] is a very useful and flexible numerical modelling technique. It is primarily used to solve electrodynamic problems of two distinct types:

1. Electrodynamic systems with arbitrary geometry for which no analytical solution exists, for example the plasmonic response of a single truncated tetrahedron. These three-dimensional structures are usually split into thousands of small, but finite cubic elements, each of which may be attributed with a dipole moment which is calculated on application of an external field. From this, the values of the electric field at any point may be calculated, as well as scattering profiles in the far-field.

2. Systems consisting of many distinct, but interacting particles which are small enough to be described by an effective polarisability, for example, arrays of metallic nanoparticles which are so small that they cannot support an observable quadrupolar mode.

It is the second of these problems which we shall use in order to analyse the response of particles in arrays. The method allows the electrodynamics of the system to be solved in a self-consistent way i.e. it takes into account the interactions between all pairs of particles in the array. At the heart of the method is the electric field of an oscillating dipole (ignoring the time dependent prefactor $e^{-i\omega t}$):

$$\boldsymbol{E}_d = \frac{1}{4\pi\epsilon_0} e^{i\boldsymbol{k}\cdot\boldsymbol{r}} \left\{ \frac{k^2}{r} \left[(\hat{\boldsymbol{r}} \times \boldsymbol{p}) \times \hat{\boldsymbol{r}} \right] + \left(\frac{1}{r^3} - \frac{ik}{r^2} \right) \left[3\hat{\boldsymbol{r}}(\hat{\boldsymbol{r}} \cdot \boldsymbol{p}) - \boldsymbol{p} \right] \right\} \tag{E.0.1}$$

The field at a given, indexed, point (i) in the system is the incident field, plus the sum of the contributions from all other particles:

$$\boldsymbol{E}_i = \boldsymbol{E}_{\mathrm{inc},i} - \sum_{i \neq j} \boldsymbol{E}_{ij} \tag{E.0.2}$$

The field contributions from all the other particles are proportional to their dipole moments, so we can introduce a new quantity, the interaction parameter, A_{ij}, which describes the degree to which a given dipole moment at point j produces a field at point i, so we now have

$$\boldsymbol{E}_i = \boldsymbol{E}_{\mathrm{inc},i} - \sum_{i \neq j} A_{ij} \boldsymbol{p}_j \tag{E.0.3}$$

where

$$A_{ij} = \frac{e^{ikr_{ij}}}{r_{ij}} \left\{ k^2 \left(\hat{\boldsymbol{r}} \otimes \hat{\boldsymbol{r}} - I_3 \right) + \left(\frac{ikr_{ij} - 1}{r_{ij}^2} \right) \left(3\hat{\boldsymbol{r}} \otimes \hat{\boldsymbol{r}} - I_3 \right) \right\} \tag{E.0.4}$$

Here, I_3 is the 3×3 identity matrix. A_{ij} is also a 3×3 matrix and is a very important tool in determining the three Cartesian components of the electric field at a point, i, due to a dipole moment at j when the displacement vector and wave-vector are known. One final assumption is made to simplify the problem considerably, and that is to assume that:

$$A_{ii} = \frac{1}{\alpha_i} \tag{E.0.5}$$

where $\alpha_i$is the polarisability of the particle at position i (i.e. $\alpha_i \boldsymbol{E}_i = \boldsymbol{p}_i$). From this the problem reduces to the following equation for N particles:

$$\boldsymbol{E}_{\mathrm{inc},i} = \sum_{j=1}^{N} A_{ij} \boldsymbol{p}_j \tag{E.0.6}$$

To transform this into an easily solvable form, we construct large column vectors $\tilde{\boldsymbol{p}}$ and $\tilde{\boldsymbol{E}}_{\mathrm{inc}}$ which are column vectors of length $3N$ and comprise the dipole moments and electric fields at all points in the following forms:

$$\tilde{\boldsymbol{p}} = \begin{pmatrix} p_{1,x} \\ p_{1,y} \\ p_{1,z} \\ p_{2,x} \\ \vdots \end{pmatrix} \quad , \quad \tilde{\boldsymbol{E}}_{inc} = \begin{pmatrix} E_{\mathrm{inc},1,x} \\ E_{\mathrm{inc},1,y} \\ E_{\mathrm{inc},1,z} \\ E_{\mathrm{inc},2,x} \\ \vdots \end{pmatrix} \tag{E.0.7}$$

Then,

$$\tilde{\boldsymbol{E}}_{inc} = \tilde{\boldsymbol{A}}\tilde{\boldsymbol{P}} \tag{E.0.8}$$

For this transformation to restore the form of equations E.0.7 when the matrix multiplication is carried out, the interaction matrix must be written as follows:

$$\tilde{\boldsymbol{A}} = \begin{pmatrix} A_{11,x,x} & A_{11,x,y} & A_{11,x,z} & A_{12,x,x} & A_{12,x,y} & \cdots \\ A_{11,y,x} & A_{11,y,y} & A_{11,y,z} & A_{12,y,x} & A_{12,y,y} & \cdots \\ A_{11,z,x} & A_{11,z,y} & A_{11,z,z} & A_{12,z,x} & A_{12,z,y} & \cdots \\ A_{21,x,x} & A_{21,x,y} & A_{21,x,z} & A_{22,x,x} & A_{22,x,y} & \cdots \\ A_{21,y,x} & A_{21,y,y} & A_{21,y,z} & A_{22,y,x} & A_{22,y,y} & \cdots \\ \vdots & \vdots & \vdots & \vdots & \vdots & \ddots \end{pmatrix} \tag{E.0.9}$$

These matrix elements must be computed individually, though the diagonal simply comprises the inverse of the polarisability of the indexed particle. Once this has been computed and the incident field has been specified, the dipole moments can be calculated by solving the equation below by inverting the matrix $\tilde{\boldsymbol{A}}$:

$$\tilde{\boldsymbol{P}} = \tilde{\boldsymbol{A}}^{-1}\tilde{\boldsymbol{E}}_{inc} \tag{E.0.10}$$

The flexibility of this method makes it very useful for many systems, as the position of each particle can be specified individually, so there is no need for the particles to be in a regular lattice. Also, the particles may all be different (i.e. have different polarisabilities), and for the case of ellipsoids, if the polarisability is known in three directions, then the system may include particles with different orientations. Furthermore, there is the possibility of studying relatively large but finite arrays of particles which is beyond the capabilities of finite-element modelling.

In summary, this technique can be used to study arrays of particles (up to a maximum of 4,000 particles by this method with 4Gb of RAM) which exhibit only dipolar modes, though it can be used to describe the dipolar component of particles large enough to support quadrupolar modes if dynamic depolarisation and radiative damping are implemented into the expression for the polarisability.

Appendix F

CDA code

The CDA results presented in this thesis were computed using a code written by myself in Matlab (in optimising the code for speed I was assisted by Tomek Trzeciak). It was written from scratch though some inspiration was derived from Matthew McMahon's thesis (Vanderbilt University, 2006). The code has been extensively optimised, and short of making some physical assmuptions about the system, further optimisation is likely to be very difficult. The code's main limitation is the number of dipoles it can model. This currently stands at approximately 4000 particles on a PC with 4Gb of RAM. It should be noted that the notation used is consistent with Draine's papers, and when compared to the rest of this thesis, some quantities are scaled by a factor of 4π.

This code accepts particle positions (in the x-y plane) from one or more tab-delimited text files. The particles are assigned material parameters and hence polarisablilities calculated taking into account the surrounding medium. The incident polarisation and k-vector are specified by the user as is the wavelength range. Taking all this into consideration, the field interaction between each pair of particles is calculated, and from this, the interaction matrix is inverted and the dipole moments of each particle are calculated. From these polarisation values the extinction and absorption cross-sections can readily be calculated and the scattering cross-section is inferred from their difference. These are plotted and exported in a text file for all wavelengths. Furthermore, dipole moments of the individual particles can be plotted on an axis representing the x-y plane where their arrows are centred on their associated particles. An AVI file can be exported showing an animation of the evolution of the dipole moments over an optical cycle.

I will briefly discuss the limitations of this particular code and ways in which they can be overcome for future use:

- All the particles must lie in the x-y plane: the code accepts particles positions from a tab-delimited text file which has two columns. This can easily be extended to three by

modifying some lines in the 'CDA_model' function, though plotting the dipole moments will no longer function correctly as they are plotted on plane.

- All the particles must be the same size: this will require the creation of a fourth column in the input file which contains information about the size.
- All the particles must be spherical: the equation for the ellipsoidal polarisability is included but it is currently not implemented. The orientation of each particle will need to be specified for the polarisability tensors to be calculated correctly for each particle (these elements form the diagonal of the matrix $A_{i,j}$).
- Only silver and gold can currently be used for the particle material: other materials may be used if permittivity values are known. A spline is fitted to these values to allow the code to operate for intermediate wavelengths. The files containing the permittivities used here have five columns (wavelength (nm), n', n'', ϵ' and ϵ'') but the second and third are not required.

The code has a main script called 'Front_End' which is the main user interface. All the important variables are specified here.

```
% CDA Model - enter parameters here

% Metal type ('Ag' or 'Au')
metal='Ag';

% Specify particle radius (nm)
a=50;

% Refractive index of surrounding medium
n_medium=1.5;

% Angles of incidence degrees
Polar=0;
Azimuthal=0;

% List all filenames to be included (comma delimited text files)
all_input_filenames={'pos1.txt';'pos2.txt'};

% Set polarisation (p is parallel to theta, s is parallel to phi)
polarisation='p';

% Set wavelength range in nm ('stopwl'-'startwl' must be divisible by
% 'increment')
startwl=400;
increment=10;
stopwl=700;

% Choose whether to produce animation ('true' or 'false') and if so at
% which wavelength
animation=true;
animation_wl=430;
```

```
loop_input_files(metal,a,n_medium,Polar,Azimuthal,all_input_filenames,...
    polarisation,startwl,increment,stopwl,animation,animation_wl);
```

'Front_End' calls 'loop_input_files' which runs through every file containing particle positions and calls the main script which solves the CDA calculation.

```
% Function to loop over all position files, run the CDA calculations and
% save and plot the results (producing an animation if requested).

function loop_input_files(metal,a,n_medium,Polar,Azimuthal,all_input_filenames,...
    polarisation,startwl,increment,stopwl,animation,animation_wl)

number_of_files=size(all_input_filenames,1);
% Loop over all files
for gg=1:number_of_files
    input_filename=char(all_input_filenames(gg));

    % Run CDA model.  Wavelength sweep occurs in CDA_model
    spectra=CDA_model(a,n_medium,Polar,Azimuthal,polarisation,startwl,...
        increment,stopwl,metal,input_filename,false);

    % Plot extinction
    figure
    plot(1000*spectra(:,1),spectra(:,2),1000*spectra(:,1),spectra(:,3),1000*spectra(:,1),
         spectra(:,4),'LineWidth',2)

    xlabel('Wavelength (nm)','FontSize',18,'FontName','Times')
    ylabel('Cross-section ( \mum^2 )','FontSize',18,'FontName','Times')
    title_text=sprintf('%dnm radius %s spheres in index n=%0.1f.\n {\\it\\theta} =%d\\circ,
         {\\it\\phi =}%d\\circ, %s-polarised.',a,metal,n_medium,Polar,Azimuthal,polarisation);
    title(title_text,'FontSize',18,'FontName','Times')
    legend('Extinction','Absorption','Scattering');
    set(gca,'FontSize',18,'FontName','Times')
    % Export extinction spectrum
    dlmwrite(strcat(input_filename,'_spectrum.txt'),...
        [1000*spectra(:,1) spectra(:,2)],'\t')
end

% Rerun CDA_model to produce animation if requested at the chosen
% wavelength
if animation==true
    figure
    CDA_model(a,n_medium,Polar,Azimuthal,polarisation,animation_wl,...
        increment,animation_wl,metal,input_filename,animation);
end
```

The function 'CDA_model' is the heart of the code. It runs other functions to compute the elements of the interaction matrix (which includes the permittivity-dependent polarisabilities of the particles). Once the matrix has been filled out, it is inverted and the dipole moments are calculated. From these dipole moments, the cross-sections are calculated and if requested, an animation of the vectors can be generated.

```
% COUPLED DIPOLE APPROXIMATION (CDA) This code uses the CDA to compute the
% dipole moments of a number of particles in an arrangement specified by a
```

```
% position matrix r.  From this the cross-sections and efficiencies can be
% calculated.
function spectra=CDA_model(a,n_medium,Polar,Azimuthal,polarisation,startwl,...
    increment,stopwl,metal,input_file_name,animation)
tic
% Convert nm to um and degs to rads etc.
a=a/1000;
startwl=startwl/1000;
increment=increment/1000;
stopwl=stopwl/1000;
Polar=Polar*(2*pi/360);
Azimuthal=Azimuthal*(2*pi/360);
eps_m=n_medium*n_medium;

% Get permittivities and fit spline
[new_wl,eps_all]=get_permittivity(startwl,increment,stopwl,metal);

% Wavevector
wavevector=[sin(Polar)*cos(Azimuthal) sin(Polar)*sin(Azimuthal) cos(Polar)];

% Incident E field has magnitude of 1
% p-pol component
E0p=[sin(Polar-pi/2)*cos(Azimuthal) sin(Polar-pi/2)*sin(Azimuthal) cos(Polar-pi/2)];

% s-pol component
E0s=[cos(Azimuthal+pi/2) sin(Azimuthal+pi/2) 0];

% Incoherent superposition of s- and p-
E0i=(E0p+E0s)./sqrt(2);

% select pol from E0
if polarisation=='p'
    E0=E0p;
elseif polarisation=='s'
    E0=E0s;
elseif polarisation=='i'
    E0=E0i;
end

% Cycle through a range of numbers of particles

Positions=dlmread(input_file_name,'\t');

r=reshape(Positions',2,[]);
r=[r;zeros(1,size(r,2))];

% Find total number of particles
Total=size(r,2);

% Calculate all displacements between particles
rdiff=calc_distances(r,Total);
% Print number of particles (optional)
disp(sprintf('Number of particles = %d',Total));

%  Set matrix size (wavelength in nm)
lambdavals=size(new_wl,1);
Alpha=zeros(lambdavals,1);
Cext=zeros(lambdavals,1);
Cabs=zeros(lambdavals,1);
Csca=zeros(lambdavals,1);
```

```
% Cycle over all wavelengths
for num=1:lambdavals
    % Wavelength
    lambda=new_wl(num,1);
    % Epsilon at this wavelength (complex)
    eps=eps_all(num);
    % Wavenumber (in medium)
    K0=2*pi*sqrt(eps_m)./lambda;
    % Wavevector
    K=K0*wavevector;

    % Calculate polarisability using Kuwata model (for matrix diagonals)
    Alpha_i=calc_polarisability(a,eps,eps_m,lambda);

    I=complex(0,1);

    Alpha(num,2)=Alpha_i;

    % Calculate Ein at the position of each particle
    Ein=zeros(1,3*Total);
    for kk=1:Total
        Ein(1,3*(Total-kk+1)-2:3*(Total-kk+1))=E0*exp(I*sum((K.*r(:,kk).')));
    end
    Ein=Ein.';

    % Calclate Aij, the interaction matrix
    Aij=single(calc_Aij(Total,Alpha_i,I,K0,rdiff));
    % Invert matrix to solve for the column vector of polarisation of each
    % particle
    P=linsolve(Aij,Ein);

    % Calculate cross sections
    Cext(num)=4*pi*K0.*imag(sum(P.*conj(Ein)));
    Cabs(num)=4*pi*K0.*sum(imag(sum(P.*conj(Alpha_i^-1).*conj(P)))-
              (2/3).*K0^3.*sum(P.*conj(P)));
    Csca(num)=Cext(num)-Cabs(num);
end

% Display time taken
t(1)=toc;
disp(sprintf('Time taken = %0.2fs\n',t'))

% Produce animation if requested
if animation==true
    p2=reshape(P,3,[]);
    video(r,p2);
end

% Return cross-sections
spectra=[new_wl Cext(:) Cabs(:) Csca(:)];
```

The function 'get_permittivity' simply extracts the permittivity values from a text file and fits a cubic spline to them according to the wavelength range specified by the user.

```
% Function to import the permittivity values from a tab-delimited text
% file, and interpolate the data with a spline over a chosen wavelength
% range.
function [new_wl,eps_all]=get_permittivity(startwl,increment,stopwl,metal)
```

```
% Get gold/silver permittivity
if strcmp(metal,'Au')
    eps=dlmread('AuJCMie.txt','\t');
elseif strcmp(metal,'Ag')
    eps=dlmread('AgPalikMie.txt','\t');
else
    disp('Permittivity values not present')
end
eps(:,2:3)=[];
eps(:,1)=eps(:,1)./1000;

% Spline fit
new_wl=(startwl:increment:stopwl)';
epsrnew=spline(eps(:,1),eps(:,2),new_wl);
epsimnew=spline(eps(:,1),eps(:,3),new_wl);

% Express permittity in a complex form
eps_all=complex(epsrnew,epsimnew);
```

'calc_Aij' is a function for computing the non-diagonal elements in the matrix (i.e. those which describe the interaction between pairs of particles). This has been optimised for computation time abut is still the slowest part of the code as it has to specify almost $(3N)^2$ elements where N is the number of particles.

```
% A time-optimised function for calculating the values of Aij which
% represent the interaction between particles in the array.  i and j are
% the particle indices and for each pair of particles there is a 3x3
% sub-matrix representing that interaction.

function Aij=calc_Aij(Total,Alpha_i,I,K0,rdiff)

% Counter
countup=0;
% Define 3x3 identity matrix
I3=eye(3);
%Specify some variables for later use
ik=I*K0;
K0squared=K0*K0;
routerA=zeros(3,3);
routerB=zeros(3,3);
Aij=single(zeros(3*Total));

% Calculate the Aij matrix Cycle through i and j (each combination is one
% 3x3 portion of Aij)
for i=1:Total
    for j=1:Total
        % Polarisation of each particle by 'itself'
        if j==i
            % Along the diagonal: inverse of polarisability
            Aij(3*i-2:3*i,3*j-2:3*j)=single(1./Alpha_i.*I3);
            continue;
        end
        countup=countup+1;

        % Components of the vector joning one particular pair of particles
        rx=rdiff(1,countup);
        ry=rdiff(2,countup);
        rz=rdiff(3,countup);
```

```
        % Dot product of displacement vector
        rsquared=rx*rx+ry*ry+rz*rz;
        % Distance between particles
        r=sqrt(rsquared);

        % Components separated for fast calculation of Aij
        ikr=ik*r;
        expikrr=exp(ikr)/r;
        Z=(ikr-1)/rsquared;
        threeoverrsquared=3/rsquared;

        % Calculate outer products (repeated elements ignored, =0)

        routerA(1,1)=rx*rx/rsquared-1;
        routerA(1,2)=rx*ry/rsquared;
        routerA(1,3)=rx*rz/rsquared;
        routerA(2,2)=ry*ry/rsquared-1;
        routerA(2,3)=ry*rz/rsquared;
        routerA(3,3)=rz*rz/rsquared-1;
        routerB(1,1)=threeoverrsquared*rx*rx-1;
        routerB(1,2)=threeoverrsquared*rx*ry;
        routerB(1,3)=threeoverrsquared*rx*rz;
        routerB(2,2)=threeoverrsquared*ry*ry-1;
        routerB(2,3)=threeoverrsquared*ry*rz;
        routerB(3,3)=threeoverrsquared*rz*rz-1;

        % Cycle through elements of the 3x3 sub-matrices
        for k=1:3
            for m=k:3
                % p and q are elements of the large matrix
                p = 3*i+k-3;
                q = 3*j+m-3;
                % Calculate elements of Aij
                Aij(p,q)= single((routerA(k,m)*K0squared+routerB(k,m)*Z)*expikrr);
                % Copy elements reflected in the diagonal
                Aij(q,p)= single(Aij(p,q));
            end
        end
    end
end
```

'calc_distances' calculates the distances between each pair of particles being modelled. These values used in 'calc_Aij' to calculate the dipolar field between each of the pairs.

```
% Function for reading a 3xTotal array of position vectors and return the
% differences between them in the correct order for further processing.

function rdiff=calc_distances(r,Total)

% Calculate number of elements in the matrix of difference-vectors
number_diff=Total*Total-Total;
% Initialise array
rdiff=zeros(3,number_diff);
% Index of all coordinates in array for which the displacement is zero
ind=1:Total+1:Total*Total;
```

```
% Loop over all elements in inital matrix of positions
for i=1:Total
    % calculate differences by shifting matrix elements 'Total' times and
    % subtracting the original matrix
    rdiff(1:3,Total*(i-1)+1:Total*i)=r-repmat(r(1:3,i),1,Total);
end

% Remove all elements where the displacement is zero
rdiff(:,ind)=[];
```

The function 'calc_polarisability' computes the polarisability of the spheres using the Kuwata polarisability function. This can be extended to model polarisable ellipsoids.

```
% Function to calculate the polarisability of particles using the Kuwata
% polarisability (currently only implemented for spheres)

function Alpha_i=calc_polarisability(a,eps,eps_m,lambda)

% Imaginary number
I=complex(0,1);

% Shape factor (1/3 for sphere)
L=1/3;

% Particle volume
V=4*pi*a^3/3;

% Kuwata parameters
AL=-0.4865*L-1.046*L^2+0.8481*L^3;
BL=0.01909*L+0.1999*L^2+0.6077*L^3;

% Size parameter
x=2*pi.*a./lambda;

% Denominator of polarisability
denom=(L+eps_m./(eps-eps_m))+AL.*eps_m.*x.^2+
       BL.*eps_m.^2.*x.^4-I.*4.*pi.^2.*eps_m.^(3/2).*V./(3.*lambda.^3);
% Polarisability
Alpha_i=V./(denom);
% Take into account 4pi for units
Alpha_i=Alpha_i./(4.*pi);
```

'video' cycles through phases and calls 'plot_dipole_moment' to plot the dipole moment at that particular phase. The plots are saved for each phase and an animation is shown on screen and saved to 'video.avi'.

```
% Function to display video of dipole moments and save as 'video.avi'.
function video(r,p2)

% Find maximum dipole moment for scaling of arrows.
scale=max(max(abs(p2)));

% Cycle through phases
countup=0;
```

```
for phi=0:5:360
    countup=countup+1;
    phi2=2*pi*phi/360;
    I=complex(0,1);
    eiphi=exp(I*phi2);

    % Plot dipole moments
    plot_dipole_moment(r(1,:),r(2,:),real(eiphi*p2(1,:)),real(eiphi*p2(2,:)),scale)

    % Set axis limits etc.
    minx=min(r(1,:)); maxx=max(r(1,:));
    miny=min(r(2,:)); maxy=max(r(2,:));

    set(gcf,'Position', [200 200 650 500],'Color','white')

    axis equal
    xlim([minx-0.2*(1+maxx-minx) maxx+0.2*(1+maxx-minx)]);
    ylim([miny-0.2*(1+maxy-miny) maxy+0.2*(1+maxy-miny)]);

    F(countup)=getframe(gcf);
    hold off
end

set(gcf,'Position', [200 200 650 500],'Color','white')

% Save avi file
movie2avi(F,'video.avi','quality',100,'compression','Cinepak')
```

'plot_dipole_moment' is based on Matlab's built-in function 'quiver' which plots arrows at particular points. These arrows have been scaled so they don't tend to overlap with other arrows and set so that they are centred on the particles (by default their tails are on the particles). Also, they have been set so that for different phases, the size of the arrows are not scaled automatically.

```
% Function to plot dipole moment. This uses the 'quiver' function which is
% present in Matlab, but the arrows have been set to be centred on the
% particles.

function plot_dipole_moment(x,y,u,v,scale)

% Scale real dipole moments by maximum dipole moment so maximum value is 1.
normalisingfactor=max(max(abs([u v])))./scale;

% Estimate the number of particles in each direction (x and y).
n=sqrt(numel(x));

% Calculate average separation of particles in each direction
dx = (max(x)-min(x))/n;
dy = (max(y)-min(y))/n;

% Total average separation is:
del = sqrt(dx.^2 + dy.^2);

% Find "occupied length proportion" of dipole moment.
occupation=sqrt(u.^2 + v.^2)/del;
maxlen = max(occupation(:));
```

```
% Ensure that occupation of arrows is never more than 0.8, and that the
% more space in the array, the larger the arrows are.
scalingfactor=0.8/maxlen;

% Scale dipole moments
u = u*scalingfactor; v = v*scalingfactor;

% Offset arrows so they are centred on the particles.
offset_x=x-u.*normalisingfactor./2;
offset_y=y-v.*normalisingfactor./2;

% Plot particle positions and their associated dipole moments.
plot(x,y,'o','MarkerFaceColor','blue')
set(gca,'FontSize',18,'FontName','Times')
xlabel('x-position (\mum)','FontSize',18,'FontName','Times')
ylabel('y-position (\mum)','FontSize',18,'FontName','Times')
hold on
h=quiver(offset_x,offset_y,u,v,1,'LineWidth',2);
set(h,'AutoScaleFactor',normalisingfactor)
```

References

[1] R.A.R. Tricker. *Introduction To Meteorological Optics*. Elsevier, 1970.

[2] M. Born and E. Wolf. *Principles of Optics*. Cambridge University Press, Cambridge, 1980.

[3] E. D. Palik. *Handbook of Optical Constants and Solids*. Academic Press Inc., London, 1985.

[4] P. B. Johnson and R. W. Christy. Optical-constants of noble-metals. *Physical Review B*, 6(12):4370–4379, 1972.

[5] H. Raether. *Surface-plasmons On Smooth and Rough Surfaces and On Gratings*. 1988.

[6] W. L. Barnes, A. Dereux, and T. W. Ebbesen. Surface plasmon subwavelength optics. *Nature*, 424(6950):824–830, 2003.

[7] M. N'Gom, J. Ringnalda, J. F. Mansfield, A. Agarwal, N. Kotov, N. J. Zaluzec, and T. B. Norris. Single particle plasmon spectroscopy of silver nanowires and gold nanorods. *Nano Letters*, 8(10):3200–3204, 2008.

[8] G. Schider, J. R. Krenn, A. Hohenau, H. Ditlbacher, A. Leitner, F. R. Aussenegg, W. L. Schaich, I. Puscasu, B. Monacelli, and G. Boreman. Plasmon dispersion relation of Au and Ag nanowires. *Physical Review B*, 68(15):155427, 2003.

[9] D. A. Genov, A. K. Sarychev, V. M. Shalaev, and A. Wei. Resonant field enhancements from metal nanoparticle arrays. *Nano Letters*, 4(1):153–158, 2004.

[10] S. Enoch, R. Quidant, and G. Badenes. Optical sensing based on plasmon coupling in nanoparticle arrays. *Optics Express*, 12(15):3422–3427, 2004.

[11] W. A. Murray, B. Auguie, and W. L. Barnes. Sensitivity of localized surface plasmon resonances to bulk and local changes in the optical environment. *Journal of Physical Chemistry C*, 113(13):5120–5125, 2009.

[12] E. C. Le Ru, E. Blackie, M. Meyer, and P. G. Etchegoin. Surface enhanced raman scattering enhancement factors: a comprehensive study. *Journal of Physical Chemistry C*, 111(37):13794–13803, 2007.

[13] M. B. Mohamed, V. Volkov, S. Link, and M. A. El-Sayed. The 'lightning' gold nanorods: fluorescence enhancement of over a million compared to the gold metal. *Chemical Physics Letters*, 317(6):517–523, 2000.

[14] J. R. Krenn, A. Dereux, J. C. Weeber, E. Bourillot, Y. Lacroute, J. P. Goudonnet, G. Schider, W. Gotschy, A. Leitner, F. R. Aussenegg, and C. Girard. Squeezing the optical near-field zone by plasmon coupling of metallic nanoparticles. *Physical Review Letters*, 82(12):2590–2593, 1999.

[15] L. A. Sweatlock, S. A. Maier, H. A. Atwater, J. J. Penninkhof, and A. Polman. Highly confined electromagnetic fields in arrays of strongly coupled ag nanoparticles. *Physical Review B*, 71(23):235408, 2005.

[16] T. Nakamura and S. Hayashi. Enhancement of dye fluorescence by gold nanoparticles: Analysis of particle size dependence. *Japanese Journal of Applied Physics Part 1*, 44(9A):6833–6837, 2005.

[17] V. G. Kravets, F. Schedin, and A. N. Grigorenko. Extremely narrow plasmon resonances based on diffraction coupling of localized plasmons in arrays of metallic nanoparticles. *Physical Review Letters*, 101(8):087403, 2008.

[18] T. Hatling, P. Reichenbach, and L. M. Eng. Near-field coupling of a single fluorescent molecule and a spherical gold nanoparticle. *Optics Express*, 15(20):12806–12817, 2007.

[19] N. A. Issa and R. Guckenberger. Fluorescence near metal tips: The roles of energy transfer and surface plasmon polaritons. *Optics Express*, 15(19):12131–12144, 2007.

[20] P. Muhlschlegel, H. J. Eisler, O. J. F. Martin, B. Hecht, and D. W. Pohl. Resonant optical antennas. *Science*, 308(5728):1607–1609, 2005.

[21] J. Aizpurua, G. W. Bryant, L. J. Richter, F. J. G. de Abajo, B. K. Kelley, and T. Mallouk. Optical properties of coupled metallic nanorods for field-enhanced spectroscopy. *Physical Review B*, 71(23):235420, 2005.

[22] S. V. Boriskina and L. Dal Negro. Multiple-wavelength plasmonic nanoantennas. *Optics Letters*, 35(4):538–540, 2010.

[23] S. Kim, J. H. Jin, Y. J. Kim, I. Y. Park, Y. Kim, and S. W. Kim. High-harmonic generation by resonant plasmon field enhancement. *Nature*, 453(7196):757–760, 2008.

[24] G. P. Wiederrecht. Near-field optical imaging of noble metal nanoparticles. *European Physical Journal-Applied Physics*, 28(1):3–18, 2004.

[25] G. Baffou, M. P. Kreuzer, F. Kulzer, and R. Quidant. Temperature mapping near plasmonic nanostructures using fluorescence polarization anisotropy. *Optics Express*, 17(5):3291–3298, 2009.

[26] G. Baffou, C. Girard, and R. Quidant. Mapping heat origin in plasmonic structures. *Physical Review Letters*, 104(13):136805, 2010.

[27] K. R. Li, M. I. Stockman, and D. J. Bergman. Self-similar chain of metal nanospheres as an efficient nanolens. *Physical Review Letters*, 91(22):227402, 2003.

[28] V. G. Veselago. Electrodynamics of substances with simultaneously negative values of ϵ and μ. *Soviet Physics Uspekhi-USSR*, 10(4):509, 1968.

[29] J. B. Pendry, A. J. Holden, W. J. Stewart, and I. Youngs. Extremely low frequency plasmons in metallic mesostructures. *Physical Review Letters*, 76(25):4773–4776, 1996.

[30] J. B. Pendry, A. J. Holden, D. J. Robbins, and W. J. Stewart. Magnetism from conductors and enhanced nonlinear phenomena. *IEEE Transactions on Microwave Theory and Techniques*, 47(11):2075–2084, 1999.

[31] J. B. Pendry. Negative refraction makes a perfect lens. *Physical Review Letters*, 85(18):3966–3969, 2000.

[32] R. A. Shelby, D. R. Smith, and S. Schultz. Experimental verification of a negative index of refraction. *Science*, 292(5514):77–79, 2001.

[33] B. Lahiri, S. G. McMeekin, A. Z. Khokhar, R. M. De la Rue, and N. P. Johnson. Magnetic response of split ring resonators (SRRs) at visible frequencies. *Optics Express*, 18(3):3210–3218, 2010.

[34] M. Kafesaki, I. Tsiapa, N. Katsarakis, T. Koschny, C. M. Soukoulis, and E. N. Economou. Left-handed metamaterials: The fishnet structure and its variations. *Physical Review B*, 75(23):235114, 2007.

[35] S. Zhang, W. J. Fan, N. C. Panoiu, K. J. Malloy, R. M. Osgood, and S. R. J. Brueck. Experimental demonstration of near-infrared negative-index metamaterials. *Physical Review Letters*, 95(13):137404, 2005.

[36] V. A. Podolskiy, A. K. Sarychev, and V. M. Shalaev. Plasmon modes and negative refraction in metal nanowire composites. *Optics Express*, 11(7):735–745, 2003.

[37] A. V. Kildishev, W. S. Cai, U. K. Chettiar, H. K. Yuan, A. K. Sarychev, V. P. Drachev, and V. M. Shalaev. Negative refractive index in optics of metal-dielectric composites. *Journal of the Optical Society of America B*, 23(3):423–433, 2006.

[38] J. F. Zhou, L. Zhang, G. Tuttle, T. Koschny, and C. M. Soukoulis. Negative index materials using simple short wire pairs. *Physical Review B*, 73(4):041101, 2006.

[39] A. N. Grigorenko, A. K. Geim, H. F. Gleeson, Y. Zhang, A. A. Firsov, I. Y. Khrushchev, and J. Petrovic. Nanofabricated media with negative permeability at visible frequencies. *Nature*, 438(7066):335–338, 2005.

[40] A. N. Grigorenko. Negative refractive index in artificial metamaterials. *Optics Letters*, 31(16):2483–2485, 2006.

[41] S. M. Xiao, U. K. Chettiar, A. V. Kildishev, V. P. Drachev, and V. M. Shalaev. Yellow-light negative-index metamaterials. *Optics Letters*, 34(22):3478–3480, 2009.

[42] H.C. Van de Hulst. *Light Scattering by Small Particles*. John Wiley & Sons, New York, 1957.

[43] C. F. Bohren. How can a particle absorb more than the light incident on it. *American Journal of Physics*, 51(4):323–327, 1983.

[44] C.F. Bohren and D.R. Huffman. *Absorption and Scattering of Light by Small Particles*. Wiley, New York, 1983.

[45] H. Tamaru, H. Kuwata, H. T. Miyazaki, and K. Miyano. Resonant light scattering from individual Ag nanoparticles and particle pairs. *Applied Physics Letters*, 80(10):1826–1828, 2002.

[46] U. K. Chettiar, A. V. Kildishev, H. K. Yuan, W. S. Cai, S. M. Xiao, V. P. Drachev, and V. M. Shalaev. Dual-band negative index metamaterial: double negative at 813nm and single negative at 772nm. *Optics Letters*, 32(12):1671–1673, 2007.

[47] C. Rockstuhl, F. Lederer, C. Etrich, T. Zentgraf, J. Kuhl, and H. Giessen. On the reinterpretation of resonances in split-ring-resonators at normal incidence. *Optics Express*, 14(19):8827–8836, 2006.

[48] Y. Z. Chu, E. Schonbrun, T. Yang, and K. B. Crozier. Experimental observation of narrow surface plasmon resonances in gold nanoparticle arrays. *Applied Physics Letters*, 93(18):181108, 2008.

[49] B. T. Draine. The discrete-dipole approximation and its application to interstellar graphite grains. *Astrophysical Journal*, 333(2):848–872, 1988.

[50] B. T. Draine and P. J. Flatau. Discrete-dipole approximation for scattering calculations. *Journal of the Optical Society of America A*, 11(4):1491–1499, 1994.

[51] T Lu, W Cai, and PW Zhang. Discontinuous Galerkin time-domain method for GPR simulation in dispersive media. *IEEE Transactions on geoscience and remote sensing*, 43(1):72–80, 2005.

[52] J. Parsons, C. P. Burrows, J. R. Sambles, and W. L. Barnes. A comparison of techniques used to simulate the scattering of electromagnetic radiation by metallic nanostructures. *Journal of Modern Optics*, 57(5):356–365, 2010.

[53] K. L. Kelly, E. Coronado, L. L. Zhao, and G. C. Schatz. The optical properties of metal nanoparticles: The influence of size, shape, and dielectric environment. *Journal of Physical Chemistry B*, 107(3):668–677, 2003.

[54] G. Mie. Beiträge zur Optik trüber Medien, speziell kolloidaler Metallösungen. *Annalen der Physik*, 330(3):377–445, 1908.

[55] B.K. Russell, J.G. Mantovani, V.E. Anderson, R.J. Warmack, and T.L. Ferrell. Experimental test of the mie theory for microlithographically produced silver spheres. *Physical review B*, 35(5):2151–2154, 1987.

[56] C. Matzler. Matlab functions for Mie scattering and absorption. Research report No. 2002-08. Technical report, 2002.

[57] D.M. Pozar. *Microwave Engineering*, volume 3rd. John Wiley & Sons, Hoboken, 2005.

[58] M. Meier and A. Wokaun. Enhanced fields on large metal particles - dynamic depolarization. *Optics Letters*, 8(11):581–583, 1983.

[59] A. Wokaun, J. P. Gordon, and P. F. Liao. Radiation damping in surface-enhanced raman-scattering. *Physical Review Letters*, 48(14):957–960, 1982.

[60] A. Melikyan and H. Minassian. On surface plasmon damping in metallic nanoparticles. *Applied Physics B-lasers and Optics*, 78:453–455, 2004.

[61] C. Sonnichsen, T. Franzl, T. Wilk, G. von Plessen, J. Feldmann, O. Wilson, and P. Mulvaney. Drastic reduction of plasmon damping in gold nanorods. *Physical Review Letters*, 88(7):077402, 2002.

[62] G. Della Valle, T. Sondergaard, and S. I. Bozhevolnyi. Efficient suppression of radiation damping in resonant retardation-based plasmonic structures. *Physical Review B*, 79(11):113410, 2009.

[63] C. Vieu, F. Carcenac, A. Pepin, Y. Chen, M. Mejias, A. Lebib, L. Manin-Ferlazzo, L. Couraud, and H. Launois. Electron beam lithography: resolution limits and applications. *Applied Surface Science*, 164:111–117, 2000.

[64] A. Hohenau, H. Ditlbacher, B. Lamprecht, J. R. Krenn, A. Leitner, and F. R. Aussenegg. Electron beam lithography, a helpful tool for nanooptics. *Microelectronic Engineering*, 83(4–9):1464–1467, 2006.

[65] M. Hu, C. Novo, A. Funston, H. N. Wang, H. Staleva, S. L. Zou, P. Mulvaney, Y. N. Xia, and G. V. Hartland. Dark-field microscopy studies of single metal nanoparticles: understanding the factors that influence the linewidth of the localized surface plasmon resonance. *Journal of Materials Chemistry*, 18(17):1949–1960, 2008.

[66] M. W. Knight, J. Fan, F. Capasso, and N. J. Halas. Influence of excitation and collection geometry on the dark field spectra of individual plasmonic nanostructures. *Optics Express*, 18(3):2579–2587, 2010.

[67] J. J. Mock, M. Barbic, D. R. Smith, D. A. Schultz, and S. Schultz. Shape effects in plasmon resonance of individual colloidal silver nanoparticles. *Journal of Chemical Physics*, 116(15):6755–6759, 2002.

[68] W. L. Barnes. Comparing experiment and theory in plasmonics. *Journal of Optics A*, 11:114002, 2009.

[69] J. J. Mock, D. R. Smith, and S. Schultz. Local refractive index dependence of plasmon resonance spectra from individual nanoparticles. *Nano Letters*, 3(4):485–491, 2003.

[70] S. J. Oldenburg, G. D. Hale, J. B. Jackson, and N. J. Halas. Light scattering from dipole and quadrupole nanoshell antennas. *Applied Physics Letters*, 75(8):1063–1065, 1999.

[71] H. Wang, K. Fu, R. A. Drezek, and N. J. Halas. Light scattering from spherical plasmonic nanoantennas: effects of nanoscale roughness. *Applied Physics B*, 84:191–195, 2006.

[72] R. Esteban, R. Vogelgesang, J. Dorfmuller, A. Dmitriev, C. Rockstuhl, C. Etrich, and K. Kern. Direct near-field optical imaging of higher order plasmonic resonances. *Nano Letters*, 8(10):3155–3159, 2008.

[73] N. Yamamoto, K. Araya, and F. J. G. de Abajo. Photon emission from silver particles induced by a high-energy electron beam. *Physical Review B*, 64(20):205419, 2001.

[74] W.K.H. Panofsky and M. Phillips. *Classical Electricity and Magnetism*. Addison-Wesley, USA, 1962.

[75] A. S. Kumbhar, M. K. Kinnan, and G. Chumanov. Multipole plasmon resonances of submicron silver particles. *Journal of the American Chemical Society*, 127(36):12444–12445, 2005.

[76] W. J. Wiscombe. Improved Mie scattering algorithms. *Applied Optics*, 19(9):1505–1509, 1980.

[77] J.A. Stratton. *Electromagnetic Theory*. McGraw-Hill, New York, 1941.

[78] R. Ruppin. Surface-modes of two spheres. *Physical Review B*, 26(6):3440–3444, 1982.

[79] J. Ng, R. Tang, and C. T. Chan. Electrodynamics study of plasmonic bonding and antibonding forces in a bisphere. *Physical Review B*, 77(19):195407, 2008.

[80] J. J. Xiao, J. P. Huang, and K. W. Yu. Optical response of strongly coupled metal nanoparticles in dimer arrays. *Physical Review B*, 71(4):045404, 2005.

[81] I. Romero, J. Aizpurua, G. W. Bryant, and F. J. G. de Abajo. Plasmons in nearly touching metallic nanoparticles: singular response in the limit of touching dimers. *Optics Express*, 14(21):9988–9999, 2006.

[82] K. H. Su, Q. H. Wei, X. Zhang, J. J. Mock, D. R. Smith, and S. Schultz. Interparticle coupling effects on plasmon resonances of nanogold particles. *Nano Letters*, 3(8):1087–1090, 2003.

[83] W. Rechberger, A. Hohenau, A. Leitner, J. R. Krenn, B. Lamprecht, and F. R. Aussenegg. Optical properties of two interacting gold nanoparticles. *Optics Communications*, 220(1-3):137–141, 2003.

[84] A. N. Grigorenko, H. F. Gleeson, Y. Zhang, N. W. Roberts, A. R. Sidorov, and A. A. Panteleev. Antisymmetric plasmon resonance in coupled gold nanoparticles as a sensitive tool for detection of local index of refraction. *Applied Physics Letters*, 88(12):124103, 2006.

[85] G. Zoriniants and W. L. Barnes. Fluorescence enhancement through modified dye molecule absorption associated with the localized surface plasmon resonances of metallic dimers. *New Journal of Physics*, 10:105002, 2008.

[86] J. Zuloaga, E. Prodan, and P. Nordlander. Quantum description of the plasmon resonances of a nanoparticle dimer. *Nano Letters*, 9(2):887–891, 2009.

[87] A. O. Pinchuk and G. C. Schatz. Nanoparticle optical properties: Far- and near-field electrodynamic coupling in a chain of silver spherical nanoparticles. *Materials Science and Engineering B*, 149(3):251–258, 2008.

[88] H. J. Li, Q. Liu, S. X. Xie, X. Zhou, H. Xia, and R. L. Zhou. Particle plasmons resonant characteristics in arrays of strongly coupled gold nanoparticles. *Solid State Communications*, 149(5-6):239–242, 2009.

[89] R. L. Chern, X. X. Liu, and C. C. Chang. Particle plasmons of metal nanospheres: Application of multiple scattering approach. *Physical Review E*, 76(1):016609, 2007.

[90] E. M. Hicks, S. L. Zou, G. C. Schatz, K. G. Spears, R. P. Van Duyne, L. Gunnarsson, T. Rindzevicius, B. Kasemo, and M. Kall. Controlling plasmon line shapes through diffractive coupling in linear arrays of cylindrical nanoparticles fabricated by electron beam lithography. *Nano Letters*, 5(6):1065–1070, 2005.

[91] Q. H. Wei, K. H. Su, S. Durant, and X. Zhang. Plasmon resonance of finite one-dimensional au nanoparticle chains. *Nano Letters*, 4(6):1067–1071, 2004.

[92] K. B. Crozier, E. Togan, E. Simsek, and T. Yang. Experimental measurement of the dispersion relations of the surface plasmon modes of metal nanoparticle chains. *Optics Express*, 15(26):17482–17493, 2007.

[93] E. J. Smythe, E. Cubukcu, and F. Capasso. Optical properties of surface plasmon resonances of coupled metallic nanorods. *Optics Express*, 15(12):7439–7447, 2007.

[94] B. Auguie and W. L. Barnes. Collective resonances in gold nanoparticle arrays. *Physical Review Letters*, 101(14):143902, 2008.

[95] B. Auguie and W. L. Barnes. Diffractive coupling in gold nanoparticle arrays and the effect of disorder. *Optics Letters*, 34(4):401–403, 2009.

[96] W. L. Schaich, G. Schider, J. R. Krenn, A. Leitner, F. R. Aussenegg, I. Puscasu, B. Monacelli, and G. Boreman. Optical resonances in periodic surface arrays of metallic patches. *Applied Optics*, 42(28):5714–5721, 2003.

[97] C. L. Haynes, A. D. McFarland, L. L. Zhao, R. P. Van Duyne, G. C. Schatz, L. Gunnarsson, J. Prikulis, B. Kasemo, and M. Kall. Nanoparticle optics: The importance of radiative dipole coupling in two-dimensional nanoparticle arrays. *Journal of Physical Chemistry B*, 107(30):7337–7342, 2003.

[98] J. Sung, E. M. Hicks, R. P. Van Duyne, and K. G. Spears. Nanoparticle spectroscopy: Plasmon coupling in finite-sized two-dimensional arrays of cylindrical silver nanoparticles. *Journal of Physical Chemistry C*, 112(11):4091–4096, 2008.

[99] Y. B. Zheng, B. K. Juluri, X. L. Mao, T. R. Walker, and T. J. Huang. Systematic investigation of localized surface plasmon resonance of long-range ordered Au nanodisk arrays. *Journal of Applied Physics*, 103(1):014308, 2008.

[100] T. Yang and K. B. Crozier. Surface plasmon coupling in periodic metallic nanoparticle structures: a semi-analytical model. *Optics Express*, 16(17):13070–13079, 2008.

[101] J. B. Khurgin and G. Sun. Impact of disorder on surface plasmons in two-dimensional arrays of metal nanoparticles. *Applied Physics Letters*, 94(22):221111, 2009.

[102] N. Papasimakis, V. A. Fedotov, Y. H. Fu, D. P. Tsai, and N. I. Zheludev. Coherent and incoherent metamaterials and order-disorder transitions. *Physical Review B*, 80(4):041102, 2009.

[103] V. A. Markel. Antisymmetrical optical states. *Journal of the Optical Society of America B*, 12(10):1783–1791, 1995.

[104] R. G. Newton. Optical theorem and beyond. *American Journal of Physics*, 44(7):639–642, 1976.

[105] C. Langhammer, B. Kasemo, and I. Zoric. Absorption and scattering of light by Pt, Pd, Ag, and Au nanodisks: Absolute cross sections and branching ratios. *Journal of Chemical Physics*, 126(19):194702, 2007.

[106] A. Arbouet, D. Christofilos, N. Del Fatti, F. Vallee, J. R. Huntzinger, L. Arnaud, P. Billaud, and M. Broyer. Direct measurement of the single-metal-cluster optical absorption. *Physical Review Letters*, 93(12):127401, 2004.

[107] O. L. Muskens, P. Billaud, M. Broyer, N. Fatti, and F. Vallee. Optical extinction spectrum of a single metal nanoparticle: Quantitative characterization of a particle and of its local environment. *Physical Review B*, 78(20):205410, 2008.

[108] P. Hanarp, M. Kall, and D. S. Sutherland. Optical properties of short range ordered arrays of nanometer gold disks prepared by colloidal lithography. *Journal of Physical Chemistry B*, 107(24):5768–5772, 2003.

[109] E. Hutter and J. H. Fendler. Exploitation of localized surface plasmon resonance. *Advanced Materials*, 16(19):1685–1706, 2004.

[110] J. M. McMahon, A. I. Henry, K. L. Wustholz, M. J. Natan, R. G. Freeman, R. P. Van Duyne, and G. C. Schatz. Gold nanoparticle dimer plasmonics: finite element method calculations of the electromagnetic enhancement to surface-enhanced raman spectroscopy. *Analytical and Bioanalytical Chemistry*, 394(7):1819–1825, 2009.

[111] J. J. H. Cook, K. L. Tsakmakidis, and O. Hess. Ultralow-loss optical diamagnetism in silver nanoforests. *Journal of optics A-Pure and applied optics*, 11:114026, 2009. 1st International Workshop on Theoretical and Computational Nano-Photonics, Bad Honnef, GERMANY, DEC 03-05, 2008.

[112] J.D. Jackson. *Classical Electrodynamics*. Wiley, New York, 1962.

[113] S. Malynych and G. Chumanov. Light-induced coherent interactions between silver nanoparticles in two-dimensional arrays. *Journal of the American Chemical Society*, 125(10):2896–2898, 2003.

[114] S. Malynych and G. Chumanov. Extinction spectra of quasi-spherical silver sub-micron particles. *Journal of Quantitative Spectroscopy & Radiative Transfer*, 106(1-3):297–303, 2007.

[115] S. Malynych and G. Chumanov. Narrow plasmon mode in 2D arrays of silver nanoparticles self-assembled on thin silver films. *Journal of Microscopy*, 229(3):567–574, 2008.

[116] B. N. Khlebtsov, V. A. Khanadeyev, J. Ye, D. W. Mackowski, G. Borghs, and N. G. Khlebtsov. Coupled plasmon resonances in monolayers of metal nanoparticles and nanoshells. *Physical Review B*, 77(3):035440, 2008.

[117] D. V. Vezenov, B. T. Mayers, D. B. Wolfe, and G. M. Whitesides. Integrated fluorescent light source for optofluidic applications. *Applied Physics Letters*, 86(4):041104, 2005.

[118] S. Zhang, D. A. Genov, Y. Wang, M. Liu, and X. Zhang. Plasmon-induced transparency in metamaterials. *Physical Review Letters*, 101(4):047401, 2008.

[119] D. J. Cho, F. Wang, X. Zhang, and Y. R. Shen. Contribution of the electric quadrupole resonance in optical metamaterials. *Physical Review B*, 78(12):121101, 2008.

[120] F.L. Pedrotti, L.S. Pedrotti, and L.M. Pedrotti. *Introduction to Optics*. Prentice-Hall, 1987.

[121] W.L. Barnes. Fluorescence near interfaces: the role of photonic mode density. *Journal of modern optics*, 45:661–699, 1998.

[122] G. Leveque and O. J. F. Martin. Optical interactions in a plasmonic particle coupled to a metallic film. *Optics Express*, 14(21):9971–9981, 2006.

[123] K. R. Catchpole and A. Polman. Plasmonic solar cells. *Optics Express*, 16(26):21793–21800, 2008.

[124] S. P. Sundararajan, N. K. Grady, N. Mirin, and N. J. Halas. Nanoparticle-induced enhancement and suppression of photocurrent in a silicon photodiode. *Nano Letters*, 8(2):624–630, 2008.

[125] P. Matheu, S. H. Lim, D. Derkacs, C. McPheeters, and E. T. Yu. Metal and dielectric nanoparticle scattering for improved optical absorption in photovoltaic devices. *Applied Physics Letters*, 93(11):113108, 2008.

[126] C. Hagglund and B. Kasemo. Nanoparticle plasmonics for 2D-photovoltaics: Mechanisms, optimization, and limits. *Optics Express*, 17(14):11944–11957, 2009.

[127] Y. A. Akimov, W. S. Koh, and K. Ostrikov. Enhancement of optical absorption in thin-film solar cells through the excitation of higher-order nanoparticle plasmon modes. *Optics Express*, 17(12):10195–10205, 2009.

[128] S. V. Boriskina and L. Dal Negro. Sensitive label-free biosensing using critical modes in aperiodic photonic structures. *Optics Express*, 16(17):12511–12522, 2008.

[129] C. Forestiere, G. Miano, G. Rubinacci, and L. Dal Negro. Role of aperiodic order in the spectral, localization, and scaling properties of plasmon modes for the design of nanoparticle arrays. *Physical Review B*, 79(8):085404, 2009.

[130] U. Fano. Effects of configuration interaction on intensities and phase shifts. *Physical Review*, 124(6):1866, 1961.

[131] F. Hao, P. Nordlander, M. T. Burnett, and S. A. Maier. Enhanced tunability and linewidth sharpening of plasmon resonances in hybridized metallic ring/disk nanocavities. *Physical Review B*, 76(24):245417, 2007.

[132] F. Hao, Y. Sonnefraud, P. Van Dorpe, S. A. Maier, N. J. Halas, and P. Nordlander. Symmetry breaking in plasmonic nanocavities: Subradiant LSPR sensing and a tunable fano resonance. *Nano Letters*, 8(11):3983–3988, 2008.

[133] F. Hao, P. Nordlander, Y. Sonnefraud, P. Van Dorpe, and S. A. Maier. Tunability of subradiant dipolar and fano-type plasmon resonances in metallic ring/disk cavities: Implications for nanoscale optical sensing. *ACS Nano*, 3(3):643–652, 2009.

[134] N. Verellen, Y. Sonnefraud, H. Sobhani, F. Hao, V. V. Moshchalkov, P. Van Dorpe, P. Nordlander, and S. A. Maier. Fano resonances in individual coherent plasmonic nanocavities. *Nano Letters*, 9(4):1663–1667, 2009.

[135] S. D. Liu, Z. S. Zhang, and Q. Q. Wang. High sensitivity and large field enhancement of symmetry broken au nanorings: effect of multipolar plasmon resonance and propagation. *Optics Express*, 17(4):2906–2917, 2009.

[136] M. Z. Liu, T. W. Lee, S. K. Gray, P. Guyot-Sionnest, and M. Pelton. Excitation of dark plasmons in metal nanoparticles by a localized emitter. *Physical Review Letters*, 102(10):107401, 2009.

[137] R. Singh, C. Rockstuhl, F. Lederer, and W. L. Zhang. Coupling between a dark and a bright eigenmode in a terahertz metamaterial. *Physical Review B*, 79(8):085111, 2009.

[138] J. B. Lassiter, H. Sobhani, J. A. Fan, J. Kundu, F. Capasso, P. Nordander, and N. J. Halas. Fano resonances in plasmonic nanoclusters: Geometrical and chemical tunability. *Nano Letters*, 10(8):3184–3189, 2010.

[139] Z. H. Liu, N. M. D. Brown, and A. McKinley. Evaluation of the growth behaviour of gold film surfaces evaporation-deposited on mica under different conditions. *Journal of Physics-Condensed Matter*, 9(1):59–71, 1997.

[140] E.M. Purcell. *Electricity and Magnetism*. McGraw Hill, 1965.

[141] M. J. Berg, C. M. Sorensen, and A. Chakrabarti. Extinction and the optical theorem. part I. single particles. *Journal of the Optical Society of America A-optics Image Science and Vision*, 25(7):1504–1513, 2008.

[142] M.L. Boas. *Mathematical Methods in The Physical Sciences*. John Wiley & Sons, USA, 1983.